NAVAL
POSTGRADUATE
SCHOOL

MONTEREY, CALIFORNIA

DISSERTATION

REDISTRIBUTION MECHANISMS AND QUANTIFICATION OF HOMOGENEITY IN FRICTION STIR WELDING AND PROCESSING OF AN ALUMINUM SILICON ALLOY

by

Jeffrey C. Woertz

September 2012

Dissertation Supervisor: Terry McNelley

Approved for public release; distribution is unlimited

THIS PAGE INTENTIONALLY LEFT BLANK

REPORT DOCUMENTATION PAGE		*Form Approved OMB No. 0704-0188*

Public reporting burden for this collection of information is estimated to average 1 hour per response, including the time for reviewing instruction, searching existing data sources, gathering and maintaining the data needed, and completing and reviewing the collection of information. Send comments regarding this burden estimate or any other aspect of this collection of information, including suggestions for reducing this burden, to Washington headquarters Services, Directorate for Information Operations and Reports, 1215 Jefferson Davis Highway, Suite 1204, Arlington, VA 22202-4302, and to the Office of Management and Budget, Paperwork Reduction Project (0704-0188) Washington DC 20503.

1. AGENCY USE ONLY (*Leave blank*)	2. REPORT DATE September 2012	3. REPORT TYPE AND DATES COVERED Dissertation	
4. TITLE AND SUBTITLE: Redistribution Mechanisms and Quantification of Homogeneity in Friction Stir Welding and Processing of an Aluminum Silicon Alloy		5. FUNDING NUMBERS	
6. AUTHOR(S) Jeffrey C. Woertz			
7. PERFORMING ORGANIZATION NAME(S) AND ADDRESS(ES) Naval Postgraduate School Monterey, CA 93943-5000		8. PERFORMING ORGANIZATION REPORT NUMBER	
9. SPONSORING / MONITORING AGENCY NAME(S) AND ADDRESS(ES) N/A		10. SPONSORING / MONITORING AGENCY REPORT NUMBER	
11. SUPPLEMENTARY NOTES The views expressed in this thesis are those of the author and do not reflect the official policy or position of the Department of Defense or the U.S. Government. IRB Protocol number _____N/A_____.			
12a. DISTRIBUTION / AVAILABILITY STATEMENT Approved for public release; distribution is unlimited		12b. DISTRIBUTION CODE A	

13. ABSTRACT (maximum 200 words)

The uniformity (homogeneity) of nondeforming particle distributions in a cast alloy's microstructure is highly important in controlling the material's strength, ductility, and fatigue resistance. Friction stir processing (FSP) is an effective post-casting technique for redistributing constituent material into a more homogeneous state, although the mechanism of particle transport remains unclear and no concise method exists for quantifying and comparing homogeneity.

Advective and diffusive redistribution processes are investigated in Al-7% Si and AA356 to determine the magnitude and rate of particle transport within a high-temperature deforming metallic matrix. High temperature deformation experiments were conducted via Equal Channel Angular Processing (ECAP), hot rolling, and FSP. Processed material was then examined using optical / scanning electron microscopy. The experimentally observed particle transport was compared against modeled and analytically predicted transport, while microstructural homogeneity was measured and compared using digital image analysis and a six-parameter variance model.

FSP redistribution is proposed to be the result of a matrix shear / layer sliding advective mechanism, the probable result of fine layers of material (ranging from 5 to 15 μm in thickness) that are sheared and rotated by the tool's pin face. Diffusive processes have only a small role in FSP redistribution. FSP is shown to increase homogeneity by a factor of ~5 (compared to as-cast), increasing linearly with tool RPM over the measured range.

14. SUBJECT TERMS Redistribution, Homogenization, Friction Stir Processing, Homogeneity, Aluminum Silicon, Mechanical Mixing, Diffusive Mixing, Advective Mixing, Al-7% Si, AA356, ECAP, FSP, Shear, Layer Sliding		15. NUMBER OF PAGES 279
		16. PRICE CODE
17. SECURITY CLASSIFICATION OF REPORT Unclassified	18. SECURITY CLASSIFICATION OF THIS PAGE Unclassified	19. SECURITY CLASSIFICATION OF ABSTRACT Unclassified	20. LIMITATION OF ABSTRACT UU

THIS PAGE INTENTIONALLY LEFT BLANK

REDISTRIBUTION MECHANISMS AND QUANTIFICATION OF HOMOGENEITY IN FRICTION STIR WELDING AND PROCESSING OF AN ALUMINUM SILICON ALLOY

Jeffrey C. Woertz
Commander, United States Navy
B.S., Civil Engineering, University of Illinois (Urbana-Champaign), 1992
M.S., Mechanical Engineering, Massachusetts Institute of Technology, 2002
M.S., Naval Architecture and Marine Engineering, Massachusetts Institute of Technology, 2002

Submitted in partial fulfillment of the
requirements for the degree of

DOCTOR OF PHILOSOPHY IN MECHANICAL ENGINEERING

from the

**NAVAL POSTGRADUATE SCHOOL
September 2012**

Author: _____
Jeffrey C. Woertz

Approved by:

_____   _____
Terry McNelley   Young Kwon
Distinguished Professor (Emeritus)   Distinguished Professor
Mech. and Aero. Engineering   Mech. and Aero. Engineering
Dissertation Supervisor   Dissertation Committee Chair

_____   _____
Luke Brewer   Hong Zhou
Associate Professor   Associate Professor
Mech. and Aero. Engineering   Applied Mathematics

_____
Sarath Menon
Research Professor
Mechanical Engineering

Approved by: _____
Knox Millsaps, Chair, Department of Mech. and Aero. Engineering

Approved by: _____
Douglas Moses, Vice Provost for Academic Affairs

iii

THIS PAGE INTENTIONALLY LEFT BLANK

ABSTRACT

The uniformity (homogeneity) of nondeforming particle distributions in a cast alloy's microstructure is highly important in controlling the material's strength, ductility, and fatigue resistance. Friction stir processing (FSP) is an effective post-casting technique for redistributing constituent material into a more homogeneous state, although the mechanism of particle transport remains unclear and no concise method exists for quantifying and comparing homogeneity.

Advective and diffusive redistribution processes are investigated in Al-7% Si and AA356 to determine the magnitude and rate of particle transport within a high-temperature deforming metallic matrix. High temperature deformation experiments were conducted via Equal Channel Angular Processing (ECAP), hot rolling, and FSP. Processed material was then examined using optical / scanning electron microscopy. The experimentally observed particle transport was compared against modeled and analytically predicted transport, while microstructural homogeneity was measured and compared using digital image analysis and a six-parameter variance model.

FSP redistribution is proposed to be the result of a matrix shear / layer sliding advective mechanism, the probable result of fine layers of material (ranging from 5 to 15 μm in thickness) that are sheared and rotated by the tool's pin face. Diffusive processes have only a small role in FSP redistribution. FSP is shown to increase homogeneity by a factor of ~5 (compared to as-cast), increasing linearly with tool RPM over the measured range.

THIS PAGE INTENTIONALLY LEFT BLANK

TABLE OF CONTENTS

LIST OF FIGURES

xiii

LIST OF TABLES

THIS PAGE INTENTIONALLY LEFT BLANK

LIST OF ACRONYMS AND ABBREVIATIONS

AA	Aluminum Association
AGG	Abnormal Grain Growth
ALE	Arbitrary Lagrange Euler
AR	Aspect Ratio
ECAP	Equal Channel Angular Processing
C_f	Particle Surface Coefficient of Friction
COV	Covariance
CV	Coefficient of Variation
cPs	Centipoise
D_{EQ}	Equivalent Diameter
FS	Friction Stir
FSP	Friction Stir Processing
FSW	Friction Stir Welding
HAZ	Heated Affected Zone
hp	Horsepower
H_s	Homogeneity Parameter
HPT	High Pressure Torsion
HY	High Yield
IPM	Inches per Minute
LSEM	Large Strain Extrusion Machining (LSEM)
MDF	Multi-directional Forging
MPa	Megapascal
MSAAF	Multi-scale Analysis of Area Fractions
MMC	Metal Matrix Composite
NAB	Nickel Aluminum Bronze
RPM	Revolutions per Minute
RVE	Representative Volume Element
SEM	Scanning Electron Microscope
sec	Seconds
SPD	Severe Plastic Deformation

SZ	Stir Zone
T_{Melt}	Melting Temperature
T_{Homog}	Homologous Temperature
TMAZ	Thermo-mechanically Affected Zone
TWI	The Welding Institute
VAR	Variance
2D	Two-Dimensional
3D	Three-Dimensional
$\delta\theta$	Angle of Shear
μm	Micron

ACKNOWLEDGMENTS

I am grateful for the guidance and participation of all my committee members: Professor Sarath Menon, Professor Luke Brewer, Professor Hong Zhou, and Professor Young Kwon. In particular, I would like to thank my advisor, Professor Terry McNelley, for his many hours of discussion, advice, and perspective. As is often the case, the destination was in the journey.

I would like to thank Dr. Chanman Park and Will Young for their assistance in the laboratory. In addition, I would like to extend much appreciation to Alberto Orozco Caballero for his metallographic advice, as well as to John Mobley and staff for their support with the machining work.

Most importantly, I would like to thank my wife, Christy, for her unquestioning support and confidence in me throughout these three years. To my sons, Sam and Will, I also say thanks for helping me to remember that there's always time to have a catch.

THIS PAGE INTENTIONALLY LEFT BLANK

I.   INTRODUCTION

A.   RELEVANCE OF THIS WORK

The effect of particle distribution in microstructures is widely understood to be an important feature in controlling a material's strength, ductility, and fatigue resistance. In many cast alloys, the microstructure consists of stiff, nondeforming particles, often irregularly dispersed in a softer, deformable metallic matrix, leading to poor mechanical properties. Uniform (or homogeneous) distributions of these constituent particles and other inclusions are well documented as improving the mechanical characteristics of the material when compared to the as-cast condition. The term "redistribution" can be used to describe the reordering of microstructure particle arrangements, ideally from an inhomogeneous to a homogeneous state. Post-casting techniques, such as friction stir processing (FSP), have been employed to improve uniformity, and when compared to other processing methods, FSP is a particularly effective method for redistributing constituent material. Despite this, the final microstructure particle distributions are highly dependent on process parameters (i.e., RPM, tool geometry) and generally unpredictable [1].

In order to better control the evolution of microstructure particle distributions, a more complete understanding of redistribution mechanism(s) must be acquired. This includes identifying the modes, magnitude, and rate of particle transport within a deforming metallic matrix, as well as factors that influence that transport. Also, an improved ability to define and quantify the homogeneity of a particle distribution is required, so that measurement of these distributions can be more directly correlated to process inputs and a material's mechanical performance. This work focuses on development in these two areas through modeling, experimental, and analytical approaches. Ultimately, an improved understanding of the factors that influence microstructure homogeneity may lead to more systematic methodologies for process parameter selection and tool design.

B. HOMOGENIZATION AND REDISTRIBUTION

1. Inhomogeneity in Common Marine Materials

This work will investigate primarily the effects of redistribution in deforming Al-Si model systems; however, similar observations involving redistribution have been made for a wide range of particle-containing materials. Materials such as Nickel Aluminum Bronze (NAB), high yield (HY) Steels, and AA5083 are common in many marine applications. Their microstructural homogeneity, and subsequently, their mechanical properties, can vary greatly according to the conditions in which the material was cast, formed, or processed [2]–[4]. Unlike the Al-Si system, some of these materials may also undergo transformations during the FSP thermal cycle that may influence the homogenization process. Nevertheless, the final structures of these materials often contain irregular dispersions of hard particles and other inclusions that affect mechanical performance. The three previously mentioned naval structural materials merit brief discussion, as the outcomes of this work may have practical applications for these materials' processing techniques.

NAB components, such as naval propellers, can be fabricated only by casting techniques. This process involves thick sections and slow cooling rates after casting. The prolonged cooling time results in coarse and inhomogeneous microstructures leading to poorer mechanical properties. Often, NAB materials are not heat treatable and relatively few options exist for strengthening of such components. FSP has been shown to produce more homogenous microstructures in NAB materials and may be an effective means for selective strengthening the surface of such components [2].

HY steels, used in submarine hull construction, frequently exhibit microstructural banding due to hot rolling of the inhomogeneous as-cast material. The result is alternating layers of the various constituents, leading to increased susceptibility to shear localization [3]. Banding of local inclusions may also occur, such as the case with MnS inclusions in HY 100 steel. MnS banding has been shown to increase strain localization in areas of high particle concentration, as compared to a more uniform inclusion arrangement [4].

AA5083, commonly used in sheet and plate form for naval and ocean going vessels, provides for excellent formability, strength, corrosion resistance, and weldability. Inclusions in aluminum alloys, such as dispersions of iron rich particles, can be detrimental to ductility and toughness, since damage often occurs at the matrix–particle interface during cold rolling in alloys containing hard particles [7]. Particle interface damage is more prevalent when particles are large or irregularly dispersed particles. This damage is not eliminated during recrystallization and can act as a source of nucleation sites for cavities during forming or processing. During tensile straining, diffusion and plastic flow at these particle interfaces leads to cavity growth, which can cause failure as the cavities become larger and / or interlink [7].

Al-Si model systems were chosen as a starting point for the investigation of redistribution and homogenization processes, since 1) the mechanical properties for these systems are well documented, 2) chemical and phase transformations should not occur so long as the material remains below the melting point, and 3) metallographic images from such a system are readily converted into quantifiable data. Eventually, the findings and methods introduced in this study could be extended to more complex, multi-phase systems.

2.   Microstructural Effects of Homogeneity in the Al-Si System

The microstructures in wrought aluminum are often characterized by stiff, nondeforming constituent particles that are present either as impurities or as intentional additions intended to control microstructure and other properties. The potential of such constituents to affect material properties is widely recognized. Particle size distribution, directionality, and spacing are known to exert a strong influence on microstructure and the material's mechanical properties [1]. Despite this fact, methods to quantify the homogeneity or uniformity of constituent distributions in metallic materials have only recently begun to receive renewed attention [8]–[13]. Also, the factors and mechanisms involved in redistribution of constituent particles have not been clarified.

Microstructure homogenization by redistribution of nondeforming particles often leads to marked increases in toughness and ductility, especially when combined with

3

grain refinement. However, not all deformation processing for grain refinement may lead to particle redistribution. As a brief example, Garcia et al. [14] conducted Equal Channel Angular Processing (ECAP) at ambient temperature following a redundant strain path for an as-cast Al-7% Si alloy and reported that the distribution of the initially nonuniformly distributed Si particles was not altered significantly despite the imposition of very large redundant strains. Figures 1.1 (a), (b), and (c) compare the microstructures observed in an Al-7% Si alloy (Na-modified) in the as-cast condition, after 4 ECAP passes by the redundant straining Route B_c, after FSP at 800 RPM at a 50.8 mm/min (2 in/min) traverse rate, respectively.   Homogenization via ECAP may require higher processing temperatures, thus activating diffusive processes that may result in particle motion through a softened Al matrix.

In contrast, FSP produces dramatic microstructural refinement.   After severe deformation by FSP, second-phase particles within the stir zone microstructure of the Al-Si alloy appear to have fractured and moved through the matrix, transforming the microstructure from a clustered, inhomogeneous state to a distinctly homogenous condition.

(a)   (b)   (c)
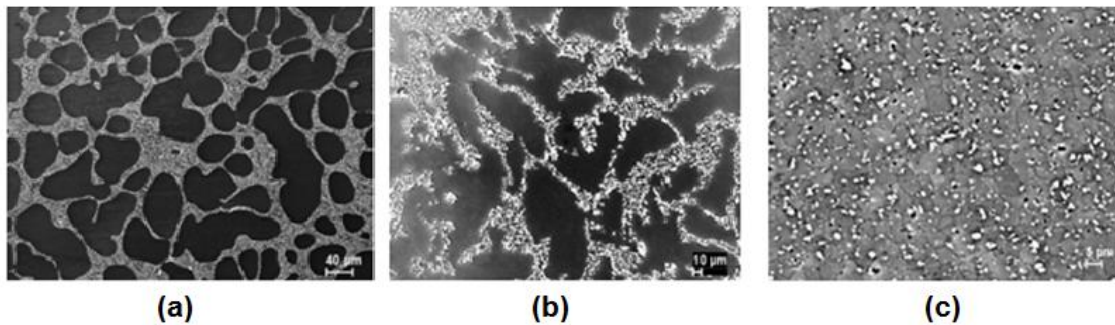
Figure 1.1 Secondary electron images showing the microstructures in Al-7% Si (Na-modified) alloy. The hard Si particles appear white in these scanning electron microscope (SEM) images: (a) as-cast; (b) after 4 passes by Route B_c in ECAP and (c) after FSP at 800 RPM / 50.8 mm/min (2 in/min) where the primary and eutectic constituents are no longer easily distinguished. From [15].

Momentarily setting aside a rigorous definition of a microstructural homogeneity, Al-Si alloys have been extensively studied in regard to the mechanical effects of the Si particle distribution.   Micro-mechanisms of fracture are significantly affected by the

characteristics of the Al matrix, the particle-matrix interface, degree of constituent clustering, and a number of other particle characteristics. Many reports [15]–[21] have repeatedly confirmed, both experimentally and computationally, that the size, shape, volume fraction, spacing, gradation, clustering tendency, and orientation of reinforcement particles can all significantly alter a particle-containing material's ductility, strength and toughness during static, dynamic, and fatigue loading. That is, the orientation and size characteristics of the reinforcement particle distribution may create conditions whereby strain localization in the surrounding matrix can lead to fracture [6]. As a result, any existing crack will have a preferential path by which to propagate as void growth and coalescence occurs at these sites.

Despite the overwhelming amount of microstructural, mechanical testing, and computational evidence attesting to the importance of uniformity and homogeneity in microstructures, the mechanism(s) involved in the redistribution of nondeforming constituent particles in a severely deformed two-phase solid remain unclear. Furthermore, only a few objective measures of homogeneity have been either proposed or widely employed within the materials research community [8].

C.   REDISTRIBUTION AS MASS TRANSPORT

In the FSP of an Al-Si alloy, it can only reasoned that the redistribution of the second phase Si particles is a mass transport process. Discrete clusters of Si particles are broken up and physically dispersed within the stirred volume, with many particles undergoing fracture and some material being pulled in from beyond the radius of the tool shoulder. If it can be successfully argued that mass transport processes, either advective (i.e., bulk deformation) or diffusive (i.e., vacancy migration) processes are activated during FSP. The first logical approach to better understanding their relative contributions is to systematically identify and evaluate the effects of all possible diffusive transport potentials.

1.   Bulk Transport and Diffusive Processes

Mass transfer is the net movement of mass from one point to another point [27]. In FSP, there is clear evidence of advective transport (bulk matrix motion) as evidenced

by the variegated flow patterns often observable in the stir zone. This bulk motion is governed by the processing parameters, namely: tool geometry, rotational speed, downward force, and bulk material properties. The bulk matrix motion transports whole and fractured particles from location to location. However, microscopy suggests that bulk deformation may not fully account for the total particle transport and the degree of homogenization often noted in FSP. Complete homogenization may therefore be a result of the relative motion between a particle and its surrounding medium due to vacancy migration, i.e., a diffusive process. Otherwise, the final microstructure might be accurately predicted based solely on the displacement field corresponding to the imposed strain.

Shear is the deviatoric portion of a stress field which produces flow [27], and a hydrostatically confined shear should be the appropriate stress state for FSP conditions. Multi-pass ECAP can achieve high homogeneous monotonic shear strains, and at very high numbers of passes, the microstructure can appear more uniform due solely to shape change. ECAP microstructures, however, differ from those in FSP in that a clear bias in particle orientation is readily observed, similar to that seen in rolling operations. Furthermore, large shape changes driven by these homogeneous strain paths do not result in the primary regions becoming populated with particles, rather the particle-depleted regions become increasingly thin. As a result, it can be argued that large homogeneous monotonic strains alone cannot produce redistribution as one observes in FSP.

2.   Additional Driving Potentials

During redistribution, perhaps due to temperature, strain path, or strain rate, the activation of one or more diffusive transport potentials may develop within a volume element of material. These potential(s) are additive and serve to act in combination with the bulk transport caused by matrix flow. The term "drift" can used to describe the combined effect of all the relevant transport potentials fields: electrical, thermal, chemical, stress, and centrifugal [23]. Note that, the effects of an electrical potential will be considered negligible in deformation processing. Drift is always occurring to some degree, but it is unclear whether the magnitude of these potentials can be developed

sufficiently such that particle drift would explain the resultant microstructures within a stir zone. The mass transport driving potentials are summarized in Table 1.

Table 1.1   Mass transport driving potentials. After [23].

Electrical Potential Gradient, $E=d\phi/dx$	qE	q = charge
Temperature Gradient dT/dx	$-(Q/T)dT/dX$	Q = heat transport
Chemical Potential Gradient	$-kT(\delta Log\gamma/\delta x)$	γ = Thermodynamic Activity coefficient
Stress Gradient	$-dU/dx$	U = Elastic interaction energy in stress field
Centrifugal force	$m\omega^2 r$	m = effective molecular mass, ω = angular velocity

3.   Redistribution Investigation Strategy

Many limitations exist in realistically modeling the redistribution of many small irregularly shaped particles that may be traveling with and / or through a rapidly deforming metallic matrix at high temperature. A combined experimental, computational, and analytical approach is the most effective strategy for better understanding the role of strain path, strain rate, and temperature in FSP redistribution. The reported literature describes FSP as a high-temperature, shear-dominated extrusion process wherein the frictionally heated matrix material can be treated as a flowing, non-Newtonian fluid, or a high temperature visco-plastic. If advective and / or diffusive processes are inducing particle transport in this state, these phenomena might be observable at lower deformation strain rates by subjecting the material to a similar shear-extrusion strain path at elevated temperature. Also, physical behaviors might be captured at ambient temperature by deforming a particle-containing visco-plastic analog material. In either case, experimental observations of second phase particle motion could be used to validate modeling and analytical approaches.

D.   MEASURING AND QUANTIFYING HOMOGENEITY

1.   Homogeneity Defined

The term "homogeneity" can be broadly defined as a departure from variability where a finite limit is imposed on the degree of that departure [23]. Homogeneity is of obvious importance in a variety of fields wherein the effect of mixing parameters must be characterized and quantified. In the food science, pharmaceutical and chemical engineering industries, the final distribution of a mixture may be a primary determinant in product quality. These fields encounter mixtures of many types (e.g., slurries, particle containing visco-plastics), but encounter the same obstacles in defining and measuring homogeneity, which is often termed "mixedness" or "mixing quality". As in those fields, the main difficulties in microstructural investigations are: (1) determining what measurable parameters and length scale best characterize the mixture and (2) determining an appropriate method for measuring those parameters on multiple length scales.

2.   Measurable Parameters

As a result of the work in other fields, a variety of statistical approaches is already available to describe mixture distributions. These methods might be readily applied to metallic materials subjected to homogenizing processes such as FSP. The statistical aspects are relatively straightforward. The initial task is to select and apply a set of relevant, straightforward normalized parameters which can fully characterize the homogeneity of dispersions in a metallic system. Size, shape, area fraction, spacing, clustering tendency, and orientation appear to be the most logical variables to quantify at the outset, given the recognized mechanical effects of these quantities.

3.   Approach for Measuring Microstructural Homogeneity

Depending on the material, characteristic particle parameters have been observed to correspond with various distribution types, including but not limited to: random, lognormal, gamma, Weibull, or Poisson distributions [12]. In the transition to a more homogeneous state, the distribution of a microstructure's particle parameters (i.e., particle size, spacing, aspect ratio) is changing due to matrix deformation, particle comminution,

and possibly diffusive processes. Measurement of that change first requires an accurate, standardized method for analyzing particle distributions and microstructure image. Fortunately, this task can be accomplished through digital image analysis. To analyze homogeneity, additional steps are required. A microstructure's image must be divided into many sub-regions and the distributions of particle parameters within individual sub-regions must be statistically compared. In doing so, a homogeneity index can be generated based on regional variances. This objective measurement of homogeneity could then be used to compare two materials directly and possibly, to link the measured parameters of a micrograph to a material's expected mechanical performance.

E.   PROPOSED OUTCOMES OF WORK

1.   Particle Redistribution

The redistribution observed during deformation of metallic materials is a mass transport process. At a minimum, second phase constituents experience displacements corresponding to the impose strain state. To examine the further effects of redistribution, a multi-faceted approach will be employed which draws upon the research of communities outside of metallurgy who have examined analogous transport problems. This portion of the work will:

- Carry out systematic experimental investigation for Al-Si systems over a range of strain paths and strain rates as a function of temperature. Experimental work for the investigation will include hot rolling, ECAP at elevated temperature, and FSP.

- Estimate the magnitude of deformation-induced driving potentials through computational and analytical modeling. Compare the experimentally observed motion of nondeforming particles with the predicted motion due to advection and diffusive potential drivers using material properties of the Al-Si system.

- Execute analog transparent visco-plastic media shearing experiments to compare the clustered particle dispersion behavior with modeled results.

- Determine the morphological effects (e.g., the degree of particle fracture and stir zone (SZ) size variation) that result from varying RPM / IPM and tool design during FSP, and correlate these effects to microstructural homogeneity.

- Identify an explanation for the processes involved in homogenization and redistribution during FSP, i.e., determine the degree to which a particle is transported by bulk motion versus via diffusive processes and investigate the possibility of advective (mechanical mixing) mechanisms.

- Model a volume element's deformation and matrix reordering using a discrete layered approach involving shear and rotation, i.e., synthetically deform a microstructure to specified strains.

2. Homogenization Quantification and Standardization

Quantification of homogeneity requires the capability to accurately digitize and analyze a microstructure. This capability has greatly expanded in MATLAB Digital Analysis Toolbox in the past several years. The focus of this effort will be to build upon the prior efforts of Spowart et al. [1]–[13], in order to assemble a multi-parameter description of homogeneity for two- phase metallic materials. This portion of the work will:

- Develop a reliable and accurate digital quantitative measurement method for capturing the important particle distribution parameters over multiple length scales (e.g., particle size, population, spacing, aspect ratio, volume fraction, and directionality).

- Introduce an overarching multi-parameter definition of homogeneity for a metallic material containing dispersed particles, such that a single homogeneity value can be assign to a microstructure at a given length scale.

- Apply the developed multi-parameter model in characterizing and comparing microstructures—e.g., of Al-Si alloys in the processed and as-cast conditions, as well as synthetically generated microstructures

- Employ the multi-parameter model in examining the mixing quality for different tool geometries over varying FSP RPM / IPM conditions, as well as to quantify the mixing quality in different regions of the SZ and TMAZ.

II. BACKGROUND AND LITERATURE REVIEW

A. MICROSTRUCTURAL EFFECTS OF PARTICLE DISTRIBUTIONS

For decades, it has been recognized that a material's microstructure dictates its macro-scale properties. Furthermore, the heterogeneity of the material's microstructure, i.e., the distribution of reinforcement phases or unintended inclusions, can significantly alter end quality. The characteristics of the included material cover a wide range: size, shape, spacing, clustering, directionality, stiffness, interfacial conditions, etc. The effects of these parameters are discussed in the following section.

1. Particle Size and Spacing

When a hard, nondeforming second phase is dispersed in a soft matrix at room temperature, gradients in deformation are produced as the material is placed under thermal or mechanical loads. The gradients arise due to the fact that the more rigid particles do not deform as much as the far-field matrix, so long as the particle / matrix interface remains intact. To maintain compatibility, the matrix close to the particle is constrained by the interface, resulting in deformation gradients. These gradients often produce what Ashby [25] termed "geometrically necessary dislocations," resulting in increased work hardening. The degree of work hardening is directly related to the size and distribution of the second phase constituent, where, for a given volume fraction, smaller more closely spaced particles increase the rate of work hardening. Essentially, the effect of putting a distribution of particles in a matrix material is to cause zones of high stress between the particles, which links them together in a fiber-like stress distribution, oriented along the line of loading [26]. This idea is particularly important when linked with continuum plasticity models, such as Eshelby's model, which proposes that, in a small volume of matrix material, flow around a particle will occur if the applied stress exceeds the flow stress [27]. Together, the two concepts could be extended to determine the physical conditions in which a hard particle can have mobility through a soft, solid medium.

2. Particle Shape

The influence of the shape of particle reinforcements is also of substantial interest. Most particle-reinforced MMCs and alloys contain angular, sharp-cornered particles, rather than spherical particles that are more easily modeled. Li and Ramesh [28] show numerically that high aspect ratio elliptical and cylindrical particles, uniformly aligned in the direction of loading, provide more effective reinforcement than spheroidal particles in high strain rate compressive deformation. This analysis assumed perfect particle matrix bonding, uniform arrangement, and no variation in particle alignment. Similarly, Geni and Kikuchi [29] showed that SiC reinforced aluminum with uniformly distributed, high aspect ratio particles has increased tensile strength as compared to the same material with spheroidal particles. Their analysis of a nonuniform model showed, however, that fracture occurs where the local particle volume fraction is the largest and in areas of high aspect ratio particles, and that global fracture occurs by linkage of these locally fractured areas. Their overall conclusion was that the mechanical properties of a composite material are improved if the particles are equiaxed and distributed uniformly in the base matrix. In order to increase the ultimate strength and ductility of the material, it is better to increase the particle volume fraction than to increase the aspect ratios for rigid, well-bonded particles.

3. Clustering Effects

The effect of the reinforcement spatial distribution on the mechanical behavior in a model MMC under uniaxial tension was studied by Segurado et al. [30]. Homogeneous microstructures were generated in the form of random dispersions of spheres. Inhomogeneous materials were idealized as an isotropic, random dispersion of spherical regions, each of which was a cluster. Numerical simulations showed that the reinforcement material's average maximum principal stress ranged from 12% to 16% higher for the inhomogeneous materials. It was also found that the presence of clustering increased the number of fractured particles by 3 to 6 times, leading to a significant reduction of the composite flow stress and ductility.

Leon [18] found through three-dimensional (3D) tensile deformation modeling of particle-reinforced metal matrix composites (MMC) that the flow stress and degree of hardening of a composite material is lowest for a highly graded particle arrangement but highest for an irregular microstructure. Composites with clustered particles exhibit higher flow stress due to more severely strain-hardened matrix compared with composites with uniformly distributed particles. Clustered regions were found to be preferred sites for damage initiation and damage accumulation ahead of a propagating crack [16].

Sreeranganathan et al. [31] numerically investigated the effects of porosity and reinforcement particle clustering on the mechanical properties of extruded, discontinuously reinforced aluminum alloy composites possessing nonuniform microstructures with long-range spatial correlation. They reported that spatial clustering of the reinforcement particles reduced the strain-hardening capacity of the composites while the porosity significantly lowered the 0.2% offset yield strength. It should be noted that, in practice, extrusion and large hydrostatic pressures decrease the number of pores and improve interfacial bonding strength, thus improving the mechanical properties of the composites [32]. At smaller scales, Law et al. [33] have recently shown that random, nonclustered and highly clustered particle arrangements result in the highest and lowest flow stress, respectively. Particle fracture in a reinforced nano-composite is also more likely with a less clustered particle arrangement. The less clustered arrangement showed particle damage beginning earlier and the fraction of damaged particles to be higher as compared to regular rectangular or highly clustered arrangements. This result indicates that, below a particular particle length scale, reinforcement behavior is altered and clusters effectively act as particles of a larger size.

4.   Crack Propagation

One of the desirable characteristics of particle-reinforced composites is the ability to deflect cracks and slow crack propagation by reducing the crack tip driving force. Ayyar and Chawla [34] found that as an applied tensile load is increased, particles ahead of a crack tip fracture and tend to attract a crack and affect its trajectory. Clustered and

homogeneous particle distributions were modeled. The particle influence on crack path was greater in a homogeneous distribution due to a larger number of direct crack-particle interactions. This particle "shielding" effect is significantly reduced or lost when particles ahead of the crack tip are already fractured [34]. These models did not incorporate plasticity, which tends to relieve the stress at the crack tip, but the simulations correlated well with experimental observations.

5. Particle Interface Conditions

Tensile testing often shows a preference for fracture near the matrix / particle interface [15]. A numerical analysis from Romonova et al. [35] investigated tensile and compressive fracture behavior of an AA6061 / Al_2O_3 particle-reinforced composite. The result showed that the heterogeneity of the composite gives rise to a complex stress state near the particle interface, which is undergoing deformation in either tension or compression. Particle fracture was found to occur by two mechanisms: interface debonding leading to void formation, and particle cracking. A higher particle surface roughness resulted in higher stress concentrations and earlier crack nucleation in the vicinity of the interface. The onset of particle fracture is directly affected by the strength of the interfacial layer. This effect is especially pronounced in the case of a spherical particle where de-bonding is usually the dominant fracture mechanism. By strengthening the interface layer, the de-bonding mechanism is prevented. With regard to redistribution, these reported results indicate that particle fracture may be a relevant parameter with which to assess the frictional condition present at the particle interface, and thus particle mobility.

B. REDISTRIBUTION IN THERMO-MECHANICAL DEFORMATION

Knowing that particle size and volume distributions have a direct and important impact on mechanical performance, the next issue that arises is understanding how beneficial size and spacing distributions can be practically achieved in real materials, particularly in discontinuously reinforce MMC's or two phase alloys. To do so, it is first necessary to understand second phase constituent behavior when subjected to various strain paths. In this section, several high-strain, high-temperature deformation processes

are compared in their ability to produce homogenized structures. Those processes reviewed are Friction Stir (FS), hot extrusion, hot rolling, Equal Channel Angular Processing (ECAP), Large Strain Extrusion Machining (LSEM), Multi-axial forging, and High Pressure Torsion (HPT). Table 2.1 lists some key characteristics of each of these processes.

Table 2.1   Characteristics of several thermo-mechanical deformation processes. After [21]–[48].

	FSP	ECAP	Extrusion	Rolling	Multi-axial Forging	HPT	LSEM
Hydrostatic Confinement	x	x	x			x	
Rotation	x				x	x	
Shear	x	x	x			x	x
Compression Loading	x	x	x	x	x	x	
High Temperature	x		x	x	x	x	
High Deformation Rate	x						x

1.   Friction Stir (FS)

Friction stir (FS) technologies [21] have emerged as solid-state Friction Stir Welding (FSW) or processing (FSP) methods, and have been increasingly used in naval and aerospace applications. In fabrication by welding, significant interest has always existed in development of weld processes that might produce more homogeneous weld zones. FS has great advantages in this area when compared to conventional fusion welding where, in practical applications, little can be done directly to control microstructural homogeneity. For aluminum naval sheet and plating in particular, conventional welding techniques must incorporate large design strength knockdowns to account for alloy type, geometric imperfections, softening in the heat-affected zone, residual stresses, etc. For some heat-treated aluminum alloys, the local material strength in the Heated Affected Zone (HAZ) can be reduced by 50% or more, as compared to the the parent material's strength [22].

The microstructures produced by FSW / FSP are sensitive to many considerations, but they are frequently highly homogeneous, refined in grain size, and exhibit the

attendant benefits in mechanical properties. As an example, stress-strain data from the stir zone (SZ) of a Na-modified FSP Al-7% Si alloy showed that the ductility of the as-cast material is improved up to 40%, while the strength is only marginally affected [17]. Furthermore, the previously discussed MnS inclusions, present in wrought steels, may be refined in size and redistributed as equiaxed particles by FS without residual damage in the form of matrix or particle cracking [36]. Similarly, the as-cast AA356 microstructure consists of an Al-Si eutectic embedded in a primary dendritic Al solid solution matrix, and the conversion of the cast structure to a homogeneous particle distribution results in greatly improved yield strength / ductility combination [37].

FS appears to be particularly effective in refinement and homogenization when compared to other thermo-mechanical processes. The recovery, recrystallization, and grain coarsening mechanisms are reasonably well understood, whereas the constituent redistribution mechanism is not [38]. It is recognized that systematic grain size variation occurs within the SZ / weld nugget. At times, abnormal grain growth (AGG) is encountered in regions affected by the tool shoulder. Constituent particles may or may not be involved in grain size variation and AGG. In regard to redistribution, this work considers only particle morphology and distribution, which, in turn, will affect grain size and grain growth. However, the latter topics, however, are not treated here. Though it is often reported / observed that FSP processes lead to substantially homogenized microstructures with uniformly distributed and refined micro-constituents, complete homogenization is generally not obtained in single-pass FS structures—i.e., they often have residual band-like features or onion ring patterns in which grain size varies and constituent particles are not uniformly distributed. In addition, steep temperature and strain gradients are produced in the regions separating the stir zone and the base material. These gradients and the accompanying phase transformations in turn produce large, undesirable variations in the microstructure's mechanical properties [1].

2. Hot Extrusion and Hot Rolling

Extrusion processes employ a variety of die shapes and geometries that can form a wide array of microstructures. In some cases, die wall friction during extrusion can

produce a gradient in strain across a billet's volume, with material moving faster at the periphery than at the center [39], resulting in inhomogeneous and often elongated bands of microstructure constituents. Extrusion is generally executed at temperatures above the material's recrystallization temperature so as to preclude work hardening, an approach which lowers the material's flow stress and reduces the required die pressures. As compared to the parent as-cast materials, more uniform microstructures can develop during high temperature extrusion processes if the reduction ratio is severe [40]. Even so, the degree of homogenization achieved during extrusion is low.

Hot-rolled microstructures are not unlike extruded material, usually having a final "pancaked' morphology with elongated stringers aligned in the direction of rolling. With a properly selected thickness reduction, redundant shear is avoided and the rolling will tend to produce a homogeneous strain, but again, complete homogenization is not usually seen. Elongated bands are compressed in the thickness direction resulting in a reduction in overall particle spacing and increased dispersion of particle agglomerations. The result can lead to improved mechanical properties in the rolling direction [40].

3. Compressive Forging Processes

Palmiere et al. [41] examined redistribution effects in an AA 2618 / SiC 17% MMC by subjecting it to either axisymmetric compression or extrusion at high temperature. They found that the ductility of the particle reinforced MMC increases with increasing deformation temperature, as indicated by the larger strain to failure. The MMC's maximum flow stress also decreased markedly as temperature rose above 350°C. Higher deformation temperatures and strain led to a moderately more homogeneous spatial distribution of particles in the MMC as a result of SiC particles fracturing and redistributing in the alloy matrix. Also, for the same level of strain, particle fracture was considerably less frequent as temperature increased. Homogeneity assessments of spatial distribution were made by comparison with a tessellation pattern using a uniform square lattice array of particles having the overall distribution's mean diameter.

Haghshenas et al. [43] subjected cylindrical specimens of thixocast AA356 to hot compression at temperatures of 450°C, 500°C, and 540°C and strain rates of 10^{-2} sec^{-1} to

10^{-4} sec-^{1}. The samples were compressed to a total true strain of 0.60 and then quenched to ambient. At higher temperatures, the lower matrix flow stresses gave rise to greater particle redistribution. At lower strain rates, redistribution appeared more significant given that the matrix material had more time in which to flow prior to quenching. Spheroidization of the silicon was attributed to an interdiffusion mechanism.

Nie et al. [44] used high temperature multi-directional forging (MDF) to study the microstructural evolution of AZ91-10% SiC. In MDF, a compressive load is sequentially applied along the sample's three axes while maintaining the original sample dimension ratios. The particle-reinforced matrix was fabricated by stir casting and had a 10 μm mean particle size. The MDF was carried out at 420°C using a rectangular sample with dimensions of 30 mm × 30 mm × 60 mm at a pressing speed of 15 mm sec^{-1}.

Their results indicated relatively little particle motion and no significant homogenization even after 6 MDF passes. The final structure resembled a rolled material with elongated particle stringers or bands in which minimal particle fracture was observed. The banded, elongated regions of particles were attributed to improved particle / matrix interface bonding. A significant increase of grain size was also noted after 6 MDF passes, which was attributed to the long periods of heat exposure.

4.   Equal Channel Angular Processing (ECAP)

ECAP, briefly addressed in Chapter I, was originally developed by Segal [45] and coworkers as a method to homogenize the microstructures of cast billets. Processing consists of four unique routes (shown in Figure 2.1) that subject a billet of material to an approximately homogeneous shear while constrained hydrostatically. Since the cross-sectional area of a billet is unchanged during a single pass, very large homogeneous strains may be achieved in bulk material through repetitive ECAP operations. Because of the stress state and the potential to achieve high levels of strain, ECAP provides a unique platform through which to understand the potential mobility of second phase particles when subjected to large monotonic or redundant shearing strains.
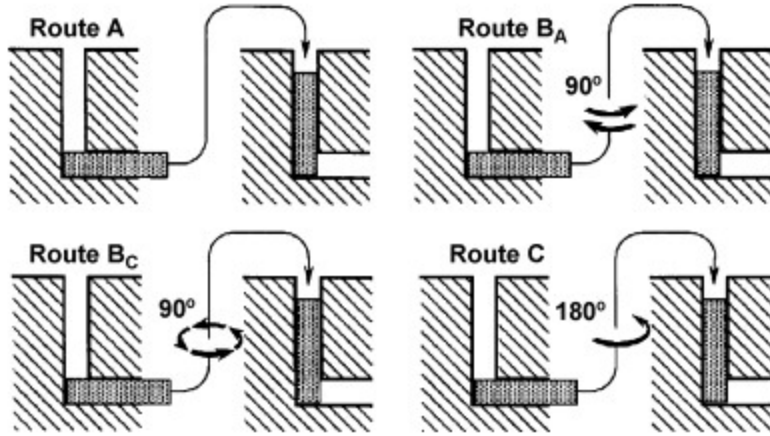
Figure 2.1   Defined ECAP Routes. From [46].

ECAP is well understood as a grain refinement process, but as reported by Garcia et al. [14] the process does not uniformly redistribute material in a processed billet at ambient temperature during redundant straining in routes C and B_C. Processing by these redundant routes resulted in significant strengthening, but a large reduction in ductility, likely a result of the fact that the nondeforming second phase did not redistribute within the matrix [17].

When subjected to the monotonic strain path, Route A, the final structure of Al-7% Si showed a refined grain size but the second phase Si particles, again, were not uniformly redistributed. Instead, elongated bands grew closer in spacing as the number of passes increases. A recognizable directionality still existed in the structure, indicating that particle displacement was due primarily to the displacement field of the externally imposed deformation. Substantial relative motion between the particles and matrix did not occur [17]. Akhmadeev et al. [45] also showed that the large cumulative plastic deformations produced in ECAP result in significant grain refinement and similar corresponding improvements in mechanical properties.

Cepeda-Jiménez et al. [46] conducted comparative study of a hypoeutectic Al-7% Si casting alloy by subjecting it to high pressure torsion (HPT) and multi-pass ECAP at ambient temperature. While the study did not focus on homogenization per se, the results

(represented in Figure 2.2) confirmed Garcia's earlier ECAP work by clearly showing that ambient-temperature, redundant ECAP straining did not homogenize a two phase structure.
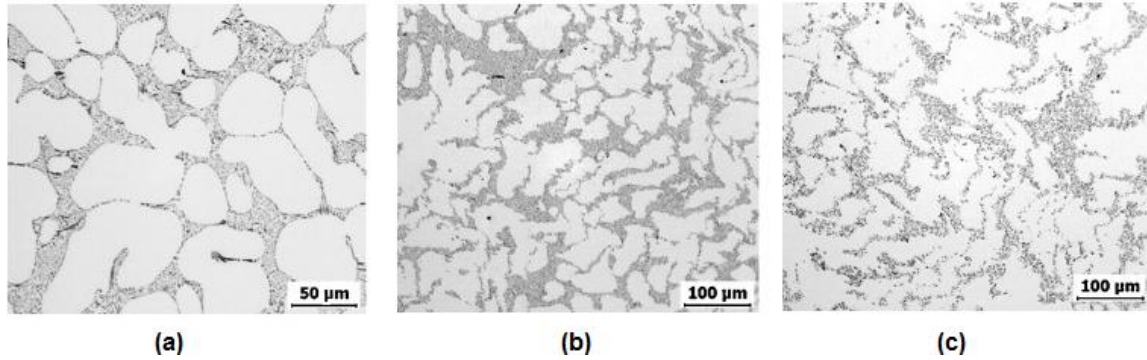
Figure 2.2 Optical micrographs Al-7% Si alloy: (a) as-cast, (b) 4 pass ECAP by Route B_c at ambient temperature (c) 8 pass ECAP by Route B_c at ambient temperature. From [46].

5.   Large Strain Extrusion Machining (LSEM)

Large Strain Extrusion Machining (LSEM) involves a cutting tool to remove a continuous chip from a metal surface. Typically, the process involves strains of 5 to 6 depending on the rake angle, depth of cut, and geometry of the shear zone. With the correct input parameters (cutting speed, cut depth, material characteristics, rake angle, etc.), the resulting chips can exhibit submicron size grains. [48]   Little is known regarding the process's potential to redistribute dispersed particles. Although LSEM will not be examined in this work, it is worth noting that LSEM produces a very fine sheared layer below and ahead of the cutting edge, which is pushed upwards by the tool face. The resulting chips appear more homogeneous than the base material, but have clearly visible shear bands consisting of discrete layers of base material that are stacked vertically as the chip is extruded (see Figure 2.3). LSEM and FSP appear to have some similarity with regard to the stress state and strain path during deformation, but the two processes differ distinctly in that FSP material is constrained by high hydrostatic pressure, which tends to forge the material.
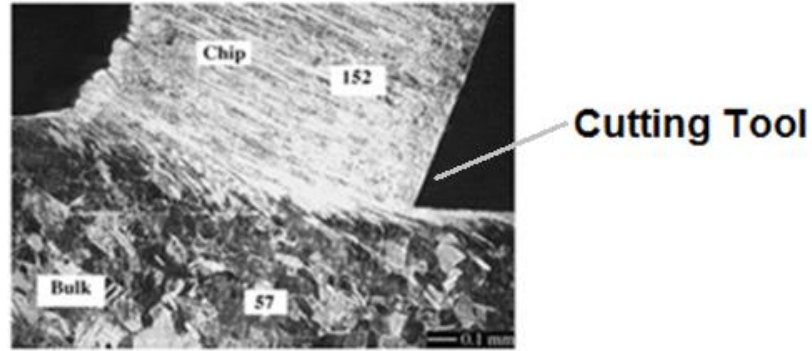
Figure 2.3 Cross-section view of a chip formed via LSEM, showing a narrow deformation zone and "flow-line" type chip microstructure. Note the improved homogeneity of the chip as compared to the bulk. After [48].

6.   High Pressure Torsion (HPT)

High pressure torsion (HPT) subjects a disk of material to a high applied pressure and concurrent torsion straining, leading to submicron and potentially nano-sized grains [49]. HPT has recently attracted much attention, and numerous reports are now available that describe the application of this processing method to a range of pure metals and solid solution alloys. Only a small number of reports are available on the application of HPT processing to two-phase metallic alloys and the resulting microstructural evolution. Studies of HPT processing at elevated temperature are more limited.

Langdon et al. [49] subjected a Zn–22% Al eutectoid alloy to HPT using a 10 mm diameter, 0.8 mm thick disk at ambient temperature. The ambient temperature results showed evidence for homogenization at the outer edges of the sample for 4 rotations where the directionality of the strain is no longer well-delineated. This result represented an approximate equivalent strain of 90. It should be noted, estimates for equivalent strain in FSP materials are lower by an order of magnitude. At these high strains, the homogeneity of the material improved, but a lamellar structure was still faintly apparent. From this result, a reasonable argument can be made that even extraordinarily high heterogeneous strains do not lead to complete homogenization, at least at ambient temperature. Rather, bands of material are simply being elongated and thinned to such an extent that the band thickness approaches the constituent particle size. As in LSEM processing, the HPT results suggest that a degree of homogeneity may be achieved

21

through the mechanical thinning and reordering of the particle-containing material. In either high or low equivalent strain processing methods, an elevated temperature may still assist in redistribution by accelerating particle transport diffusive processes.

In HPT processing of Al-7% Si [46], the initial compression combined with the prolonged shearing of the primary Al dendrites, produced an apparently homogeneous Si particle distribution in the Al matrix at the periphery of the HPT 10 mm diameter disk (Figure 2.4(b)). At this edge location, an approximate equivalent strain of 73 can be calculated. At the disk's center (Figure 2.4(a)), with an equivalent strain of 1.8, the Si particles are clearly not distributed homogeneously but do appear follow flow lines corresponding to the torsional strain path.
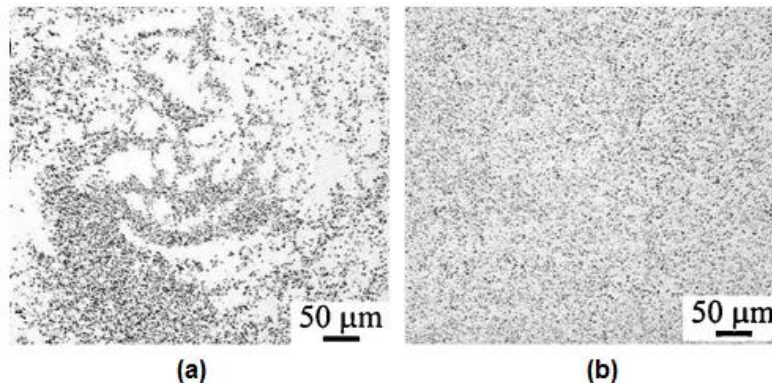
Figure 2.4 Optical micrographs of the HPT 10 mm diameter disk of Al-7% Si after five turns (a) at the disk center (b) on the outer disk periphery at r =0.4 mm (80% of the disk radius). From [46].

C.   REDISTRIBUTION IN MIXING PROCESSES

If redistribution, particularly in the case of FSP, were to be viewed as mass transport process involving mechanical mixing, the high apparent viscosity of a flowing metal would dictate that the process be laminar in nature. Laminar mixing is deterministic and can be more precisely described as either dispersive or nondispersive. As described by Kaufman et al. [50], dispersive mixing is characterized by extensional flow and shear stresses, which promote the breakup of cohesive agglomerations.

22

Nondispersive, or distributive mixing, involves the spatial separation and repeated rearrangement of a component to increase spatial homogeneity.

1. Dispersive and Nondispersive Mixing

Often, mixing is thought of in terms of a liquid-liquid phase or liquid-solid phase, but seldom in terms of a rigid solid embedded in a soft solid. For soft solids or fluids of very high viscosity (rheological materials), inertial forces very quickly dissipate once the motive force is removed. Close to a rotating source, i.e., an impeller blade, very large velocity gradients exist, producing a region of very high shear gradients [51]. As a representative volume element passes through this region, it is progressively thinned and elongated (shown in Figure 2.5), analogous to the deformation of metallic material undergoing monotonic, homogeneous shear.
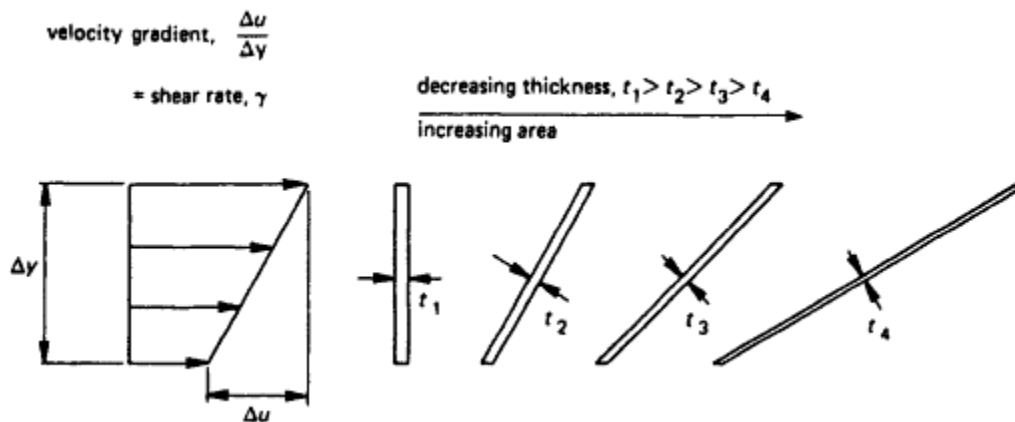
Figure 2.5 Thinning of a volume element in a viscous shear flow. From [51].

Extensional flow (shown in Figure 2.6) occurs in when directional velocity increases, again leading to a thickness reduction and an increased surface area. From a geometric perspective, the extensional flow may be analogous to the deformations observed in hot rolling. It should be noted, that the stress resulting from either shear or extensional flows can result in the breakup of agglomerations [51]. The combined effects of shear and extension represent the mixing action occurring in dispersive type flows.

23
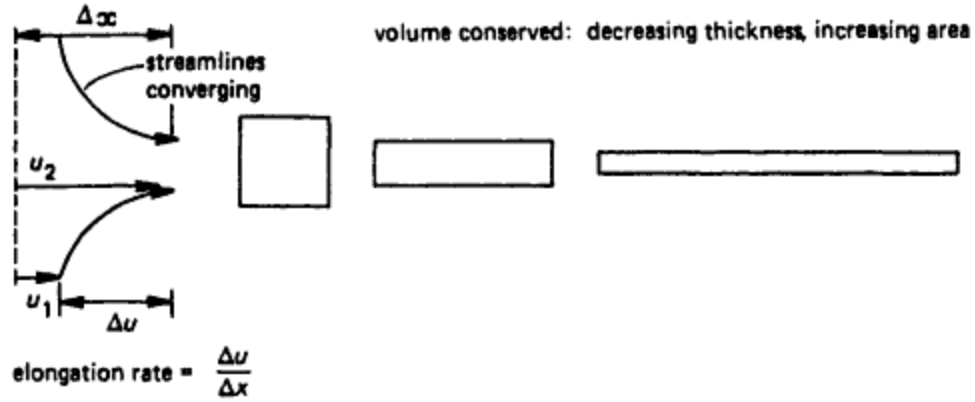
Figure 2.6   Thinning of a volume element in an extensional flow. From [51].

In nondispersive mixing, redistribution occurs by physically cutting the initial volume element into smaller elements and separating the cut sections through repetitive twisting and folding [51]. A schematic of the nondispersive mechanism is shown in Figure 2.7.
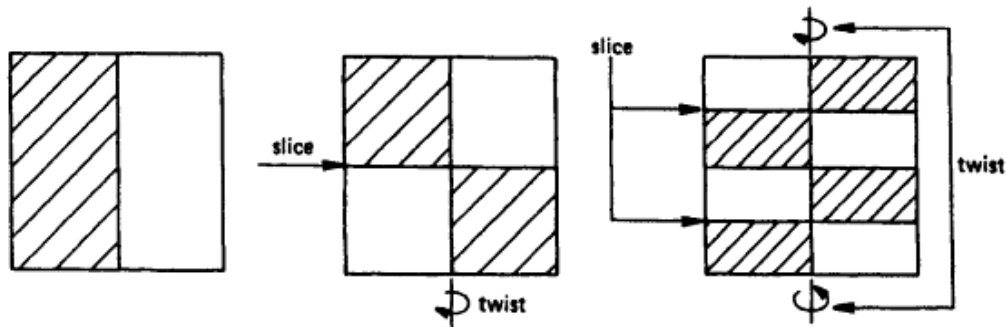
Figure 2.7 Nondispersive mixing of a volume element via cutting and folding. From [51].

2.   Diffusive Assistance in Mixing

Molecular diffusion is always occurring in combination with shearing and extensional flows. Arguably, total homogenization cannot occur in two immiscible fluid phases without diffusive action. As with metallic materials, a pattern of banding would be visibly recognizable even with very thin elements. For low Reynolds number circumstances (i.e., high viscosity fluids), the net atomic diffusion is insignificant, as predicted by the Stokes-Einstein relation in Equation 2.1

24

$$D \propto \frac{1}{\mu}$$

<div align="right">Equation 2.1</div>

Here, D is diffusivity (m^2 sec^{-1}) and μ is the dynamic viscosity (Pa-sec)

Until the elemental thicknesses begin to approach the length scale of the diffusion distance, the effect of diffusive action will remain unnoticeable. In the special case of shear around a concentric cylinder (as seen in FSP and shown schematically in Figure 2.8), each successive revolution results in increased thinning until the effect of diffusion is measurable. In all cases, the effect of diffusion will be increased as the available surface area is increased [51].
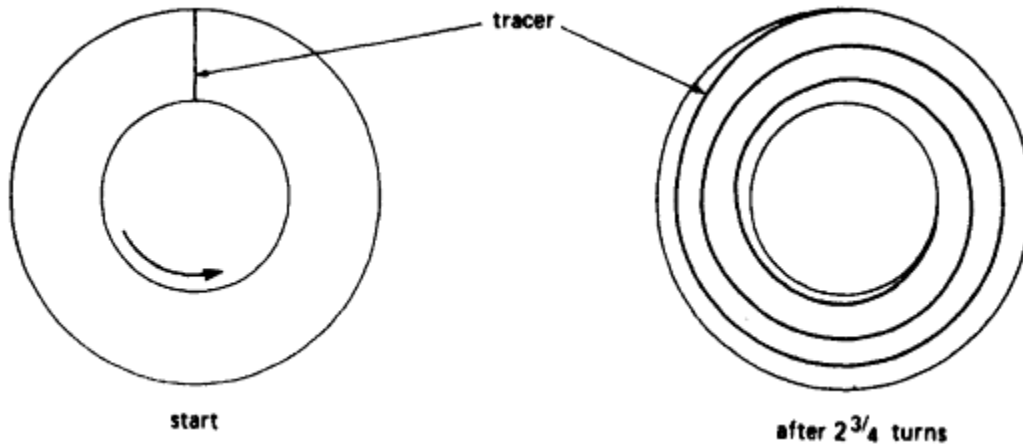
Figure 2.8   Thinning of a volume element in a rotational shear flow. From [51].

D.   RELATED FIELDS OF STUDY

Other fields of study have observed and employed redistribution / mixing processes to achieve desired outcomes. Attaining proper mixing homogeneity is a common concern in many industries such as pharmaceuticals, food science, and chemical engineering.   As an example, inadequate mixing of volatile compounds led to a catastrophic nuclear-chemical waste explosion in 1993 [52]. Despite their importance and relevance in many modern fields, mixing processes are often ad hoc and one of the least efficient steps in production. Alvarez-Hernandez et al. [53] determined that when a

poor agitator was used, 98% of the power expended in the mechanical stirring of a low Reynolds number fluid produces no detectable convective mixing. It was found that minor changes in agitator design produced an order of magnitude improvement in mixing effectiveness.

1. Inclusion Motion in Geological Applications

Over several decades, structural geology has investigated the kinematics of deformable and rigid inclusions embedded within a ductile matrix. Geologists encounter redistribution phenomena in many natural occurring scenarios, e.g., as solid material is transported within the upper layers of the Earth's crust, or when entrained solid matter is transported through glacial movement. In areas where rigid inclusions are present in slow moving geologic flows, visible indications of relative motion are usually observed. "Strain shadows," regions of low matrix strain which are shielded by a rigid object, form as a result of the inhomogeneous deformation of the ductile matrix adjacent to the object [54]. Inclusion fracture often occurs as a result of a shear gradient in the flow of the surrounding matrix [54]. "Foliation drag," visible flow patterns in the surrounding ductile matrix, is the result of a friction at the boulders interface [54].

In related geologic study, Bilby et al. [55] used elastic field theory for ellipsoidal inclusions and inhomogeneities to solve the problem of a slowly deforming viscous material containing an ellipsoidal inclusion of different viscosity. Their result was applied to the kinematics of rock deformations, as well as to the mixing and homogenization of viscous liquids. Most geologic analysis has concentrated on how inclusions change shape or rotate in the course of progressive deformation, but more recent studies have focused on how diverse structures develop the due to the heterogeneous flow field around rigid inclusions. The approach uses modified hydrodynamic continuum models to characterize solid flow fields. The idea dates back to 1922 with Jeffery's theory for the motion of ellipsoidal rigid bodies in an infinitely extended viscous medium [56]. The theory has been found to be general in nature, and applicable for modeling the heterogeneous flow around both equiaxed and nonequiaxed inclusions during matrix deformation.

In short, these and other well understood geologic occurrences may be useful tools in helping to identify and describing nondeforming particle motion at a much smaller length scale. Though the length and time scales vary greatly, consistent fundamental processes are at work that may be analogous to the microscale material motion observed in FSP and other fabrication processes.

2. Homogeneity in Food Science Applications

In the food science industry, homogeneous dispersions are critically important to recipes and therefore product outcomes. Food products typically require blending of rheological and particulate materials, e.g., dough or batter entrained with particles of varying size and rigidity. Large industrial mixers using various impeller blade designs are used to blend and homogenize materials. Much work has been done in this area to maximize mixing efficiency, depending on the constituent materials. Peighambardoust et al. [57] demonstrated that simple shearing did not effectively decrease the weight or size of glutenin particle clusters in a dough matrix. Z-blade mixers at comparable levels of mechanical energy input, which apply both elongation and shear to the material, were shown to be more effective in dispersing agglomerations within the matrix. In emulsions and batters, it is often the shear and extensional stress that are responsible for the reduction in entrained droplet or bubble sizes.

Studies of cake batter rheology largely focus on viscous behavior. Chesterton et al. [58] demonstrated that elastic effects dominate at the shear rates used in commercial mixing. In batter mixes, apparent viscosity is inversely dependent on air volume fraction. Low viscosity emulsions with high air volume fractions (0.39–0.45) showed shear-thinning at low shear rates (10^{-1}–10^1 $\sec^{-1}$) with shear thinning behavior ceasing above 10^1–$10^{1.3}$ $\sec^{-1}$. For higher viscosity slurries with low air volume fractions (0.11–0.15) the shear thinning continued up to shear rates of 10^2 $\sec^{-1}$. This finding implies for high viscosity rheological flows, element thinning can be sustained without instability for very high rates of shear seen during FSP.

3. Mixing in Chemical Engineering Applications

Polymer composite mixing involves many of the same principles just discussed. Many practical examples exist: mixing of resins and powdered modifiers, or carbon black in synthetic rubber polymers. Goncharov et al. [59] investigated methods to homogenize flouro-plastic powder in YD-128 epoxy resin in order to optimize the composite's anti-friction properties. When agglomerations of 100 to 500 μm diameter particles were placed in regions of high shear in a viscous matrix, the agglomerations broke up and the particles experienced fracture. The amount of fracture was dependent on the magnitude of internal friction in the matrix and was found to decrease significantly with small increases in matrix temperature (due to the lower internal matrix friction). However, the same small temperature increase raised mixing times threefold, which indicates some degree of matrix resistance is desirable to reduce particle size and distribute particles. Goncharov et al. [59] also observed that an excessive sustained temperature rise results in a low apparent viscosity causing more rapid particle deposition once stirring ceases.

E. DRIVING GRADIENTS IN MIXING AND HOMOGENIZATION

In metallurgy, solid state mixing is seldom discussed other than in terms of traditional diffusion or in the specific case of granular flow. Neither situation fully describes the level of redistribution observed in friction stir processing. Based on the known data for chemical diffusion mass transfer rates, over the time frame which friction stir occurs, chemical diffusion simply does not have sufficient time to account completely for observed particle motion. Likewise, a mere geometric rearrangement of particles should result if redistribution were due only to the strain path. Such a predictable rearrangement would likely be discernible in the available microscopy, which it is not.

1. Transport Drivers

Mixing discussions are generally limited to viscous materials, but a significant portion of the published literature indicates that FSP material may exhibit a short-term viscous nature during the process's peak pressure and temperature regime, nearest to the tool pin. It may be reasonable to expect that the material behavior is exhibiting both plastic and viscous qualities at this operating point during FSP [60]. Given that many of

the aforementioned deformation processes can also be conducted at high peak temperatures and strain rates, it could be reasonably be hypothesized that FSP mixing is more strongly influenced by the strain path, indicative of a mechanism more similar to mechanical mixing processes.

Nevertheless, second phase diffusive transport through a solid matrix has been shown both experimentally and analytically. The transport potentials, mentioned in Chapter I, can be employed to derive expressions for particle velocities under various gradient conditions. In addition to the well-known diffusion laws for chemical / thermal transport, lesser known analytical methods also exist for void and inclusion motion due to electro-magnetic and stress gradients [61]. In each case, the underlying argument for particle motion is framed in terms of diffusive flow, i.e., surface diffusion, interfacial diffusion, and volume diffusion. In the case of stress driven motion, Li et al. [64] postulate that interfacial diffusion is the dominant mechanism for motion and that a normal stress gradient on the interface is the major driving force. Their prediction shows that inclusion velocity is proportional to the magnitude of stress gradient and that an inclusion will tend to move toward a region of lower stress in nonuniform materials. Figure 2.9 shows a schematic of the problem's initial formulation. In FSP materials, approximating the magnitude of particle motion will be contingent on how accurately the total driving gradient can be estimated based on the assumed stress state of stir zone material in the processing temperature regime.
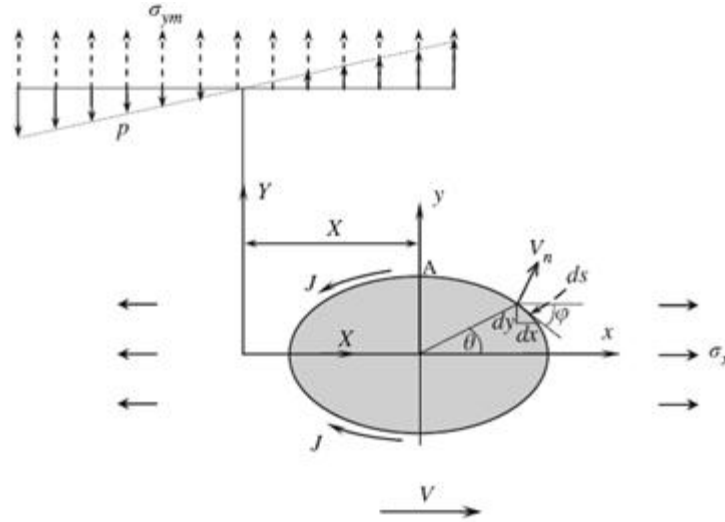
Figure 2.9 Schematic for the 2D motion of an elliptical inclusion in infinite, isotropic material under gradient stress field where J is the atom flux along the interface and p is a linear stress gradient. From [64].

The stress driver proposed in the above discussion is assumed to be of a hydrostatic nature. Such a gradient would accelerate vacancy flux, resulting in a diffusive flow of matrix material around the particle. In FSP, a hydrostatic gradient may be influenced by the tool's downward axial force, the thermal expansion of the SZ material, the geometry of a constituent particle clusters, and the deformation strain path. The degree to which gradient develops may also depend on the stiffness of the matrix material and rate of deformation.

2.   Shearing as a Dispersion Mechanism

As discussed earlier, the food science and chemical engineering fields have extensive experience in studying and characterizing mixtures and mixing processes, particularly in the case of shearing flows. Homogenization of milk is a relevant and ubiquitous example [65]. A homogenizer applies a rapid shear to an emulsion and then pushes the material through a small extrusion orifice at high pressures (typically approaching 30 MPa). As a result of this mechanical process, the highly nonuniform suspension of large stiff, immiscible globules is made uniform, and the second-phase globules are decreased in size by a factor of five or more. Intuitively, there are clear parallels between FSP of multi-phase alloys and this emulsion processing technique:

30

- A rapid, violent shear is applied under high confinement pressures.
- An immiscible two phase mixture is extruded through a highly confining region.
- Clusters are dispersed resulting in a mixture of more uniform size and spacing.

Similar shearing processes have been conducted on particle-reinforced elastomers where carbon black particle agglomerations are dispersed when subject to a shearing flow. Manas-Zloczower et al. [66] found that carbon black particles in a polymer shearing flow experienced rupture at a critical shear rate which is inversely proportional to the viscosity (i.e., stiffness) of the matrix material. The ruptured particle remnants are then distributed advectively and diffusively in the flow. Diffusive effects caused the smaller carbon particles to form a dispersed ring of material in the polymer matrix. Three to eight minutes of shearing time were required, however, for the diffusive effects to become noticeable.

Studies of chemical slurries, which are high-viscosity fluids containing particulates such as platelets in a blood flow, etc., all definitively show that shearing plays a distinct role in a particle's net migration via enhanced diffusion. Eckstein [68] showed that spherical particles migrate in the direction of the minimum shear rate in a visco-elastic fluid. Broday et al. [69] further showed that particle shape and aspect ratio have strong influences on the net migration in a shearing flow. It is reasonable to expect that similar shear dependent mechanics caused by shearing flows may be playing a yet unaddressed role in particulate migration and redistribution during FSP.

3. The Viscous Behavior of High Temperature AA356

During homogenization and shear flow, fluid emulsions and visco-fluids dissipate energy largely through viscous friction caused by the large velocity gradients present in the fluid. Solid metal in the SZ subjected to FSP and at a high temperature most likely experiences some degree of both viscous and plastic dissipation mechanisms. This idea of combined constitutive characteristics is largely overlooked in discussion of FSP. Early

31

investigations reported on the stir zone's bulk flow characterization using marker-embedded plasticine as an analog material [70]. Recent drop forge viscosity measurements of AA356 at a temperature of 0.9 T_{Melt} showed that the material's viscosity decreased linearly from 100 Pa-s to 10 Pa-s when sheared at rates ranging from $10^2 \sec^{-1}$ to $10^3 \sec^{-1}$ [71].

This result suggests that AA356 mechanical behavior during the solid to liquid transition might be viewed as a continuum (vice a step function) based on the relative values of plastic dissipation and viscous friction. Note that, this idea is not suggesting the material undergoes a phase transformation, only that the transition in mechanical behavior is more continuous than abrupt in this elevated temperature regime.

F.   MODELING ASPECTS

1.   Overview of Friction Stir Modeling

Apart from possibility of diffusive processes in FS, material transport may have a significant advective component, not unlike viscous flow. Advection is more commonly referred to in fluid mechanics, and the term is often used interchangeably with convection. Convection, however, is the additive effects of advection and diffusion. Advection describes only the transport of entrained material resulting from the velocity of a surrounding flow field. In the case of a particle embedded in a highly plastic solid near its melting temperature, this behavior can occur. The advection equation in one dimension is given in Equation 2.2.

$$\frac{\partial u}{\partial t} + w(x,t)\frac{\partial u}{\partial x} = 0 \qquad \text{Equation 2.2}$$

Here, $u(x,t)$ represents some unknown particle concentration

$w(x,t)$ represents some local velocity field

and requires the initial condition: $u(x, t = 0) = u_o(x)$

32

Numerous studies have concluded that the stir zone displays flow-type properties as the material is swept around the pin surface and deposited at the rear. Colegrove and Shercliff [72] modeled FSP of a bulk single phase material using ANSYS Fluent and introduced a pin slip interface condition which is controlled by localized shear stress. The slip condition can be interpreted in two ways. Colegrove's initial Fluent model over-predicted frictional heat generation in the weld zone, but it was found that realistic values could be attained by inserting either (1) a viscosity relationship representing material softening near the solidus temperature, or (2) introducing material slip at the tool interface.

Computational results showed that both the viscous and slip conditions more realistically modeled observed flows and tracer paths as compared to those models that applied a solid-state, full-stick condition. Debate continues on how best to model or represent the actively disturbed material close to the pin surface, and, in particular, whether a viscous or plasticity constitutive relation best describes the behavior. Arbegast [73] suggested that the microstructure and plastic flow field in a friction stir weld closely resemble the hot worked microstructure of typical aluminum extrusion and forging, and proposed that the process could be modeled in terms of conventional metal working zones: (a) preheat, (b) initial deformation, (c) extrusion, (d) forging, and (e) post heat cool down.

High temperature numerical models have been developed for analogous extrusion cases, but again only for bulk single phase materials. DEFORM [74] , STIR-3D [75], CTH [1], and a number of other independently developed codes [76] involving thermo-mechanical plasticity models have been applied to the problem. None to date, however, have attempted to model or identify multiphase mixing mechanisms occurring during the short duration of the friction stir pass. This shortfall is primarily due to the inability of such codes to capture the fluid-solid interaction of a multi-particle second phase material. Adding particles of varying stiffness, shape, and interfacial character quickly escalates the numerical complexity beyond current capability.

FSP has become an increasingly frequent subject of study in the numerical modeling community, but the complexity of the process and the number of controlling

process parameters make predictive modeling a difficult task even for an isotropic, single-phase material. The current state of modeling is able to compute global velocity fields and temperature distributions in isotropic materials. Cho and Dawson [79] modeled texture evolution during friction stir welding of stainless steel using a polycrystal plasticity model together with a three-dimensional, thermo-mechanically coupled, finite element formulation. They were able to identify trends in the strengthening and weakening of the texture and material flow lines in relation to the relative magnitudes of the deformation rate and RPM. Study of the material flow lines, in combination with marker studies, have shown that material traveling around the tool pin comes back very close to its starting location [1], [79]. Boyce et al. [80] were able to conduct simulations on the micro-scale by developing a multi-scale finite element methodology for the study of texture and residual strain. The simulation methodology applied an elasto-viscoplastic plasticity relation and tracked selected elements in a coarse, macroscopic model followed by more resolved simulations of those selected elements at the microscopic level.

All of the approaches to date are generally accomplished in one of three mesh frameworks: Lagrangian with continual remeshing (rezoning), Eulerian, and Arbitrary Lagrange Euler (ALE). Meshless methods are improving and are the most likely future candidates to capture localized FSP stir zone fully. However, due to the high degree of material distortion and large strain rates, even meshless methods cannot yet model stir zone flow / particle behavior.

2. Lagrangian Approach

Lagrangian solutions are more efficient, requiring fewer computations per time step. This approach also permits a clear definition of material interfaces and boundaries. Lagrangian simulations, however, are limited in the degree of allowable deformation [81]. In such cases, the analysis can only be carried out to the point where mesh distortion causes the analysis to be stopped due to either an extremely small stable

time step or mesh tangling. In some situations, the analysis may extended by refining the mesh or remapping the newly distorted region with a new mesh. Both of these options greatly increase computational time.

The simulation can also be extended by eroding nodes (i.e., discarding the node or transforming it into an unconnected node) at some prescribed geometric strain, but this option reduces simulation fidelity. Also of note, contact and sliding interfaces are difficult to implement and result in increased computational time. In general, a pure Lagrangian approach is not viable for FSP modeling.

3.   Eulerian Approach

Euler solvers are well suited for modeling fluid and gas behavior since the numerical mesh is fixed in space and the material flows though the mesh. The fixed mesh is capable of tracking large material deformation and flows, since there is no mesh distortion [81]. Much greater computational time is required to maintain material interface conditions and limit numerical error. Often, Eulerian and Lagrangian solvers can be coupled to capture the interactions of multiple materials. ANSYS AUTODYN is one such coupled Eulerian-Lagrangian solver. Computational time is greatly increased during fluid-solid coupling since the solid material's stress tensor and the material history must be transported to each cell in the Eulerian mesh during each time step. Despite their increased capability, from a time and computational expense perspective, Eulerian and coupled Eulerian solvers are not practically able to simulate a full microstructure containing thousands of particles being subjected to FS type deformations.

4.   Arbitrary Lagrange Euler (ALE)

ALE solvers providing increased flexibility in modeling severe deformations in that combines aspects of both the Lagrangian and Eulerian approaches. In this approach, the Lagrangian material interfaces are maintained, but the mesh is allowed to relax to some extent, helping to preclude grid tangling [81]. As in the Lagrangian approach, with very large strains the mesh must still be remapped with each time step. Therefore, in the case of FSP, the modeling advantages are limited. Here, in the interest of time savings

and software availability, the best approach is to apply a coupled Eulerian technique and simplify the model to a representative volume element (RVE).

G. QUANTIFICATION OF HOMOGENEITY

1. Requirements for Quantifying Homogeneity

Homogeneity in metallic materials is frequently discussed in a qualitative manner, but is seldom quantified. As stated previously, relatively little work has been directed at unifying the metallurgical community in quantifying homogeneity or developing a standard of homogeneity. Much argument has taken place concerning optimal techniques for measuring and reporting homogeneity in MMC's and other multi-phase alloys, yet few if any methods are either widely accepted or implemented. A difficulty in quantifying homogeneity is identifying the scale at which homogeneity becomes most important. At low magnification, a material can appear homogeneous, but at smaller length scales, which may control crack and instability growth, the material may be clearly inhomogeneous. The obvious conclusion is that in order to achieve the greatest benefit from homogenizing processes, is imperative to identify:

- The critical length scale for achieving homogeneity

- The parameters which define a material's homogeneity

- A standard method of assessing homogeneity for a broad range of materials and processes.

2. General Approaches

The problems of identifying good and bad distributions in multi-phase systems are common across a wide range of fields and are not unique to metallurgy. Polymer processing in particular has much in common with mechanical mixing of high temperature metallic materials. Figure 2.10 schematically illustrates an explanation of good and bad distributive mixing [82]. The method by which these distributions can measured and quantified as good and bad is still debated. The issue becomes particularly complex when particles are of irregular shape, size, and orientation.

36
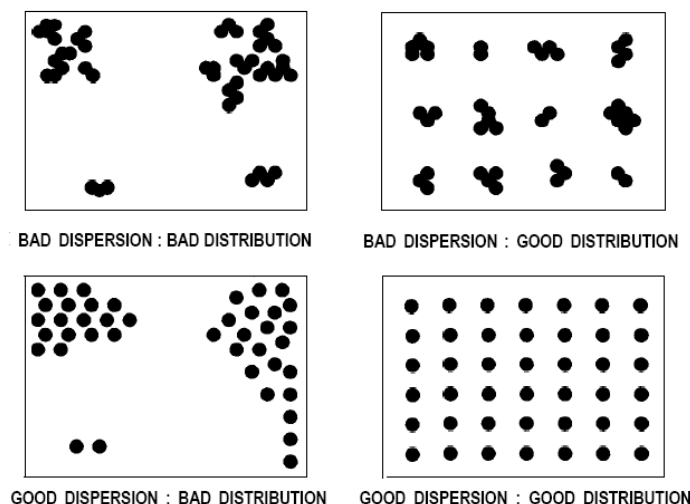
Figure 2.10 Schematic of qualitative dispersive and distributive mixing characterizations. From [82].

Danzer et al. [83] investigated the use of mathematical pattern recognition in images to identify chemical homogeneity in solids. They point out that chemical homogeneity is based on the measurement of sample composition at multiple sample points. A volume of material is homogeneous when the composition is the same at all sample points. The typical sampling methodology consists of composition measurement and statistical evaluation, wherein and sampling errors will directly affect the subsequent statistical evaluation. They further point out that the most critical factor in applying any statistical model is the dependence on the local frequency of concentration fluctuations. These local concentration fluctuations of course depend on the length scale under consideration. Liebich et al. [85] built upon this work using multi-variate techniques to recognize spatial concentration fluctuations for multi-element material images. This work forms the mathematical basis for distinguishing and mapping multiple phases, which is implemented in MATLAB Image Analysis Toolbox and other analysis software often available in imaging suites.

3. Specific Methodologies

a. *Field Methods and Tessellations*

Once one or more material phases can be mathematically identified and represented in an image, a variety of methods has been used to begin describing homogeneity. Individual methods have distinct strengths and weaknesses when used in analyzing structures of varying volume fraction or a uniform particle size. Approaches include field methods (e.g., area fraction or second phase density), inter-particle spacing methods (e.g., near neighbor distance or two point correlations), and tessellation methods (e.g., Dirichlet tessellations, Delaunay triangulations or Voroni diagrams) [86]-[91]. Difficulty arises because none of these individual methods can fully and accurately characterize even simple distributions over a wide range of length scales. Field quantities are useful in providing and evaluation of spatial distribution when sampling is conducted over a wide range of samples and length scales, but these quantities provide no measure of morphological parameters or clustering. Inter-particle spacing will provide an indication clustering tendencies, but tessellations are generally needed to quantify morphology.

Tessellation allows for the extraction of detailed particle-by-particle information based on the geometry of the resulting polygonal cells. Normally, tessellation methods use particle centroids to establish the tessellation's cell borders. Clearly, an error is introduced since actual particles do not exist as points. Despite the inherent error, Spitzig et al. [86] showed Dirichlet tessellations can be effective at quantifying spatial morphology for microstructures that have either less than 1% second phase volume fraction or uniform particle sizes. Yang et al. [87] extended the use of tessellation methods to finite-sized bodies in order to limit the error induced by particle size variation. Yang also found that the coefficient of variation (CV), i.e., the ratio of standard deviation to mean often used to characterize spatial parameters, is of limited value when measuring homogeneity for finite sized bodies due to its sensitivity to wide ranging particle size distributions.

b. *Probabilistic and Deterministic Methods*

Varieties of probabilistic and deterministic techniques have been implemented to quantify the spatial characteristics, and conversely use defined input characteristics to generate synthetic microstructures for follow-on computational analysis. Torquato et al. [88] developed a nearest-neighbor distribution function for random distributions of identical hard spheres, which showed good agreement with theoretical predictions. An extensive collection of recent collaborative work in the area of microstructural quantification originates from Gohkale, Tewari, Schoppp, and Spowart [89]. This group generated computer simulations of coarse constituents in hot-rolled AA7075 plate and incorporated realistic constituent particle morphology, nonuniform arrangement, and partially anisotropic orientations. Their methodology permitted synthetic generation of microstructural windows that incorporate short-range (on the order of particle size) and long-range (several hundred times the particle) microstructural heterogeneities and spatial patterns. The geometry of simulated microstructures was based on the following parameters:

- Volume fraction of constituent particles.
- Size and shape distribution of the constituent particles.
- Sizes, shapes, orientations and densities of particle rich bands / clusters.
- The ratio of constituent particle density in the particle rich regions to the average global constituent particle density.

Two-point correlation functions were used for microstructure representation and were closely matched with corresponding real microstructures. The technique enabled simulations of virtual alloy microstructures over a range of volume fractions and particle sizes. Tewari and Gokhale [90] developed digital imaging techniques to quantify and represent microstructural clustering and an estimation of microstructural contact distributions. The technique is based on an estimation of void space probability and is used to calculate particle contact distributions in metal matrix composites that have the same volume fraction and size distribution of SiC particles but different degrees of spatial clustering [11].

Spowart et al. [13] extended two-point correlation functions to three-dimensional microstructures using measurements performed on orthogonal metallographic planes. They showed that if the direction dependence of the two-point correlations has an axis of symmetry, then measurement on just the vertical plane containing the symmetry axis is sufficient for estimation of both the direction-dependent and mean two-point correlation functions. Measurements on, at most, three planes are sufficient if there is no symmetry axis. The method was applied for characterization of spatial heterogeneity and clustering of SiC particles in a series of discontinuously reinforced aluminum (DRA) composites having varying degrees of microstructural heterogeneity.

Spowart later proposed an alternative approach for quantifying and incorporating microstructural homogeneity into an elastic-plastic finite element code by simultaneously modeling the micromechanical length scales associated with the individual reinforcement particle size and particle spatial distribution [91]. Spowart used these multi-scale techniques to characterize the microstructures of discontinuously reinforced composites undergoing FSP [9] and later as input for generating synthetic microstructures.

c.   *Multi-scale Methods*

Spowart's multi-scale analysis of area fractions (MSAAF) technique identifies a representative length scale for a two-phase microstructure by measuring the standard deviation (σ) of second-phase area fraction between different microstructure sub-regions as a function of length scale to sub-region size ratio (Q). In the isotropic form, the MSAAF technique then measures coefficient of variation (ψ) of a microstructural property over an array of square sub-regions of edge-length Q. The coefficient of variation was shown to obey the relation in Equation 2.3 [11]. Here, A_f is the second-phase area fraction, and α is a texture parameter, mainly sensitive to second-phase morphology and alignment.

$$\psi = \frac{\sigma}{A_f} = \frac{1}{\sqrt{A_f / (1 - A_f) + \alpha(Q-1)^{-2\xi}}}$$ Equation 2.3

40

In the directional form of MSAAF, the microstructure image is decomposed into strips of length Q in order to determine a directional homogeneous length scale. By increasing the Q parameter on pixilated grey scale intensity in an isotropic or anisotropic synthetic microstructure, Spowart showed that that the measured ψ, i.e., the two-parameter measure of homogeneity, decreases logarithmically as the length scale is increased.

THIS PAGE INTENTIONALLY LEFT BLANK

III. ELEVATED TEMPERATURE ECAP AND MODELING

A. PREFACE

This chapter investigates the development of hydrostatic pressure gradients and quantifies the degree of diffusive particle motion developed in large strain, high temperature deformation processes by assessing:

1. ANSYS AUTODYN modeling results for high temperature ECAP of an aluminum billet containing nondeforming particles.

2. ANSYS AUTODYN modeling results for particle-containing volume elements subjected to various high temperature stress states.

3. An analytical solution for diffusive particle motion based on the Eshelby model for the stress field developed around an ellipsoidal inclusion in a deformable matrix.

4. Experimental results of high temperature ECAP of an Al-7% Si alloy

B. INTRODUCTION

Elevated temperature ECAP was conducted on a Na modified Al-7% Si hypoeutectic alloy. In addition, the process was computationally modeled as a bulk material containing rigid nondeforming particles in order to evaluate the potential for diffusive motion of particles in hydrostatic pressure gradients over a range of pressing temperatures and strain rates. Additional modeling investigated the potential for diffusive motion of clustered particles by examining the development of pressure gradients in discrete, particle-containing volume elements subjected to various stress states over a range of temperatures and strain rates.

As previously discussed, ECAP as a severe plastic deformation (SPD) method during which grain size can be reduced down to the sub-micron level in metallic materials [92]. Due to the unique stress state to which the test sample is subjected, ECAP is useful in investigating the mechanism(s) for redistribution of microstructure constituents. More specifically, the test coupon experiences a simple shear while subject

to a large hydrostatic pressure, which is akin to the most likely stress state developed in FS materials. The stress levels developed in quasi-static ECAP are functions of load, die geometry, die wall friction, and temperature.

It is proposed that the particular load state present during ECAP can induce observable diffusive motion of second-phase micro-constituent particles if the surrounding matrix material is adequately softened by heating. If a sufficiently large differential pressure can developed across a particle as a result of the ECAP load state, the particle, theoretically, could be transported through the softer matrix. This scenario could also be described as a diffusive flow process, where the surrounding matrix around the particle experience relative motion at the interface. Through computational and analytical methods, the purpose here is to identify the magnitude of pressure gradient which might be developed and predict the distance over which a particle might move during a deformation cycle. Such results would provide insight as to whether a diffusive transport process is sufficient to account for the level and type of redistribution often seen in SPD's, FSP in particular.

C.   EXPERIMENTAL AND MODELING APPROACH

1.   Experimental Procedure

An ECAP die with a 160 mm channel length was used to process the Na modified Al-7% Si samples at 300°C and 400°C using redundant straining following Route C. Schematics for ECAP Route C and the die are shown in Figures 3.1 through 3.4.
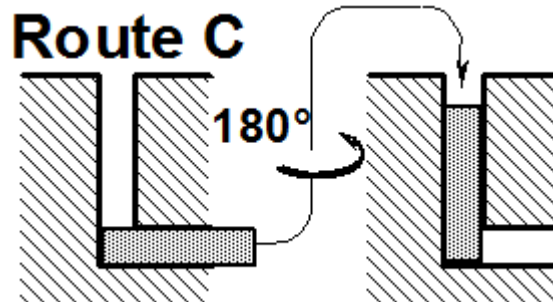
Figure 3.1   Schematic of ECAP Route C which has rotations of 180° between successive passes. From [92].
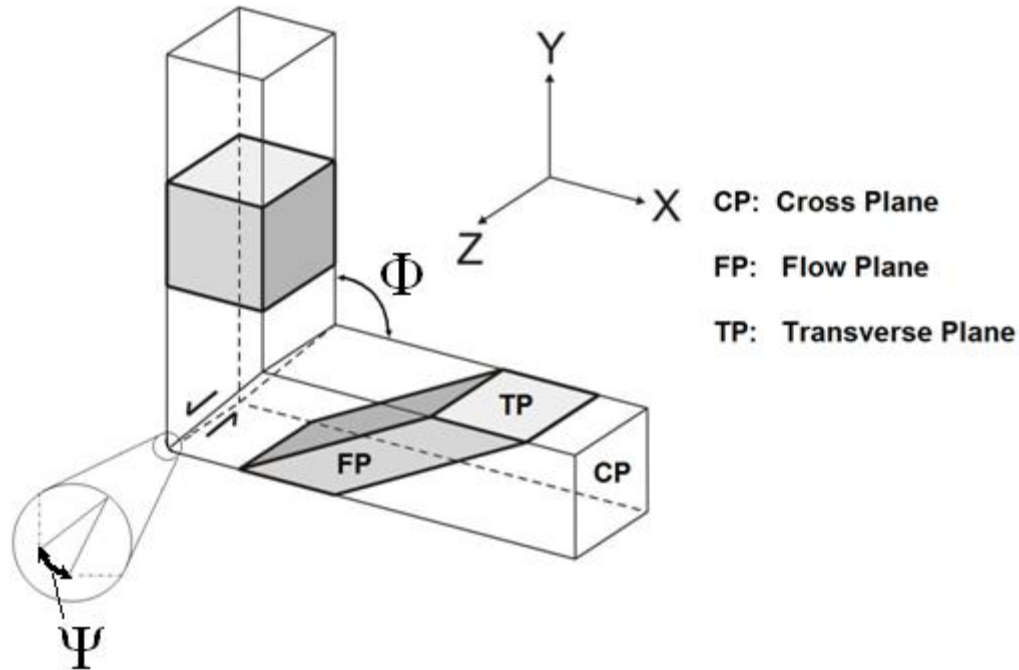
Figure 3.2 A schematic of a billet deformation during a single pass through an ECAP die. The angle between die channels is $\Phi=90°$; the shearing of a cylindrical billet during pressing is shown and the angles Φ and Ψ, which is the relief angle at the outer radius of the channel intersection, are defined. After [95].

The ECAP die is constructed of A45 steel outer body containing a hardened A2 tool steel inner channel. The inner channel is removable for cleaning and sample extraction. The die was retrofitted with five surface-mounted TEMPCO strip heaters, capable of supplying a total of 2250 watts of input power. Input power was distributed via three independent 110V wall plug circuits, each regulated by a rheostat to control heat up rate. Each circuit was designed to carry less than 15 amps of current to ensure continuity of power during testing. The heat capacity of the 24 kg die was estimated at 434 J/kg-K, which resulted in a maximum heat up rate of 400°C per hour assuming 20% conductive and convective thermal losses (see Appendix A for detailed computations). In order to minimize heat loss, noncombustible insulating silica batts were used to surround the die. The die's steel base plate was insulated from the test platform using silicate cloth. The in-situ sample temperature was monitored using a hand held Fluke 62 digital infrared thermometer, which has an accuracy of +/- 1 % of measured value.
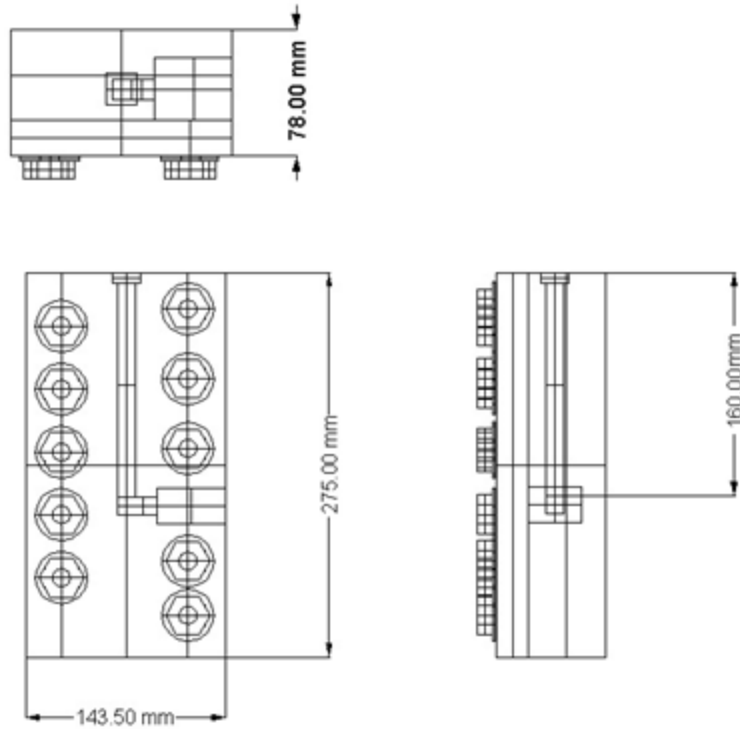
Figure 3.3   ECAP die dimensioned drawing
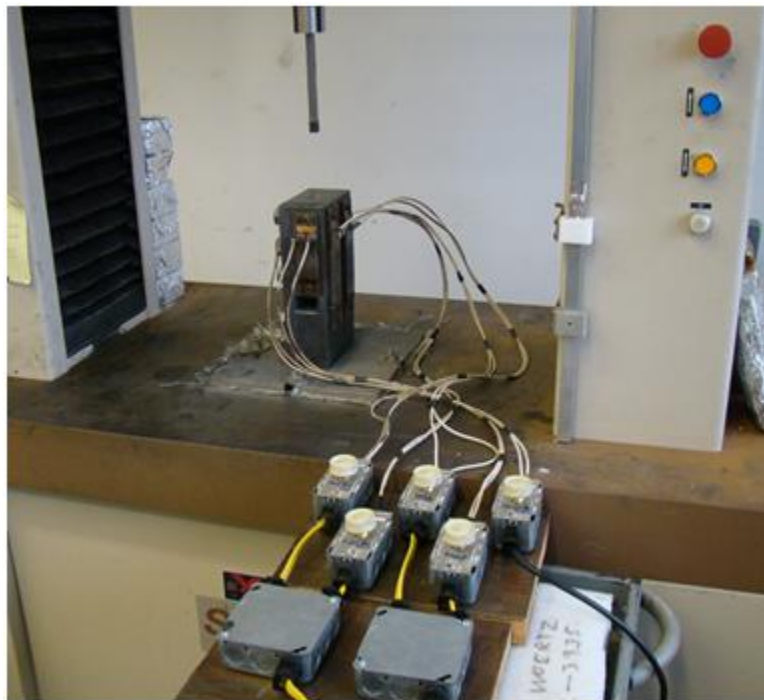
Figure 3.4   Constructed ECAP die apparatus.

The Na modified Al-7% Si was cast at Centro Nacional de Investigaciones Metalúrgicas (CENIM) and delivered as a 100 mm x 50 mm x 50 mm bulk sample. Testing samples were machined as rectangular billets measuring 50.8 mm in length, 12.7 mm in width, and 12.7 mm in depth. Machining and post-processing sectioning was conducted using a low speed diamond saw to preclude excessive material heating. The test sample dimensions were selected to accommodate the ECAP die. The die was rigidly mounted in a SATEC Systems Uni-drive press (model MII-2OUD) and a 220 kN load cell (Model 1120AF-50K). During hot pressing, the test sample was inserted into the test block (shown in Figure 3.4) and allowed to come to test temperature at the same rate as the die block. Heating rates were controlled according the data in Table 3.1 to preclude excessive thermal stresses from developing the block.

Table 3.1   Heat up rate data for elevated temperature ECAP pressing.

Temperature Range	Percent of total available power	Watts per hour	Observed time to reach target temperature
0 to 100°C	25%	562.5	20 minutes
100°C to 200°C	50%	1125	40 minutes
200°C to 300°C	75%	1687.5	60 minutes
300°C to 400°C	100%	2250	120 minutes

Once at the desired temperature, a dummy aluminum sample was placed on top of test sample and the two samples were pushed through the die channel intersection in succession. To limit the effects of friction, the die channel walls were coated with P37 Molykote® anti-seize paste, which is designed to provide effective dry film lubrication up to a temperature of 1400°C. Appropriate ventilation was required during the heat up process, as significant formaldehyde out-gassing occurs when the paste transitions to a dry film at 150°C.

Force and displacement data were monitored but not recorded during the pressing to provide an indication of plunger binding or excessive friction. An A304 stainless steel plunger with a minimum length of 110 mm was required to press the sample fully. Longer plunger lengths resulted in Euler buckling of the plunger shaft at elevated

temperature. Detailed calculations regarding the plunger design and geometry can be reviewed in Appendix A.

The samples were each processed in a 10 second pressing time resulting in an effective single pass strain rate of 10^{-1} $\sec^{-1}$. Sample sets consisting of billets that had experienced 1, 2, 3, and 4 passes were processed at temperatures of 300°C and 400°C, which is a homologous temperature of approximately 0.65 T_{Melt} and 0.75 T_{Melt}, respectively. The cumulative strain repetitive passes is calculated by Equation 3.2 [95].

$$\varepsilon_N = \left(\frac{N}{3^{1/2}}\right)\left[2\cot\left(\frac{\varphi}{2}+\frac{\psi}{2}\right)+\psi\csc\left(\frac{\varphi}{2}+\frac{\psi}{2}\right)\right]$$

Equation 3.2

Applying the values for the die in use, each ECAP pass results in a total strain of 1.055, where ε_N is the cumulative strain, N the number passes, φ the angle between die channel, and ψ is the relief angle at the outer radius of the channel intersection. Angles φ *and* ψ were shown previously in Figure 3.2.

2.   Modeling Approach

Three-dimensional (3D) computational modeling was conducted using ANSYS AUTODYN to ascertain the extent to which a hydrostatic pressure gradient might be developed within a processed ECAP billet containing discrete inclusions. The rise of intra-cluster pressure gradients is dependent on two geometric factors: (1) the strain path of the deformation process and (2) the spacing and arrangement of the particles within the cluster. In the ECAP modeling, a coupled Eulerian-Lagrangian method was used with the billet as an Eulerian body containing rigid, nondeforming Lagrangian spheres. A coupled solver was required due to the fact that a high strain rate ($\sim10^{1}\sec^{-1}$ to $10^{2}\sec^{-1}$), high temperature process was being modeled in such a way that the particles must be able to move relative to the matrix material. Inertial effects were considered small in this simulation. ANSYS AUTODYN [97] was the most readily available software package capable of capturing this behavior. Simulations were constrained to a single dual-processor desktop workstation.

Due to computational constraints, achieving mesh resolutions to capture detailed cluster-induced gradients was not possible during a full-scale ECAP simulation. AUTODYN's coupled solver permitted only the use of tetrahedral and brick elements, adding to the computational cost. Mimicking the two-dimensional (2D) problem with three-dimensional (3D) elements resulted in numerical instabilities that did not allow the simulation to run to completion. This was most likely a result of the high aspect ratio of the billet when the thickness was reduced to a small number of elements. Using the full billet thickness with a small number of elements resulted in an overly coarse mesh and poor results. As a result, a simplified 3D scaled model of the ECAP die was ultimately used which incorporated a limited number of second phase constituent particles at a constant elevated temperature. A practical limit of 45 particles was identified based on computational time. Particle diameter was sized at 5% of the billet cross-sectional width. In reality, Si particle sizes are 4 orders of magnitude smaller than the billet thickness, however such small particles could not be modeled easily due to the computational expense of the inflation layers joining the particle to the billet body. A typical mesh for the 3D model can be reviewed in Appendix B.

The modeling investigated the effects of ECAP Route C. Others have modeled the effects of ECAP for single and multi-pass effects, primarily investigating mechanical behavior of the billet material at ambient conditions. As identified in a number of reports [98], multi-pass, low strain-rate modeling is usually done with Lagrangian billets using a long, multi-bend die model, such as that shown in Figure 3.5. This approach has a number of drawbacks when the billet material must be an Eulerian body. An Eulerian body cannot be loaded with a directly applied force or pressure. Instead, the billet must be acted upon by a Lagrangian body, which in turn, must be guided through each of the bends. Either the Eulerian billet must be made long enough to pass through the successive bends or the rigid pusher block must successfully move through the bends. Both of these approaches are expensive to model and the number of passes is limited before instabilities occur, particularly at high temperatures and strain rates.

49
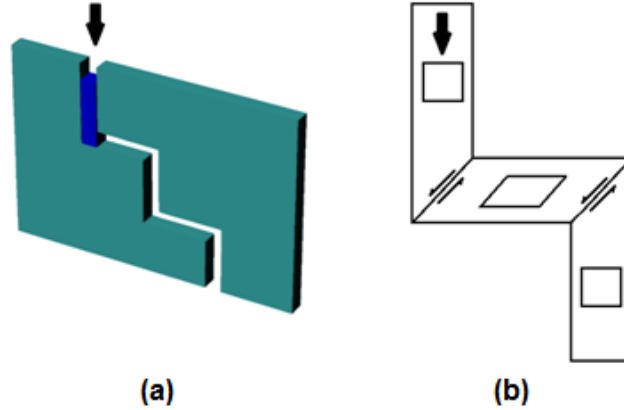
Figure 3.5   Schematic of (a) typical multi-turn dies for ECAP multi- pass modeling and (b) multi-turn redundancy of for Route C.

Instead of a multi-bend die, the redundant strain path was modeled in a novel two step process, where the inclusion-containing billet is pushed and through a single 90° turn with a rigid plunger. At the completion of the first step, the billet pressing direction is reversed to complete Route C. The body of the rigid Lagrangian die prevents the Lagrangian particles from escaping the Eulerian billet should they migrate to the billet's surface. As shown in Figure 3.6(b), plunger blocks were used at both ends of the billet to provide a means of pushing the sample during each half cycle as well, as well as maintaining a constant billet volume (i.e., precluding the formation of free surfaces.) The two step process can be then repeated for multi-pass simulations at various strain rates and temperatures, so long as numerical instability is avoided. Figure 3.6(a) shows a sample billet containing 45 interior particles arrayed in 5 discrete clusters, requiring approximately 125,000 elements.
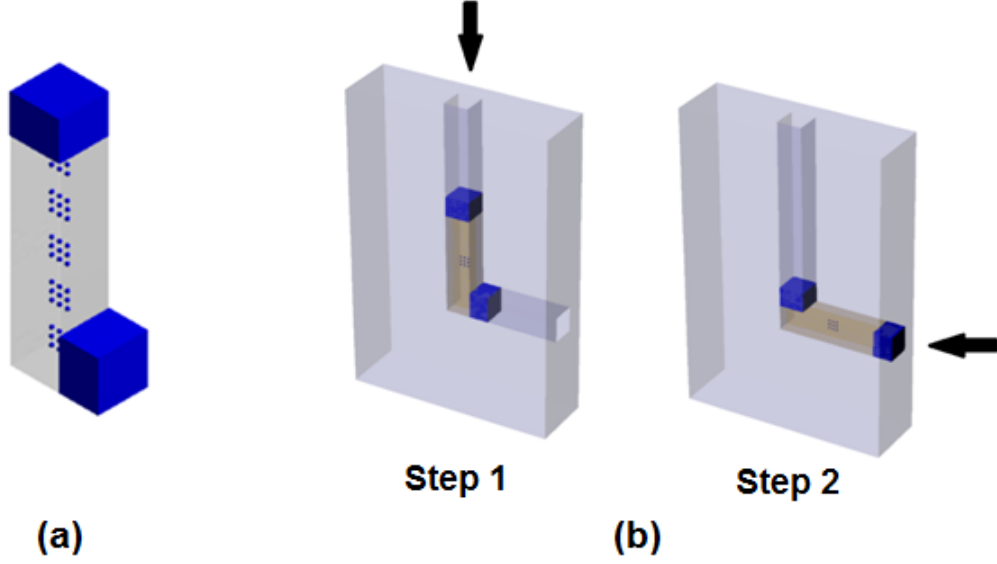
Figure 3.6 (a) ECAP 3D model billet containing 45 planar particles arranged in 5 discrete cluster arrays embedded on the thickness centerline. (b) A schematic of the two-step Route C in the scaled ECAP die.

D.   RESULTS

1.   Modeling Results

The stress tensor (σ_{ij}) and the hydrostatic component of pressure (σ_H) for driving stress-induced diffusive motion of nondeforming particles are given by:

$$\sigma_{ij} = \begin{bmatrix} \sigma_1 & 0 & 0 \\ 0 & \sigma_2 & 0 \\ 0 & 0 & \sigma_3 \end{bmatrix} \qquad \text{Equation 3.2}$$

$$\sigma_H = \frac{1}{3}\left(\sigma_1 + \sigma_2 + \sigma_3\right) \qquad \text{Equation 3.3}$$

Here, σ_{ij} is the stress tensor, σ_1, σ_2, and σ_3 are the principal stress components, and σ_H is the hydrostatic stress.

51

The modeling for ECAP Route C showed that the development of hydrostatic stress gradients due to homogeneous shear is minimal, at least when simulating ECAP as a bulk process with relatively large particles. This observation is shown in the results of Figures 3.7 through 3.9. Figures 3.7 and 3.8 show that a very high hydrostatic pressure can develop in the billet at higher strain rates, and a very brief pressure gradient develops as a result of a void formation at the interior corner of the channel. The hydrostatic gradient is solely the result of the void surface formation at the point of shear, caused by the excessive strain rate. Void formation was an artifact of the modeling, not a result of a specified void formation criterion. Slight aberrations in plunger timing at high strain rates resulted in momentary excess volume, into which the billet material expands due to hydrostatic pressure. An explicit example of such a void formation can be reviewed in Appendix C. Note that, very high stress levels in a highly constrained plastic flow often lead to cavity formation [102]. These voids allow for portions of the material to experience hydrostatic tension as the billet tries to expand into the newly created void. Shortly after void formation, the continued displacement of the plunger places the material back into hydrostatic compression and the gradients immediately disappear. In addition to the inhomogeneity created by the void, a free surface can develop if the pushing and backpressure plunger speeds are not precisely coordinated. This free surface creates also an inhomogeneous interior material flow.

Again, particles displace from their original locations during the simulations and appear to be dispersed, however the motion is not due to a driving gradient in hydrostatic stress. Inhomogeneous flows of matrix material develop at the high strain rates and "advect" the particles. Particles not in the region of inhomogeneous advecting flows did not move appreciably from their original location. This same result was generally obtained when repeated over a range of temperature and particle surface frictional conditions.
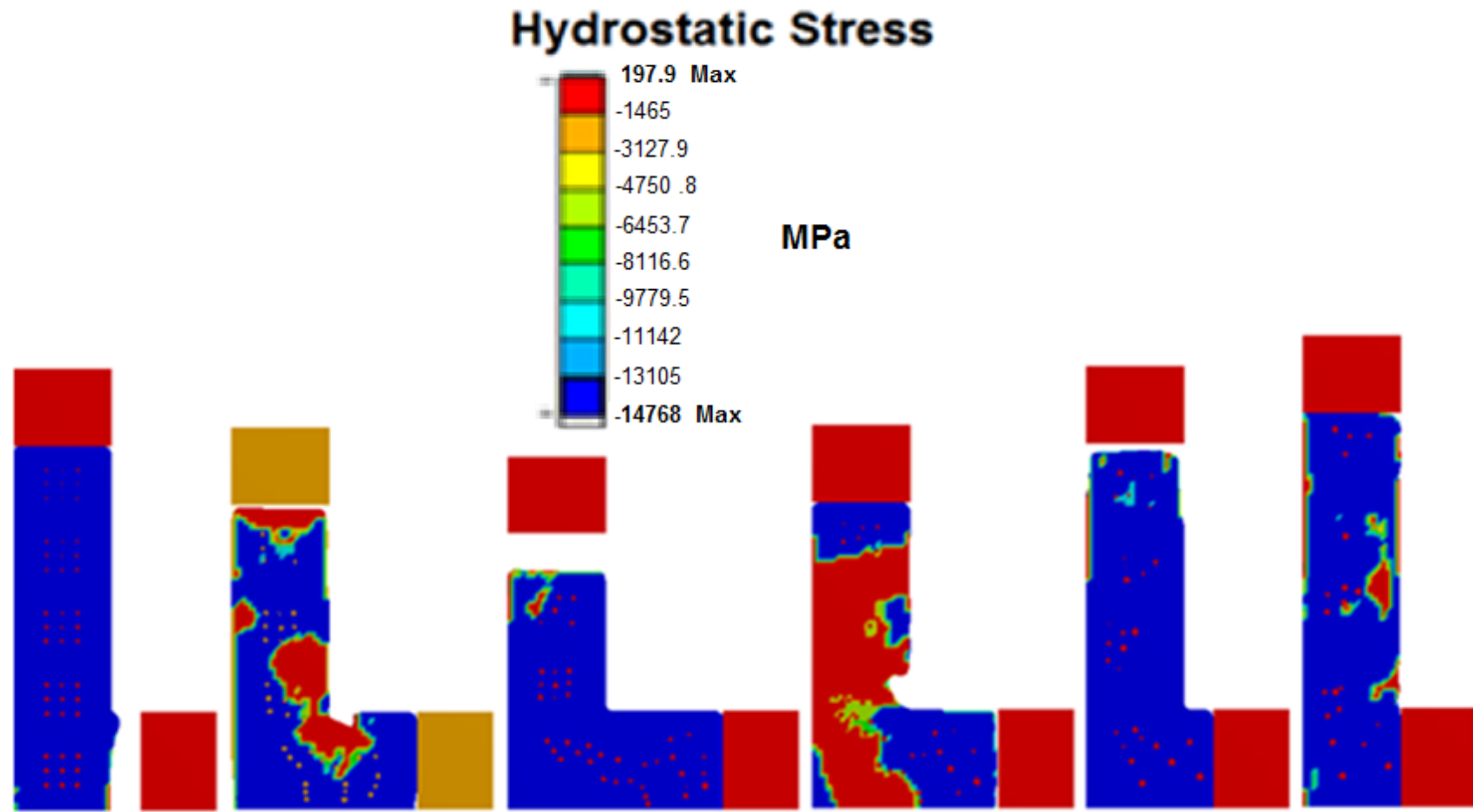
Figure 3.7   Hydrostatic stress gradients during 2 ECAP passes at 0.7 T_{Melt} and a 10^1 sec^{-1} strain rate.
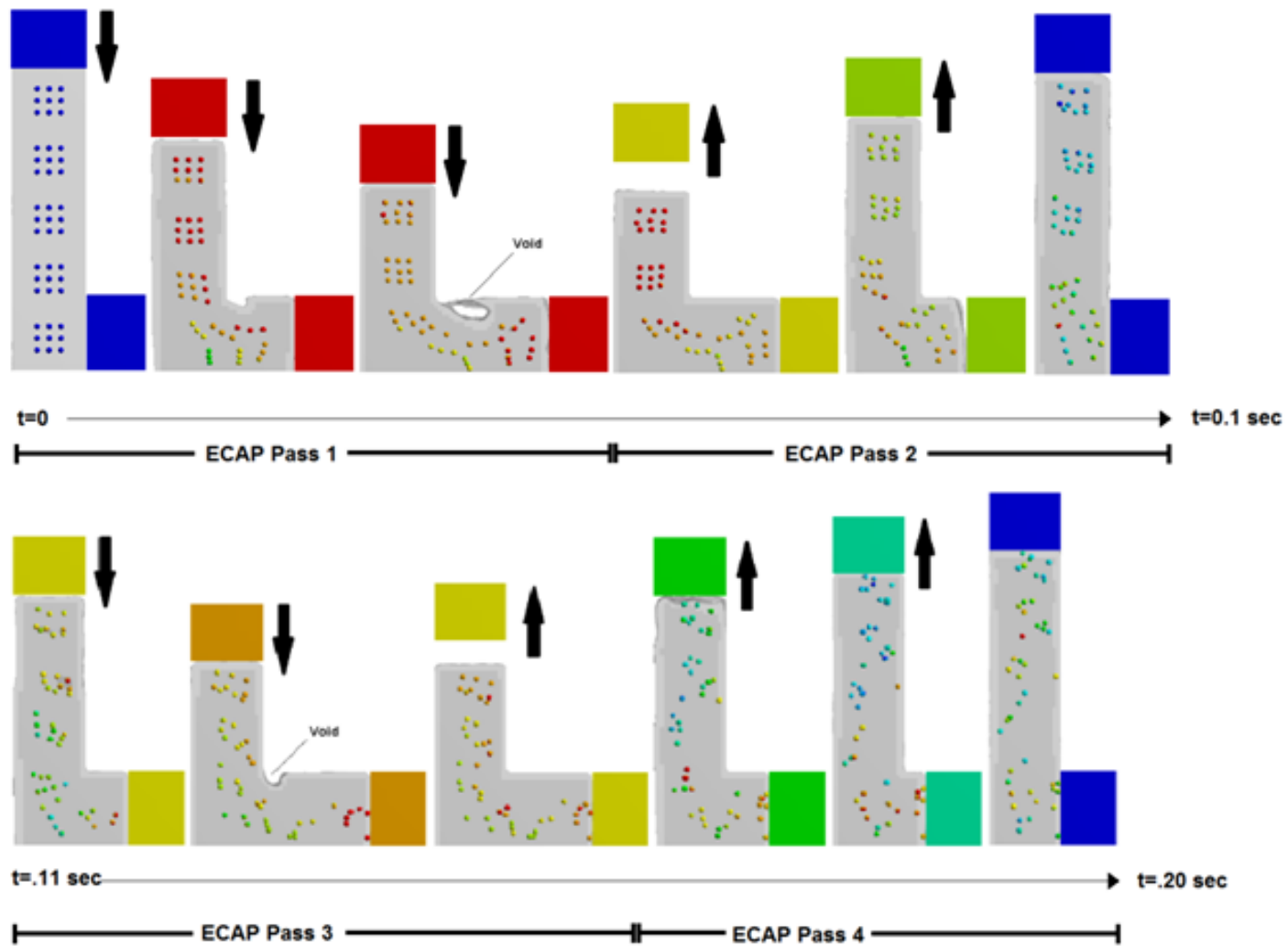
Figure 3.8 ECAP deformation cycle for passes 1 through 4 showing particle displacements; modeled at 0.7 T_{Melt} , strain rate of $10^{1.3}$ sec^{-1}, and $C_f = 0$.

In Figure 3.9, the simulation of pressing at a low temperature resulted in reduced particle dispersion as compared with the high temperature results. Low temperature modeling was conducted at lower strain rates, closer to that of actual ECAP, in order to avoid numerical instabilities. Variation in frictional conditions at the particle-matrix interface had relatively little effect on particle displacements regardless of temperature. Figure 3.9(b) and (c) show the minimal effects of changing the particle surface frictional coefficient (C_f) from 0.9 to 0, for the same simulation at ambient temperature at a low strain rate, 10^0 sec^{-1}. Again, a higher strain rate simulation could not be conducted at ambient temperature in a numerically stable manner. Figure 3.9 also shows the development of the hydrostatic pressure during shear for both cases. In neither case did a gradient develop in the vicinity of the particle cluster. The small amount of observable particle displacement is most likely due to free surface which develops at the billet's forward nose as the plunger momentarily losses contact with the billet.
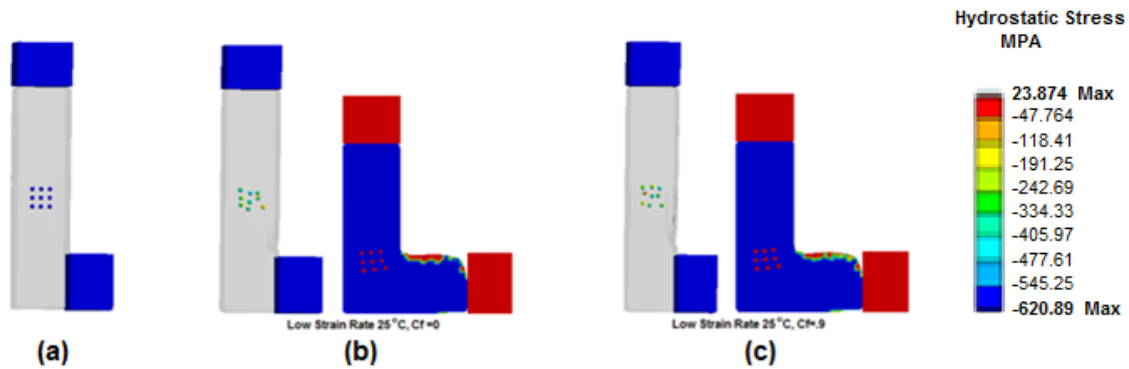
Figure 3.9 (a) Original billet configuration is a 9 particle array in the billet's center (b) ECAP 4 pass Route C results at 25°C, strain rate of 10^0 sec^{-1} , C_f= 0 and corresponding hydrostatic pressure (c) ECAP 4 pass Route C results at 25°C, strain rate of 10^0 sec^{-1}, C_f=.9 and corresponding hydrostatic pressure.

These bulk scale simulations show the gradients in hydrostatic pressure do not appear to be generated as a result of homogenous shear, regardless of strain rate, temperature, or particle frictional constraints. To further support this observation, Figure 3.10 shows a simulation with high particle surface friction (C_f =0.9), high temperature (0.7 T_{Melt}), and high strain rate.
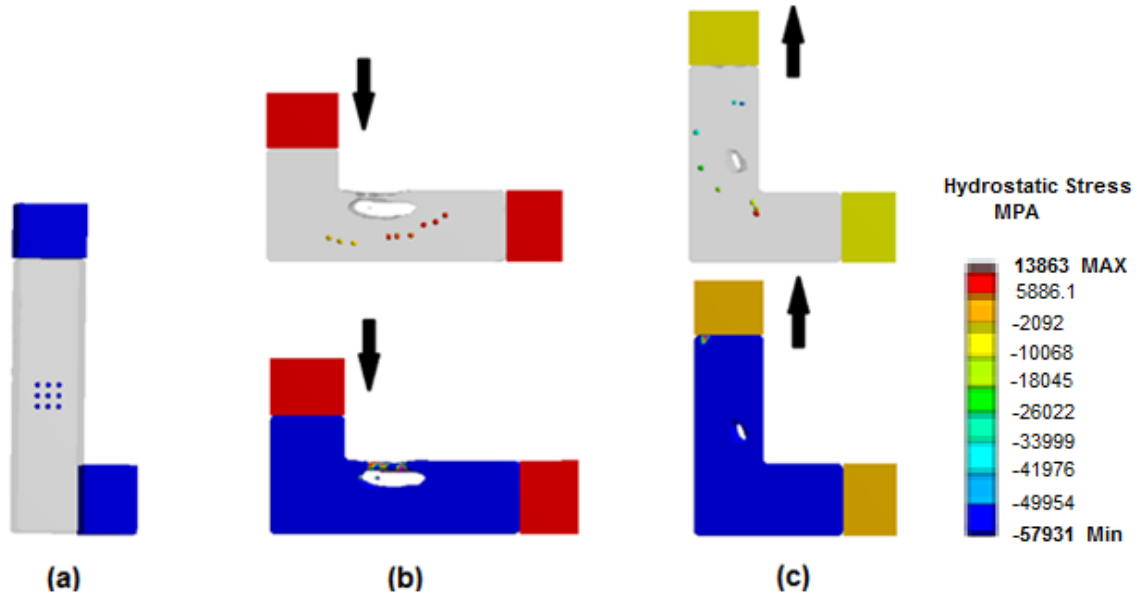
Figure 3.10 (a) Original billet configuration with an array of 9 particles (b) ECAP pass 1 using Route C at 0.7 T_{Melt}, strain rate of $10^{1.9}$ sec^{-1} with a C_f =0.9 and the corresponding hydrostatic pressure during shear (c) ECAP pass 2 with Route C at 0.7 T_{Melt}, strain rate of $10^{1.9}$ sec^{-1}, C_f =0.9 and the corresponding hydrostatic pressure gradient during shear.

As can be seen in Figure 3.10, no significant hydrostatic pressure gradients develop in the vicinity of the particle cluster during the ECAP simulation. The extraordinarily high pressures are the result of the rigid plunger timing. Even very small differences in displacement can result in a very high momentary pressure in the billet. Regardless, a uniform billet pressure results from the plunger displacement and the pressure remains largely uniform throughout the shearing operation. Gradients in hydrostatic tension again form as a result of cavitation, but tend to recede once the void has fully formed and begins to collapse. This void formation results in inhomogeneous flow patterns around the void. In this case, the particles act as flow markers, suggesting that although the particles appear dispersed in the final billet, the motion is more advective than diffusive in nature. If the void formation does not occur or is limited in growth, the observed particle motion is minimal as can be seen in Figure 3.11, where the shearing rate is reduced by a factor of 20. In this case, minor pressure gradients appear

due to a small void formation, but no pressure gradients or inhomogeneous flows develop around the cluster, and the particles largely return to their starting locations after redundant strains.
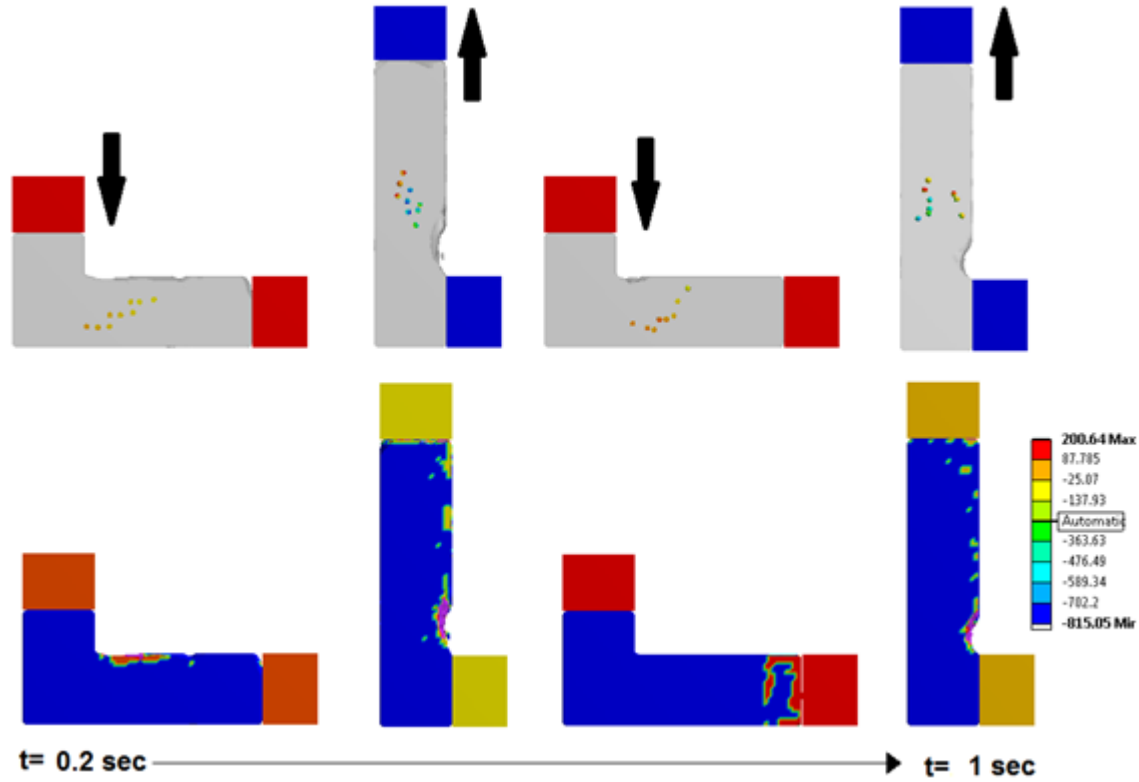
Figure 3.11 ECAP 4 pass Route C results at 0.7 T_{Melt} at a strain rate of 10^{-6} sec^{-1} with a $C_f = 0.9$ and the corresponding hydrostatic pressure.

An analog ECAP experiment was conducted using a viscous polymer gel having approximately the same viscosity as the Al-Si alloy at high temperature and shear rate. The purpose of the experiment was to validate the degree and mechanism of particle spreading seen in the ANSYS modeling. Results from the analog gel ECAP (located in Appendix D) showed similar behavior to that shown in Figure 3.11. Cluster dispersion was observed to be the result of matrix flow caused by friction at the die channel boundary. In summary, these simulations show that pressure gradient development is not significant during homogeneous shearing in ECAP, regardless of the strain rate, temperature, or frictional condition at the particle interface. The only time when

significant particle dispersal occurred is when an inhomogeneity is introduced into the strain field, such as a void formation or the introduction of a free surface.

The question remains as to whether the bulk matrix mesh is fine enough in resolution to show the development of pressure gradients in and around clusters of nondeforming particles. To show more detail, individual volume elements of nondeforming particle clusters of varying geometry were modeled at high temperature in plane strain with a hydrostatic confinement pressure and a shear. Although the modeling approach approximates a 2D plate, 3D brick elements were required for ANSYS AUTODYN.

Relevant literature was consulted in order to select a realistic estimate for confinement pressure, A review of other reports of Al-Si alloys showed that axial forces for similarly sized tools (10 mm shoulders with 3 mm diameter frustum pins), the downward axial forces ranged from 5 to 13 kN over a range of RPM and traversing rates [104]. Based on this data, an approximation of average static pressure can be made by calculating force per unit area under the tool shoulder and adding the additional pressure caused by thermal expansion of the material within the stir zone. This estimate is approximately 100 MPa. Also, data from computational models for the stress distribution of the FSP indicate reasonable estimate of 100 MPa [78]. For these reasons, a pressure of 100 MPa was estimated under the tool shoulder, representing the volume element's confining pressure. Note that, this pressure is much lower than that seen in the ECAP modeling, which was deemed an artifact of the modeling process. A Lagrangian volume element containing symmetric arrays of non deforming Lagrangian particles was then sheared under varying conditions to identify the development of pressure gradients prior to the element tearing due to excessive strain. Figure 3.12 shows typical results for the pressure gradient development in two different geometries: (a) a dispersed 17 particle cluster and (b) a more tightly packed 9 particle cluster.
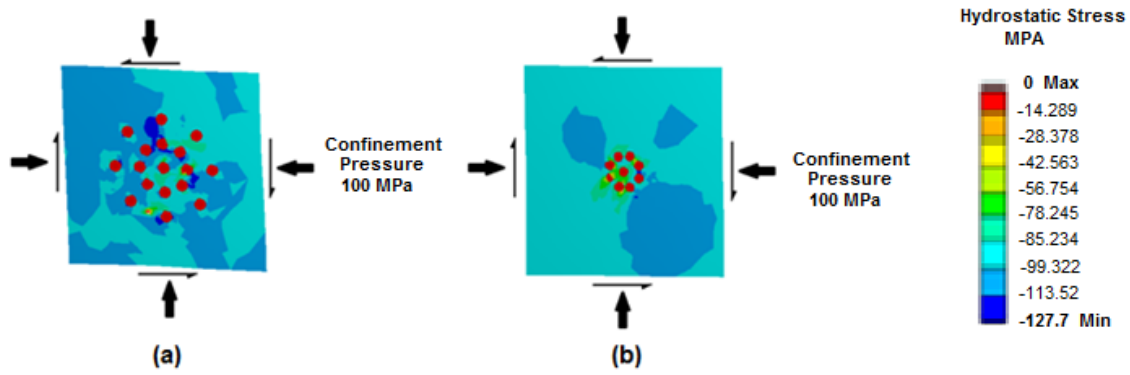
Figure 3.12 Hydrostatic pressure gradients developed in volume elements which are sheared at a rate of 10^1 sec^{-1} in plane strain under a 100 MPa confinement pressure at 0.7 T_{Melt}: (a) 17 particle cluster sheared to a total strain of .20 (b) 9 particle cluster sheared to a total strain of 0.10.

It was observed that the gradients develop rapidly at the onset of the application of the applied forces, change rapidly with time, but tend to dissipate as the straining progresses. Due to the limitations of a Lagrangian model, motion of the particles cannot be accommodated. Rather, void formation results at the particle interface as strain is increased to some critical value. Notably, differential gradients ranging up to and beyond 100 MPa can result between adjacent particles, even at elevated temperatures. Of note, tighter clusters tended to form smaller intra-cluster gradients, acting more as a single deformable body. This observation suggests that tightly packed particles may not develop a deformation-induced diffusive driving force. Also, the magnitude of the gradient is highly direction dependent; consequently, it is difficult to discern the direction a particle would tend to move without integrating the pressure profile around the entire particle's surface for each time step. As a result, it is more convenient to examine specific directional gradients in order to assess the factors that affect the magnitude of the diffusive driving force. Specific examples of those gradient measurements are shown in Figures 3.13 through 3.16. Note that, although the resultant pressures are negative due to hydrostatic compression, the plots show magnitude for convenience. Qualitatively, it can be said that sufficiently large differential pressures can be developed to drive a small amount of particle motion, and the gradient magnitude is strongly controlled by the constraint pressure and particle spacing. The expected amount of particle motion

however, would be small, probably on the order of a particle diameter. For this reason, relatively little particle rearrangement should be expected in the Al-7% Si hypo-eutectic alloy due to homogeneous shear during ECAP at elevated temperature. Also, the results show that levels of intra-cluster pressure gradients are probably not sufficient to account fully for the level of redistribution seen in friction stirring. In the time required for 1 revolution of the tool (0.15 sec to .015 sec) the eutectic particles, ranging in size from 1 to 5 μm (before fracture), would have to relocate 20 to 50 μm to reach the center of the particle-depleted primary regions. Put simply, the lowest possible estimate for particle velocities would be on the order of 60 diameters/sec.
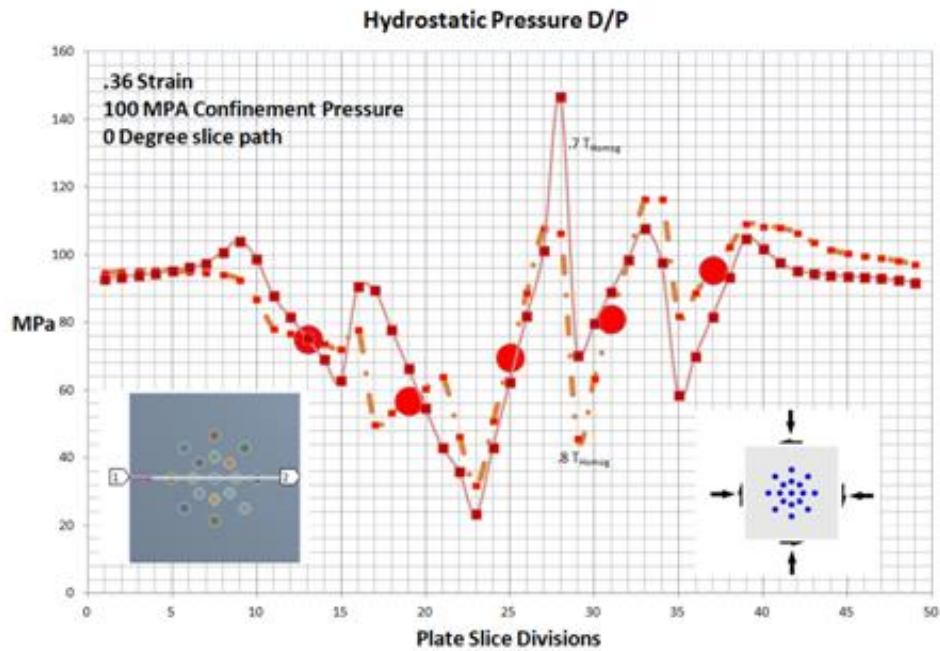
Figure 3.13 Differential pressure (MPa) across a particle cluster under hydrostatic compression and plane shear for a symmetric 17 particle Si cluster in an Al plate at 0.7 T_{Melt} and 0.8 T_{Melt} with 0.36 strain.
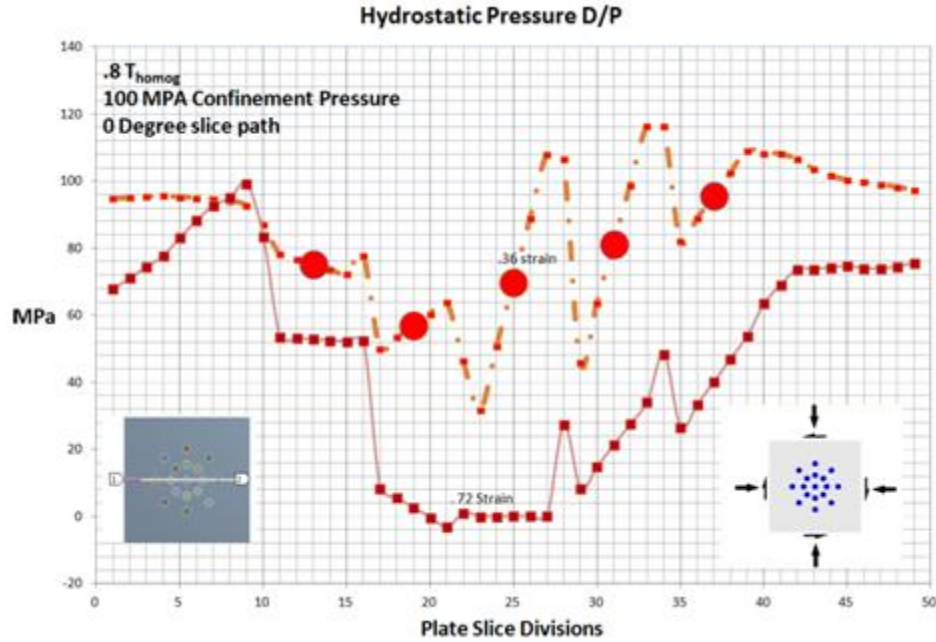
Figure 3.14 Differential pressure (MPa) across a particle cluster under hydrostatic compression and plane shear for a symmetric 17 particle Si cluster in an Al plate for 0.36 strain and 0.72 strain at 0.8 T_{Melt}.
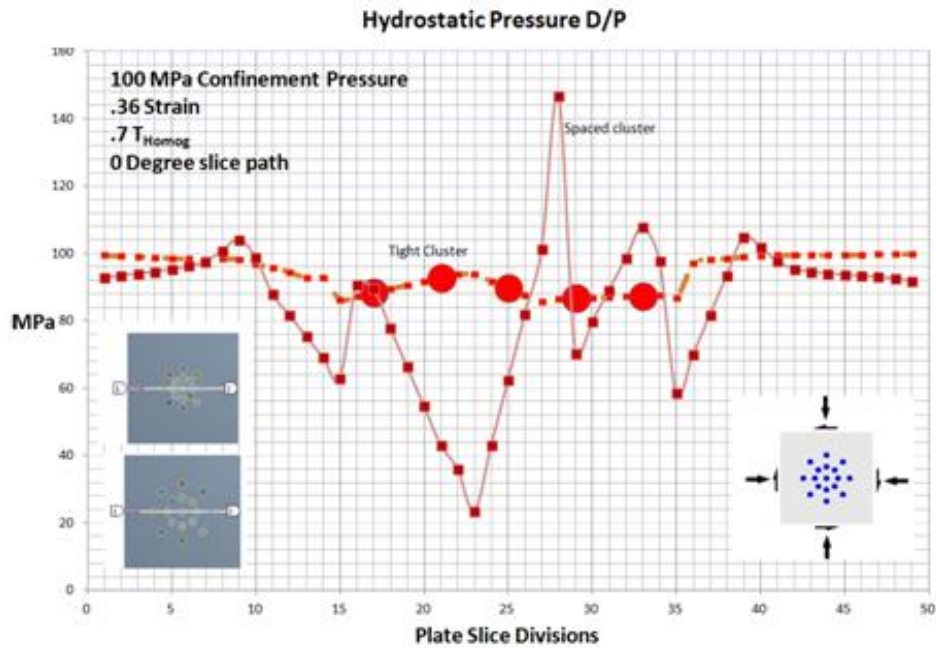
Figure 3.15 Differential pressure (MPa) across a particle cluster under hydrostatic compression and plane shear for a symmetric 17 Si particle tight and loosely spaced cluster in an Al plate 0.7 T_{Melt}.

61
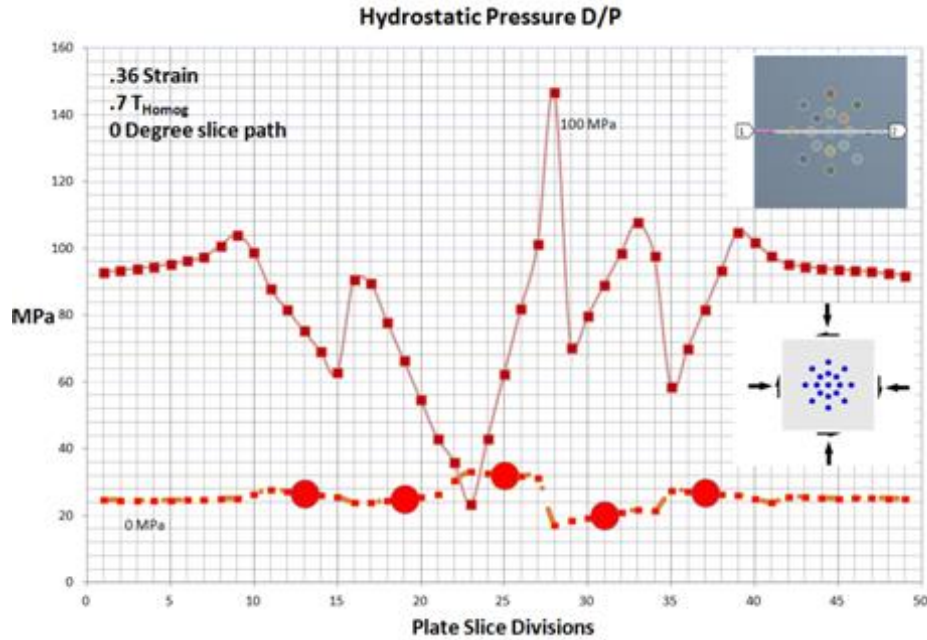
Figure 3.16 Differential pressure (MPa) across a particle cluster under hydrostatic compression and plane shear for a symmetric 17 Si particle in an Al plate at 0.7 T_{Melt} for 0 MPa and 100 MPa confinement pressure.

Several additional observations can be made from Figures 3.13 through 3.1. First, a particle-to-particle gradient is less likely to develop at higher temperature as the material softens. Second, an increasing strain results in lower intra-cluster gradients, although a larger overarching gradient develops across the body. Third, in the absence of a confining pressure or tightly packed clusters, virtually no gradient in pressure is developed, and lastly, the gradient magnitude which develops appears to be closely correlated to the magnitude of the confining pressure, in this case 100 MPa. These observations are consistent over the range of variables explored.

2. Experimental Results

a. *As-Cast Material and Metallographic Preparation*

The as-cast Al-7% Si contained a high degree of porosity; however, the overall microstructure (shown in Figures 3.17) was of typical morphology for a hypo-eutectic Al-Si alloy. The samples were prepared according to Table 3.2, and electro-polishing was accomplished in accordance with *Smithells Metal Reference Book*, 5th

62

Edition [107]. Optical microscopy was conducted using a Nikon Epiphot 200 with a Nikon DS-2Mv Digital Sight. Secondary electron imaging was conducted with a Zeiss Neon 40 Field Emission Scanning Electron Microscope (SEM) using a 20 keV accelerating voltage and a 5 mm working distance.

Table 3.2   Metallographic preparation sequence for Al-7% Si.

Polishing Media	Time	Method
Aluminuminum oxide P1200	Until flat with uniform scratch direction	Light hand pressure in linear motion on flat backing
20% by volume solution 6 micron alumina powder in water/ microfiber pad	Until uniform scratch direction	Light hand pressure in circular motion at 120 rpm wheel speed
20% by volume solution 3 micron alumina powder in water/ microfiber pad	Until uniform scratch direction	Light hand pressure in circular motion at 120 rpm wheel speed
20% by volume solution 1 micron alumina powder in water/ microfiber pad	Until uniform scratch direction	Light hand pressure in circular motion at 120 rpm wheel speed
1 liter solution: 200ml Percholric Acid, 700 ml Ethanol, 100 ml glycerol	23 seconds	Polish at 45 V at -20°C
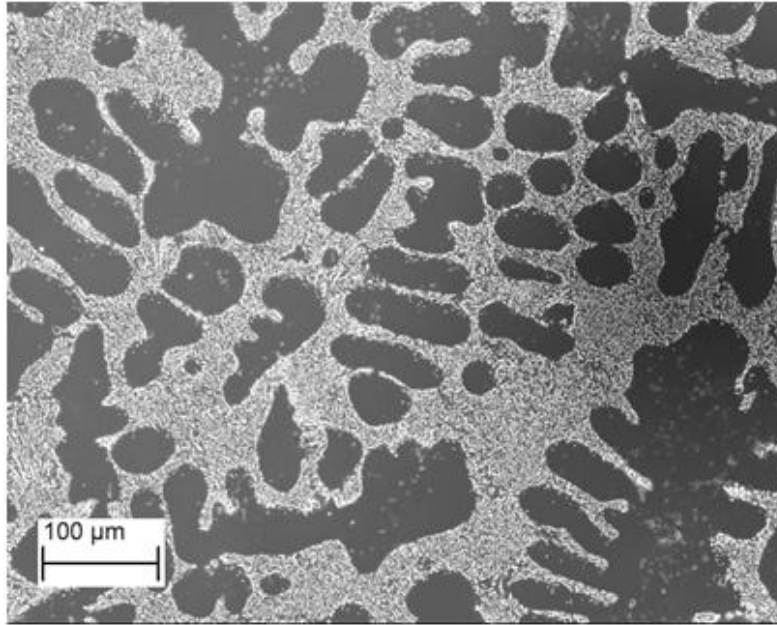
Figure 3.17   As-cast Al-7% Si secondary electron image.

b. 300^oC ECAP Results

Billets were sectioned to examine deformation behavior in the cross plane (CP), flow plane (FP), and transverse planes (TP), indicated previously in Figure 3.8. Most pertinent findings were expected to be seen in the flow plane.   The transverse and cross planes showed little additional information, however, additional images for the cross and transverse planes can be reviewed in Appendix E.

As previously discussed, the purpose of the elevated temperature ECAP was to assess the role of temperature in particle motion driven by the stress state. It was hypothesized that a matrix-diffusive-flow process would result if a significant differential pressure developed across a particle in the confines of a sufficiently softened matrix. If such behavior occurred on a significant scale, perhaps redistribution would be observed, even at the low strain rate of at 10^{-1} sec^{-1}, at which the pressing was conducted. Conducting the testing at higher strain rates was not possible due to the mechanical limitations of the experimental setup.

Selected images of the ECAP billets pressed at 300^oC are shown in Figures 3.18 through 3.22. The images suggest that the particles are not moving

significantly as a result of diffusive process. The initially crisp boundaries of the Si particle clusters are relatively unchanged and particle separation within the clusters was not appreciable at 300°C (0.65 T_{Melt}). The redundant straining has mostly restored the original microstructure at the completion of four redundant ECAP passes using Route C. For all of the multipass samples, a small degree of particle displacement was observed at boundaries of particle-depleted regions. This movement might be attributed to either particle translation with the deformed matrix, or the particle may have been diffusively driven via the imposed stress gradients. Such particle motion could only occur if very high, localized stress gradients (on the order of 100 MPa) are developed between Si individual particles. As seen in the modeling, such a large driving pressure is difficult to achieve in a softened solid, but it can be developed under the certain circumstances. The pressure estimate of 100 MPa, later used in the calculation for an ellipsoidal particle's diffusive motion given by Li et al. [64], would be sufficient to drive the neighboring particles up to 1 particle diameter within the time frame of the deformation.
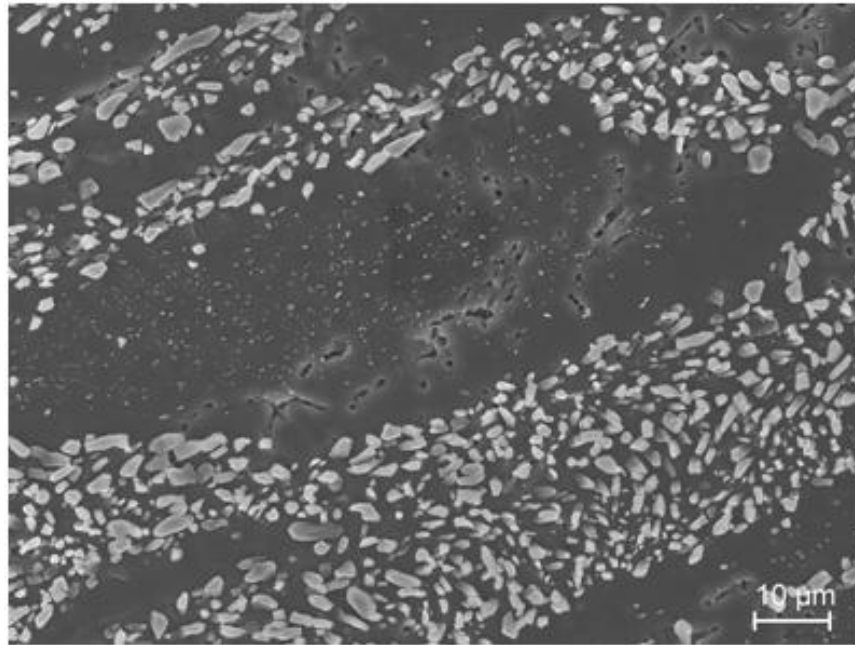
Figure 3.18 One pass 300°C Al-7% Si secondary electron image of the flow plane.
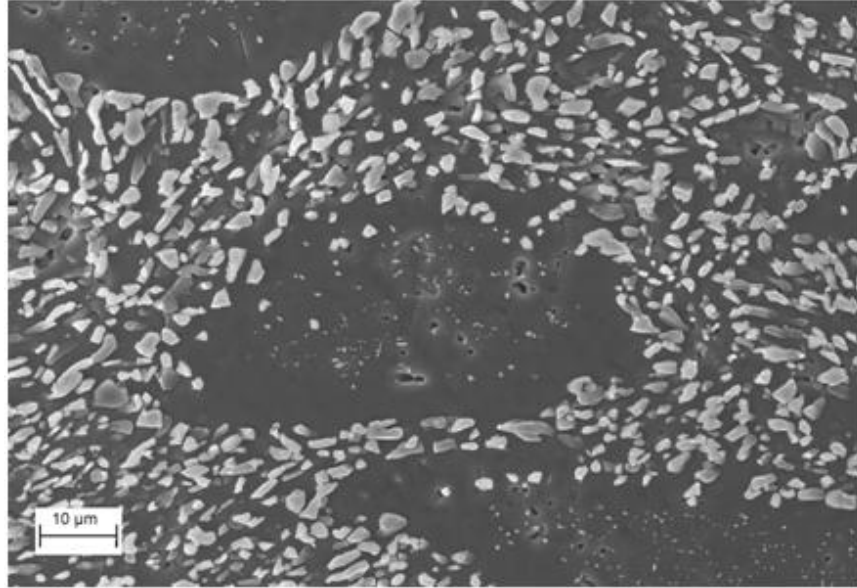
Figure 3.19 Two pass 300°C Al-7% Si secondary electron image of the flow plane after Route C.
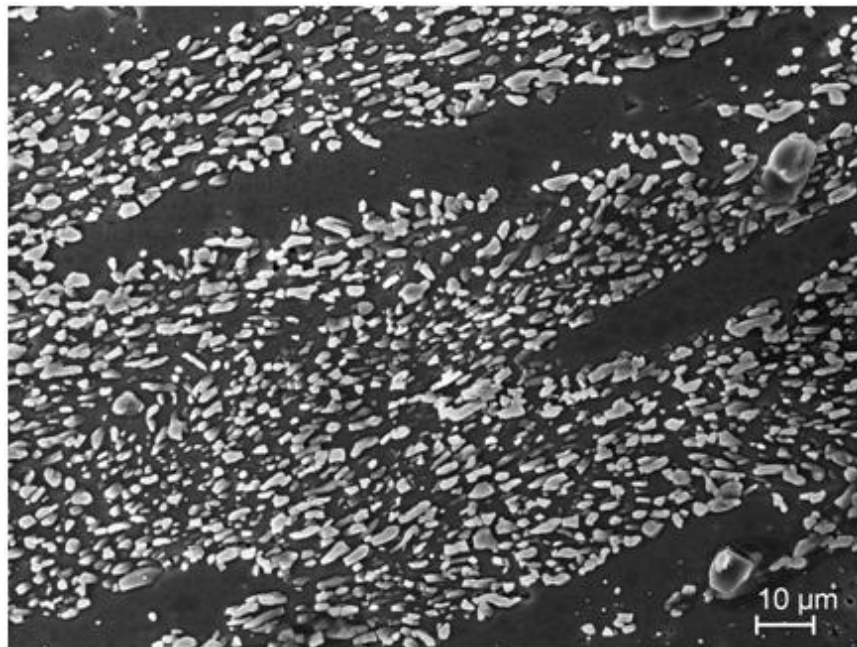
Figure 3.20 Three pass 300°C Al-7% Si secondary electron image of the flow plane after route C.
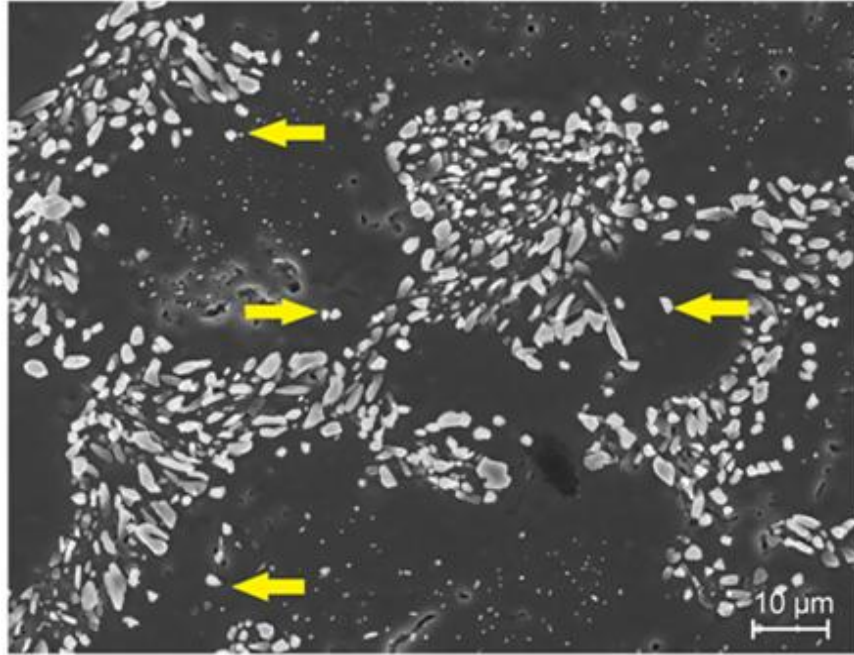
Figure 3.21 Four pass 300°C Al-7% Si secondary electron image of the flow plane with particles highlighted that appear to have moved diffusively after route C.

(a)   (b)
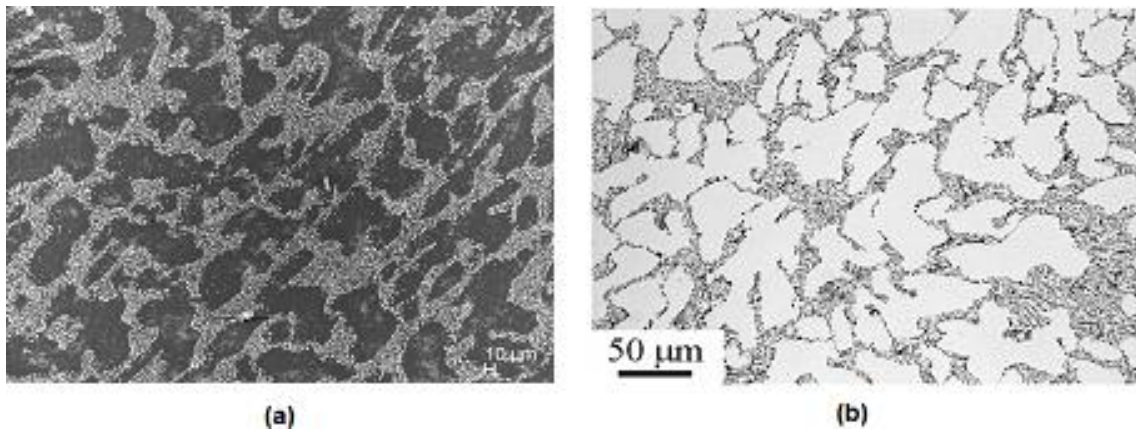
Figure 3.22 (a) Four pass 300°C secondary electron image of flow plane and (b) optical image of flow plane four at ambient temperature (25°C) Al-7% Si, after route C. From [15].

c.   400°C ECAP Results

The same redundant-strain ECAP experiment was conducted on the Na modified Al-7% Si at 400°C, approximately 75% of the materials melting temperature. The higher temperature caused a number of experimental issues not seen in the 300°C experiment. The observed results did not reflect a homogeneous ECAP shear. During

67

the experiment, the anti-seize paste lubrication became ineffective and failed to adhere to the ECAP die wall. As a result, the degree of wall friction became significant relative to the high temperature flow stress of the material. The billet deformations observed were indicative of material behavior seen during industrial high temperature extrusion processes. Material along the edges of the billet was monotonically strained to very high levels, as the outer layers served to lubricate the billet's passage during pressing. The inner core of the billet remained largely undisturbed as material from the front and outer layers flowed through the outer region, a process illustrated schematically in Figure 3.23. Due to the clearance gap required for the plunger to pass through the die channel, a small amount of billet material was also back extruded around the plunger with each successive pass. Selected images after the 400°C ECAP are shown are shown in Figures 3.24 through 3.31.
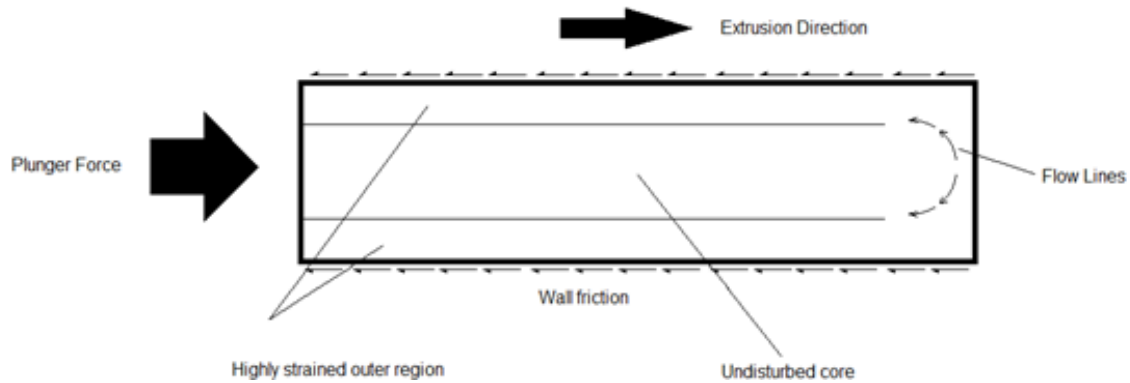
Figure 3.23 ECAP billet schematic illustrating the apparent flow field during 400°C pressing of the Al-7% Si alloy.

68
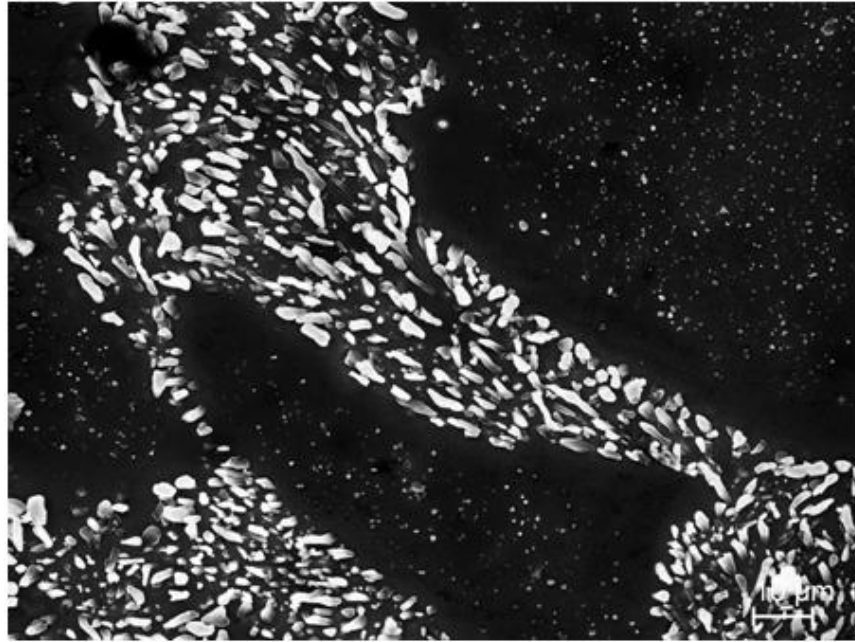
Figure 3.24 One pass 400°C Al-7% Si secondary electron image of center core in the flow plane after Route C.
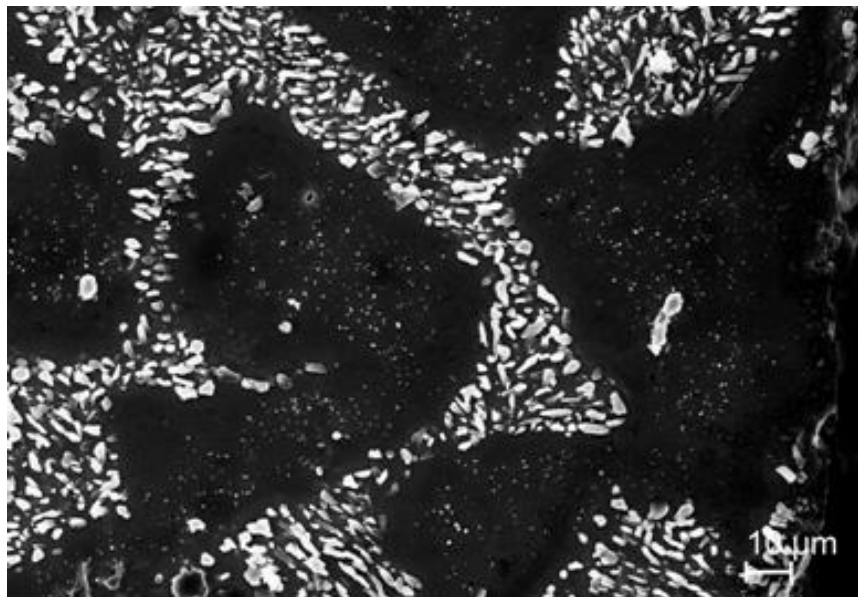
Figure 3.25 Two pass 400°C Al-7% Si secondary electron image of center core in the flow plane after Route C.
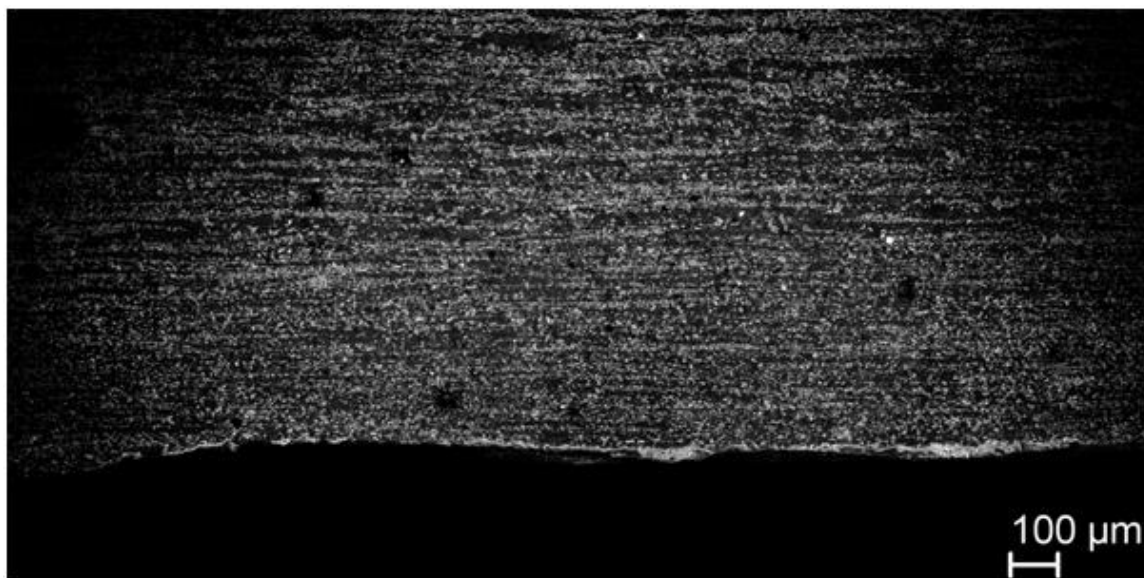
Figure 3.26 Two pass 400°C Al-7% Si secondary electron image of the bottom edge of the flow plane after Route C.
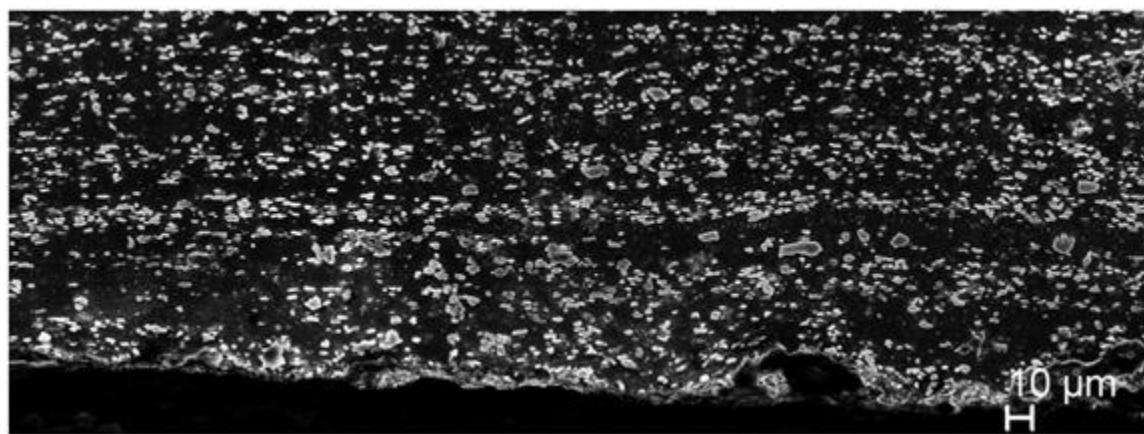
Figure 3.27 Higher magnification two pass 400°C Al-7% Si secondary electron image of the bottom edge of the flow plane after Route C.
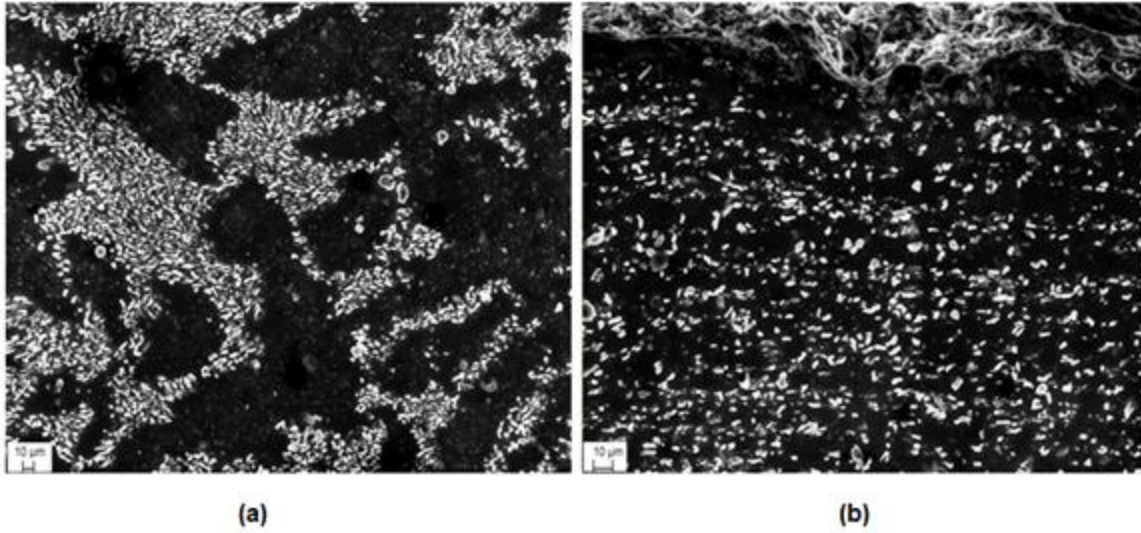
Figure 3.28 Three pass 400°C Al-7% Si secondary electron image of (a) center core and (b) upper edge of the flow plane after Route C
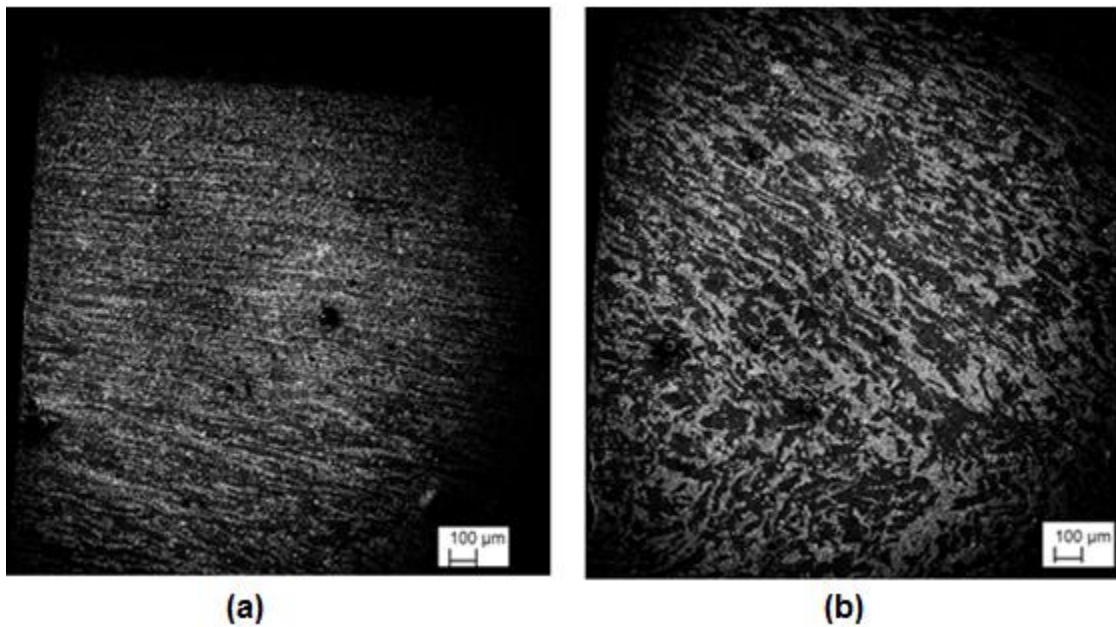
Figure 3.29 Three pass 400°C Al-7% Si secondary electron image of (a) upper edge and (b) upper core region of flow plane after Route C.
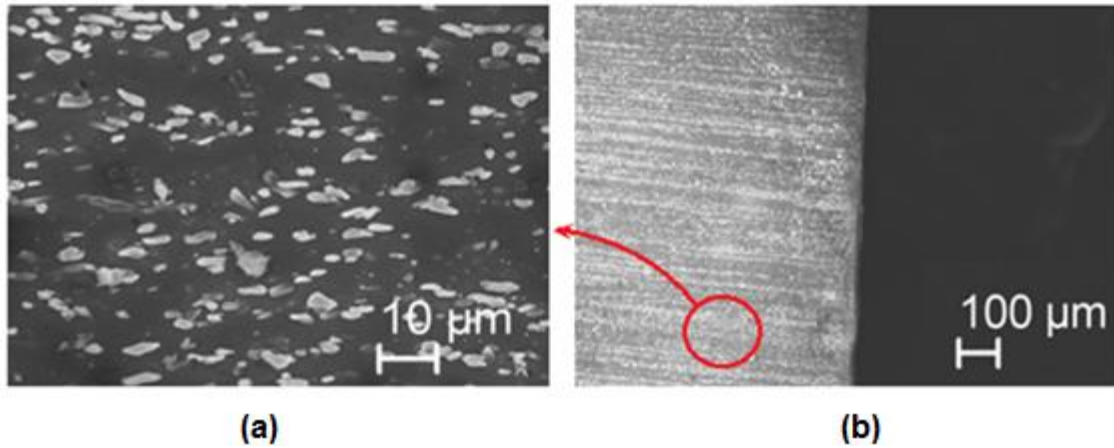
Figure 3.30 Four pass 400°C Al-7% Si flow plane secondary electron image of (a) lower right edge (b) middle right edge of sample after Route C.
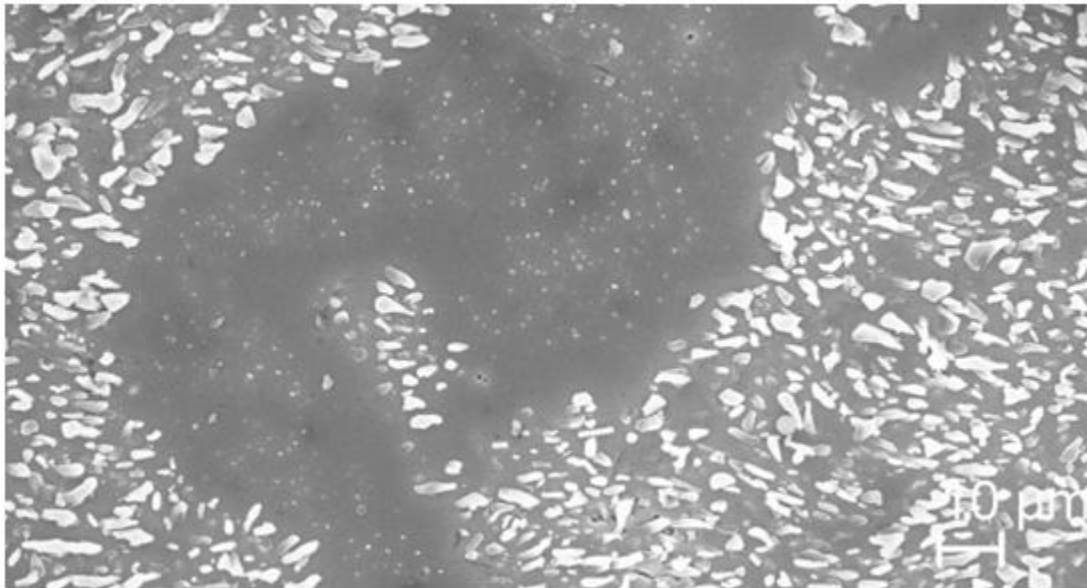
Figure 3.31 Four pass 400°C Al-7% Si secondary electron image of mid-core region after Route C.

E.   DISCUSSION

Figure 3.32 shows the phase diagram for the Al-Si system. The hypo-eutectic Al-7% Si used for the ECAP experiment has a liquidus temperature of 618°C and a solidus temperature of 577°C [108].   Thus, the two foregoing experiments were conducted at 0.65 T_{Melt} and 0.75 T_{Melt}. Initially, the goal was to approach a temperature regime, closer

to that encountered in friction stirring. Due to safety concerns and the experimental issues documented during the 400°C pressing, proceeding to higher temperatures was deemed impractical. More importantly, the minimal degree of observed particle motion at the two elevated temperatures showed with reasonable certainty that the level of redistribution attained in friction stir is unlikely to be the sole result of diffusive type matrix flow driven by externally imposed shear. Here, die wall friction resulted in an apparent strain gradient, and this may be a factor in redistribution.
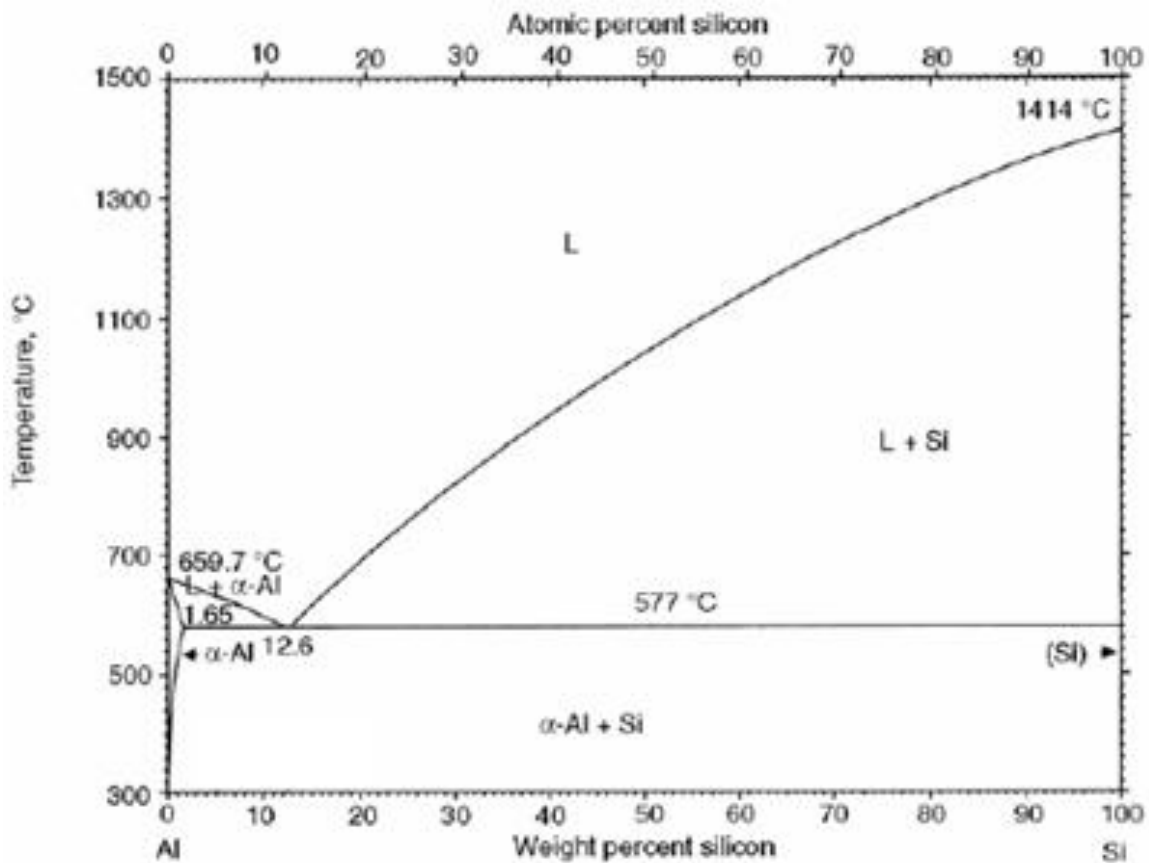
Figure 3.32 Phase diagram for the Al-Si system. From [108].

The 300°C pressing presented evidence to suggest that particle motion can occur via matrix flow, but the experimental result suggests that such motion occurs only to a small extent in a during the 10 seconds of the shearing operation. At this lower temperature, the frictional effects of the die wall appeared to be better controlled and

certainly smaller in comparison to the flow stress of the material at that temperature. As a result, the shear strain was developed reasonably uniformly throughout the billet, presenting a better opportunity for the development of localized pressure gradients. Even so, the observed particle-matrix relative motion was minimal. At the higher number of passes, the silicon cluster boundaries became increasingly irregular and occasionally particles appeared to move from the primary-eutectic boundary. Note that, the fine Si precipitates, observable in the particle-depleted regions, are formed at temperatures below the eutectic due to super-saturation of the solid solution Al matrix. The apparent displacements of the large Si particles were small however, and generally no more than 1 or 2 particle diameters. Based on calculations using the Li, et al. methodology, and published experimental diffusion data for Al-Si [110]–[113], the experimental observations appear to agree with analytically predicted values and also confirm the ANSYS results. The analytical prediction, based on the reduced stiffness of the heated matrix and the maximum expected gradient in hydrostatic stress, showed that an equiaxed particle probably would travel less than a single particle diameter during the timeframe of the pressing operation. In fact, this behavior was observed. The complete calculation for the predicted particle velocity can be reviewed in Appendix F, but the graphical results of that analysis is show in Figure 3.32.

Figure 3.33 shows the predicted diffusive particle velocity, as a function of temperature, which might result from a differential hydrostatic pressure across a 1 µm equiaxed Si particle contained in an aluminum matrix. The velocity is calculated for a wide range of differential pressures to account for uncertainty. The solid and dashed lines plotted for each pressure represent the calculation for when varying the particle / matrix stiffness ratio. As shown, a stiffer particle tends to travel faster, but above a stiffness ratio of 4, this effect is diminished. The circled region shows the temperature and pressure regime for the experiment. As can be seen from the figure, the expected particle velocities are very small.
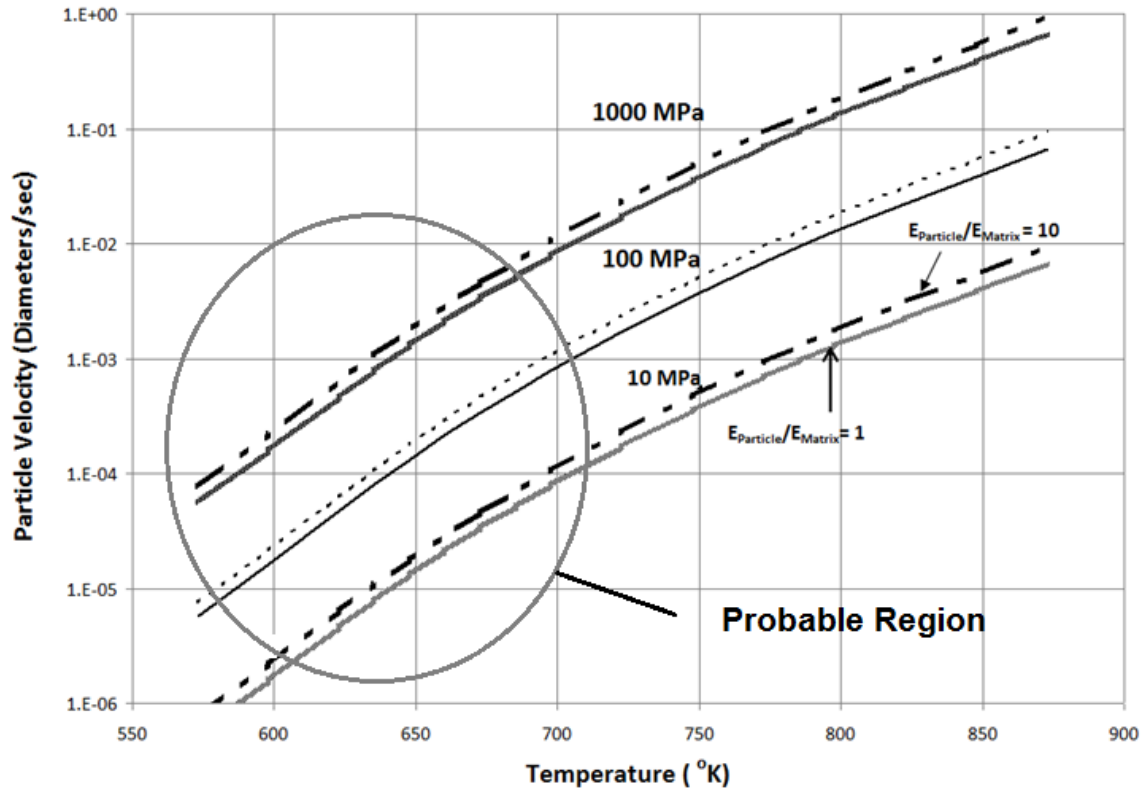
Figure 3.33 Predicted instantaneous diffusive velocity for an equiaxed Si particle subjected to a differential pressure from 10 to 1000 MPa in an Al matrix at elevated temperature.

Particularly notable, though unexpected, was the apparent monotonic strain which occurred at the billet's outer edges during the 400°C pressing. While billet core remained nearly undisturbed in all 4 passes, the billet's outer layers were subject to die-wall friction. These regions exhibited microstructures that resembled samples undergoing ECAP to very high numbers of passes (in excess of 32). In these locations, the microstructure (shown previously in Figures 3.26, 3.27, and 3.28(b)) appeared considerably more homogenous over multiple length scales than either the as-cast material or the core region for the same number of passes. The highly strained region retained a distinctly banded appearance. Although the degree of homogeneity will be addressed in a later chapter, as one proceeds from the billet's edge to the undisturbed core, the level of strain and apparent homogeneity is visibly and gradually reduced, indicating the probable presence of a strain gradient. From this observation, it can be

75

deduced that large monotonic strains may have a partial role in creating a homogeneous structure. Except for the residual bands, the resultant microstructure in the strained region might be indistinguishable from some microstructures developed by friction stirring.

F.   CONCLUSIONS

The conclusions of this section of work are summarized in bullet form:

- The homogeneous shear in elevated temperature ECAP does not produce sufficiently large particle / matrix relative motion to account for the degree of second phase redistribution at the levels seen in friction stir.

- Inhomogeneous strain paths resulting from high strain rate induced voids or unusual conditions at the boundary can produce internal material flows, which in turn can produce significant particle displacements.

- A large monotonic shear at elevated temperature can produce microstructures that appear to have more homogeneous characteristics than the parent material, although the structures tend to retain a distinct banded nature.

- Intra-cluster pressure gradients can develop as a result of a deformation process, but the gradient magnitude is strongly dependent on the constraint pressure and particle spacing. Intra-cluster gradients disappear in the absence of a hydrostatic constraint, or when particles are tightly packed.

- Deformation-induced intra-cluster pressure gradients are more difficult to develop at higher temperature when the material is softened, and tend to deteriorate as strain is increased.

- At the levels of constraint pressure and strain reported for friction stirred materials, the expected pressure gradient levels are insufficient to produce large particle motions and therefore fully account for redistribution.

IV. MECHANISM OF REDISTRIBUTION IN A TWO PHASE ALLOY CONTAINING NONDEFORMABLE PARTICLES IN A SOFT MATRIX

A. PREFACE

This chapter examines stir zone deformation and microstructural evolution during friction stir processing of AA356. The friction stir was conducted over an order of magnitude in RPM (400 RPM to 4000 RPM) at a traversing rate of 76.2 mm (3.0 inches) per minute, using both smooth-faced and threaded tool types. The purpose was to attempt to identify the physical mechanism(s) occurring in the process that lead to constituent redistribution and a more homogeneous microstructure.

B. INTRODUCTION

One of the main purposes of this investigation is to determine the mechanism(s) by which deformation may redistribute nondeforming constituents of microstructure in such a way that the resulting microstructure becomes more homogeneous. The purpose of the friction stir experiment involving RPM variation was to examine how the tool's rotational speed (at a set traversing rate) and geometry affect the base material's transition to a more homogeneous state. The ECAP work in Chapter III showed that homogeneous shear deformations under a superimposed hydrostatic stress are unlikely to produce pressure gradients sufficiently large to induce significant particle / matrix relative motions by diffusive processes. What motion occurs, either experimentally or numerically, seems to be induced by introducing strain inhomogeneity in the deformation path. Furthermore, the ECAP experimental work clearly showed that low strain rate, high temperature ECAP shearing produces very little particle / matrix relative motion and minimal particle fracture.

Although the strain rates are at least an order of magnitude higher, FS is also a shear-dominated process wherein the processed volume is also subject to a large hydrostatic pressure, probably on the order of 100 to 150 MPa [114]. The hydrostatic pressure in the region below the tool shoulder arises as a result of the downward plunge

force required to embed the pin and the temperature increase within the stir zone, which causes the softened material to expand against the cooler region of the base material. Despite the apparent similarities in ECAP and FS stress states, FS results in a dramatically different microstructure when compared to the original base material. In ECAP, only with very high number of monotonic shear passes do the microstructures approach a uniform, homogeneous state. Even then, a closely spaced, banded arrangement of particles is still readily apparent. Such banded structures are also observable in some regions of single pass FSP stir zones. These observations suggest the following possibilities and rationale for conducting this experiment:

1. In general, FS is much more effective in redistributing micro-constituents, so that the role of strain rate (i.e., RPM), is likely to be important in this process. The rate may be affecting particle fracture, pressure and temperature gradient development, the volume of extrusion material affected with each rotation, and the extrusion strain path. During FSP "extrusion," material stripped ahead of the rotating pin is subsequently forced through the thin region between the pin face and the more rigid stir zone wall, and thus the process resembles high speed extrusion.

2. Based on the results discussed in Chapter III, the pressure gradient driving diffusion-controlled particle motion must be extraordinarily steep to produce a large particle transit distance. If such a pressure gradient is not the primary mechanism, an additional physical mechanism for homogenization must exist whereby a homogeneous structure can be obtained such that the particles need not travel large distance relative to the surrounding matrix material.

3. If a representative volume element (RVE) of FS material is being monotonically strained and thinned as it travels around the pin tool, the volume may achieve strains comparable to those obtained during a multi-pass, monotonic ECAP process.

4. The FS strain path may be neither homogeneous nor continuous, and an RVE may be thinned and broken into multiple segments, more akin to distributive and nondistributive mixing.

5. A combination of diffusive motion, element thinning (large strains), and advective mixing may be all occurring to some degree.

C. EXPERIMENTAL PROCEDURE

AA356 material was subjected to friction stirring over an order of magnitude in RPM values (ranging from 400 to 4000 RPM) using a hardened H13 steel tool with a 12 mm shoulder. As with the elevated temperature ECAP, an immiscible alloy in the Al-Si system was selected in order to more easily isolate to the mechanical effects of the deformation process. Further, the acicular structure of the Si phase AA356 is well suited to revealing the onset of fracture and direction of motion at particular locations both inside and outside the stir zone.

A constant traversing rate of 76.2 mm (3.0 inches) per minute was selected in order to isolate the mechanical and distributive effects of varying the RPM. For better SZ consolidation, a tilt angle of 2° was used for all samples. Schematics for the tools are shown in Figure 4.1. The pins were frustum-shaped and 3 mm in length. One pin was smooth-faced and the other threaded.
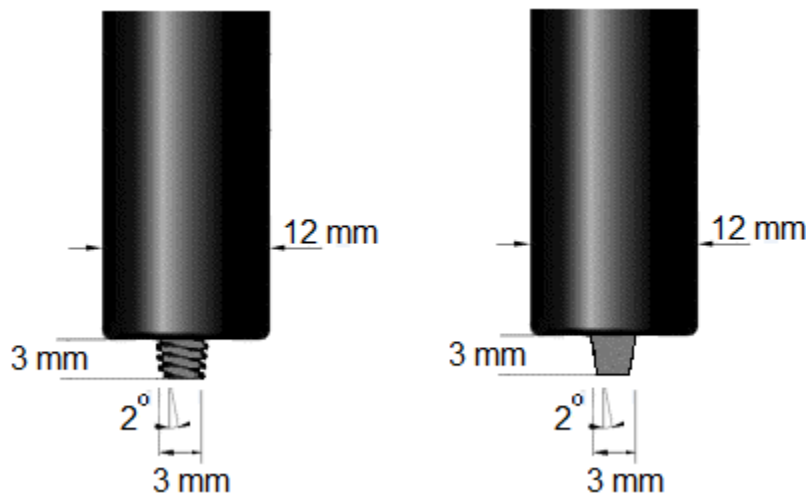
Figure 4.1   Tool profiles used during FSP of AA356.

The FSP was conducted on a LAGUN Republic 220V, 3 phase, 15 AMP milling station outfitted for FSP operation. With a maximum 5.5 kW (7.5 hp) rating, processing

was restricted to small tool sizes so as to obtain viable process zones over the range of speeds desired. Larger pins resulted either in machine stalling or in torn, unusable process zones. The FSP was initially performed with a clockwise tool rotation using the smooth tool. A counter-clockwise rotation was used with the threaded pin, which prevented the tool from drawing itself into the material and producing excessive lateral forces. Since plunge force could not be monitored with the existing equipment, the tool was plunged to a constant displacement, flush with the material's surface, i.e., friction stirring was conducted under displacement control.

Figure 4.2 shows the plan view of the resulting process regions for the smooth pin, varying RPM trial. Traverse distances were made long enough to ensure the process had achieved steady state, yet short enough to conserve material. Similarly processed plates (not shown) were obtained for the threaded tool. To avoid interference from temperature effects, ample time between runs allowed the base material to cool to room temperature prior to conducting the next run. Surface temperature was monitored with a hand-held Fluke 62 infrared thermometer.
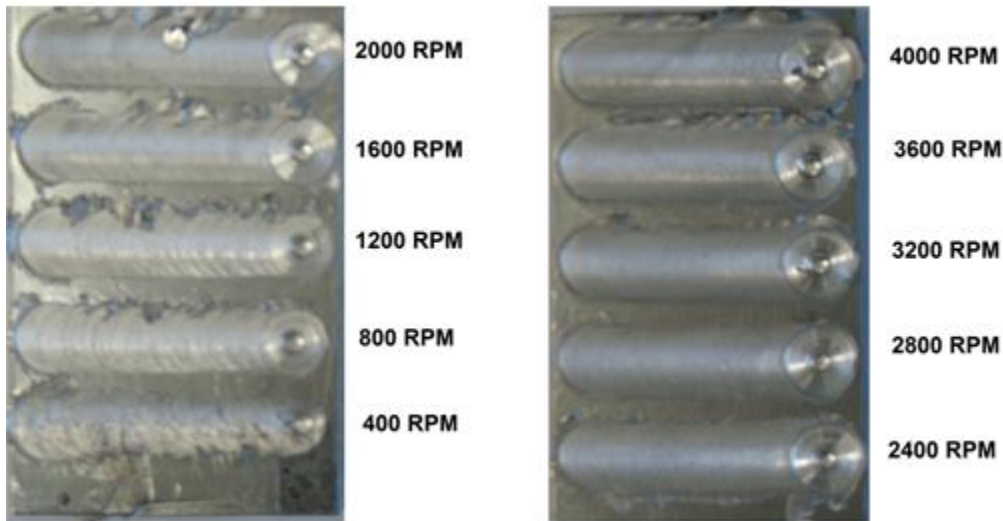
Figure 4.2 FSP AA356 Plates for the smooth pin tool RPM trial.

Each process region was subsequently sectioned in order to characterize the transverse and plan views (at the extraction site). As shown in Figure 4.3, transverse sections were taken approximately 1 shoulder diameter back from the exit hole, and the plan sections were taken at mid-depth of the stir zone at the pin extraction site. Sectioning of the plan view and transverse planes was conducted at low speed using an aluminum oxide cutting wheel on a Struers Sectom-10 bench-top saw. The sectioned samples were examined for the morphological effects of RPM and tool pin geometry. Optical microscopy was conducted using a Nikon Epiphot 200 microscope with a Nikon DS-2Mv Digital Sight. Secondary electron imaging was conducted with a Zeiss Neon 40 Field Emission Scanning Electron Microscope (SEM) using a 20 KeV accelerating voltage and 5 mm working distance.
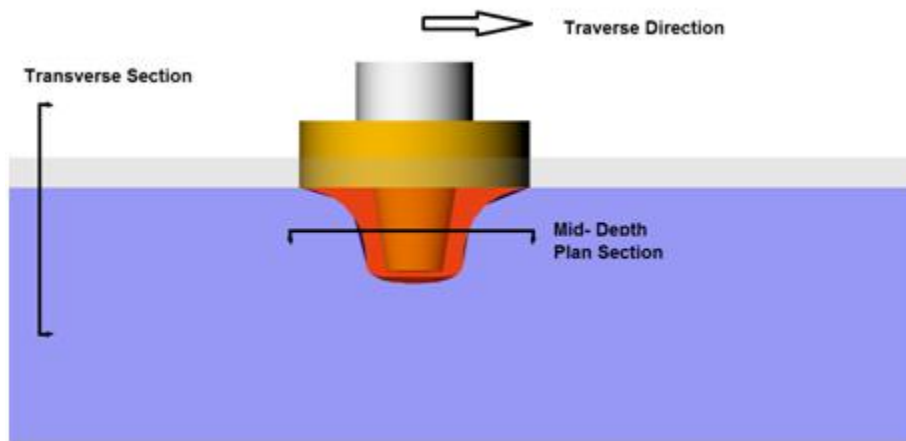
Figure 4.3   Sectioning for the FSP AA356 process zones.

D.   RESULTS AND DISCUSSION

The AA356 material was prepared for microscopy in the same fashion as the previous Na-modified Al-7% Si sample set, using mechanical polishing (see Table 3.2) followed by electro-polishing in accordance with Smithells Metal Reference Book [107]. As shown in Figures 4.4 and 4.5, the material exhibits microstructure characteristics typical of commercially cast unmodified AA356 (nominally Al–7Si–0.3Mg, wt.%). The structure is comprised of a primary Al constituent and a eutectic constituent with numerous high aspect ratio needle-like Si particles. In this state, the material is prone to

crack development, tends to be brittle, and has reduced fatigue performance [115]. To obtain practical mechanical enhancements, it is common practice to alter the as-cast flake or acicular silicon morphology by employing heat treatment or adding certain modifiers such as sodium or strontium [116]. Santella et al. [117] showed that the FSP can provide increased ultimate strength and a four-fold improvement in AA356 ductility with only a small drop in yield strength. Again, these improvements are attributed to the homogenous distribution of the Si second phase constituent, which is well beyond the capability of any casting modification.
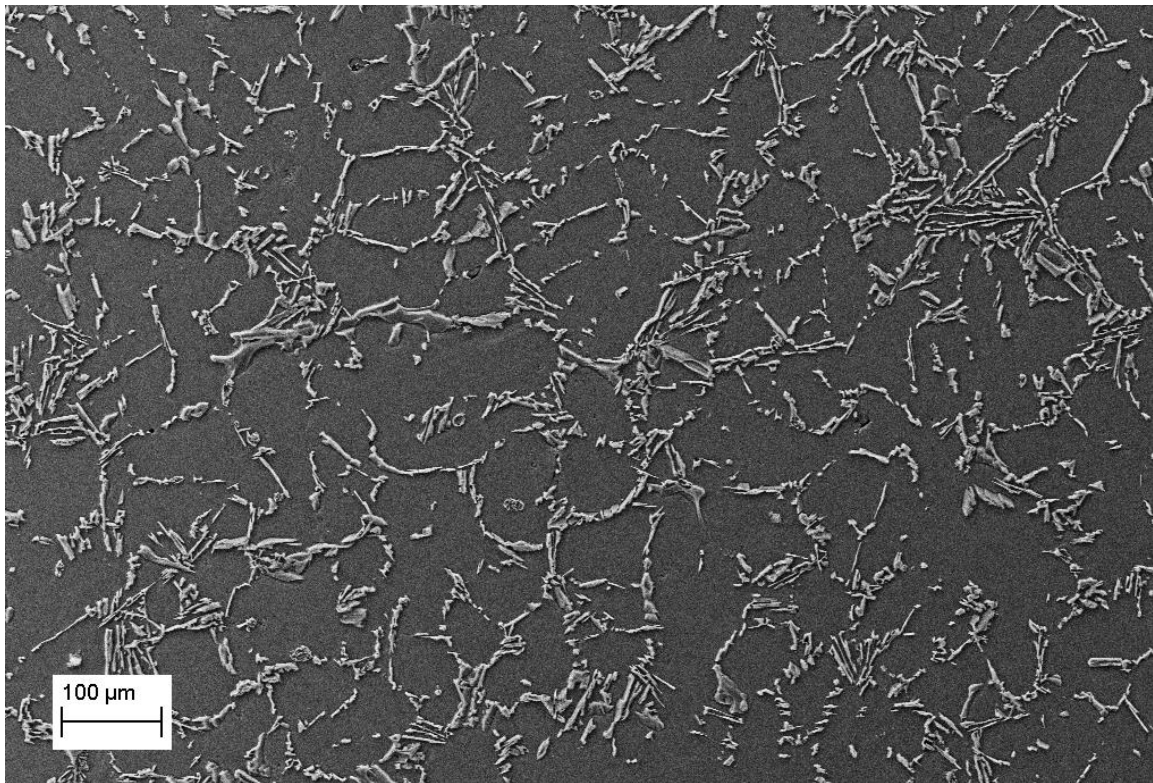
Figure 4.4 Secondary electron image of an AA356 as-cast microstructure showing the distribution of Si particles in the eutectic constituent and the Al solid solution matrix.

In this experiment, the purpose was not to access mechanical characteristics but to understand how the particles transition from the as-cast morphology into the structure seen in the stir zone. Experimentally, the acicular shape of the particles is useful in several respects: (1) the particles are more vulnerable to fracture and serve as visible

markers for the TMAZ boundary, (2) the high aspect ratio particles tend to align themselves with material flow, and (3) the separation of broken particle segments can provide insight as to the degree of relative motion between the particle and matrix.
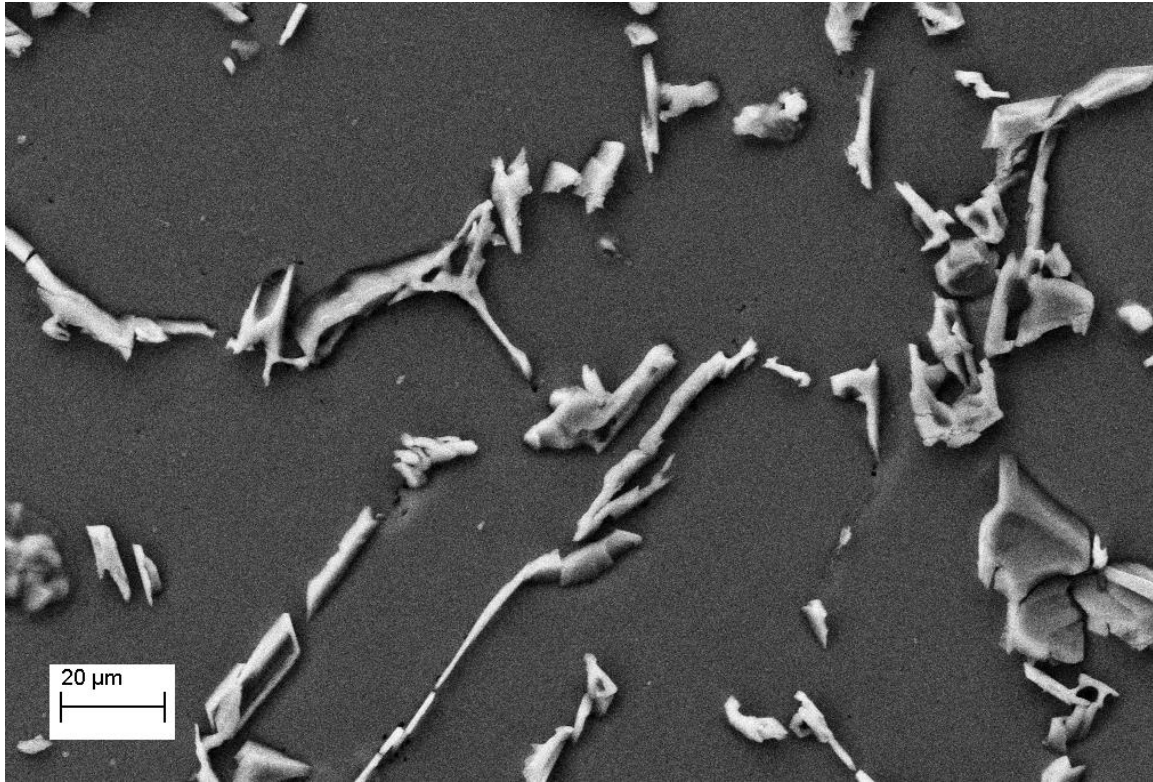
Figure 4.5 Secondary electron image of an AA356 as-cast microstructure very clearly showing the distribution of the acicular Si particles in the eutectic constituent and the Al solid solution matrix.

1.   Effect of RPM on Stir Zone Width

Optical and secondary electron imaging for the smooth-pin and threaded-pin revealed several rate dependent effects in the respective stir zones. Figure 4.6 through 4.9 show the images under discussion. Figure 4.6 shows optical images of the pin extraction site for the threaded tool at 400 and 4000 RPM, as well as for the smooth tool at 2000 RPM. First, the width of the stir zone on plan view sections varied strongly with RPM. Figures 4.7 and 4.8 show the low end of the speed range (400 and 800 RPM) where the SZ thicknesses on the advancing side measure approximately 500 μm at 400

RPM, while at 800 RPM the stir zone thickness at a corresponding location decreased to 200 μm. This trend continues through to 4000 RPM. Figure 4.9 shows secondary electron images of the advancing side thickness for the highest rotation rates, 3600 and 4000 RPM.

(a)   (b)   (c)
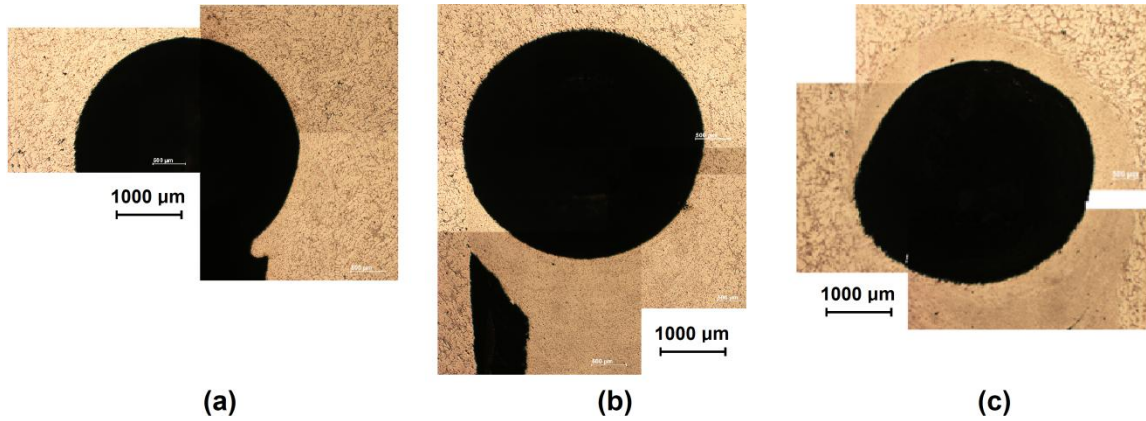
Figure 4.6 Optical image montages of the plan view of FSP pin extraction sites for (a) threaded pin FSP at 4000 RPM, (b) smooth pin at 2000 RPM, and (c) 400 RPM threaded pin.
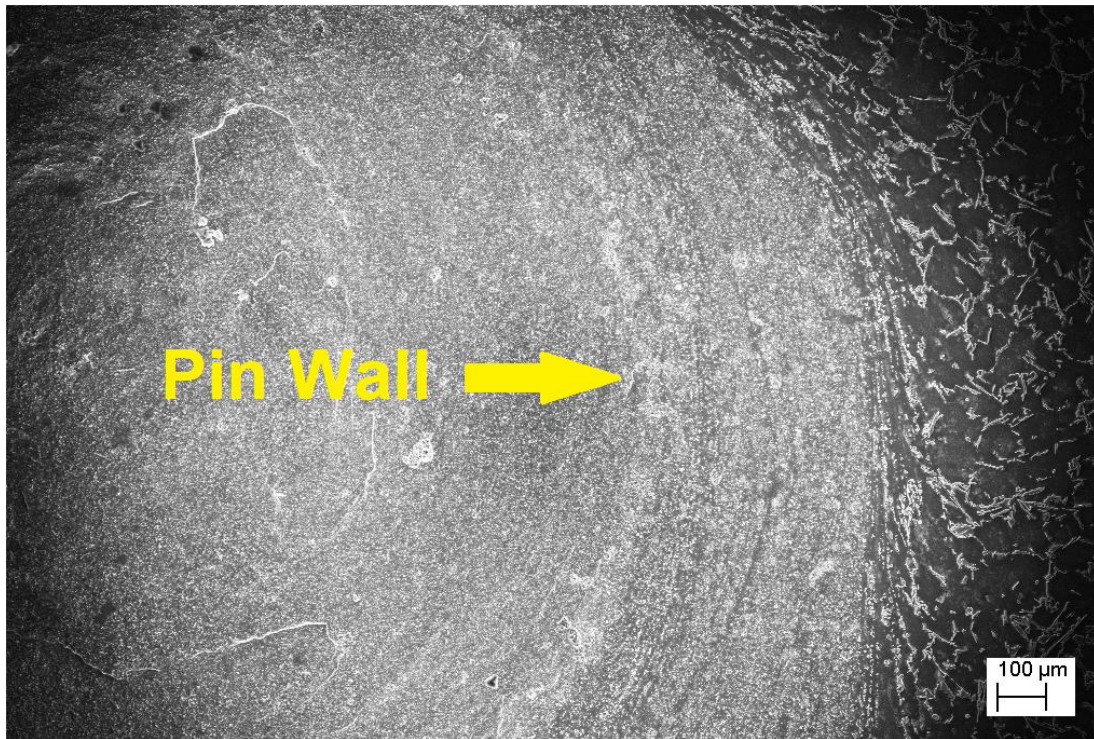
Figure 4.7 Secondary electron image of the plan view plane on the advancing side of the tool for threaded-pin FSP at 400 RPM.
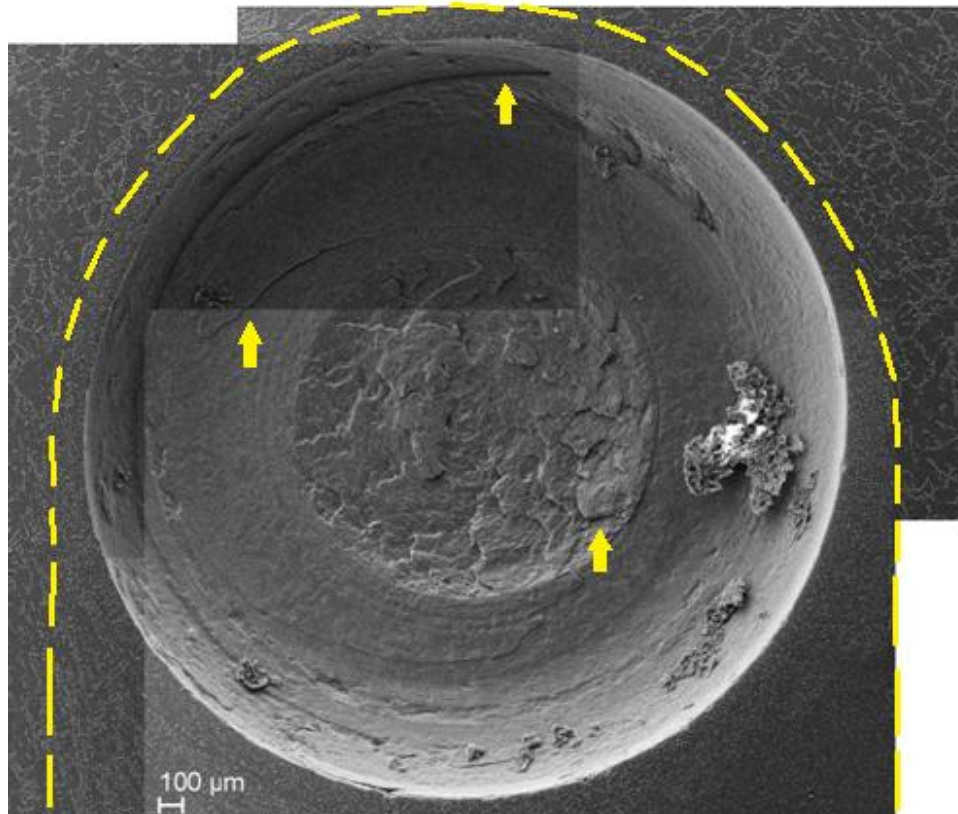
Figure 4.8 Secondary electron montage of the plan view plane for threaded-pin FSP at 800 RPM. The dashed line outlines the visibly stirred region and the arrows indicate sheet like formations observed on the bottom and sides of the pin surface at the extraction site.
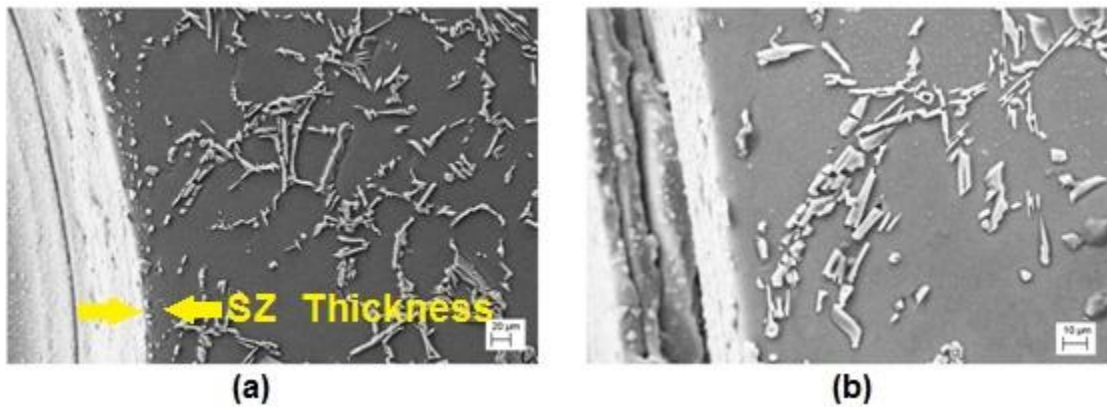
Figure 4.9 Secondary electron image of the plan view plane on the retreating side of the tool for smooth-pin FSP at (a) 3600 RPM and (b) 4000 RPM. A greatly decreased stir zone thickness is noted at the higher RPM.

Figures 4.10(a) and 4.10(b) show the SZ thickness measurements plotted for the entire range of RPM's for the smooth and threaded tools. The plot shows a highly nonlinear relationship between SZ thickness and RPM, for both the advancing and retreating sides. Figures 4.11 and 4.12 show plan views of the extent of SZ size for the threaded and smooth tool stir zone sizes, respectively, as a function of RPM. The tool's were rotated in opposite directions, so to allow for more convenient comparison, Figures 4.11 and 4.12 show the plan view from above and below the tool, respectively. The thickness reduction is most likely due to temperature rise with increasing RPM resulting in a softer, more easily sheared material in close proximity to the pin face. The net result is that a smaller volume of material is pulled into the SZ. Although no means was available to measure temperature at the pin interface, steady-state surface temperature measurements were taken during a plunge experiment (without traversing the tool) approximately 1 mm in front of the shoulder. These measurements showed that the higher RPM resulted in about a 25% rise in steady state temperature at that location (see Figure 4.13).
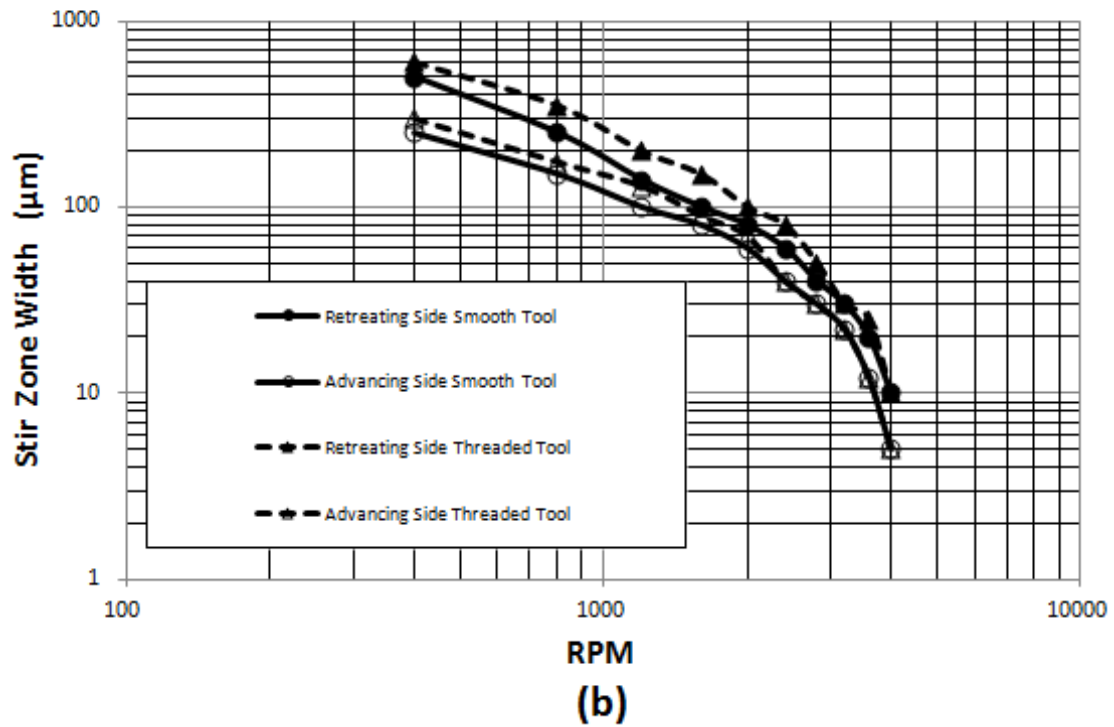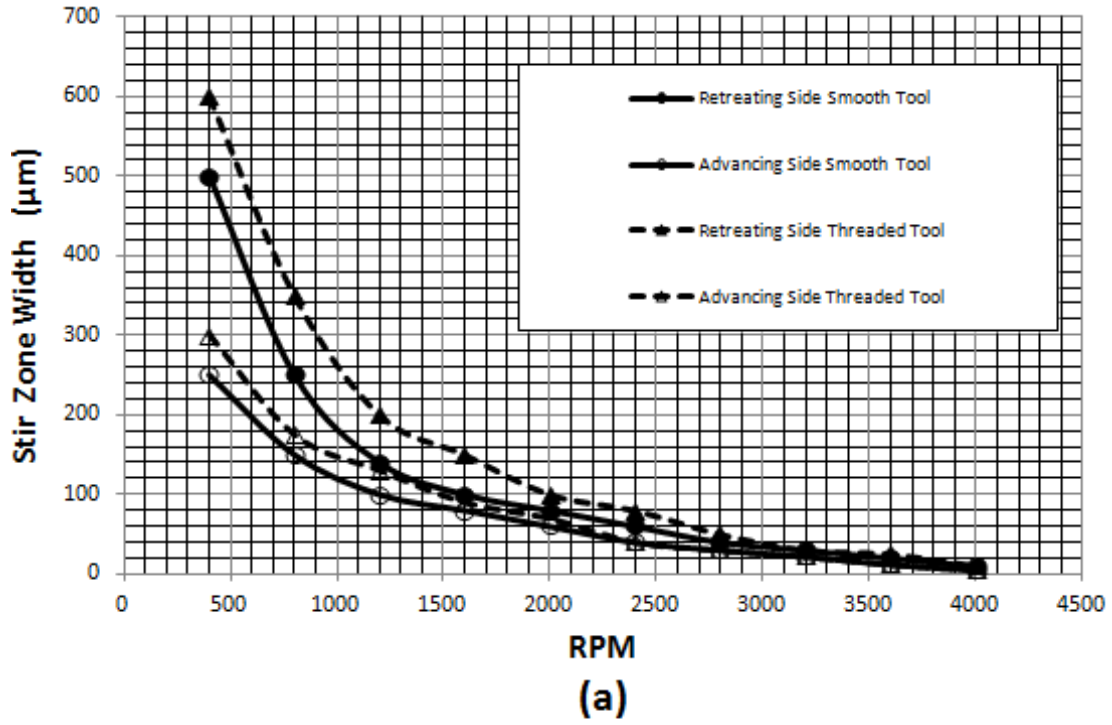
Figure 4.10 (a) Plot of advancing and retreating stir zone thickness (outward from the pin face into the work piece) vs. RPM at the extraction site during a 3 IPM traverse. (b) the same data shown on a log-log scale.
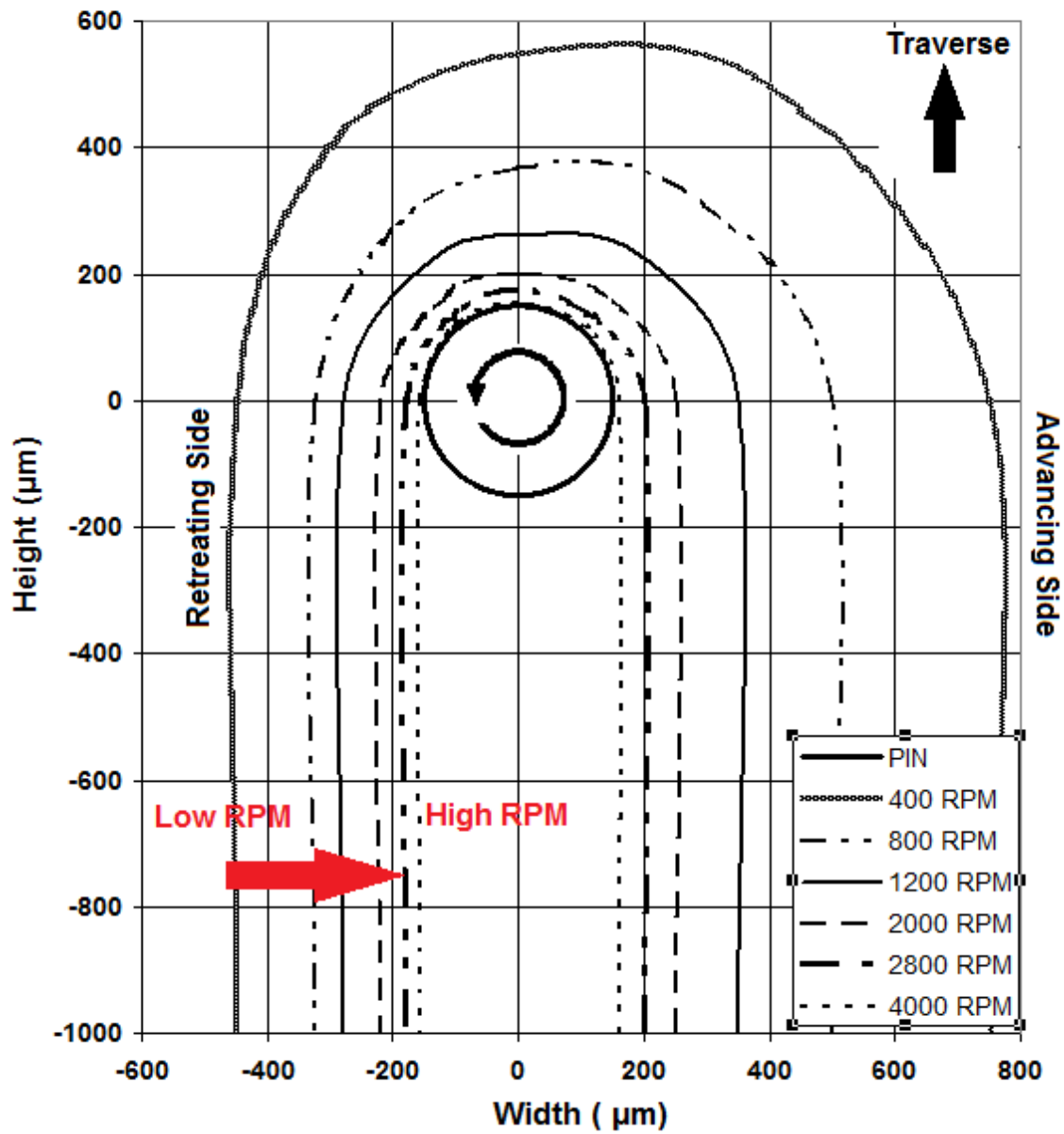
Figure 4.11 Shown from above, a plan view of the counterclockwise rotating threaded tool's stir zone size at mid-depth, shown as a function of RPM for a 3 IPM traverse.
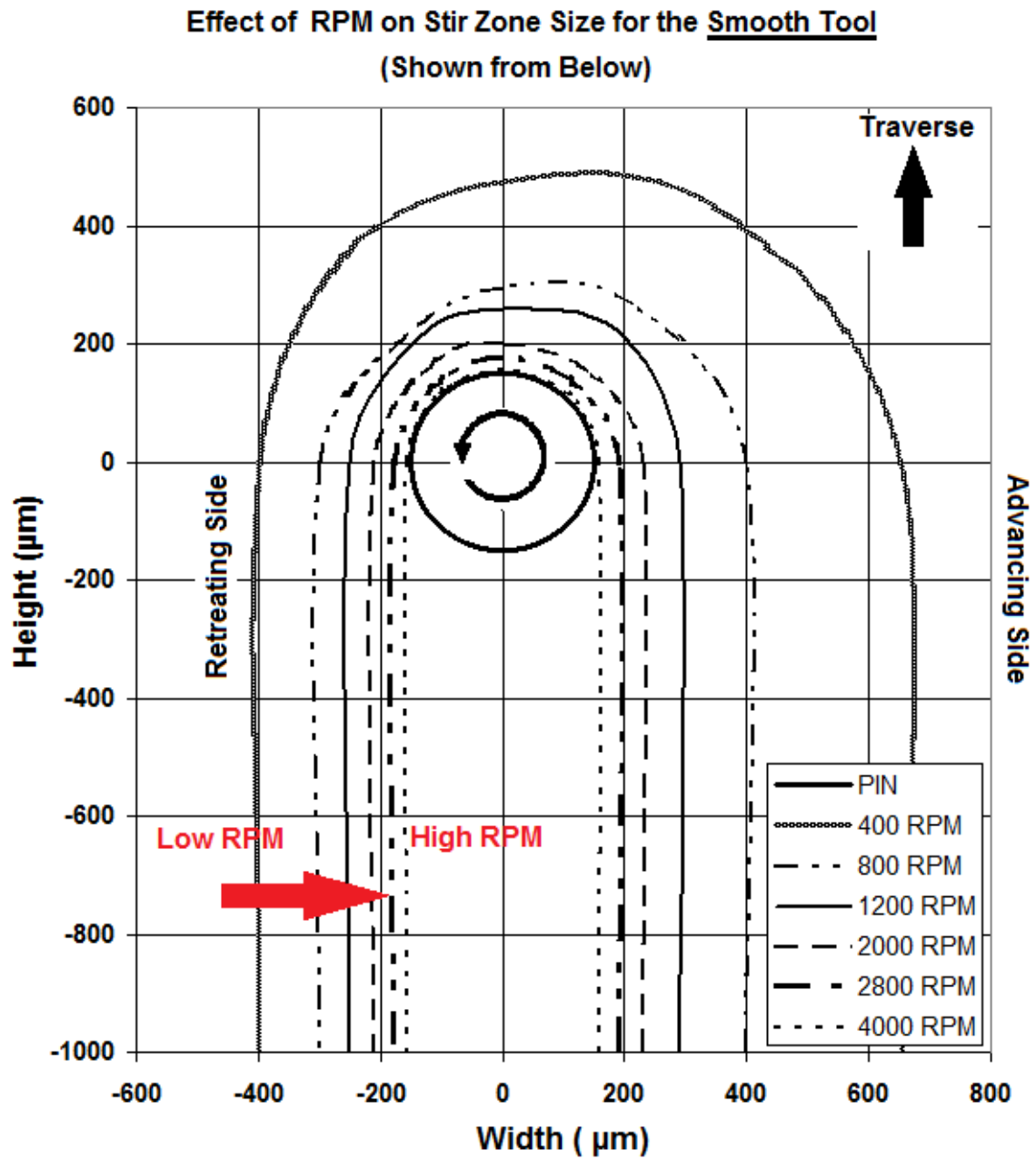
Figure 4.12 Shown from below, a plan view of the clockwise rotating smooth tool's stir zone size at mid-depth, shown as a function of RPM for a 3 IPM traverse.
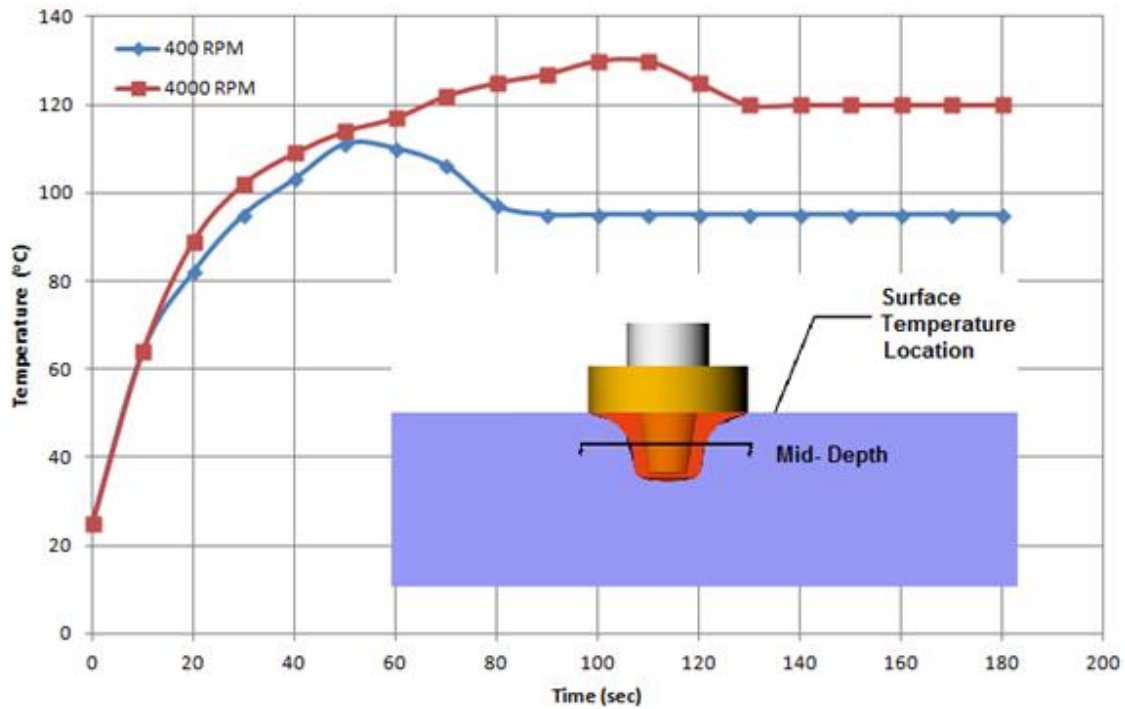
Figure 4.13 Plot of surface temperature rise 1 mm ahead of the tool shoulder during a 3 minute plunge experiment at 400 RPM and 4000 RPM with a smooth tool.

The static plunge also showed that the stir zone greatly expands in width over an extended plunge time, displayed in Figure 4.14 and 4.15 for the threaded tool at 400 RPM and 4000 RPM, respectively.
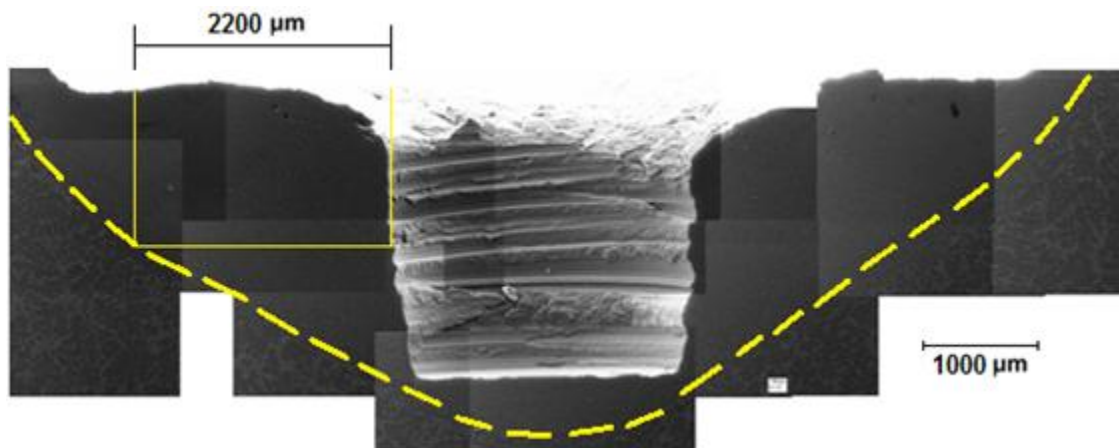
Figure 4.14 Steady state plunge stir zone thickness montage after a 3 minute plunge at 400 RPM with the threaded tool. The dashed line highlights the edge of the stir zone. At mid-depth the SZ width is approximately 2200 μm from the pin face.

90
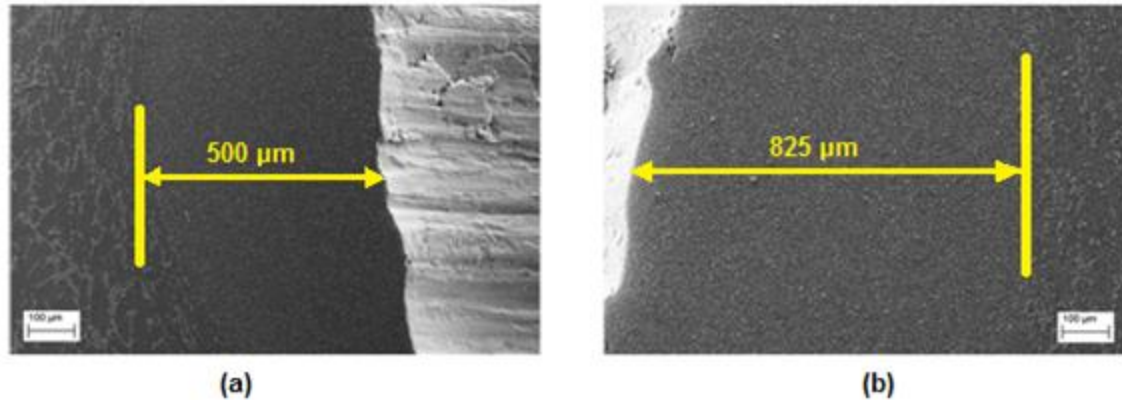
Figure 4.15 Secondary electron image of the plan view plane for (a) retreating and (b) advancing stir zone thicknesses after a 3 minute plunge at 4000 RPM with the threaded tool.

2. Void and Layered Formation

A higher RPM has been shown to provide generally better mechanical qualities in FS material [118], but RPM has other, localized effects on the material. RPM directly affects the stir zone width and void formation since it determines the volume of material which is stripped from the advancing-side wall. It was observed in this study that void formation occurs when the traversing rate and rotation rate are not properly balanced, i.e., at extreme combinations of IPM and RPM, the volume of stripped material does not approximately equal the forged volume (see Figure 4.16).
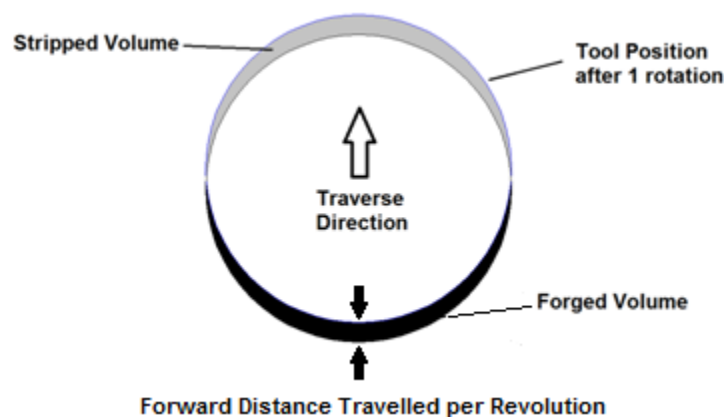
Figure 4.16   Schematic of stripped and forged volumes during a single rotation.

91

At low IPM / high RPM, the amount of material stripped ahead of the tool exceeds the forging volume opened behind the tool because the hydrostatic pressure within the stir zone forces material out from below the shoulder as flash [119]. This ultimately leaves behind insufficient material to fill the forging volume and a void develops. Although larger downward force generally can produce a wider range of void-free welds [120], in this case, excessive downward force serves to exacerbate the condition. Flash formation was visible observed during several of the high RPM trial runs, as shown in Figure 4.17. Conversely, at high RPM / low IPM, insufficient material is stripped ahead of the tool to fill the forging zone behind the tool. This issue is most likely caused by insufficient heat generation resulting in low matrix plasticity.
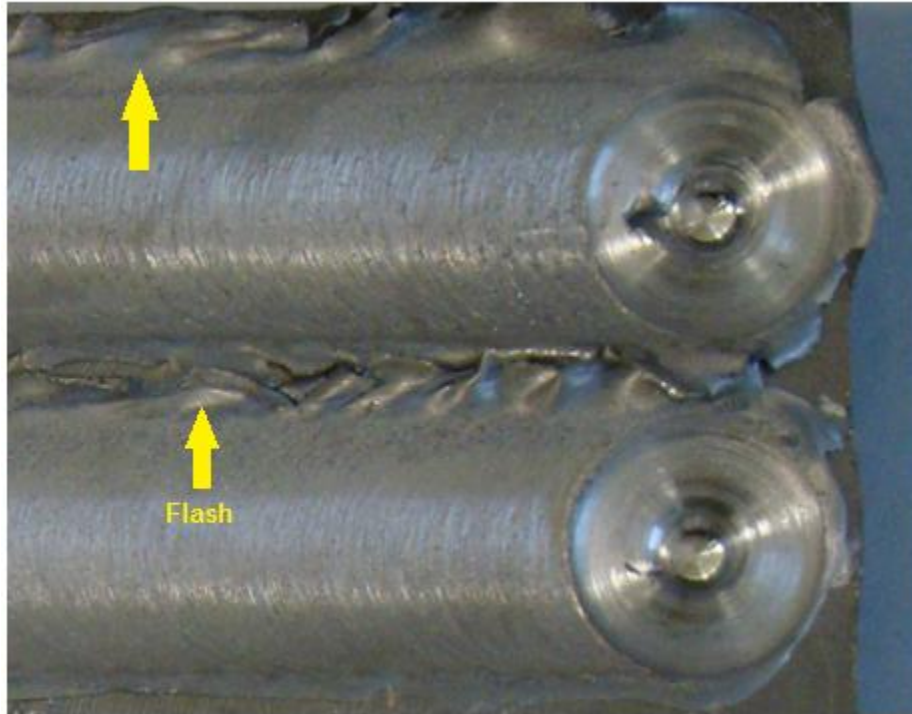
Figure 4.17 Flashing at 3600 RPM (bottom) at 4000 RPM (top) for smooth tool.

Void formation, though detrimental to weld properties and quality, may give insight into the mechanisms of redistribution of nondeforming phases. Void instability and formation in the high-strain-rate ECAP modeling was seen to improve dispersion of the rigid particle clusters since the material carrying the particles was forced to fold over

on itself as a discontinuity in plastic flow was introduced. Similarly, examining voids was useful in understanding the internal material flow occurring during the FS process. When examining a good weld, markers or seams are absent, but in the case of a void or poor forging within the stir zone, visible evidence remains to assist in determining how the matrix material and its various constituents within the stir zone were transported during the tool's rotation.

Figure 4.18, for example, shows a 400 RPM run in which large voids formed at mid-depth. The voids appear with a regular width and separation, indicating that their formation was directly related to RPM and traverse rate. The width of each void (seen at higher magnification in Figure 4.19) is approximately 200 µm. This distance corresponds closely to the forward distance traveled by the tool during a single rotation. This observation was made across the entire speed range by identifying either void formations or individual forging seams.
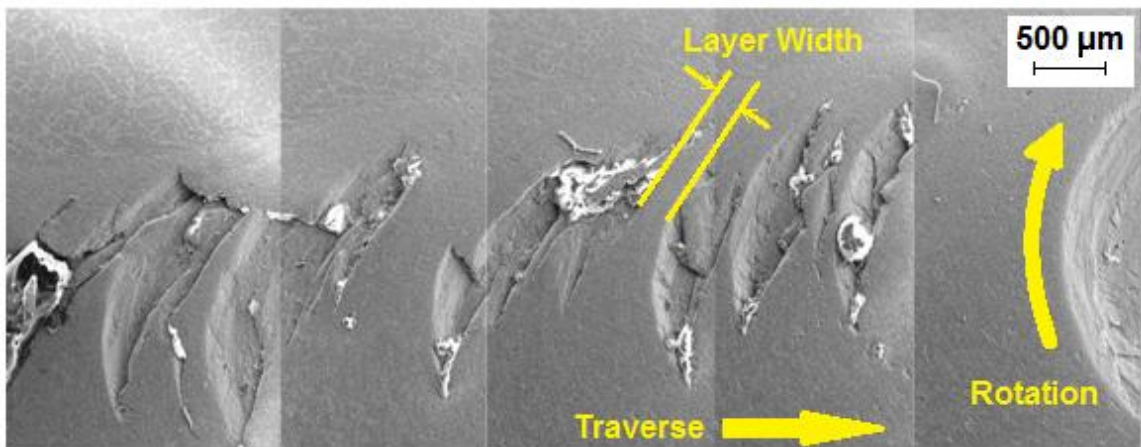
Figure 4.18 Secondary electron plan view montage of the stir zone sectioned at mid-depth for smooth-pin FSP at 400 RPM. Layer width is annotated.
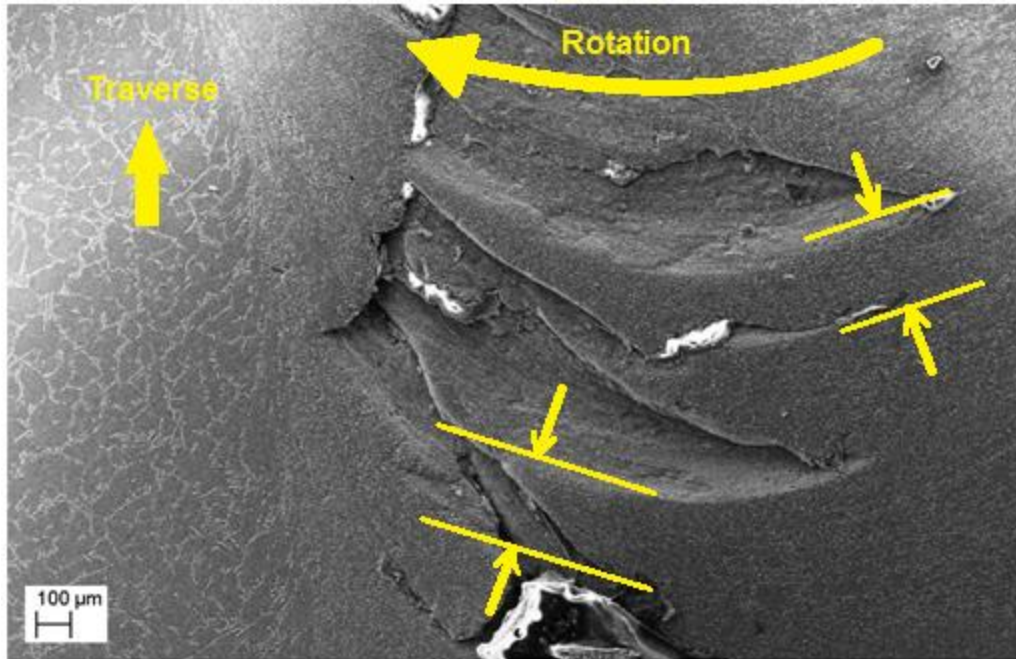
Figure 4.19 Secondary electron of the plan view sectioned at mid-depth for smooth-pin FSP at 400 RPM, shown at 50X magnification. Layer widths are annotated.

As mentioned earlier, the material in the vicinity of the pin is forced through a thin region between the tool face and the stir zone wall. As the material transits through this area, it is extruded as a thin layer. As the tool traverses, each layer is carried around to the backside of the pin where it is deposited and forged to the preceding layer. Figures 4.20 and 4.21 illustrate this process schematically. The "extrusion layer" refers to that layer of material adjacent to the pin. As stated earlier, the geometry of the deposition process corresponds closely to the material patterns seen in the microscopy. The measured extrusion layer thicknesses were plotted with tool translation distance as a function of RPM, shown in Figure 4.22. In all instances, the measured extrusion width matched closely with the calculated tool traverse distance occurring in one rotation.
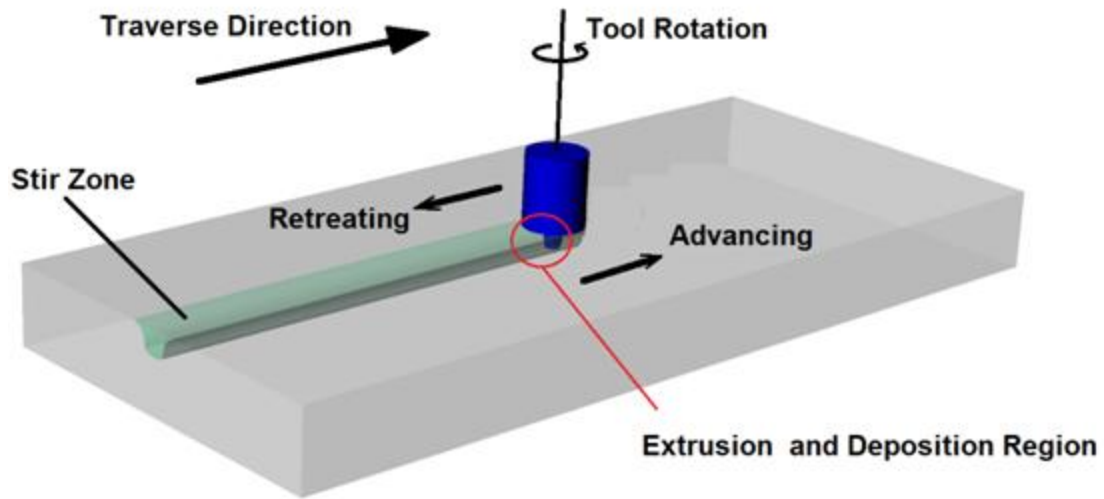
Figure 4.20 Schematic of FSP showing a counter-clockwise rotating tool traversing through the SZ. The circled area represents the region where material is extruded and re-deposited.
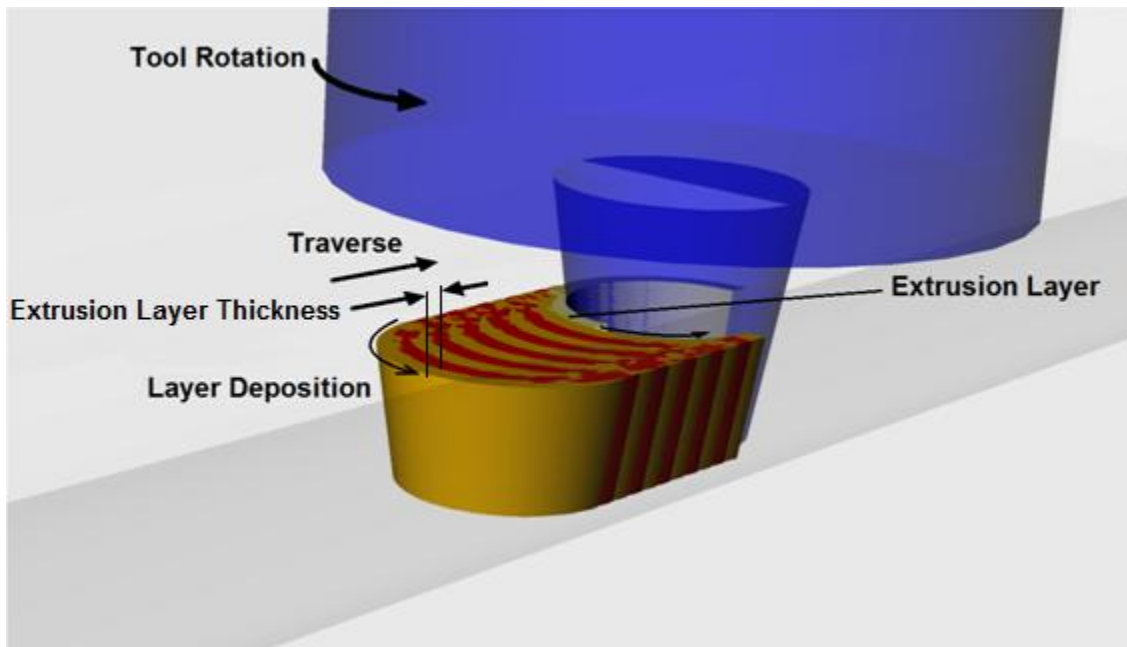
Figure 4.21 Schematic of FSP extrusion and deposition region showing material being carried around a counter-clockwise rotating pin and deposited in a repeating crescent pattern.
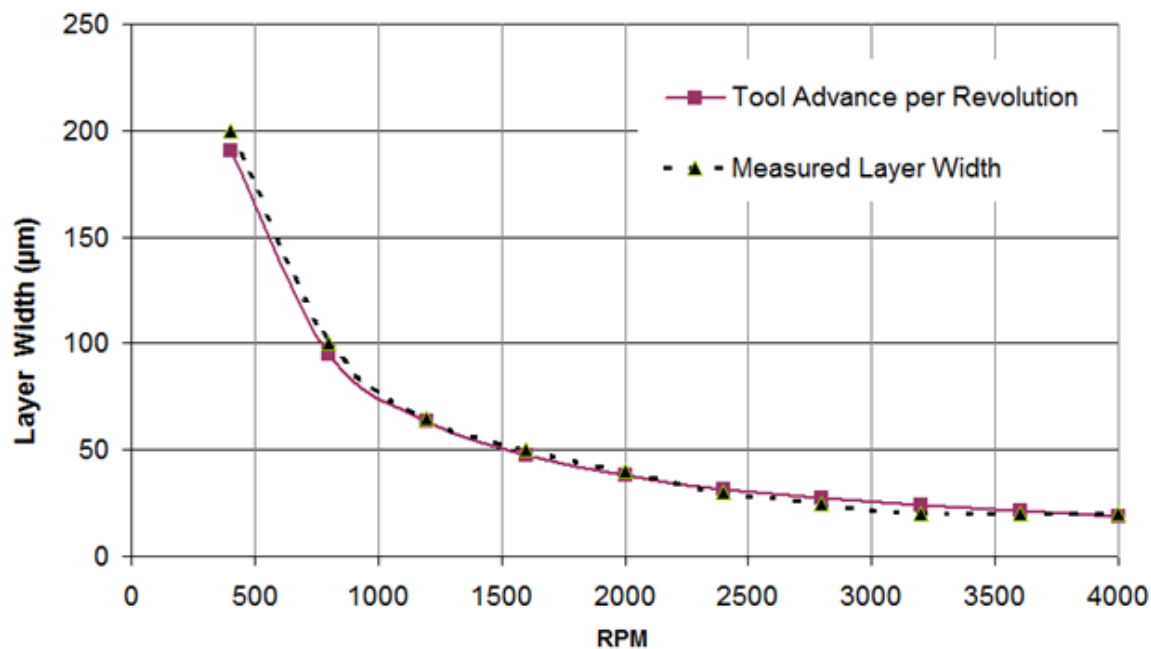
Figure 4.22 Tool translation distance per revolution and measured extrusion layer thickness plotted vs. RPM for the smooth tool.

Further inspection of the void regions as well as the pin extraction sites showed the formation of lamellar sub-layers within the larger extrusion layers. These layers appear to be highly plasticized material flowing in discrete sheets. The sheet-like sub-layers have much smaller thicknesses relative to the dimensions of the extrusion layer. Figure 4.23 shows a higher magnification image of these layers within the 400 RPM void. The sheet thicknesses range from 5 to 10 μm. Figure 4.24 shows similar sheet-like formations along the pin wall at the pin extraction site. Visible striations within sheet structures suggest that material flow may be occurring in individual strands that are roughly of the same thickness as the fragmented second phase particles. If this is the case, it would suggest that particulate can travel on individual strands of material, where a strand may be traveling at a different velocity than its neighboring strand. The sub-layers can also be seen at the extraction site, both along the wall and on the bottom of the pin extraction site. Further investigation identified the existence of these formations at the other RPM values.
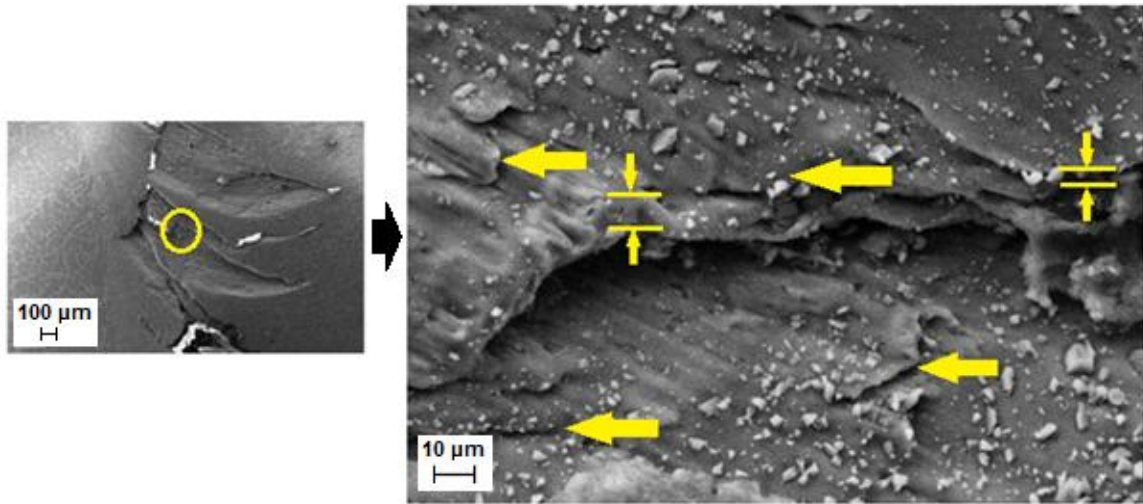
Figure 4.23 Secondary electron image of a multiple sheet-like layer formations inside a 400 RPM void. The smaller image provides a location frame of reference while the arrows denote some of the formations and their thicknesses.
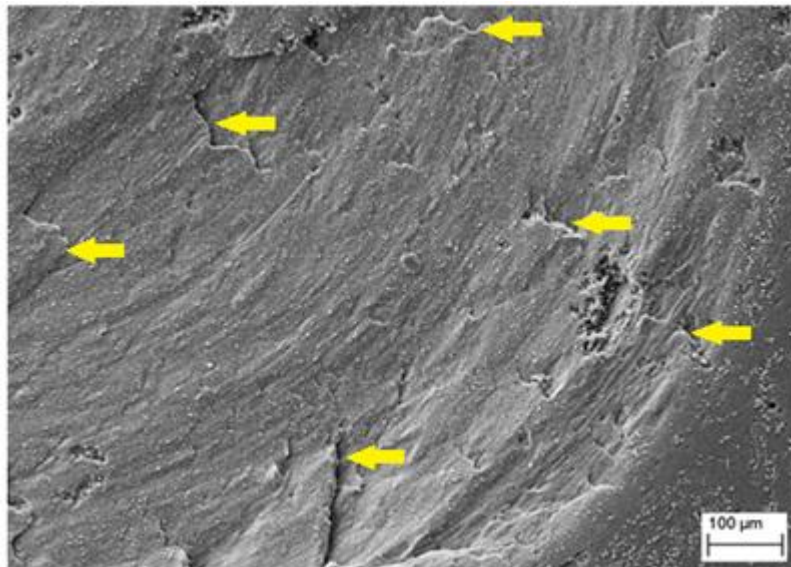
Figure 4.24 Secondary electron image of overlapping sub-layers on pin hole wall and bottom for 400 RPM smooth pin in clockwise rotation. Arrows denote some of the formations.

Additional microstructural examination at the pin bottom showed that base material is dragged and smeared in thin layers on the bottom of the pin extraction site. The thickness of the layer being stripped was again considerably thinner than the extrusion thickness. These "strip thicknesses" or sub-layers stack together to form the

97

overall extrusion thickness. Figure 4.25 shows layer thicknesses at the bottom of extraction sites that were found to range from 5 to 20 μm in thickness, decreasing in thickness as RPM increases. Similar strip thicknesses were observed along the sides of the pin wall.

(a)　　　　　(b)
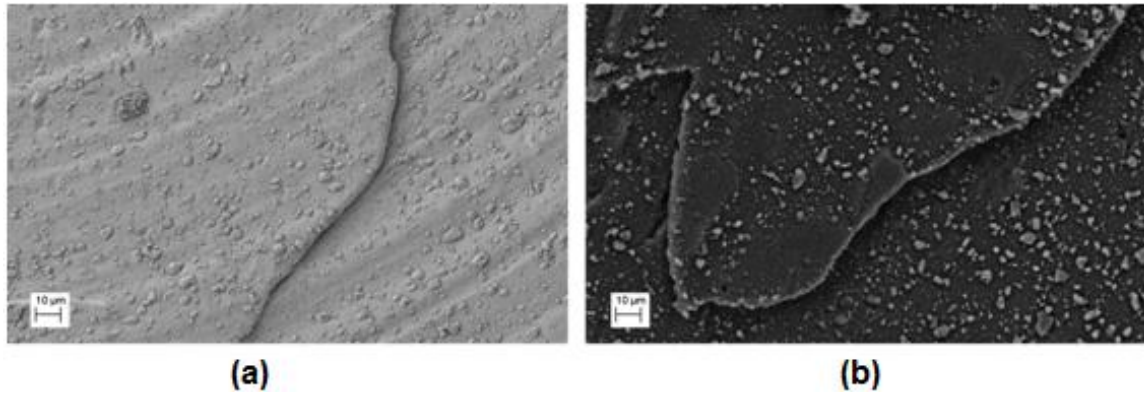
Figure 4.25 Secondary electron extraction site "stripped layers" for (a) 3200 RPM smooth tool and (b) 800 RPM threaded tool.

The 3600 RPM and 4000 RPM smooth tool samples were examined for further layering characteristics. As can been in figure 4.26 and 4.27, the void formation was extensive, but the defects allow for an unobstructed view of the internal structure of the process zone. Rotating clockwise with a smooth tool, extrusion bands of approximately 20 μm thickness can be seen behind the pin extraction site in both samples.

(a)　　　　　(b)
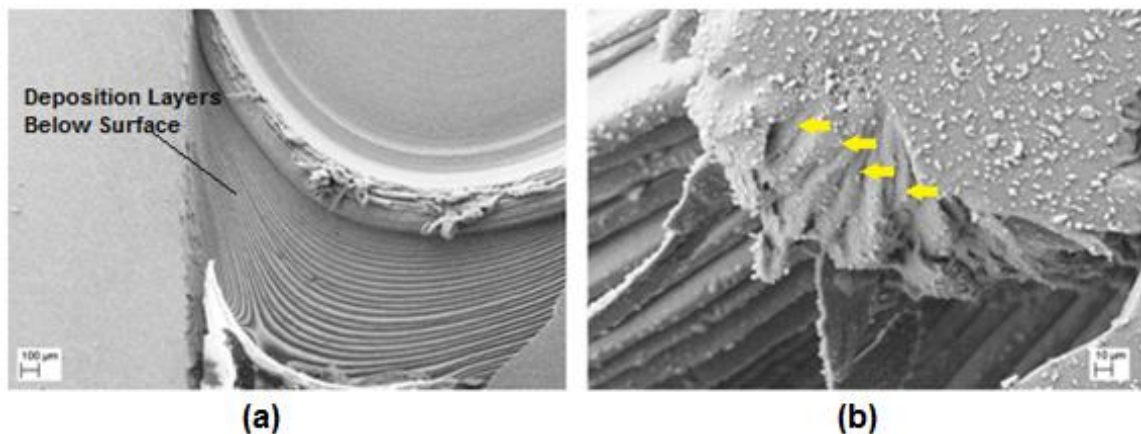
Figure 4.26 Secondary electron images of (a) extruded deposition layers below the sectioned surface for 4000 RPM smooth pin (b) retreating side sub-layer formations.

98
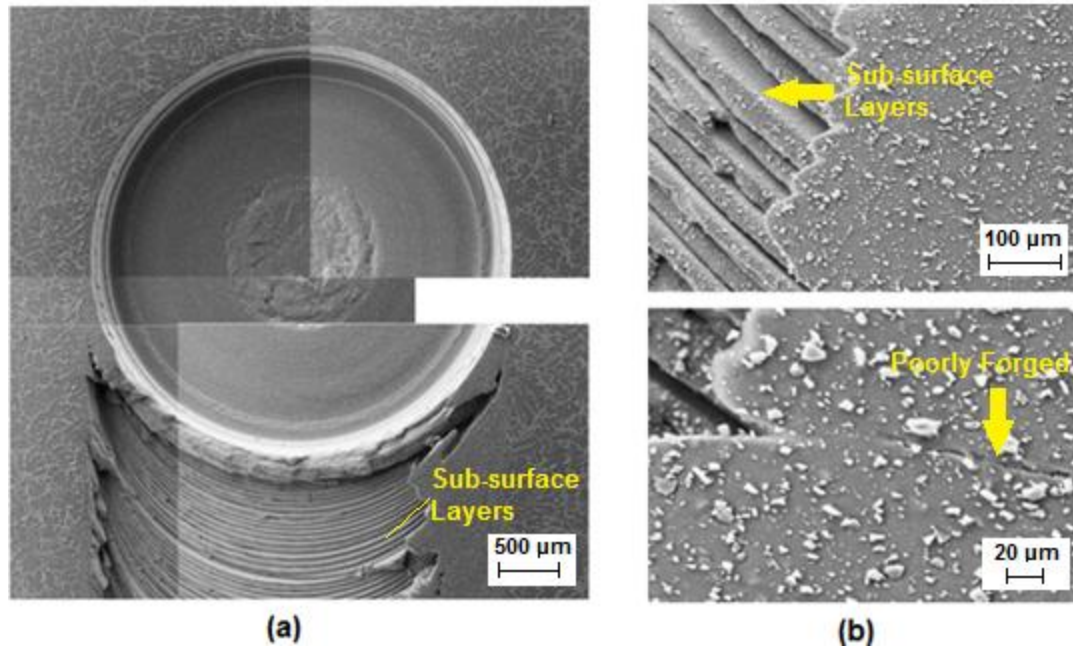
Figure 4.27 (a) Secondary electron montage of void extrusion layers for 3600 RPM smooth pin (b) (top) fully bonded extrusion layers for 3600 RPM smooth pin. (bottom) partially separated weld seam between extrusion layers.

Voids containing layered formations also appeared at lower RPM. It was again found that these extrusion thicknesses corresponded to the tool's forward traverse rate per revolution. Figure 4.28 shows optical images of the void formed using a smooth tool at 2000 RPM. The "fingers" of the extrusion layer in the lower portion of the void failed to travel the full distance to the advancing side.
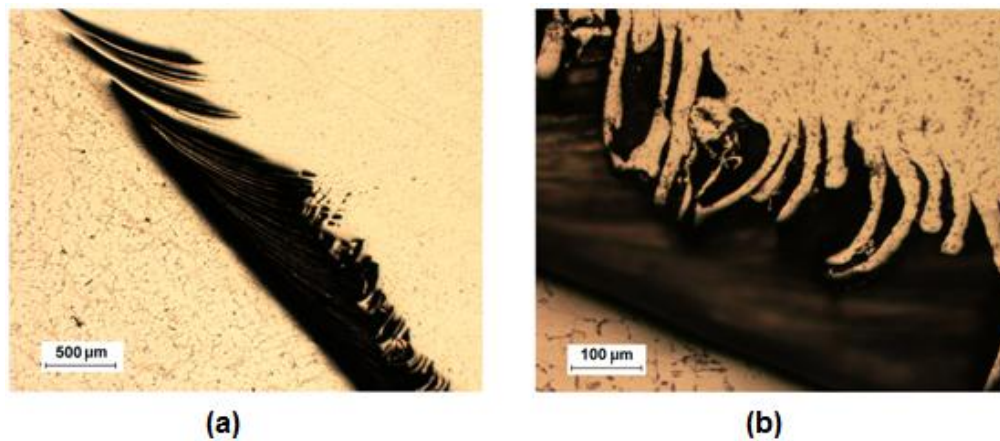
Figure 4.28 (a) Optical image of void extrusion layers for a smooth pin at 2000 RPM (b) Extrusion "fingers" failing to fully travel across the process zone.

Figure 4.29 Secondary electron plan view image of insufficiently re-bonded void extrusion layers in the lower section of the stir along the advancing side for a 2000 RPM smooth pin approximately 5 mm back from the extraction site.

The extrusion layers are repeatedly stacked on top of one another as they are delivered to the backside of the pin with each with each successive rotation, and in the case of a good stir weld / zone, the forging seam is made mostly undetectable, even at very high magnifications. A properly forged region alongside separated layers can be seen together in the lower right section of Figure 4.29. In the case of poor forging, insufficient material is present in the stir zone to fill the forge volume opened by the advancing tool, probably due to excessive flash at high RPM. As a result of the flash, the necessary hydrostatic pressure cannot be achieved to bond the extrusion layers properly across the full width of the stir zone. Under these poor process conditions, the repetitive forging operation is more visible, and one can begin to explain the formation of the "onion ring" patterns often discussed to in the FS literature. The "onion rings" are generally correlated to tool advance [121], but, to date, a full consensus on the source of the structures has not been reached. In this case, the striated patterns appear to be variation in material dispersion within the individual layers. Since the weld seams are made virtually invisible, the only remnant of the layered flow is the particle distribution

as it varies from layer to layer. Figure 4.30 shows the advancing side of a void formed by a threaded tool at mid-depth, which was rotating counter-clockwise at 1200 RPM. In this case, particle-depleted regions are visible at the boundaries of the extrusion layer forgings that appear as the "onion ring" banding when viewed at a coarser scale. In the lower portion of the image, the stir zone and TMAZ weld zone seam is visible due to the insufficient hydrostatic forging pressure.
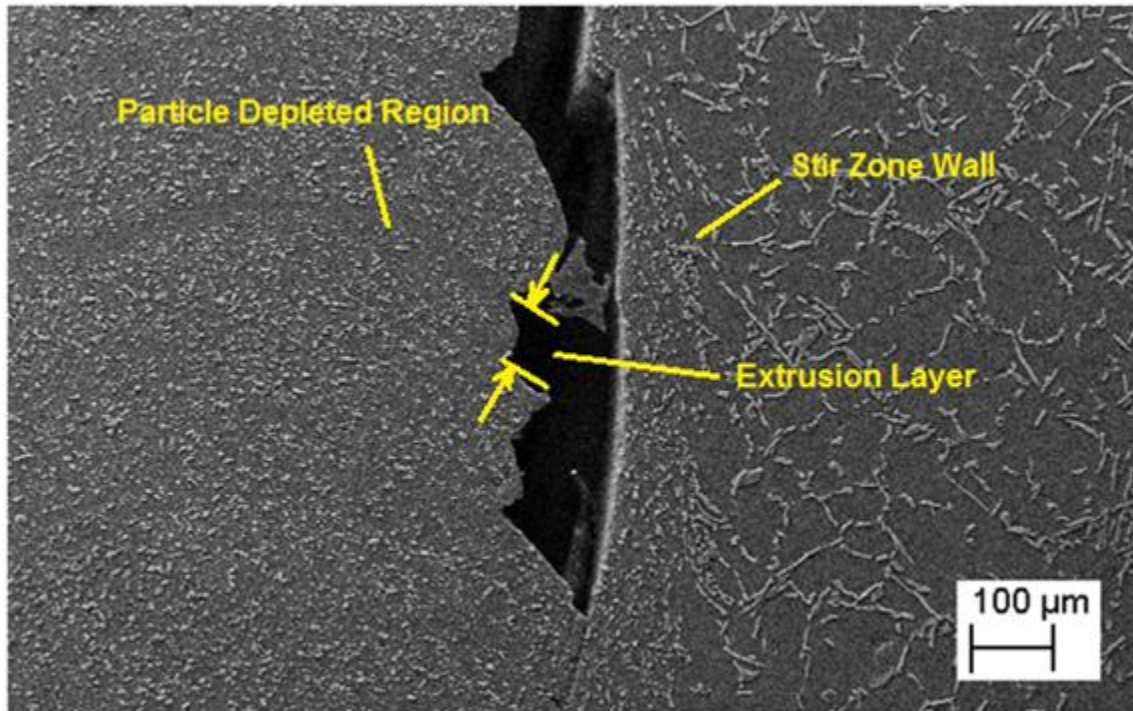
Figure 4.30 Secondary electron plan view image (a) of 1200 RPM threaded tool extrusion layers approaching the advancing side in a lower section of the SZ.

Again, under normal circumstances this forged seam is often undetectable. Particles in both the extrusion zone and along the edge of the sheared advancing wall are finely fractured. This observation would indicate that the majority of particle fracture occurs either during or prior to the onset of material stripping. If significant fracturing occurred throughout the tool's rotation, substantially different particle sizes should be expected on each side of this weld seam. The higher magnification in Figure 4.31 shows that the particles on each side of the seam are generally of the same size.

101
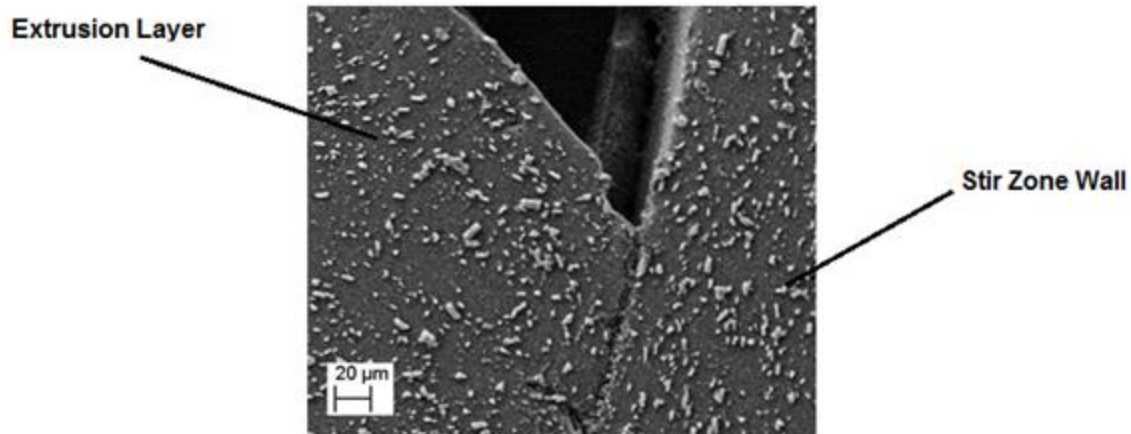
Figure 4.31 Secondary electron plan view image of 1200 RPM threaded tool extrusion layer and wall forging zone showing similar sized particles on each side of the forging seam.

Figure 4.32(a) shows another image of the retreating side extrusion layer subsurface formations for the smooth pin at 4000 RPM, taken 5 mm behind the edge of extraction site. Also shown in Figure 4.32(b) is further evidence of tightly forged layers that leave no visible surface evidence of their formation.
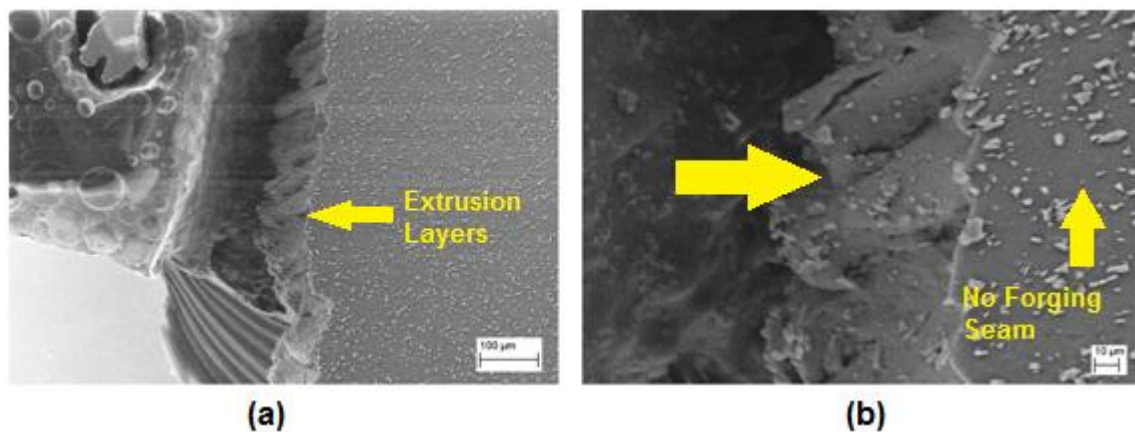
Figure 4.32 Secondary electron plan view image of threaded tool (a) 4000 RPM retreating side extrusion layers in the lower section of the stir (b) higher magnification of extrusion layers with a cleanly forged surface prior to void formation.

3. Sub-layer Formations

The extrusion layers do not appear to be stripped from the advancing side and carried around the tool pin in a single continuous layer. Rather, they appear to be comprised of still smaller sub-layers that have a smaller thickness scale than the extrusion layer itself. These sub-layers appear to stack and flow in both the horizontal and vertical planes, travelling independently of one another. Furthermore, the formations are seen to pinch off in segments. Figure 4.33 shows discrete, vertically stacked formations on the advancing side of the 2800 RPM and 2400 RPM smooth tool. The segmentation of the particle-carrying material in this manner would serve to enhance constituent dispersion.
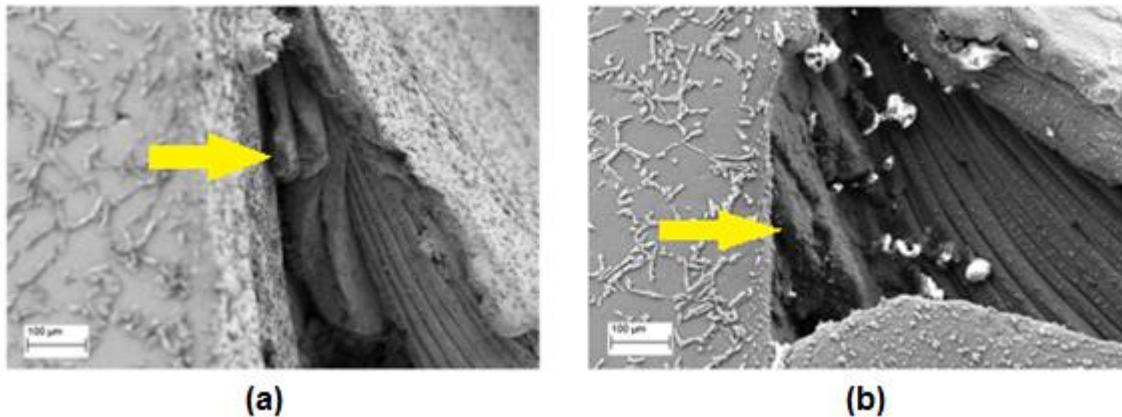
Figure 4.33 Secondary electron plan view image of smooth tool (a) 2800 RPM and (b) 2400 RPM advancing side stacked formations which are being stripped and segmented.

The observed extrusion layers also have a vertical component of motion, and do not move in a simple cylindrical path around the tool pin. This vertical motion can be attributed to the tool pin geometry, as well as the forces induced by the rotating shoulder and pin [123]. Again, layered formations are not easily detected in a satisfactorily forged stir, but they are apparent when examining voids in either the horizontal or the transverse planes. Figure 4.34 shows vertically layered flows that reach a terminal location in a void near the advancing side for the threaded tool at (a) 2400 RPM and (b) 2800 RPM. Of note, the 2400 RPM layers show signs of prior segmentation occurring with a regular 2 μm interval.
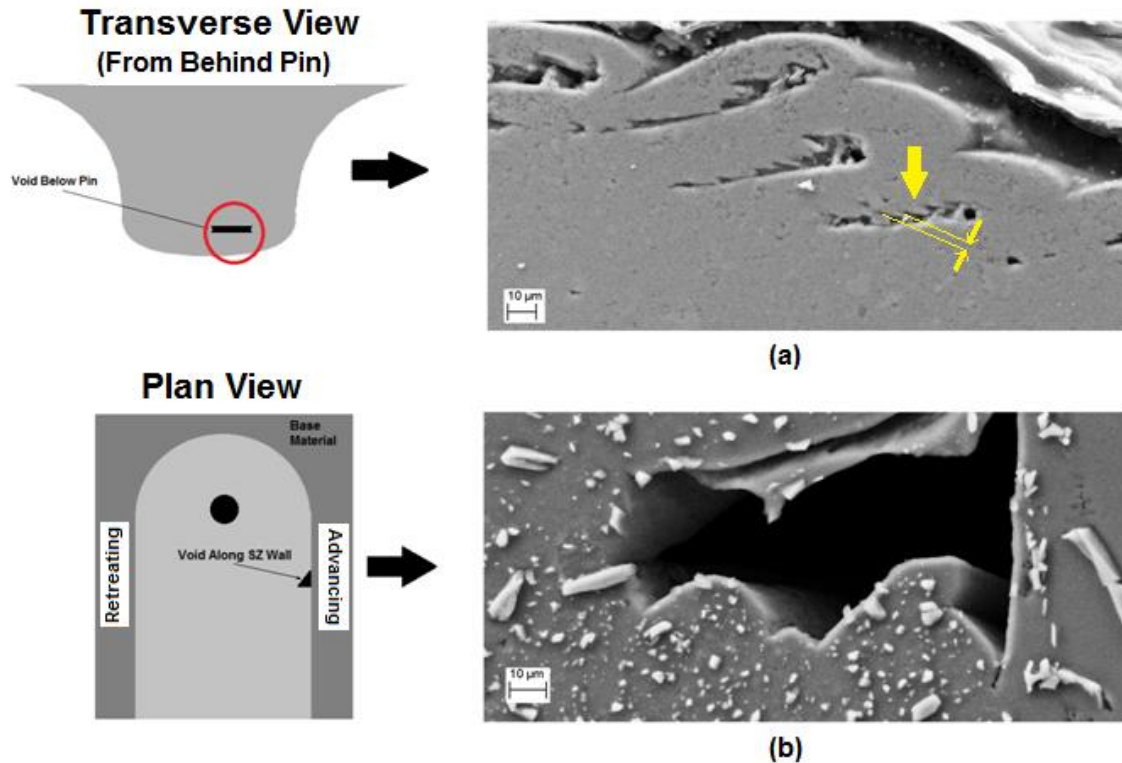
Figure 4.34 Secondary electron transverse view image (a) of 1600 and (b) 2400 RPM threaded tool advancing side layer formations terminating in a voids.

Figure 4.35 shows a void located in the transverse plane near the lower retreating side of the pin face for the smooth pin tool operating at 2800 RPM. The approximately 10 μm thick layers seen here are substantially thinner than the primary extrusion layer. This, and the previous observation, would indicate that the observed void layers continue to be thinned and / or sheared during extrusion. Individual particles can be seen to reach and pierce a layer's surface, which also suggests that particles potentially could move from layer to layer as the flow progresses. Again, such a mechanism would enhance dispersion of clusters, as two neighboring particles would be rapidly separated in this fashion. The layers shown appear to be originating from several directions, indicating a complex, multi-directional flow process within the stir zone. As the layers become unconstrained in the void, they fold over and forge together under the influence of hydrostatic pressure.
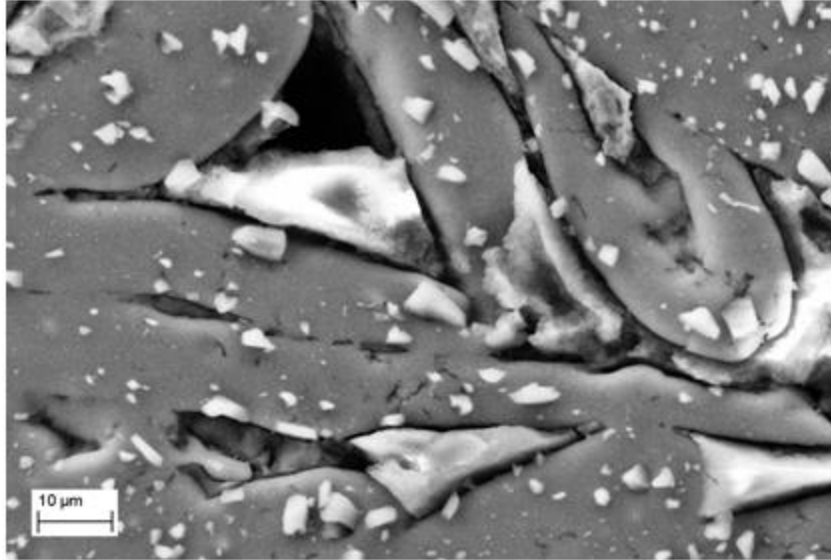
Figure 4.35 Secondary electron transverse plane image of multi-directional void layers for a 2800 RPM smooth tool. (Note that, the large white masses are residual mounting epoxy).

4.   Regions of Particle Fracture

The region of particle fracture can extend a considerable distance beyond the visibly stirred region of the base material. Mid-depth plan view measurements were taken to evaluate the maximum distance from the pin face where particle fracture occurred. Distance measurements were taken at from the top, advancing, and retreating-side tangential points of the pin extraction site. It was found that the distance to undamaged particles was roughly the same all around the pin for a given RPM. The smooth and threaded pins showed little difference in the radius of the damaged region. The general trend was a nonlinear decrease in the radius of the damaged region as the RPM was increased, as shown in Figure 4.36. Figure 4.37 shows a secondary electron image of the measurement process for the 3600 RPM threaded tool at the pin extraction site's top tangent.
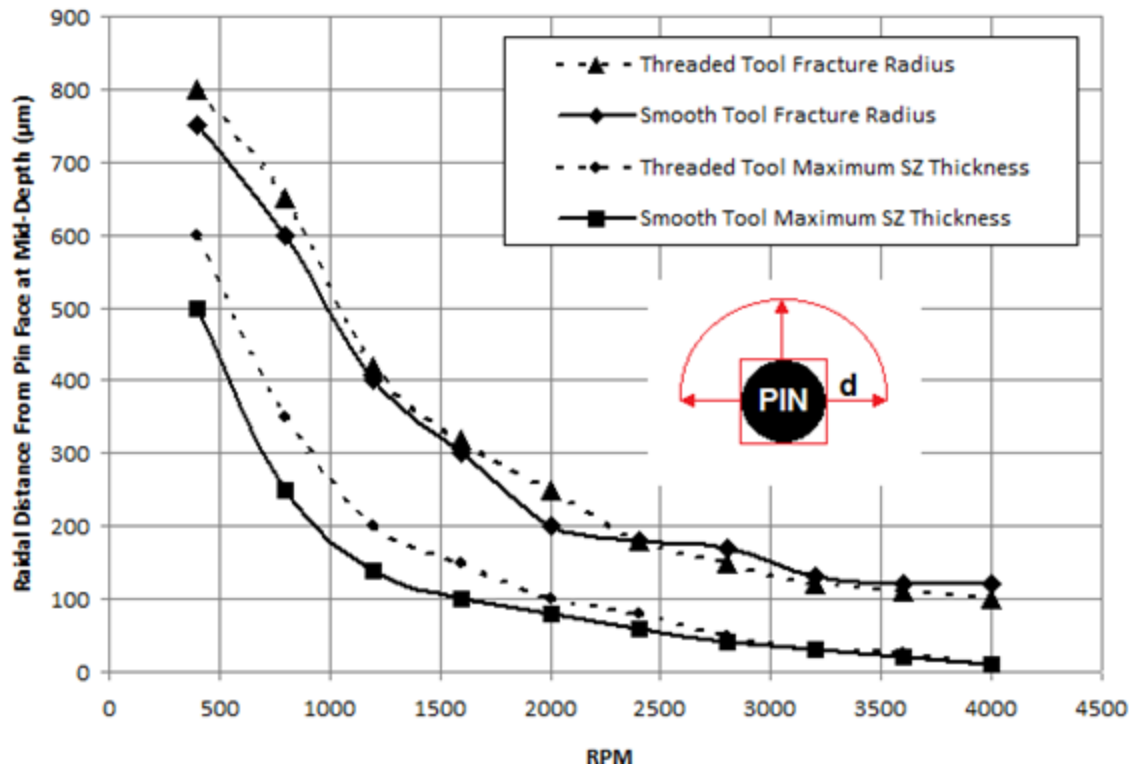
Figure 4.36 Plot of SZ thickness and maximum distance (d) to particle fracture measured from pin face as a function of RPM.
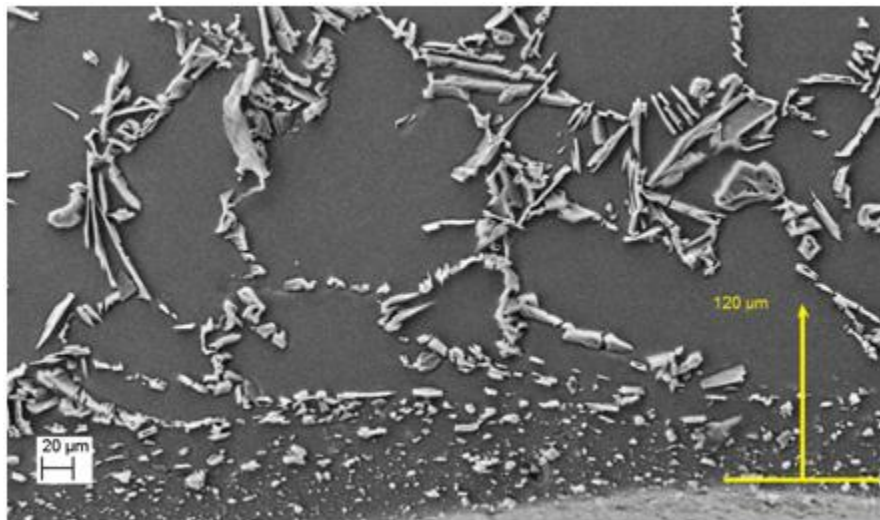
Figure 4.37 Illustration of the distance measurement for the onset of particle fracture as measured from the pin interface on the plan view section for the smooth tool at 3600 RPM.

Particle fracture also occurs in the upper and outer regions of the stir zone as a result of the shoulder's rotation. Fracture distances at the outer shoulder (observed in the transverse plane) extended roughly 2 shoulder flow thicknesses (see Figure 4.38) below sample surface, demarcated by the yellow arrows in Figure 4.38, which shows the outer retreating shoulder region for a 2400 RPM smooth tool at lower and higher magnification. Flow within the outer shoulder region is tightly constrained to a thin layer below the tool, and in many cases, has a distinctly banded nature as the particle regions are rotationally sheared and thinned (as often seen in high-pressure torsion (HPT)).
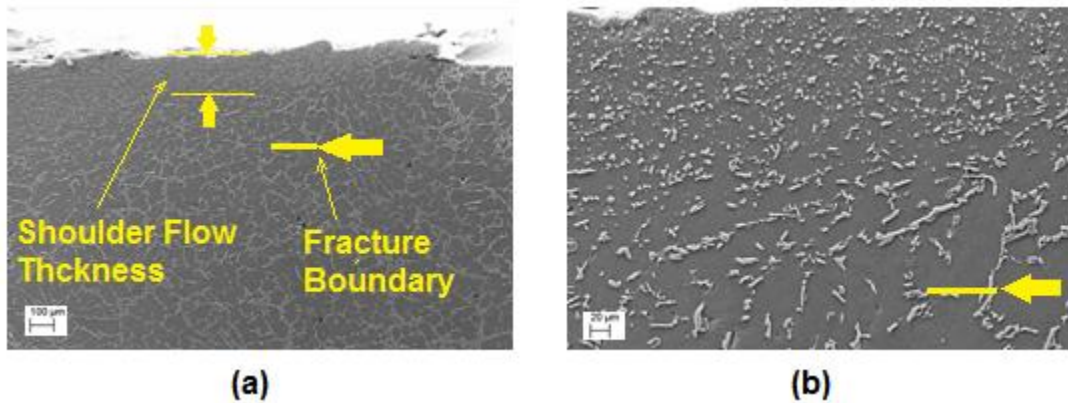
Figure 4.38 Secondary electron image of the retreating outer shoulder for a 2400 RPM smooth tool showing the lower limit for particle fracture at (a) 50X magnification (b) 200X magnification.

5.   Qualitative Redistribution

Quantification of homogeneity will be addressed in further detail in Chapter V. However, a number of initial, qualitative observations can be made regarding the degree of redistribution occurring across the range of RPM values in this work. Within the nugget, all samples showed improved uniformity relative to the as-cast material. However, there was wide variation in the degree of dispersion quality depending on the RPM. A visibly greater degree of particle size uniformity resulted near regions of high pin and shoulder velocity. These regions often show considerably different morphology than that observed in the remainder of the nugget. In regions directly beneath the pin and shoulder, all of the samples showed greatly reduced particle size and improved dispersion when compared the rest of the nugget. In addition, regions immediately adjacent to the

pin face also showed a high degree of uniformity, although, as discussed earlier, the size of this region decreases rapidly as RPM increases. Further, the threaded pin appeared to improve dispersion in some regions of the nugget relative to the smooth pin. It should be noted that, no indication of tool pin disintegration was observed in any of the FSP microscopy.

Figure 4.39 shows a comparison of the 400 RPM and 4000 RPM smooth pin stir zones. Both the 400 and 4000 RPM produced large voids in the process zone at the selected traversing rate. From a practical standpoint, particle dispersion cannot be the sole consideration in deciding an appropriate processing speed. Nevertheless, examining particle dispersion at the extremes of the RPM range revealed important effects. A distinct difference between the two speeds, with the higher RPM yielding a highly fractured second phase with more uniform spacing. The higher-speed smooth-pin trials (above 2400 RPM) resulted in generally equiaxed particles with diameters less than 5 μm, whereas the lower speed samples showed numerous particles greater than 10 μm in extent. This observation indicates that particles in a lower speed stirring are less likely to experience repeated fracture in the FS strain path.

(a)   (b)
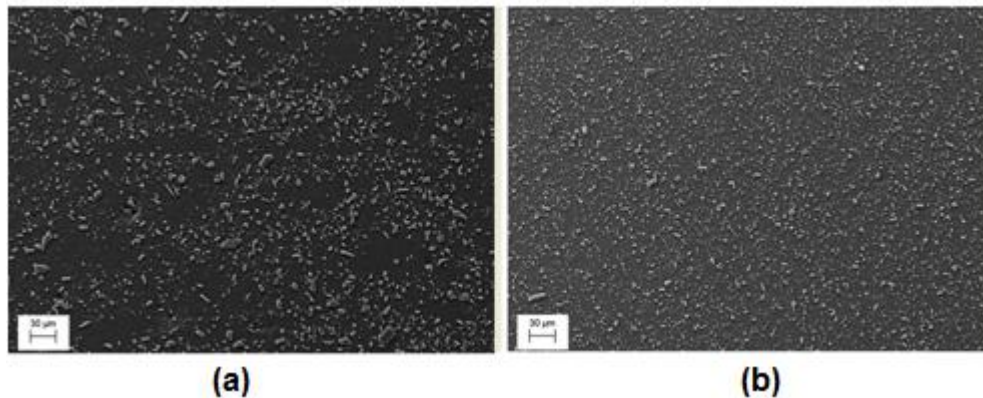
Figure 4.39 Secondary electron transverse plane images of the smooth tool stir zones at the nugget center for (a) 400 RPM and (b) 4000 RPM.

Figure 4.40 shows the same samples but at a higher magnification where the morphological differences and dispersions are more evident. At the higher magnification, both smooth-pin samples also showed a degree of particle directional

alignment, though it is more pronounced in the lower speed sample. In the 400 RPM sample, band-like clusters are separated by the particle-depleted Al solid solution regions. Higher aspect ratio particles are generally aligned left to right, probably indicating the motion of the layer in which they reside. In the higher RPM sample, there appear to be fewer high aspect ratio particles, though they also appear aligned with layer motion, and a banding pattern is not as discernible. The lack of a banded nature may reflect the fact layers are sufficiently thin at higher speed to mask variations occurring between layers. Also, the higher speed tool may be more effective at drawing in and mixing material from regions of high and low degrees of particle fracture.
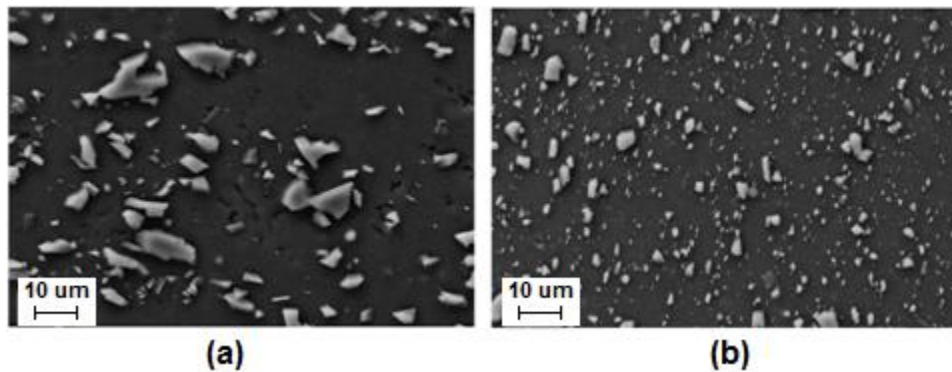
Figure 4.40 Higher magnification secondary electron transverse plane images of the smooth tool stir zone at the nugget geometric center for (a) 400 RPM and (b) 4000 RPM.

Comparison of the smooth pin versus the threaded pin at the same RPM showed minor differences in particle breakup and dispersion. Figure 4.41 compares the 2400 RPM results for both tools at low and high magnification. Figure 4.42 provides a comparison to the base material at similar magnifications. Previous results showed that that the range and severity of particle breakup ahead of both tool pins is approximately the same. With the process parameters of this trial, the more complex strain path did not appear to produce a significant improvement in particle dispersion. For the threaded tool to be more effective, it must create increased particle fracture during extrusion, generate thinner layering, or better distribute material from regions where fracture is more prevalent.

(a) Smooth 2400 RPM   (b) Threaded 2400 RPM

(c) Smooth 2400 RPM   (d) Threaded 2400 RPM
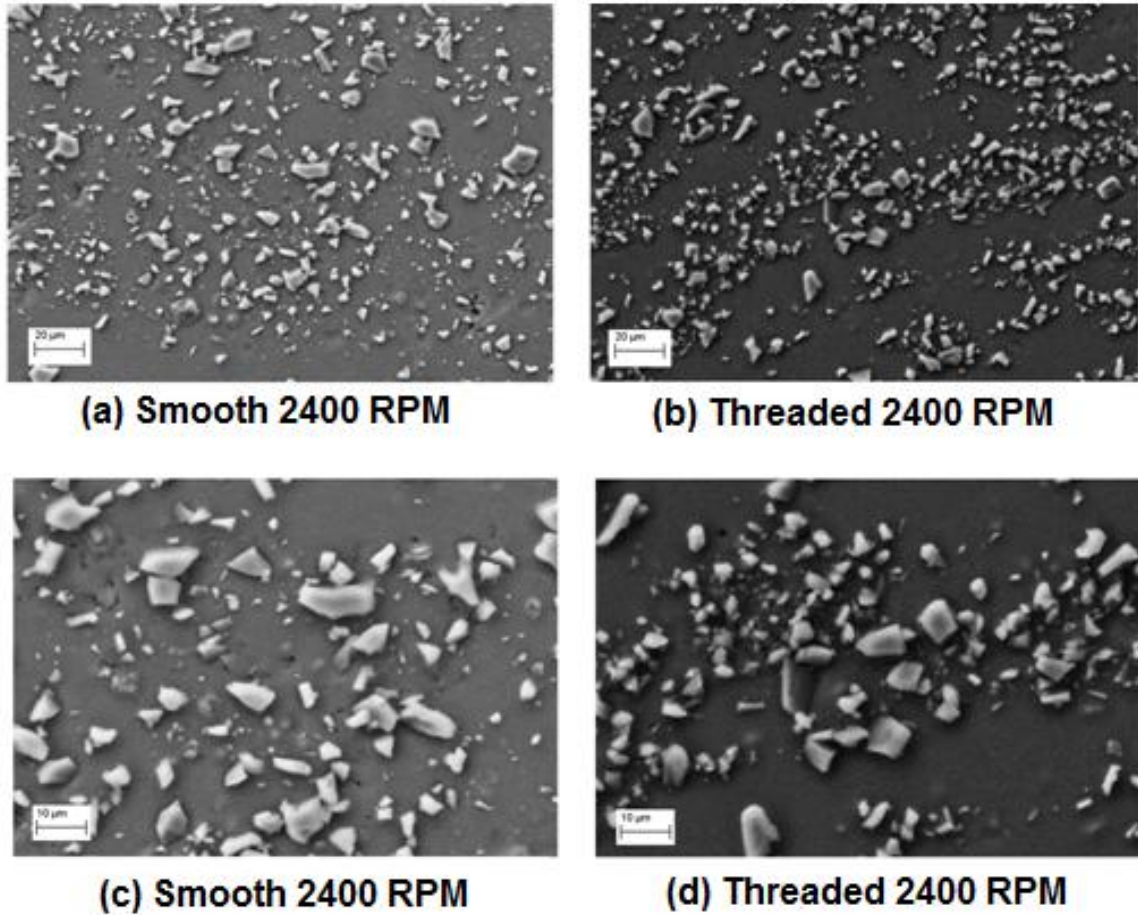
Figure 4.41 Secondary electron transverse plane images of the stir zone at the nugget's geometric center for (a) 2400 RPM smooth tool and (b) 2400 RPM threaded tool (c) higher magnification 2400 RPM smooth tool (d) higher magnification 2400 RPM threaded tool. Note that, some particles are not greatly reduced in size due to void formation which disrupted plastic flow.

(a)   (b)
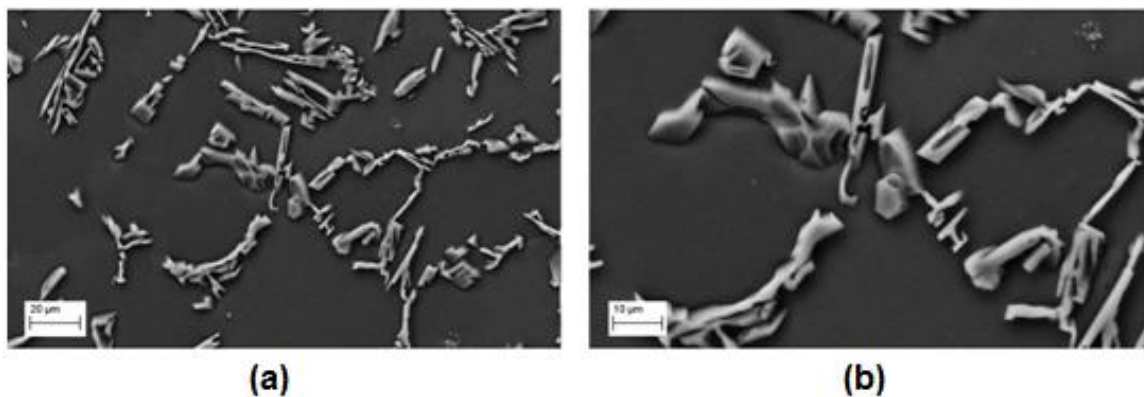
Figure 4.42 AA356 as-cast material at (a) low and (b) high magnification shown for comparison to FSP material in Figure 4.41

The threaded tool performed better at low to mid-range RPM values where void formation was less prevalent. Figure 4.43 shows the 1200 and 1600 RPM images for the smooth and threaded tools. In this RPM range, the threaded tool resulted in visibly better dispersion at the nugget's center.
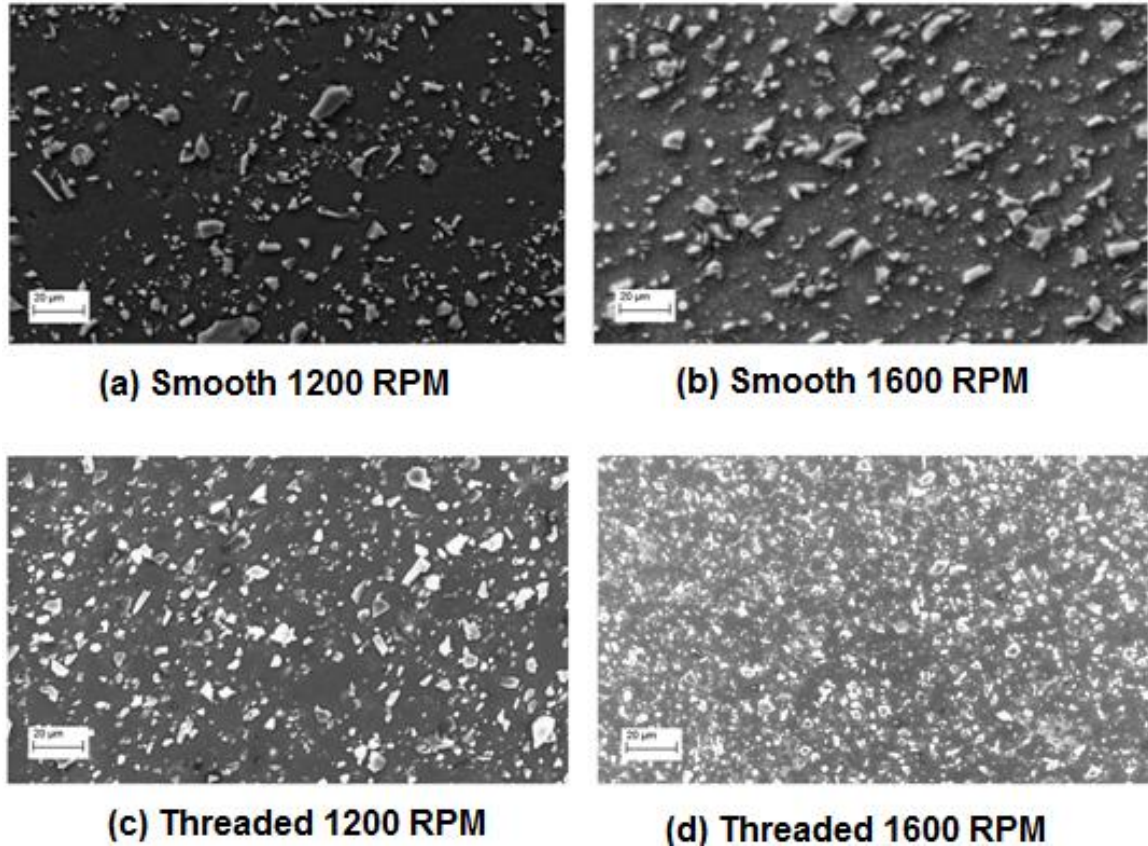
Figure 4.43 Secondary electron transverse plane images of the stir zone at the nugget's geometric center for (a) 1200 RPM smooth tool and (b) 1600 RPM smooth tool (c) 1200 RPM threaded tool (d) 1600 RPM threaded tool.

In most cases, the region of directly beneath the center of the shoulder showed considerably greater dispersion and uniformity for the threaded tool, as shown in Figure 4.44. The highest degree of particle fracture occurs at the outer portion of the shoulder where the highest shearing velocity and matrix strain occurs, again akin to what is observed in HPT. The threaded tool is more effective at drawing this highly fractured material from the outer shoulder into the upper portion of the stir center. However, dispersions near the geometric center of the nugget were quite similar for the two tools at

111

the higher speeds. Although, a sufficiently high RPM is necessary to achieve adequate matrix circulation, high RPM / high tool-traverse rate combinations incite severe void formation. These voids block the extrusion layer's flow path and thus limit particle dispersion throughout the nugget.
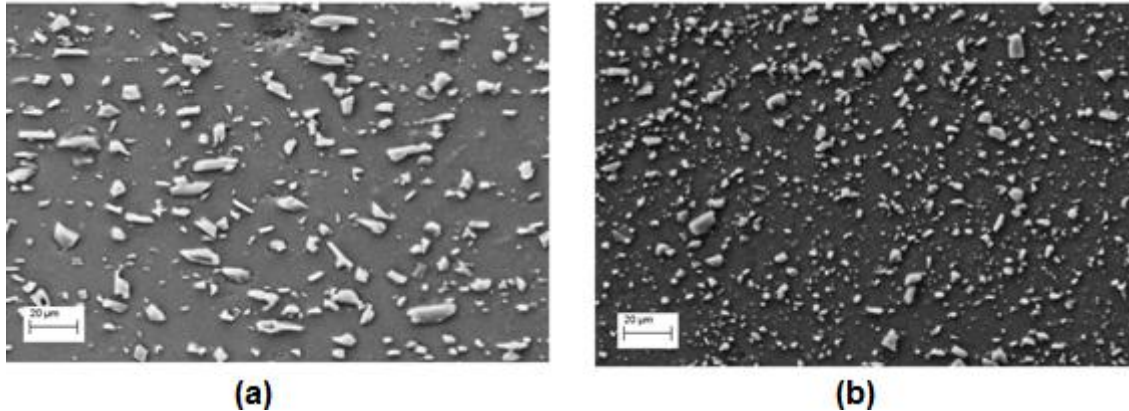
Figure 4.44 Secondary electron transverse plane images of the stir zones 100 μm below the center shoulder surface for (a) 2400 RPM smooth tool and (b) 2400 RPM threaded tool.

E.   CONCLUSIONS

The mechanism of constituent particle redistribution was found to be a flow-like process whereby very thin layers of matrix material advectively transport fractured particle pieces. The results of the investigation reported in this chapter may be summarized as follows:

1.   Extrusion and Forging

The microscopy strongly suggests a layered and segmented flow of the matrix in which the base material adjacent to pin face is stripped during a shearing action by the tool on the advancing side. As the tool moves forward, a discrete layer is formed on the retreating side of the pin as stripped material passes between the pin face and the stir zone wall. The extrusion layer is then deposited at the rear of the pin, and, under ideal circumstances, is forged to preceding layers. The thickness of these primary extrusion layers is dictated by the forward translation distance of the pin in one rotation. A similar stripping process occurs at the bottom of the pin and beneath the shoulder.

2. Sub-layer Formation and Variegation

In the incomplete welds, the discrete layers stripped by the tool are significantly thinner than the extrusion layer exiting the tool's retreating side. The stripped layers appear to be cut into sections during motion along the strain path and flow does not take the form of single, contiguous volumes. Layered formations or sheets can be observed in the void regions of both the horizontal and transverse planes. These sub-layer formations combine to form the extrusion layer. Within the SZ, these sub-layers appear to move both horizontally and vertically. The same process is very likely occurring within a well-forged SZ, only it is not visible since the volume ahead and behind the tool is conserved.

The variegation, or "onion ring" structure, observed in the stir zone, appears to be layer-to-layer differences in particle dispersion. As the layers are made thinner through higher tool RPM, these variegations are decreasingly visible, resulting in generally more uniform appearance in the stir zone. If the effect of diffusive particle motion is assumed small (which is likely), the largest effect on particle rearrangement would be governed by the characteristic thickness of these stripping layers.

3. Particle Fracture and Dispersion

The stir zone dispersions are greatly enhanced by particle fracture. Due to the tool's rotation and the cooler / stiffer matrix, particles lying a significant distance ahead of the tool begin to fracture well before the arrival of the traversing tool pin because of matrix deformation. A lower pin RPM showed a larger area of particle fracture. Fractured particles residing in the stripped thin layers subsequently travel with these layers.

Fractured particles observed on extrusion layers nearing completion of the strain path are generally of the same size and aspect ratio as those residing in the thin region of highly distorted stir zone wall from which the material originated. For this reason, the majority of particle fracture in the lower section of the stir zone appears to occur either during or before material is sheared from the base.

4. Pin Geometry Effects

The tool pin geometry has a significant effect on the final nugget dispersion in that it determines the strain path of the layered subsections of the material. The desired effects of a more complex flow path can be negated by void formation due to inappropriate IPM / RPM combinations. Voids disrupt and block motion of layers preventing the delivery and mixing of material from different region of the nugget.

V. A NEW METHOD FOR QUANTIFICATION OF MICROSTRUCTURE HOMOGENEITY IN TWO PHASE MIXTURES

A. PREFACE

This chapter proposes a general new method for quantification of homogeneity in a microstructure containing hard, fracturing particles dispersed in a matrix. Through digital image analysis of a representation of a binary microstructure, variations in particle distributions and various morphological parameters can be measured. In the method proposed here, the following particle parameters are measured: size, spacing, population, orientation, aspect ratio, and area fraction size. Using the results of that analysis, a homogeneity index can be generated by combining the statistical variance of these six constituent particle parameters in multiple sub-regions across a sample. Microstructures from selected FSP and hot-rolled samples are used to demonstrate the application of this new technique.

B. INTRODUCTION

Homogeneity of microstructures is frequently mentioned in the body of material science literature, but most often, it discussed in qualitative terms only, without any quantitative measure. Beck [124], an early pioneer in the study of the human brain's response to textured and patterned visual stimuli, showed that humans are readily able to distinguish between homogenous and inhomogeneous images. The basis of that work subsequently led to the development of automated systems that can statistically test for homogeneity in images. Stephansson et al. [125] applied such methods to analysis of the structural homogeneity of rock masses, and more recently, the approach has been applied to the development of facial recognition systems. This progression suggests a direct application for the homogeneity recognition in microstructures.

The difficulty in any recognition method is to discern the relevant parameters of interest for a discrete object, i.e., shape, size, directionality, etc. Once an individual object is recognized and measured, its relationship to neighboring objects can also be

115

measured and statistically characterized. Automated recognition methods have focused on either of two detection methods for identifying object characteristics: structural or gray level. The methods of Spowart et al. [1]–[13] used quilting methods, i.e., partitioning the overall region into square sub-regions and then sampling grey levels within those regions to determine particle population densities. This method is widely used since a digital grey level is easily measured and is a convenient criterion for estimating some object characteristics, such as area fraction. Tsuji et al. [127] were initial developers of the structural approach (which also segments an image into sub-regions), but instead detects an object's edge by measuring an abrupt change in texture or grey level, thus indicating the boundaries of the object in an image [128]. The structural approach is more like the mechanism of the human eye, but more difficult to implement in an algorithm. Recent advances in image analysis have made edge detection approaches more viable.

In this chapter, edge detection methods, available in the MATLAB Image Analysis Toolbox, are implemented to measure six particle distribution characteristics: 1) spacing, 2) equivalent diameter, 3) aspect ratio, 4) area fraction, 5) particle population and 6) directional orientation. Note that, directional orientation can be measured with respect to any pre-defined axis, e.g. the edge of the micrograph or the processing direction. The analysis then compares the statistical variance of each normalized parameter across equally sized sub-regions, termed "sectors". The effect of varying the sector size is also measured. The variances of the six parameters are then combined into a single homogeneity parameter (H_s), and selected microscopy results are analyzed in terms of H_s. It should be noted here, that the measurements for H_s consider 2D data only. The approach could be extended to 3D using well-known stereological methods, but that topic will be left for future work.

C.   METHODOLOGY

1.   Obtaining a Measurable Image

a.   Pixel Connectivity

In order to easily count and measure particle distribution using an edge detection method, a 2-D metallographic image should first be transformed into a binary (black and white monochrome) digitized image. The image is then represented as a matrix of pixel values, with each pixel representing either a 1 or a 0. In the case of a two-constituent material, the particulate phase will be represented by the 1 values and the matrix by the 0 values. The boundaries of a discrete object can be detected by examining the connectivity of each pixel with its neighboring pixels. The defined connectivity will determine whether an adjacent pixel is part of the current object, and in turn, affect the calculation of particle size. Adjacent 1 and 0 values would indicate a boundary, whereas adjacent 1 and 1 values would indicate a continuous region of the same object. In 2-D, either 8 or 4 pixel connectivity may be used, as schematically shown in Figure 5.1. In the case of real microstructures, particles are seldom connected at the corners, so 4 pixel connectivity is a more appropriate choice for the detection scheme.

(a)   (b)
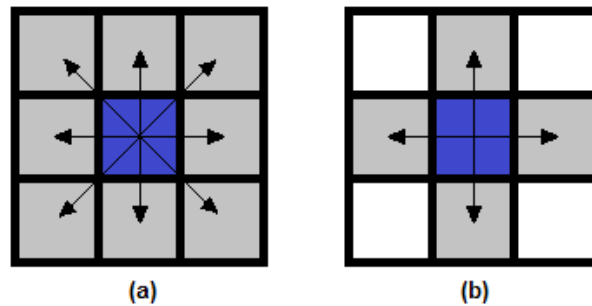
Figure 5.1 Schematic of (a) 8 pixel connectivity and (b) 4 pixel connectivity showing the adjacent pixels which would be counted as part of an object in each case.

b.   Image Filtering and Cropping

Microscopy originating from the optical microscope is generated as a color (RGB) image, and those from the Neon 40 SEM are generated as gray-scale images. An additional filtering step is required to transform an RGB image into a gray-

117

scale image. Once in gray-scale image format, based on the existing contrast level, gray thresholding transforms the image into a black and white image. Note that, this approach is not effective for low contrast images. The selected filter and threshold values must be chosen judiciously for each image, as they have a large effect on the accuracy of the final binary representation. Figure 5.2 shows an example of an image obtained on the Zeiss Neon 40 SEM, which was accurately transformed into a binary representation. The SEM images have a formatted size of 1024 x 768 pixels. In order to implement a measurement algorithm more easily, a square image is cropped from the original rectangular image. Although values for the images are measured in pixels, the measured values are later scaled from pixels to microns. Note that, particles consisting of only a few pixels can be filtered according to their size, as they often tend to be metallographic artifacts that can skew the statistical results.

(a)   (b)
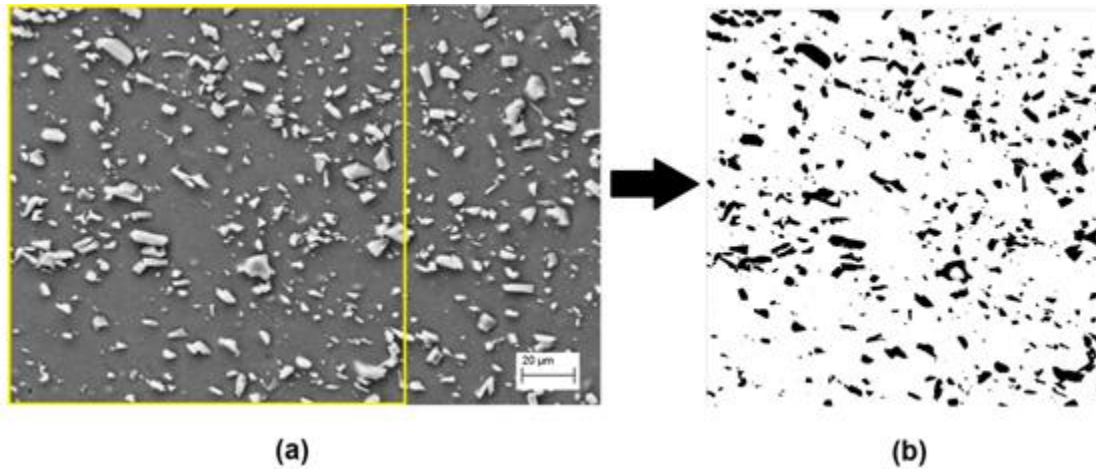
Figure 5.2 (a) Zeiss Neon 40 image of the transverse stir zone from a 1600 rpm FSP AA356 sample and (b) 4 pixel connectivity binary cropped image from the original image.

2.   Measuring the Binary Image

Once the particle distribution is made into a binary image, six particle parameters are measured in order to asses overall morphological homogeneity: 1) spacing, 2) equivalent diameter, 3) aspect ratio, 4) area fraction, 5) directional orientation, and

6) particle population. Depending on the type of material type, other parameters may be added such as Ferret diameter, shape factor, etc. Likewise, parameters that are less relevant may be removed.

a.   *Spacing and Particle Population*

Spacing is measured from the centroid of each particle. Although edge-to-edge measurements are more accurate, implementation is difficult and computationally expensive. Euclidean distance (given by Equation 5.1) is measured from the centroid coordinates of a particle to those of every other particle in the image, and the process is repeated for each subsequent particle, with redundant measurements being ignored.

$$d = \sqrt{\left(X_2 - X_1\right)^2 + \left(Y_2 - Y_1\right)^2} \qquad \text{Equation 5.1}$$

Here, d is the ordinary Euclidean distance between two particles, and (X_1, Y_1), (X_2, Y_2) are the centroid coordinates of two discrete particles. As each centroid is determined, the corresponding particle is recorded in the population count.

b.   *Area Fraction*

Each particle's area is calculated by finding the total number of connected pixels for a given object. Once done for all particles, the total area is summed and divided by the total area of the cropped region.

c.   *Equivalent Diameter*

Each particle's measured pixel area is converted to an equivalent diameter (D_{EQ}) for a circle of the same area, given in Equation 5.2. The calculated length is then scaled to microns according to the magnification scale of the original image.

$$D_{EQ} = \sqrt{\frac{4(Particle\_Area)}{\pi}} \qquad \text{Equation 5.2}$$

d. *Aspect Ratio and Orientation*

An ellipse, which has the same normalized second moment of inertia as the object area, is drawn around the identified pixel region. The minor and major axis lengths of the ellipse are measured in pixels. The particle aspect ratio (AR) is calculated by dividing the major axis length by the minor axis length, shown by Equation 5.3.

$$AR = \frac{L_{Major\_Axis}}{L_{Minor\_Axis}} \qquad \text{Equation 5.3}$$

In this model, orientation is calculated by measuring the angle between the ellipse's major axis and horizontal. Orientation angle (θ) can range from -90° to $+90^o$. Note that, the measurement of θ can be made with respect to any pre-defined axis, when a particular directional measurement may be of unique importance, e.g., a rolling or extrusion direction. Figure 5.3 shows a schematic of a pixilated object being measured for aspect ratio and orientation angle.
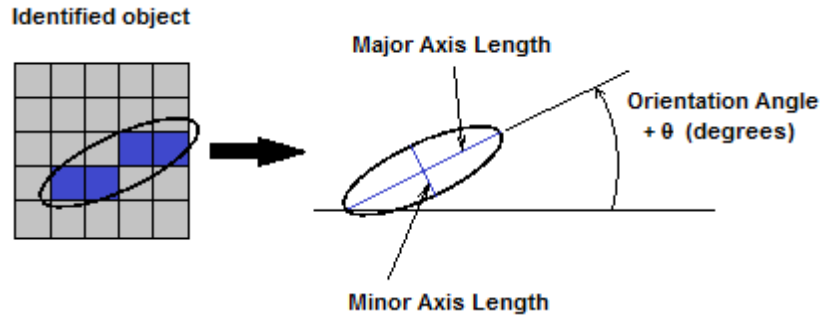
Figure 5.3 Schematic of a pixilated object being measured for aspect ratio and orientation angle.

3. **Assessing Homogeneity**

Homogeneity, in the purest sense, is uniformity in composition or structure. A homogeneous microstructure may not necessarily be mechanically desirable, i.e., a

structure may consist entirely of high aspect ratio particles all oriented in the same direction, yet still be uniform. This section will focus solely on assessing uniformity of a structure.

For a variety of mathematical reasons, variance is a convenient means to assess homogeneity [129]–[131]. Variance is the average of the squared distances from the mean distribution value, and a measure of the data spread in a discrete distribution. Furthermore, the variance of a distribution can be measured with respect to multiple parameters, while accounting for the statistical dependency of those parameters. The variance for a distribution is given by Equation 5.4 [129].

$$VAR(X) = \frac{1}{N} \sum_{i=1}^{N} [x_i - \mu]^2 = [\sigma(X)]^2 \qquad \text{Equation 5.4}$$

Here, $VAR(X)$ is the variance of the parameter $X's$ distribution of N data points, xi is ith data point in the distribution, and μ is the population mean. For a single variate distribution, variance is equal to the square of the standard deviation. In the case of multiple parameters, the total variance is given by Equations 5.5 [129].

$$VAR\left[\sum_{i=1}^{N} X_i \right] = \sum_{i=1}^{N} VAR(X_i) + 2 \sum_{i=1}^{N} \sum_{j=i+1}^{N} COV(X_i, X_j) \qquad \text{Equation 5.5}$$

Here, COV(X_i, X_j) is the covariance of two data sets. The covariance is the statistical dependence of two variables and is given by Equation 5.6 [129].

$$COV(X_1, X_2) = \sum_{i=1}^{N} \frac{(x_{1i} - \mu_{X_1})(x_{2i} - \mu_{X_2})}{N} \qquad \text{Equation 5.6}$$

Here, X_1 and X_2 are two different parameter distributions. For six parameter distributions, this equation will result in a 5 x 5 upper triangular covariance matrix. The algebraic sum of the matrix elements will represent the latter term in Equation 5.5.

a.   *Image Segmentation*

In a perfectly uniform image, all sub-regions of the image would have identical values for all six measured parameters. By measuring the differences between sub-regions, a quantitative evaluation of uniformity can be conducted. These differences may be quantified by measuring the statistical variance of the six parameters over the range of sub-regions. A low variance would serve as indication of homogeneity for the particular parameter being measured. A combination of all the parameter variances serves as an overall indication of homogeneity at a given sub-region size (i.e., length scale).

To create systematic sub-regions, the cropped binary square microstructure image is subdivided into smaller square sectors. Those sectors are then statistically analyzed using each of the six parameters. The characteristics of each square region are then compared in terms of the variance of their normalized mean values. This analysis occurs over a range of sub-region sizes to assess the effect of scale on the homogeneity measurement.   Figure 5.4 shows the effect of scale on homogeneity quantification using variance measures. The same material at different magnification will have very different regional variances depending on scale. In fact, for the sector size selected, the as-cast is relatively uniform from sector to sector. As the sector size decreases however, the variances should rise in a less uniform material. Another effect is immediately noticeable at higher magnification. If the sectors become too small, more sectors read values from empty regions, and the variance from sector to sector will begin to decrease. This trend is important to note when interpreting results.
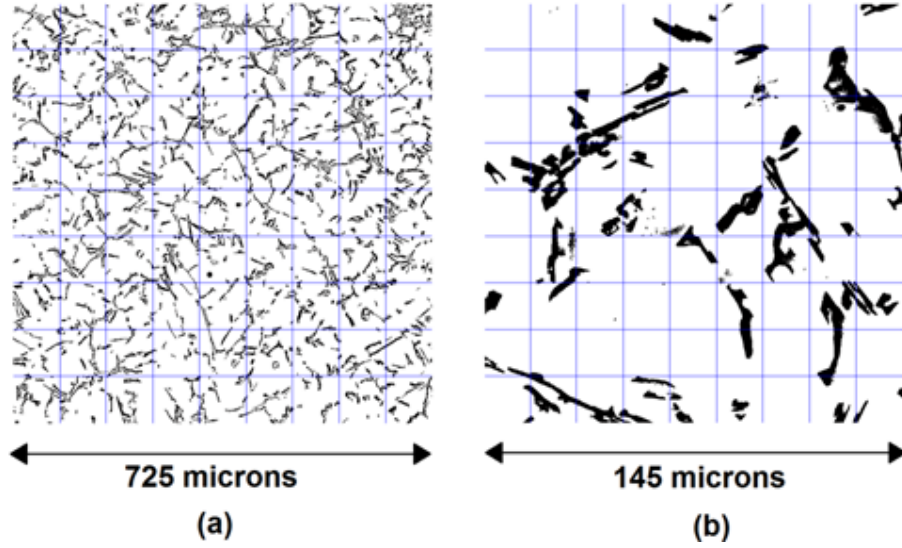
Figure 5.4 As-cast AA356 at (a) 100X and (b) 500X magnification, where each micrograph is segmented into 81 square sectors. In (a) the sector areas are too large, and in (b) too small to provide an effective statistical measure.

b.   *Homogeneity Evaluation*

Since, in each case, the measurement of a selected parameter mean occurs across an equal number of subgroups (the number of sectors); a suggested Homogeneity index (H_s) for a particular length scale can be expressed by the relation shown Equation 5.7. This index represents a normalized measure of variation in the sample with respect to all the selected parameters. Here, $N = 6$ would represent the number of measured parameter distributions.

$$H_s = 1 - \left(\sum_{i=1}^{N} VAR(X_i) + 2\sum_{i=1}^{N}\sum_{j=i+1}^{N} COV(X_{i,}X_j) \right) \qquad \text{Equation 5.7}$$

Equation 5.6 holds regardless of whether the variables have statistical dependence. A total variance for the sample may be calculated according to the following procedure:

123

<u>Homogeneity   Index Evaluation Procedure:</u>

1.   Divide the binary image to a selected number of square sectors.

2.   Calculate the mean values for each measured parameter for all sectors.

3.   Normalize each distribution of sector mean values to 1.

4.   Calculate that variance of each normalized distribution.

5.   Calculate the covariance for each parameter relation, e.g., $COV(X_1, X_2)$ to $COV(X_5, X_6)$. For the six selected parameters, 15 covariance values will result. Sum the covariance values and multiply by 2.

6.   Sum the calculated variance and covariance terms and subtract from 1.

Since measured values are normalized, the above procedure will result in a homogeneity estimate ranging from 0 to 1, with a value of 1 indicating perfect homogeneity, i.e., all variances are zero since all sectors are identical in their parameter distributions. Note that, using a single sector will result in $H_s = 1$ since the measured sector is compared only to itself. An explicit example of the implementation is flowcharted in Appendix G. The MATLAB code developed for this algorithm can be reviewed in Appendix H.

D.   RESULTS AND DISCUSSION

1.   As-cast AA-356

Homogeneity evaluation results for the as-cast AA-356 are shown in Figure 5.5. The results here are used to demonstrate the effect of scale on the homogeneity value. A 100X magnification sample is analyzed across 81 sectors (80 µm sector width). This sample was previously shown in Figure 5.4(a). Figure 5.5 shows the normalized parameter values obtained. This example shows that, for a low magnification and a large sector size, the sample can still appear statistically homogeneous.
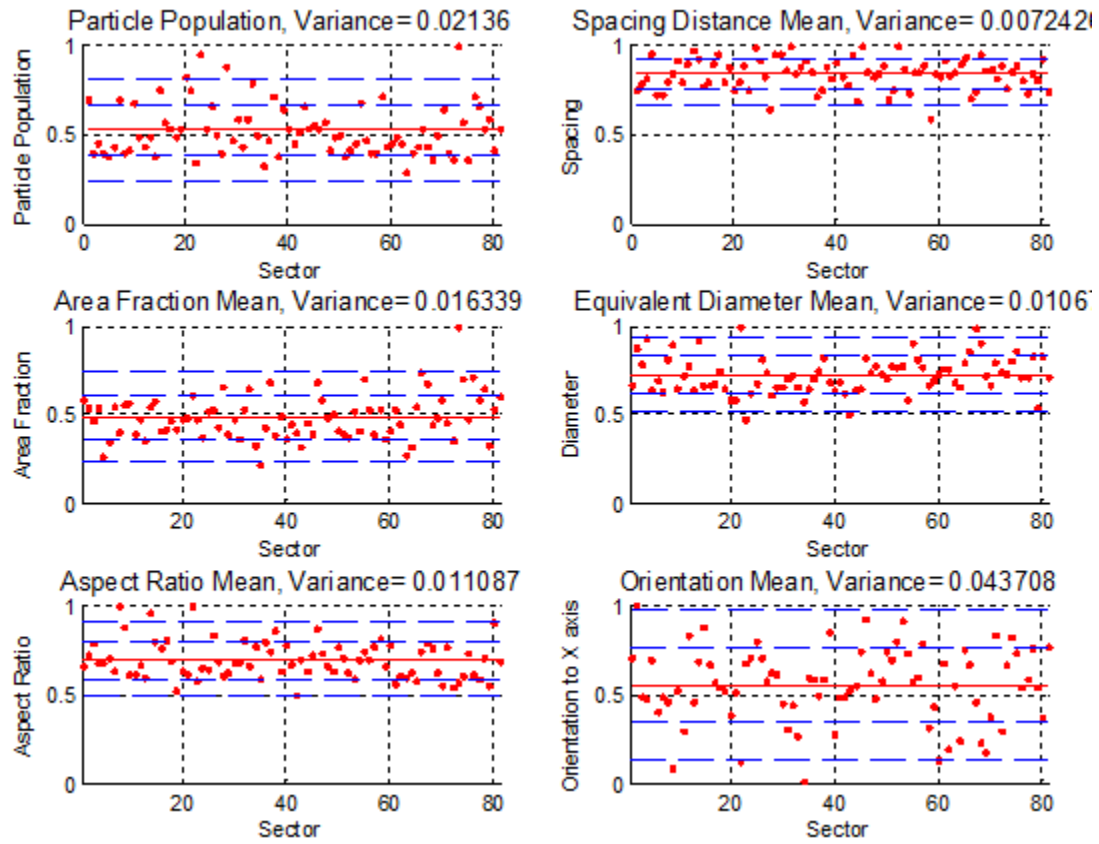
Figure 5.5 The normalized parameter values measured from as-cast AA356 at 100X magnification segmented into 81 square sectors (80 µm sector width). The solid, centered line indicates the mean value, and the vertically-spaced dashed lines are drawn in one standard deviation increments from the mean.

125

By comparison, Figure 5.6 shows the normalized parameters for a 500X magnification micrograph of as-cast AA356 (previously show in Figure 5.3(a)) also analyzed using 81 sectors (16 μm sector width).
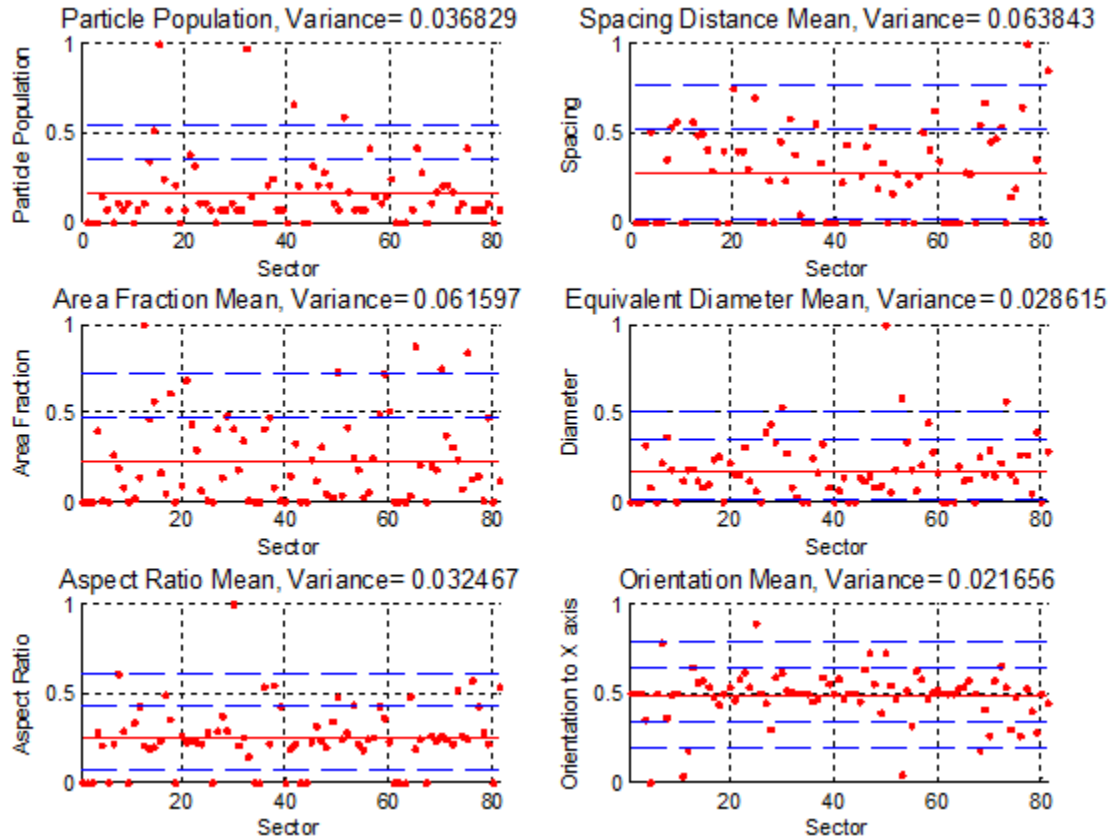
Figure 5.6 The normalized measured parameter values for AA356 at 500X magnification obtained over the range of 81 sectors (16 μm sector width). The solid line indicates mean value, and the dashed lines are vertically spaced at one standard deviation from the mean.

A few observations can be made regarding Figures 5.5 and 5.6. First, neither of the above segmentation scales is adequate in capturing the particle scale of homogeneity. At the higher magnification, the image is still morphologically consistent from sector to sector, and the computed variance remains low. A sufficiently small sector width is required to capture the true characteristics of the distribution. However, at the higher magnification, a high grid resolution results in the width of each sector becoming smaller

than the characteristic length of the particles. As a result, more sectors are either measuring empty regions or measuring portions of particles. Note the frequency of zeros in Figure 5.5. (Also note that, due to the orientation parameter varying between -90° and $+90^o$, a normalized 0.5 value would represent a zero orientation). Because of the high number of empty regions, more sectors become similar and the overall variance value decreases, causing homogeneity to increase. For these reasons, the H_s plot will have a characteristic shape with the value initially dropping as the grid resolution is increased. A material with smaller, more uniformly dispersed particles will exhibit a flatter curve, which takes longer to reach a minimum. The grid resolution where the H_s value reaches a minimum is the last valid length scale to assess H_s. At this point, the sector size will be on the order of the particle size in the micrograph. However, as long as a minimum H_s value has not been reached, two samples may be compared directly at the same grid resolution to judge relative homogeneity. Figure 5.7 illustrates these ideas schematically.
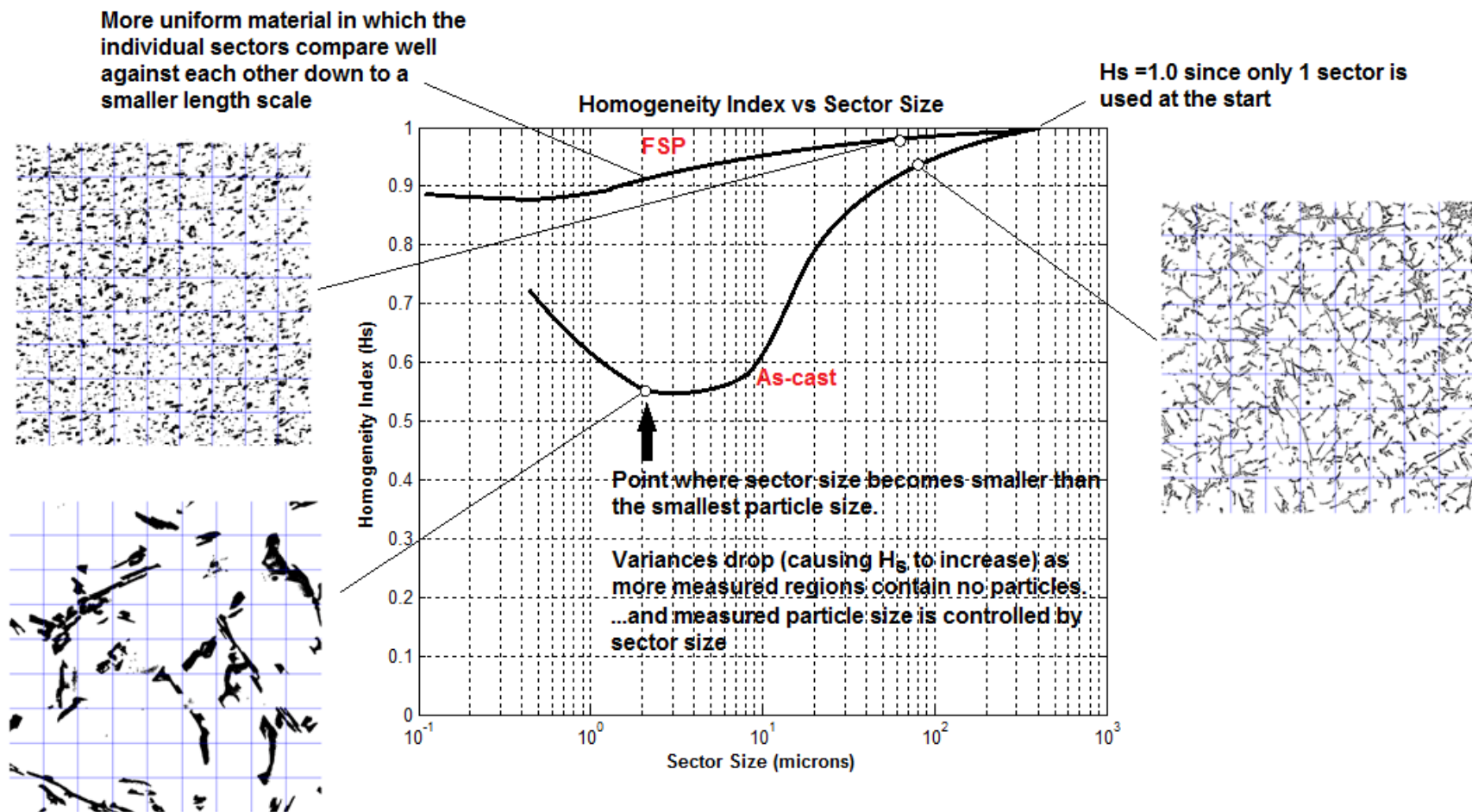
Figure 5.7 Schematic of typical Homogeneity index (H_s) plots showing minimum as the sector grid size approaches the particle size. Notional H_s plots for FSP and as-cast AA356 are shown.

128

To illustrate the effects of sector size and image magnification, four different samples of as-cast material were measured for homogeneity at four different magnifications, across a range of sector sizes. The results are shown in Figure 5.8. Minimums in the Homogeneity parameter (H_s) are reached in the vicinity of 10 μm, the approximate characteristic particle length and spacing for the microstructure. Lower magnification images tend to show smoother trends, but the more erratic plots at the higher magnifications may be due to the low numbers of particles in the measured region. Results for the four magnifications differ due to local variations in morphology in the as-cast samples. At high magnification, the morphological character of the overall microstructure can be missed. Based on the convergence region of the plot minimums, a reasonable estimate for an as-cast H_s value could range from 0.2 to 0.5. It should be noted that considerably longer computational time is required to measure the image at fine grid resolutions. Also, the lower magnifications require very high pixel resolution for accurate particle measurement. The approach is best suited to a range of sector sizes close to the mean particle size (perhaps mean diameter ± several particle diameters) and where the number of particles in each sub-region is sufficiently high to obtain a statistically meaningful measurement.
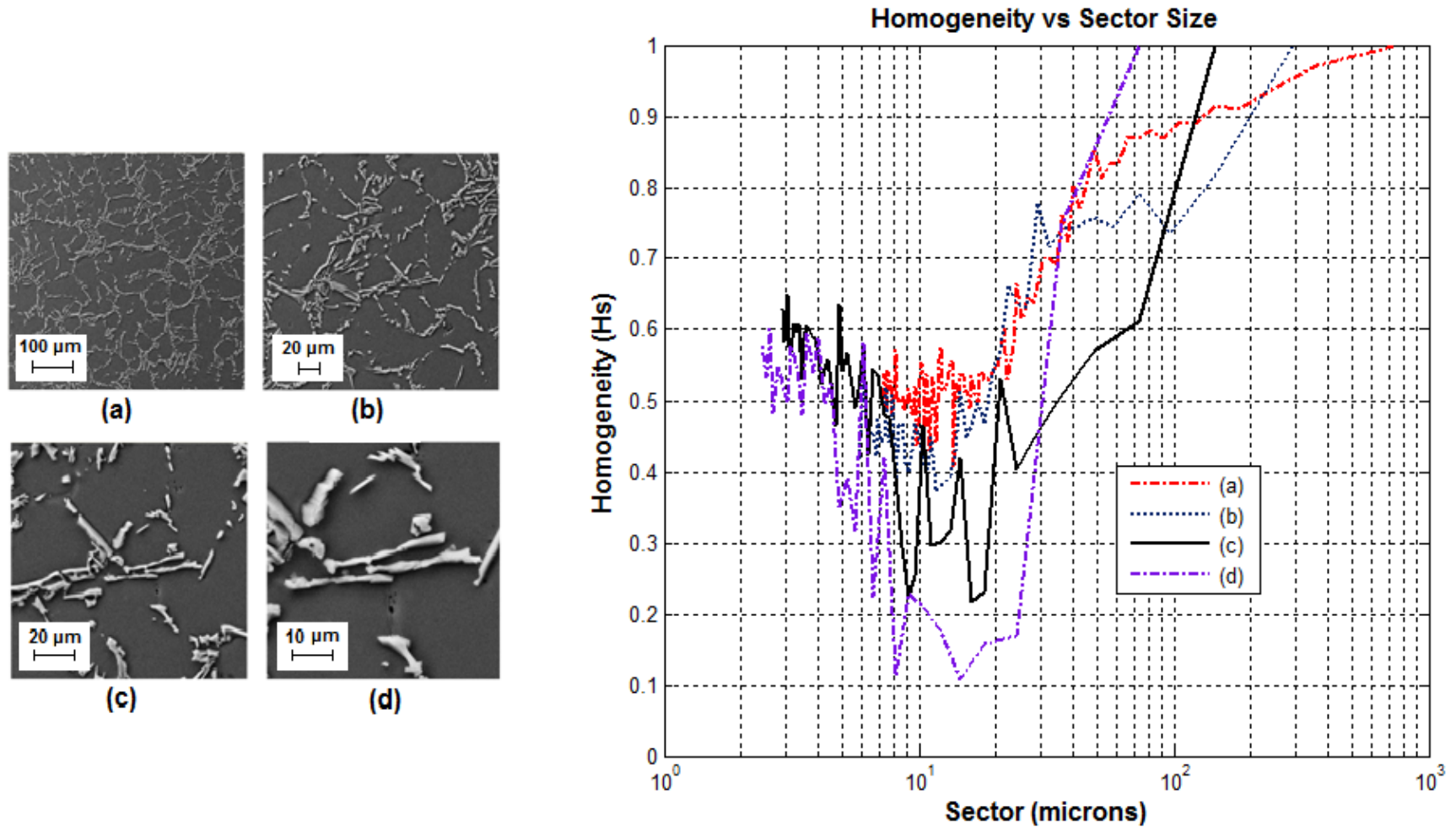
Figure 5.8 The calculated Homogeneity (H_s) based on the measured parameter values for (a) AA356 where (b),(c), and (d) are 2, 5, and 10 times smaller in area than (a). Measurements were obtained over a wide range of sector sizes, at different sites but for the same as-cast material. The plot illustates the index sensitivity to the number of particles in the image.

2.   Homogeneity in Friction Stirred Material

An AA356 plan view 3200 RPM FSP sample was analyzed at magnifications of 100X, 200X, 500X, and 1000X. In this case, the measurements were taken at the same site within the sample in order to assess the repeatability of the homogeneity calculation using different image magnifications.   Figure 5.9 shows the FSP AA356 at low magnification and the binary image segmented into 400 sectors (a sector width of 14.5 μm). Here, particles are roughly 5 μm in size, so the 14.5 μm sector size should encompass most particles. This implies that H_s will have not yet reached a minimum and that the measurement will be meaningful.
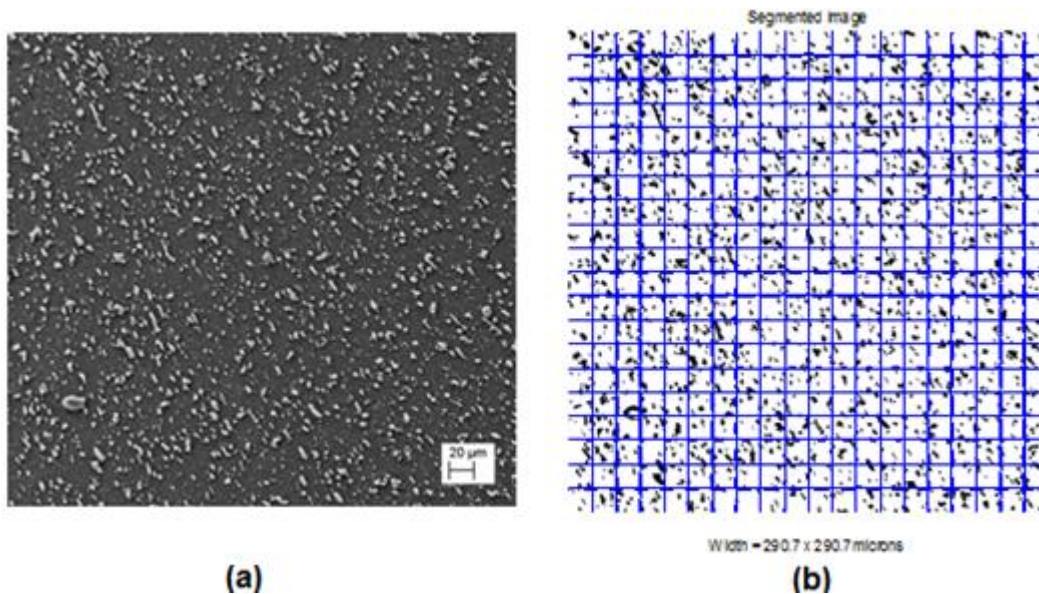
Figure 5.9 (a) The secondary electron image of a 3200 RPM FSP AA356 transverse section at 200X magnification and (b) the binary image of the same sample segmented into 400 sectors with a 14.5 μm sector width.

Figure 5.10 shows the measured parameters for this FSP AA356 micrograph at 200X magnification with the 14.5 μm sector size. The data spread shows tighter banding and fewer zero values than the as-cast material, indicating a valid length scale   The characteristic particle size and spacing distances are smaller than in the as-cast example,

131

consequently H_s will take more measurement cycles to reach a minimum when the constituent material is more finely dispersed.
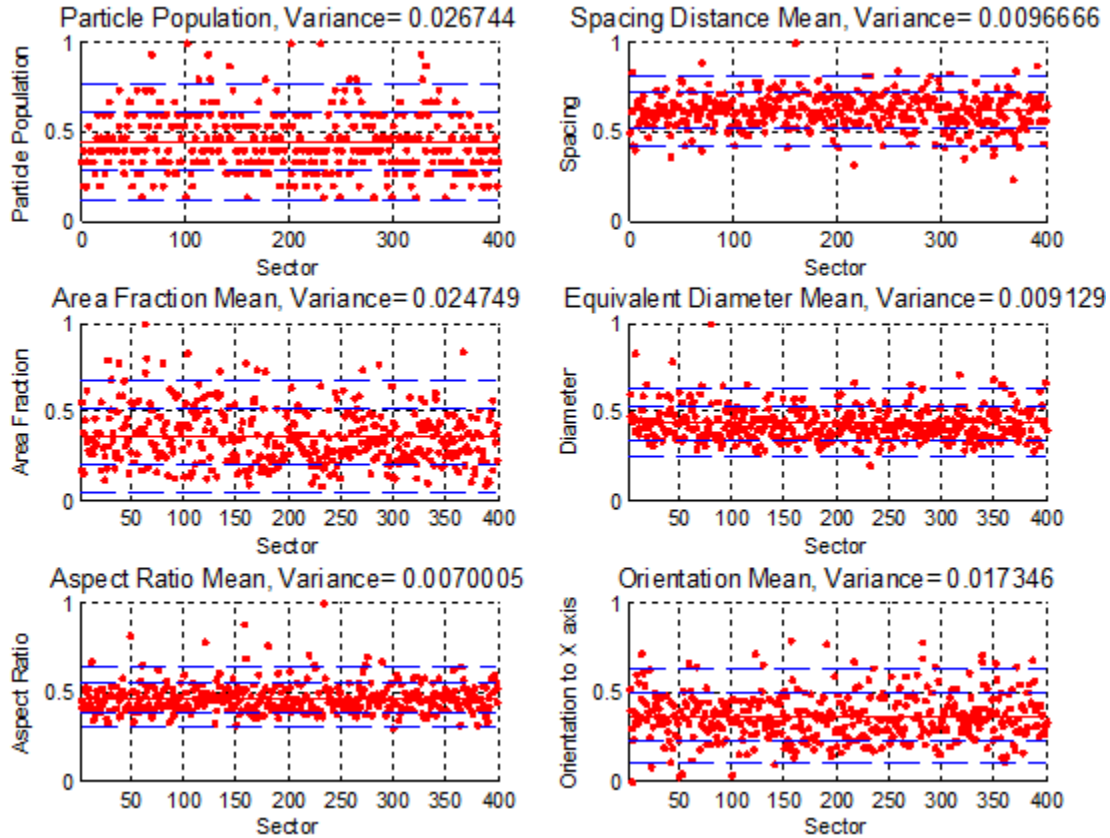
Figure 5.10 The normalized measured parameter values for a 3200 RPM FSP AA356 transverse section at 200X magnification obtained across 400 sectors. The solid red line indicates mean value, and the dashed blue lines are spaced at one standard deviation from the mean.

Figure 5.11 (plotted on a semi-log scale) shows the H_s calculation for the FSP AA356 as a function of sector size. The results indicate that calculation is consistent for a variety of magnifications, except when the magnification is too low. At low magnification, the measurements occur over a much larger area and individual sectors have a larger probability of showing variability the entire width of the sample, i.e., there are many more particles in the image. As a result, the H_s value decreases sooner. Also, at 100X magnification, the image's large pixel size is larger than many of the particles.

132

Since more than one particle may reside in a pixel, a measurement error is introduced. This problem could be alleviated with higher resolution imaging, but it illustrates that consideration must be given to pixel-particle size relationship, as well as the number of features in the image during measurement. Torrala [132] shows the human eye can visibly recognize a scene with a 32 x 32 pixel resolution and that complex individual objects can be recognized by as few as 30 pixels. This data might be used to select a measurement length scale such that individual particles are comprised of at least some minimum number of pixels. Nevertheless, the results indicate that with sufficient image resolution, a consistent H_s value can be obtained regardless of the magnification.
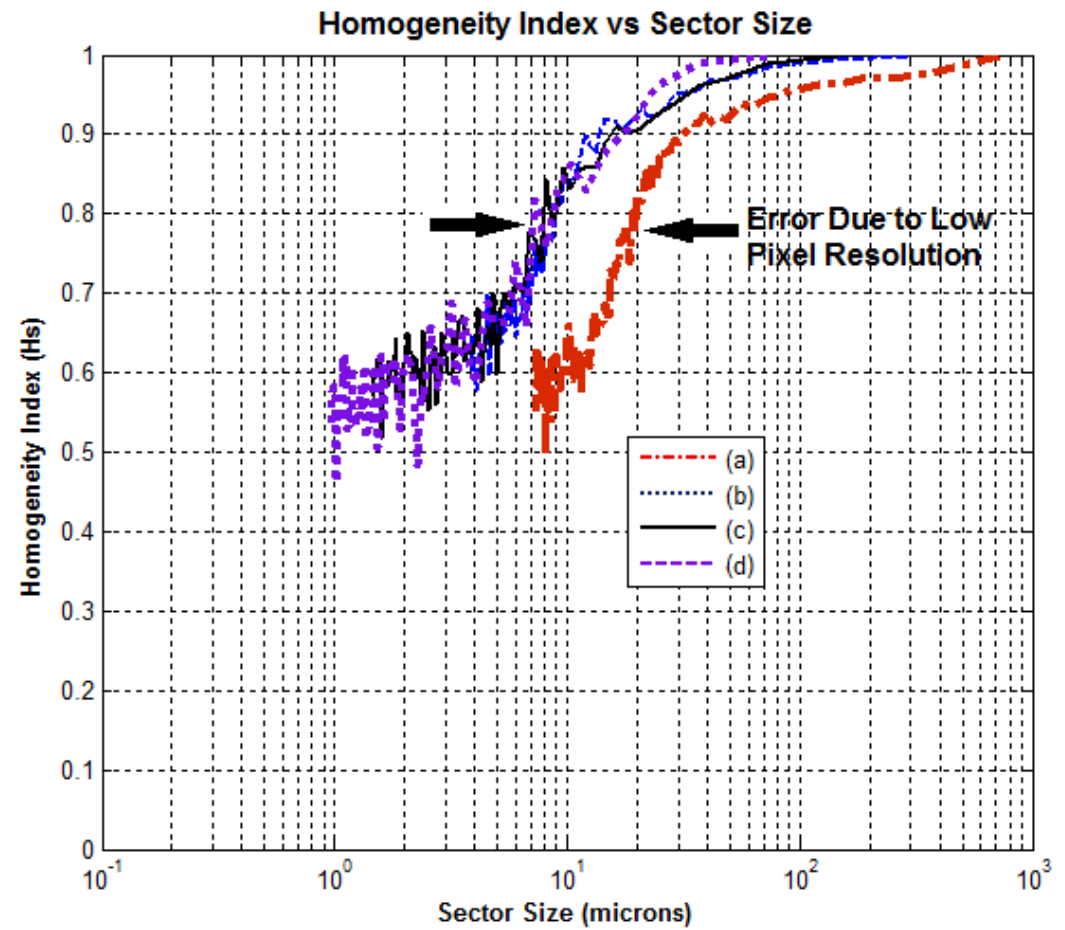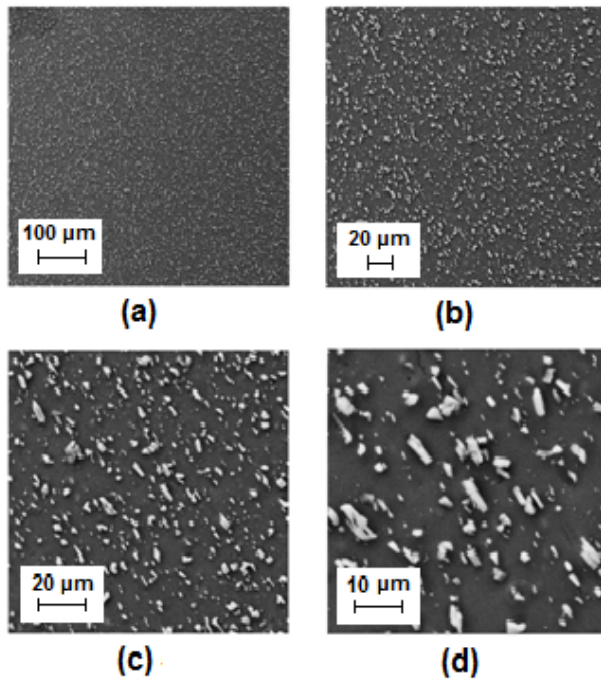
Figure 5.11 The calculated Homogeneity (H$_s$) based on the measured parameter values for 3200 RPM FSP (a) AA356 at where (b),(c), and (d) are 2, 5, and 10 times smaller in area than (a). The measurements were obtained over a wide range of sector sizes, at the same central location on the same sample.

3. As-Cast and Friction Stirred Homogeneity Comparison

With the capability of obtaining a consistent evaluation for homogeneity, sample to sample comparisons can be made at equivalent length scales. Figure 5.12 shows the H_s comparison based for 3200 RPM FSP AA356 at 200X, 500X, and 1000X magnifications, as measured from secondary electron images. At the characteristic length scale of the as-cast material (10 to 20 µm), the FSP material has an H_s value of 0.85–0.90 and the as-cast material a value of approximately 0.15–0.45. It is important to note that the magnification is not affecting the homogeneity, but rather the number of features in the image. In the case of as-cast material, with a relatively low number of features, a lower magnification (on the order of 200X or lower) may provide an appropriate length scale for measuring H_s. Conversely, the high number of features in a FSP sample may require higher magnification (on the order of 500X or higher). Nevertheless, depending on the sample selection, FSP increased homogeneity by two to five times as compared to the as-cast material. Furthermore, the FSP material maintains a measurable homogeneity down to approximately 1 µm, compared to 15 µm for the as-cast material.

(a) 200X Magnification

(b) 500X Magnification

(c) 1000 X Magnification
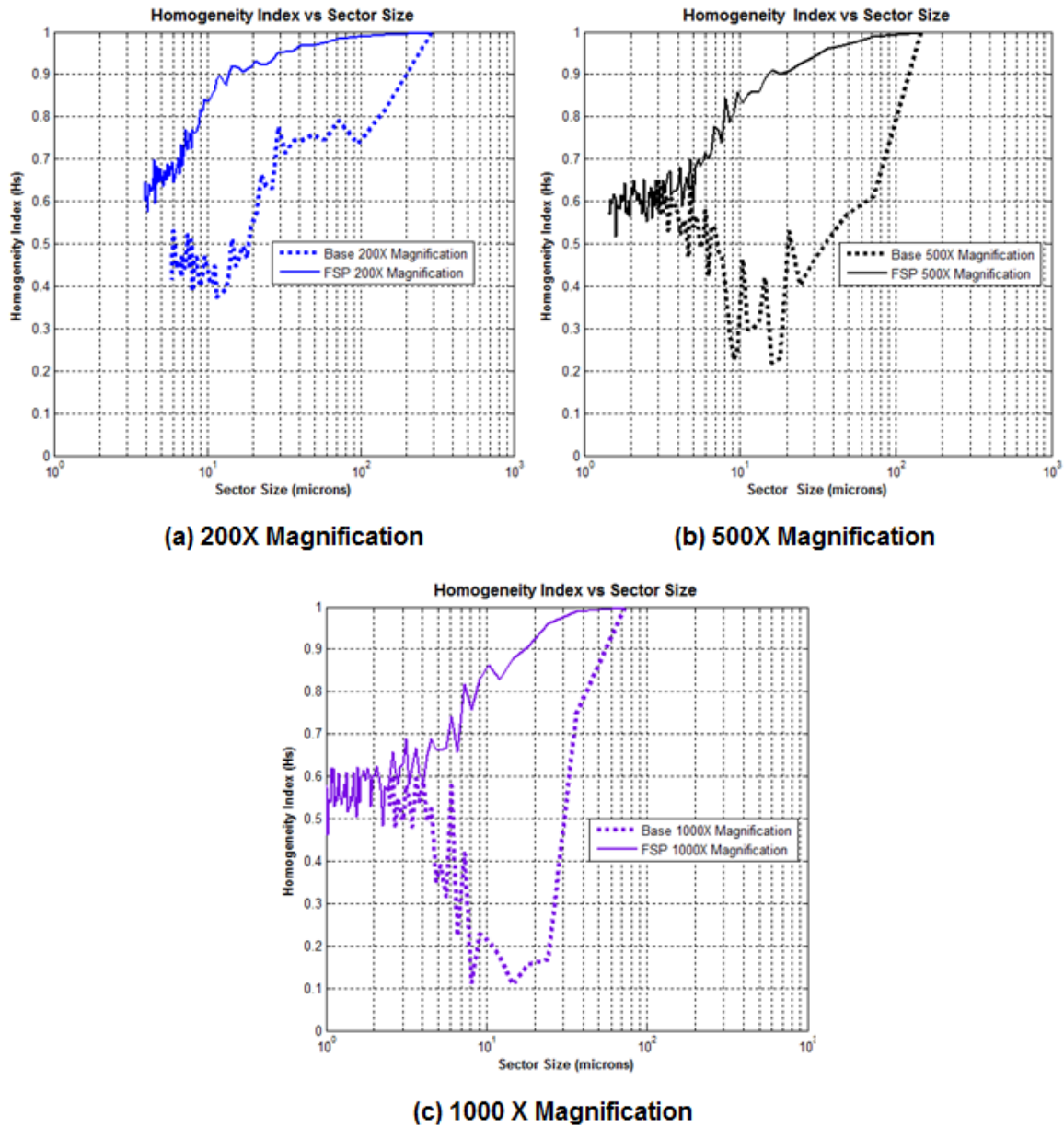
Figure 5.12 Homogeneity Index (H_s) comparison based on the measured parameter values for 3200RPM FSP AA356 and base material at (a) 200X, (b) 500X, and (c) 1000X magnification.

4.   Homogeneity Comparison as a Function of RPM

A homogeneity analysis was conducted on plan view FSP threaded tool samples using secondary electron images taken at 1000X magnification. Figures 5.13(a) and (b) show the results of the analysis.   A clear and measurable relationship exists which indicates improved homogeneity with increasing RPM.

By taking a single value from each plot at the length scale where the 400 RPM data reaches a minimum (at approximately 8 μm), the trend in H_s is more evident. Figure 5.14 shows H_s linearly increasing with RPM for the case of the threaded tool at the 8 μm length scale. Since H_s has a maximum value of 1, the value would likely approach that value asymptotically as RPM increase further.

The evidence suggests that RPM is an important factor in controlling the homogeneity of constituent dispersions. A finding of Chapter IV showed that RPM was a controlling factor in determining the width of stripped layers during pin rotation. Since a higher RPM corresponds to both thinner strip layers and improved homogeneity, it could reasonably be concluded than thinner layer widths can be correlated to dispersions that are more homogeneous.
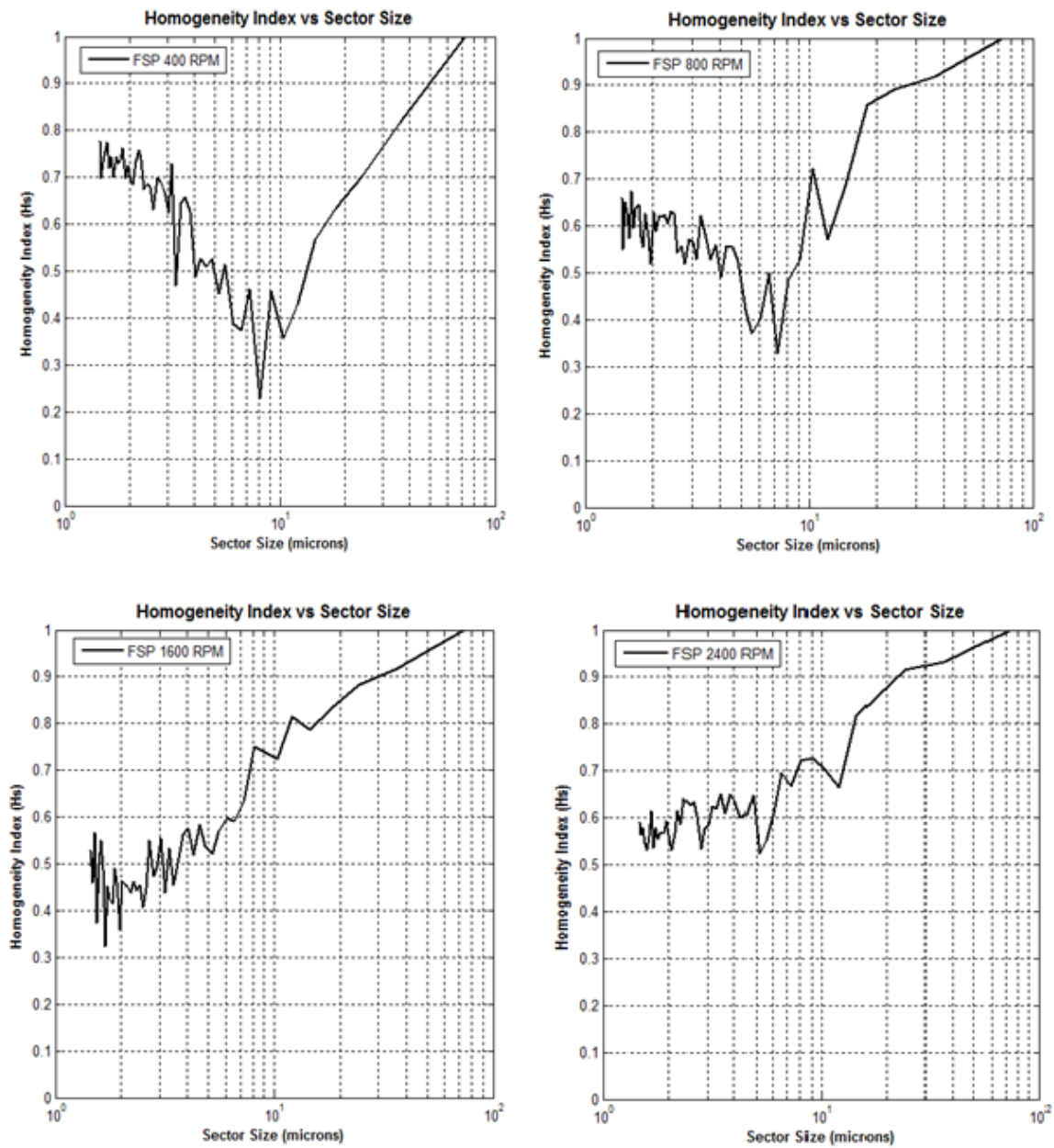
Figure 5.13(a) Homogeneity (Hs) comparisons in the stir zone center for FSP AA356 with a threaded tool at selected RPM ranging from 400 to 2400 RPM.
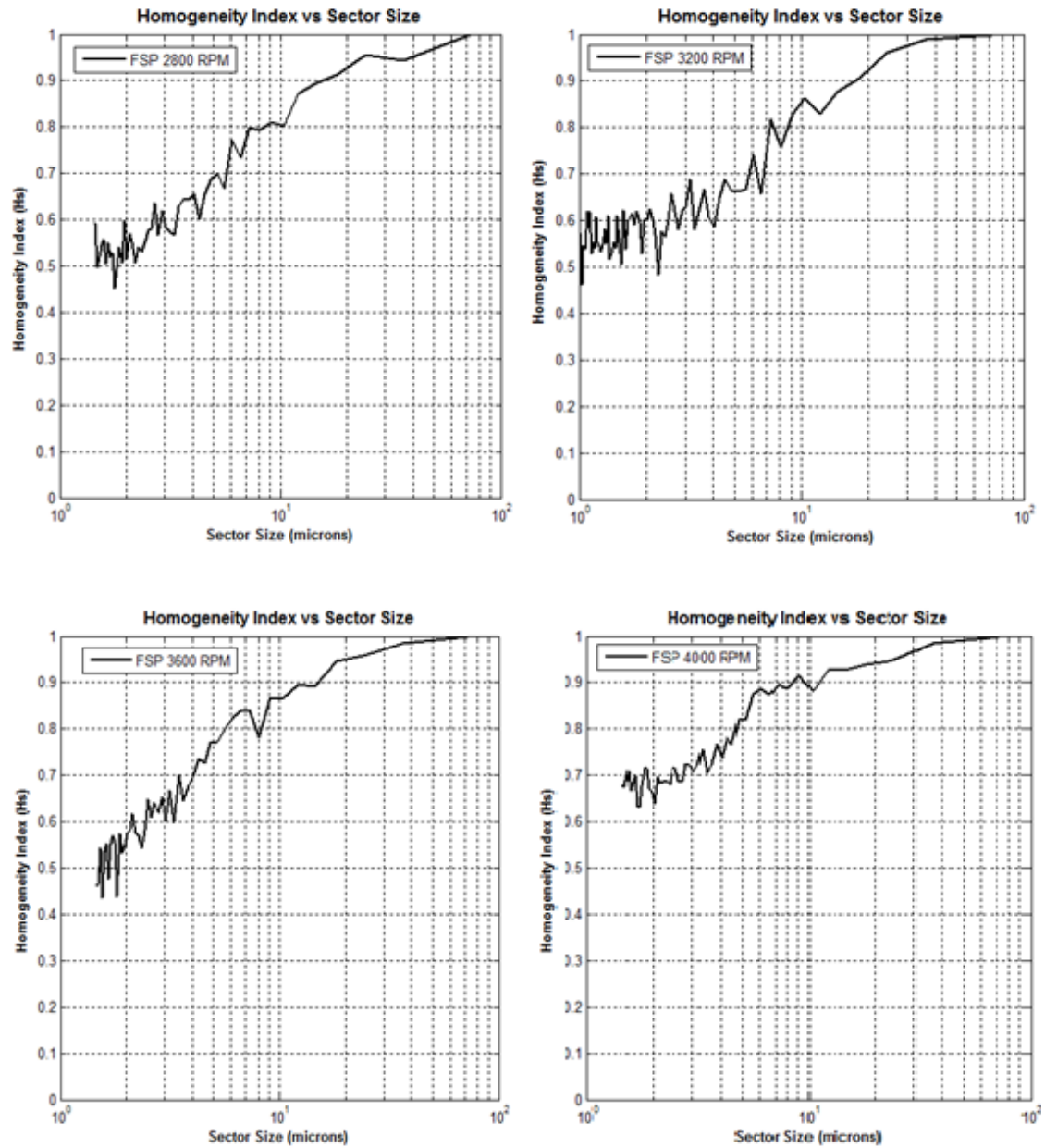
Figure 5.13(b) Homogeneity (H$_s$) comparisons in the stir zone center for FSP AA356 with a threaded tool at selected RPM ranging from 2800 to 4000 RPM.
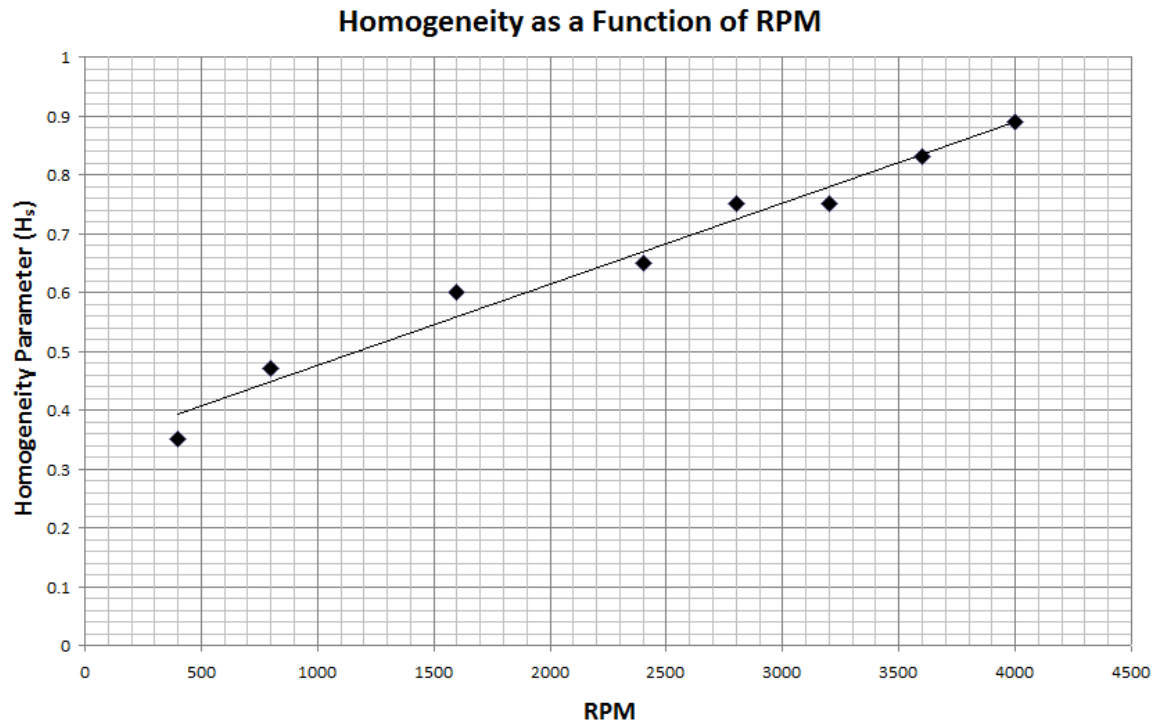
Figure 5.14   Homogeneity (H_s) data in the stir zone center for FSP of AA356 with a threaded tool. Data is measured at the 8 μm sector width (the point where lower RPM H_s values reach a minimum).

5.   Threaded and Smooth Tool Homogeneity Comparison

Values for H_s were measured at the low and high ends of the RPM range for the threaded and smooth tools. The results are show in Figure 5.15. The difference between the tools is not drastically different at either the high or the low RPM. For these particular tool geometries and speed combinations, RPM appears to have a much larger effect on dispersion and homogeneity outcomes. This conclusion must not be extended to all tool geometries, but it is important to note that the dispersion quality for an individual tool is a measurable quantity.
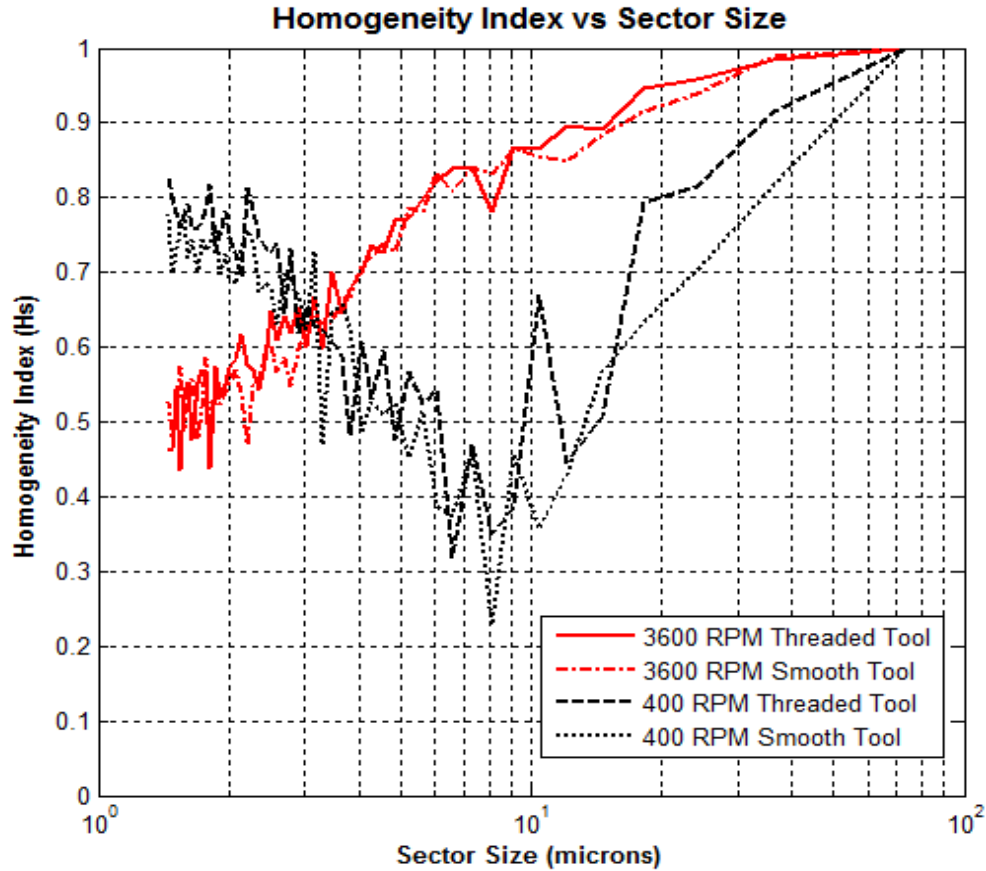
Figure 5.15 Homogeneity (H$_s$) data for FSP AA356 in stir zone center for a threaded tool and smooth tool for at 3600 RPM and 400 RPM.

6.   Stir Zone Mapping

The SZ for an 800 RPM threaded tool at is mapped for homogeneity at 8 discrete locations. Also included for comparison is a sample for the base material. The numerical measurement is consistent with visible observations. The highest measured homogeneity is in the shoulder region, shown in Figure 5.16. Figure 5.17 shows the locations and micrographs of the measurement locations. For comparison purposes, measurements should be taken where the sector resolution approaches the particle size for the coarsest material, in this case the base material. At the base material's minimum, around 10 μm, H$_s$ shows a value of approximately 0.30, while the more dispersed regions show values ranging from 0.70 to 0.85 or higher.
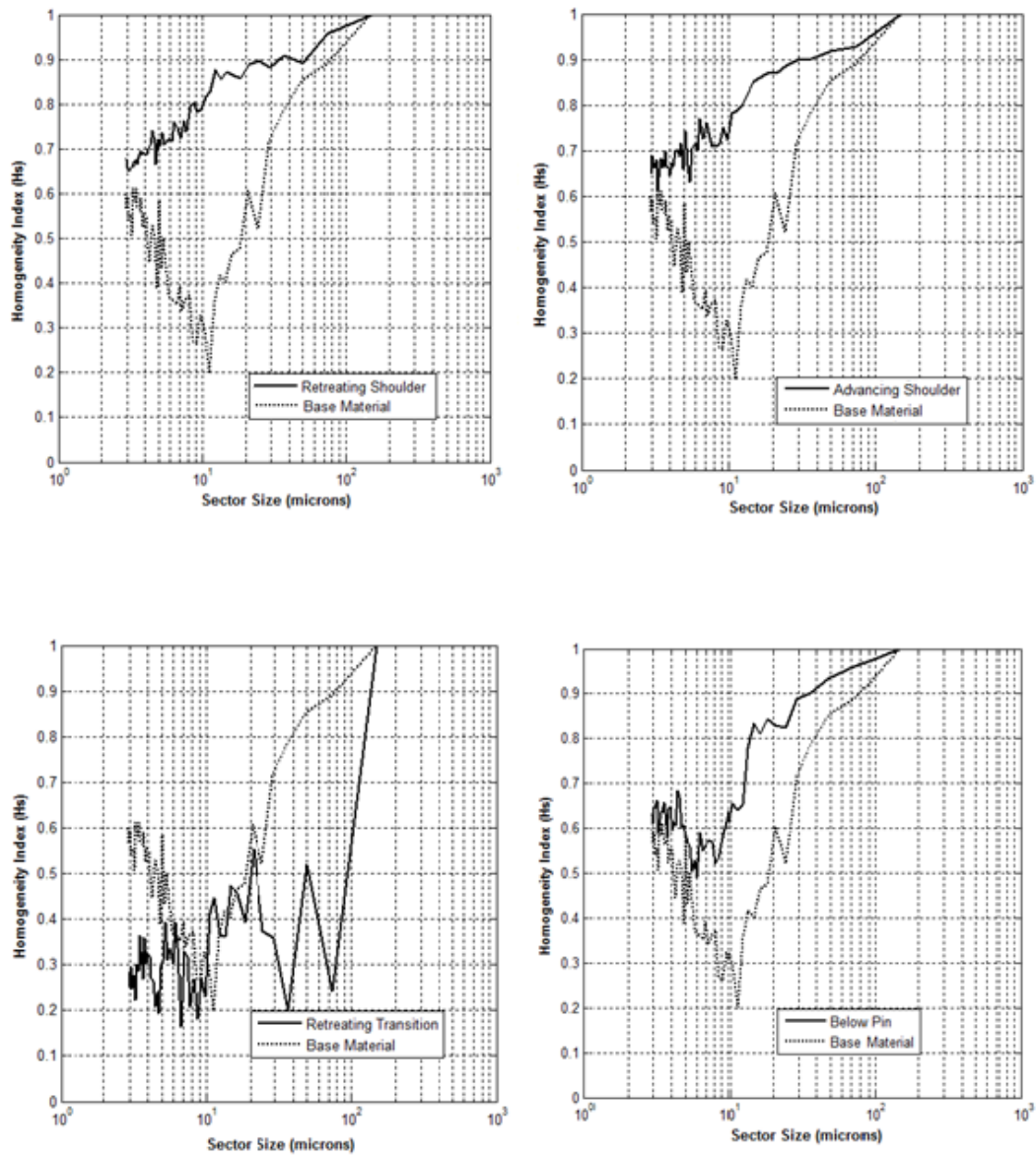
Figure 5.16(a) Homogeneity (H$_s$) data for FSP AA356 in various stir zone locations (compared to as-cast) for a threaded tool at 800 RPM.
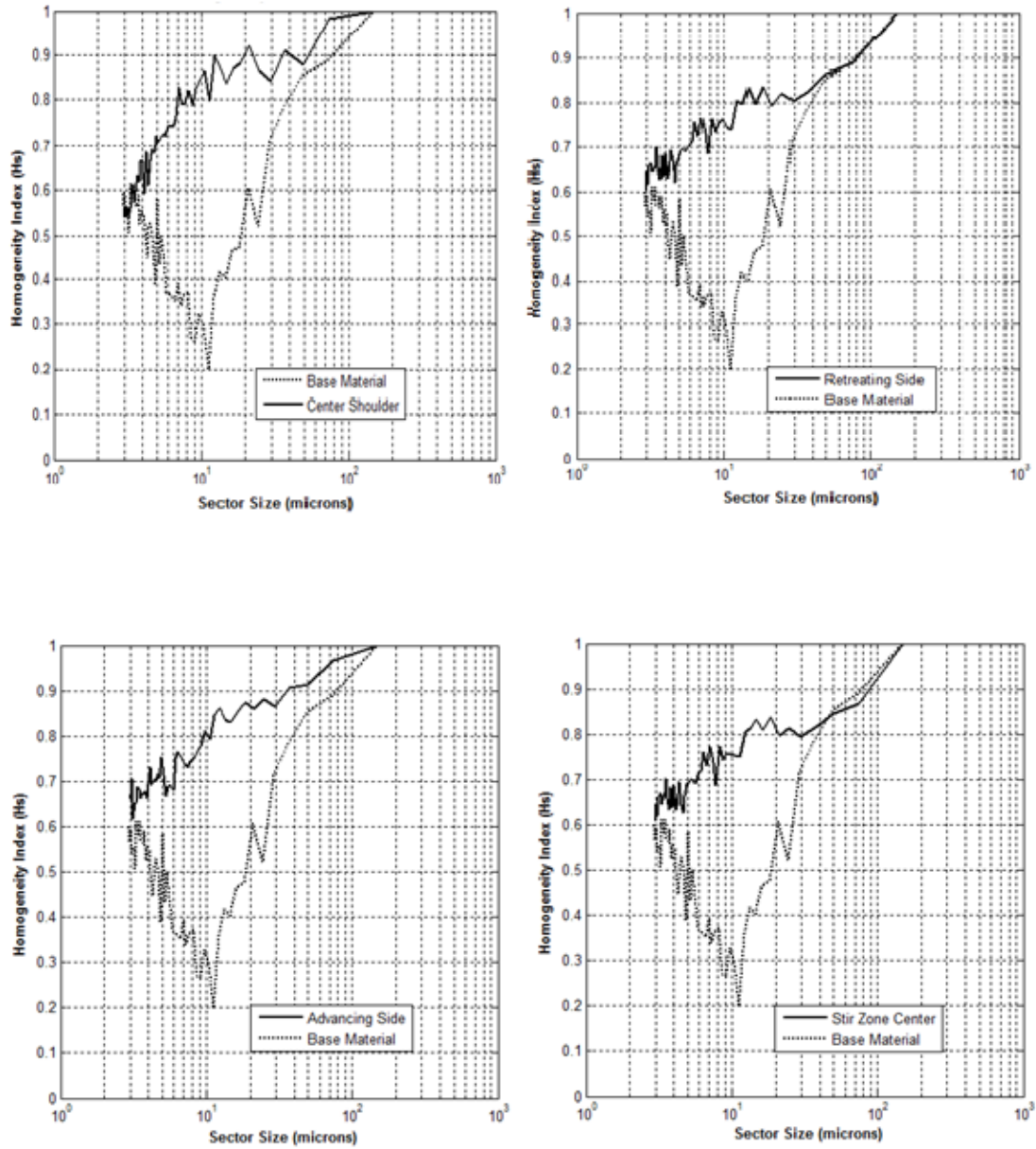
Figure 5.16(b) Homogeneity (H_s) data for FSP AA356 in various stir zone locations (compared to as-cast) for a threaded tool at 800 RPM.
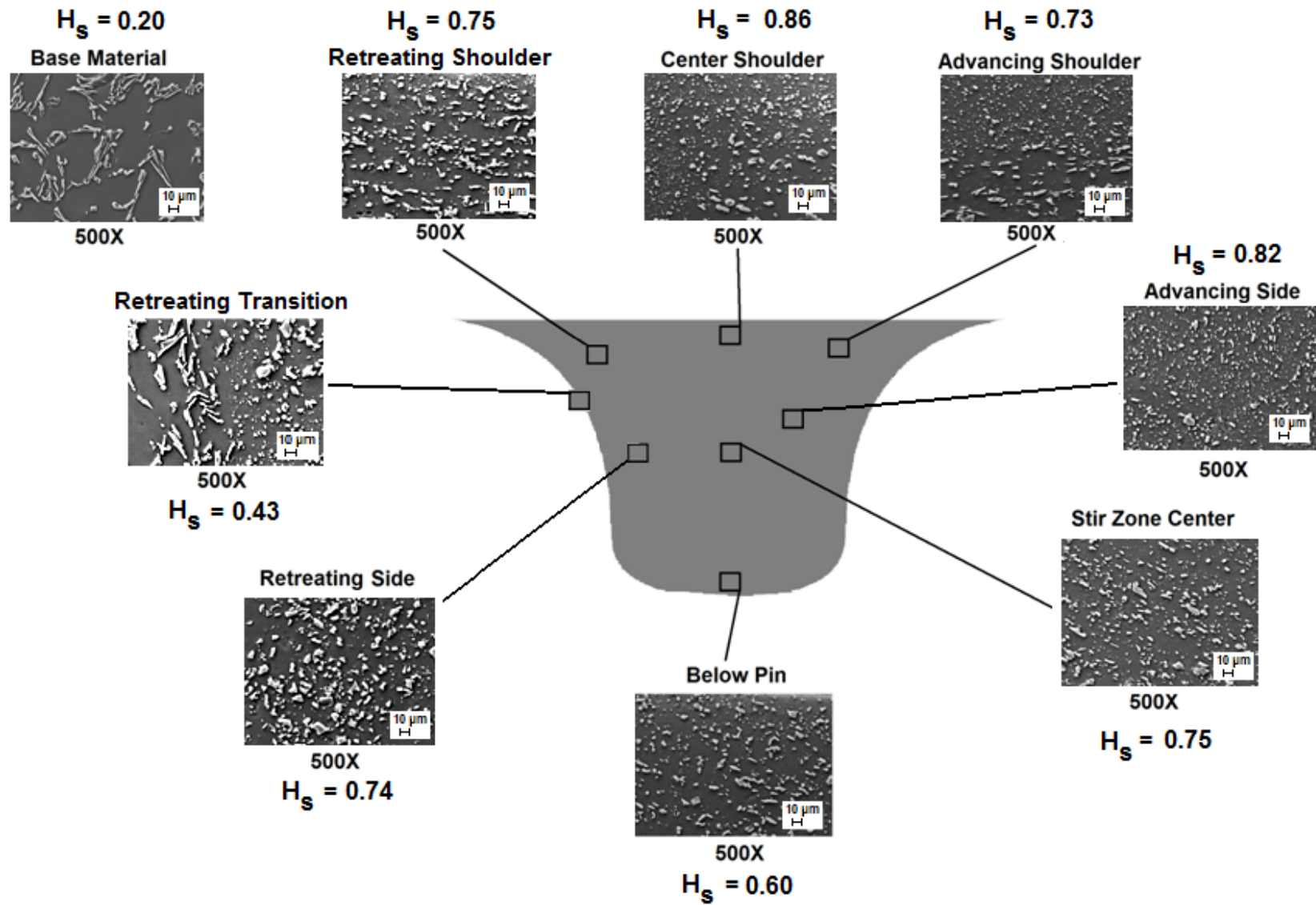
Figure 5.17 Homogeneity (H$_s$) sample locations corresponding to the plots of Figure 5.16 for FSP AA356 using a threaded tool at 800 RPM. The H$_s$ index is measured at the 10 μm length scale.

In this instance, the SZ mapping is not meant to be comprehensive, but rather an example of how the quality of a stir can be numerically characterized according to region. The 800 RPM stir showed considerable nonuniformity in the SZ microscopy, which is reflected in the homogeneity data set. With a sufficiently high resolution image of the entire SZ, a full homogeneity map could very quickly be calculated.

7.   FSP Effects on Particle Parameters

A benefit to the edge detection approach is that individual particle characteristics are measured for the entire particle population. As a result, distributions fits can easily be made for a particular parameter. Figures 5.18, 5.19, 5.21 and 5.22 show the best fit distributions for four particle parameters: 1) equivalent diameter, 2) aspect ratio, 3) orientation, and 4) spacing distance, as measured across the entire sample. Numerous distribution trial fits were conducted including: Lognormal, Exponential, t, Inverse Gaussian, Poisson, Weibull, and Extreme Value. The results are shown in the form of probability plots, where each data marker represents a particle in the distribution. Both as-cast and post-FSP distribution fits are shown for comparison. In order to avoid confusion, the plots show only the distribution fit having the highest confidence level. Although the plots show the distribution fits for the 800 and 3200 RPM FSP runs, distribution shapes were consistent for the entire range of RPM values.

The as-cast and post-FSP equivalent particle diameter (D_{EQ}), which is the scaled particle area, tended to follow a Weibull distribution. Particle aspect ratio (AR) tended toward either a lognormal or an exponential distribution. In both cases, the plots show a significant reduction in particle size and aspect ratio following FSP at 800 RPM and 3200 RPM. Figure 5.20 shows the mean value of both D_{EQ} and AR plotted over the entire range of RPM. The highest fractional reduction D_{EQ} and AR occurs at low RPM, and gradually decreases as RPM is increased. With large differences in the measured H_S value between the high and low rpm, this suggests that small changes in the mean value of particle size and aspect ratio are less important than the uniformity of the distributions. As the distribution line becomes vertical, the distribution is tending toward greater uniformity.

145
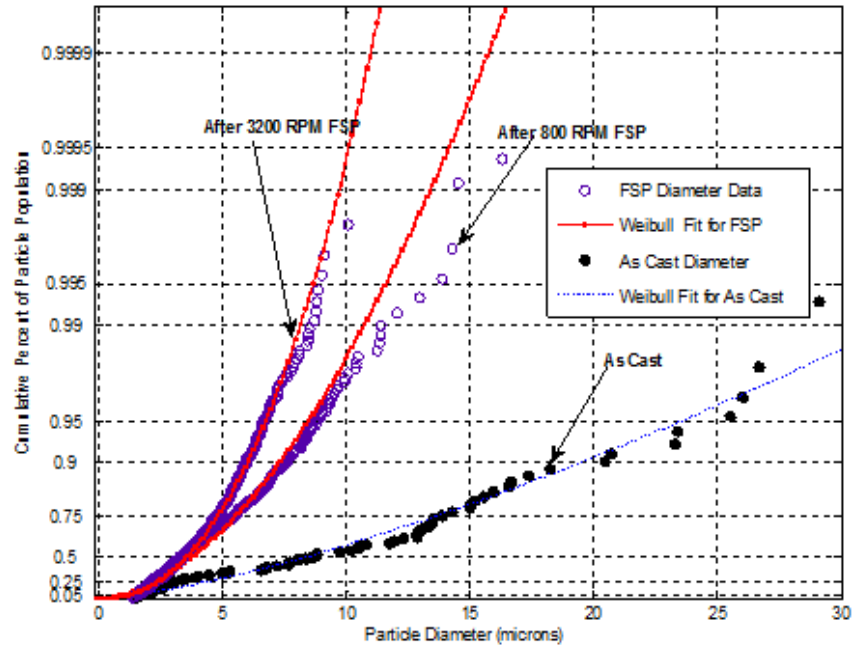
Figure 5.18 Particle equivalent diameter distributions for AA356, both as-cast and after FSP using a threaded tool at 800 and 3200 RPM. Also shown are the highest probability distribution fits.
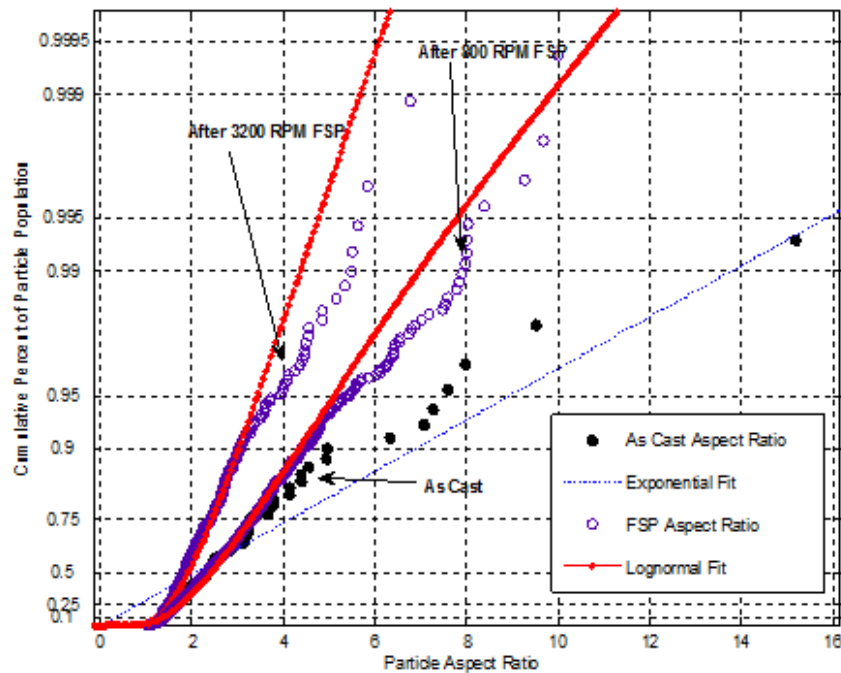
Figure 5.19 Particle aspect ratio distributions for AA356, both as-cast and after FSP using a threaded tool at 800 and 3200 RPM. Also shown are the highest probability distribution fits.

146
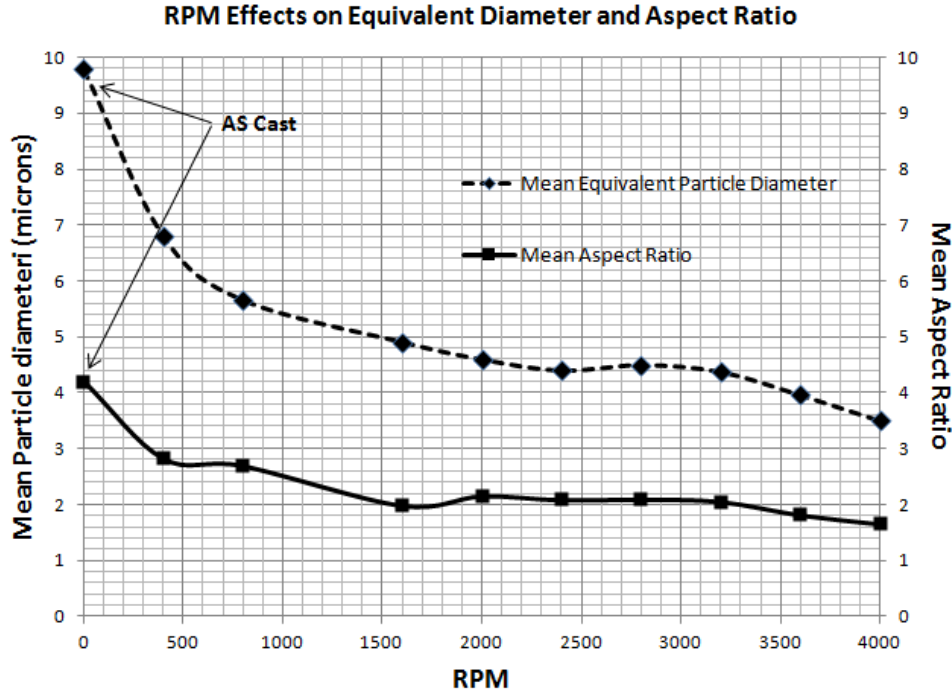
Figure 5.20 The effect of FSP RPM (using the threaded tool) on the mean equivalent diameter and mean aspect ratio for FSP AA356.

Figures 5.21 and 5.22 show the effect of RPM on the particle orientation and spacing distributions. The as-cast orientation distribution is strongly log-normal, however it tends more toward exponential with increasing RPM. This observation may not be overly important, since as the particles become increasingly equiaxed, they are less biased toward any orientation. While orientation is an important discriminating parameter for the as-cast or other acicular materials, it is less so in FSP materials.

In regard to spacing, little difference was seen in the 800 and 3200 RPM distribution curves. The best-fitt curves followed generalized extreme value distributions. A larger number of particles can be noted as compared to the as-cast material. Also, the plot shows that FSP has widened the spread of distance values, indicating particles have moved into previously unoccupied regions. Recall that, the spacing measure is a Euclidean distance from a particle to every other particle in the cropped sector. While this parameter is informative when comparing the image sectors, it does not provide a great deal of additional information when measuring the entire image.
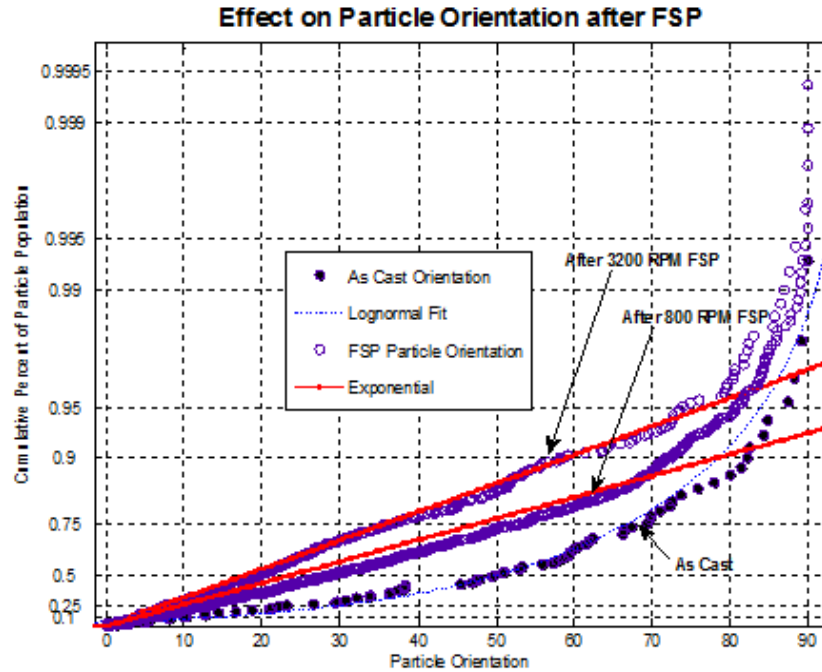
Figure 5.21 Particle orientation distributions for AA356 as-cast and after FSP using a threaded tool at 800 and 3200 RPM. Also shown are the highest probability distribution fits.
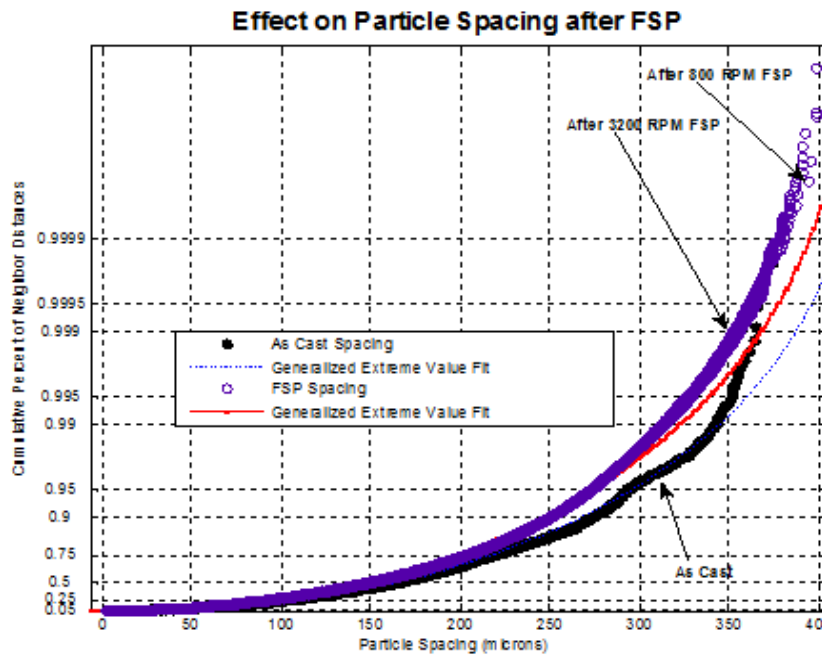
Figure 5.22 Particle spacing distributions for AA356 as-cast and after FSP using a threaded tool at 800 and 3200 RPM. Also shown are the highest probability distribution fits.

148

8. Hot Rolling and FSP Comparison

As a final exercise, AA356 was hot rolled at 300°C and 400°C, sectioned in the plane defined the rolling direction and its normal (i.e., the lengthwise edge parallel to the rolling direction). This analysis was conducted using optical microscopy. One purpose was to view the homogeneity differences between FSP and hot rolling, but the other is to show that optical RGB images can also be filtered and accurately measured. Note that, resolution limitations at higher optical magnifications will limit the capability of this methodology. Figure 5.23 shows an image comparison of a 300°C hot rolled AA356 sample taken in the plane perpendicular to the rolling direction and a 4000 RPM AA356 FSP sample taken in the center of the SZ. Figure 5.24 shows the plotted H_s comparison for the rolled, FSP, and as-cast material. To ensure both a similar number of features in the two samples and adequate pixel resolution, the H_s measurement for the FSP sample was taken over an area 5 times smaller than the hot-rolled sample. The results indicate that hot rolling achieves better homogeneity than the as-cast material, but the hot rolled material is approximately 30% less homogeneous than the 4000 RPM FSP AA356. The images in Figure 5.23 and the measurement data of Figures 5.24 and 5.25 both show that FSP is considerably better than hot-rolling at creating reduction and uniformity in the particle size distribution.

(a)　　　　　　　　　　**(b)**　　　　　　　　　　**(c)**
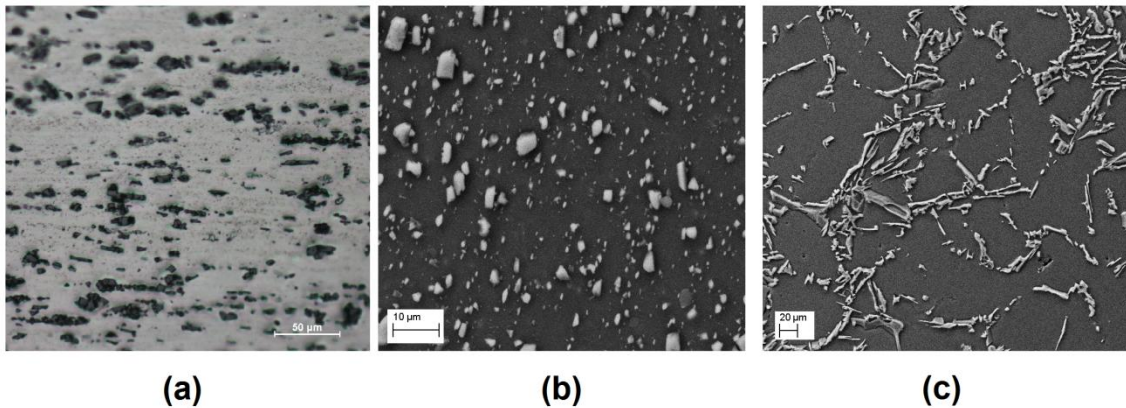
Figure 5.23 (a) RGB optical image of AA356 hot rolled at 300°C to a 10:1 reduction in the plane perpendicular to rolling direction, shown at 200X magnification (b) Zeiss Neon 40 secondary electron image of a 4000 RPM FSP AA356 in the center of the SZ shown at 1000X magnification (c) as-cast AA356 shown at 200X magnification.
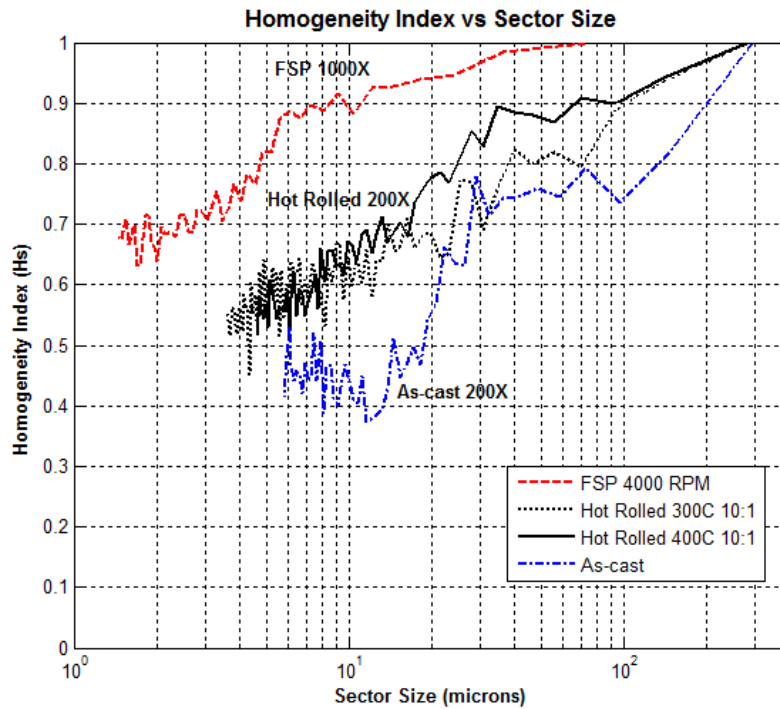
Figure 5.24 Homogeneity (H_s) data for FSP AA356 at 4000 RPM data 300°C 10:1 hot rolled AA356, 400°C 10:1 hot rolled AA356, and as-cast material. (Note that, the FSP measurement was taken over an area 5 times smaller than the hot-rolled sample.)
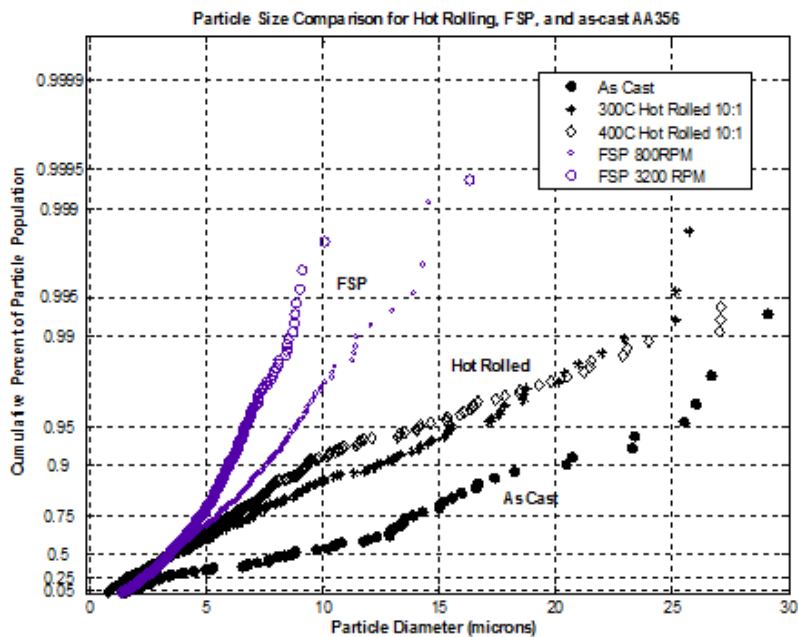
Figure 5.25 Particle equivalent diameter measurement for FSP AA356 at 400 RPM, 300°C 10:1 hot rolled AA356, 400°C 10:1 hot rolled AA356, and as-cast material.

150

9.   Extending the Method to Other Types of Materials

A multi-parameter, combined variance approach was shown to be effective at capturing homogeneity for a dispersion of discrete, hard particles in a contrasting matrix. As mentioned, the approach is flexible in that parameters can be added, removed, or weighted, depending on their relevance or importance. As it exists now, the methodology would be useful for measuring a number of similar materials containing discrete geometric objects, including MMC's, materials containing inclusions, fiber-oriented composites, or precipitate-hardened materials.

To extend the approach to other types of materials, the edge detection method requires that an object have a detectable boundary. Since detection of this boundary occurs by sensing an abrupt change in contrast, a sample of material must be prepared in such a way that the features of interest possess a contrasting edge. In an image, this edge boundary must be at least one pixel wide, but this can usually be accomplished through etching or electro-polishing. As an example, Figure 5.26 shows a notional structure containing three types of connected regions that have distinct boundaries.
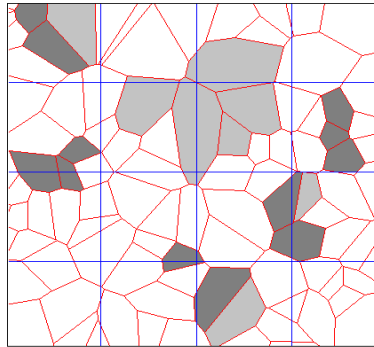
Figure 5.26 Notional structure containing connected regions of multiple types of materials.

So long as a region is distinguishable from adjoining regions, it can be isolated and measured by the same pixel counting techniques previously employed. The homogeneity parameter then need only be modified with additional parameter(s) to account for the variation in particle types occurring from sector to sector. Such a parameter might be the variation in the percentage of area fraction comprised by the three

151

types of materials. In a perfectly dispersed material, for instance, it should be expected that each material would comprise one third of the sector area. The variation from that standard could be measured and incorporated as an additional parameter.

E.   CONCLUSIONS

The conclusions of this section of the work may be summarized in bullet form:

- Using an edge detection approach, the homogeneity (H_s) of a microstructure having discrete dispersed hard particles can be precisely and consistently measured (at a given length scale) in two steps:

  1. Capturing, filtering, and segmenting the image into an N x N matrix of square sectors of equal area.

  2. Calculating the total variance of multiple normalized parameters (X_i) across the range of sectors. The total variance consists of the variance of each parameter along with the covariance of each parameter-parameter (X_i, X_{i+1}) relation.

- The accuracy of the homogeneity characterization will depend on the number of sites measured and the chosen sector size relative to the characteristic length scale of the microstructure. The characteristic length will generally be the particle diameter. The approach is flexible in that additional parameters may be added so long as they can be accurately measured.

- As the sector size approaches the characteristic length scale, the calculated homogeneity will decrease to a minimum value and then increase as the sector size becomes smaller than the characteristic length. Measurements for sector sizes below the minimum point are no longer meaningful. The homogeneity of two microstructures may be compared at the same length scale so long as the values are calculated at a valid sector size.

- In the case of AA356, FSP results in a microstructure which is up to 4 times more homogeneous, as calculated by this methodology.

- RPM during FSP has a significant effect on homogeneity. Calculated H_s values were seen to rise linearly with RPM. In this instance, tool geometry had a much smaller effect.

- Using quantitative methods, FSP was shown to be effective at improving the uniformity of particle size and aspect ratio distributions.

- Mean parameter values can be misleading in interpreting homogeneity. More relevant is the shape and uniformity of the parameter distribution. This information can also be accurately captured using edge detection approach.

VI. DIFFUSIVE AND GEOMETRIC MODELING OF REDISTRIBUTION IN FSP

A. PREFACE

In this chapter, the effects of advective mixing are simulated with a layered shearing model which repeatedly shears and rotates a representative volume element (RVE) of material. In this model, the RVE is comprised of discrete layers that glide over one another. These layers are modeled at a length scale much larger than the unit cell. As the RVE moves around the arc of the tool pin, the process repeats itself, with the layers shearing and gliding at a changing angle. The results of these simulations are measured and compared against actual FSP SZ microstructures using the methodology presented in Chapter V. Also, the drift velocity (from all potentials) is discussed and incorporated into a directionally biased diffusive-type model to investigate redistribution in a synthetic microstructure of spherical, nondeforming particles.

B. DESCRIPTION OF THE REPRESENTATIVE VOLUME ELEMENT SHEARING AND ROTATION MODEL

In previous chapters, FSP was shown to be highly effective for intermixing of constituents in the AA356 alloy. Deformation-assisted, high-temperature diffusive processes were found to be insufficient to account for the magnitude of particle motion necessary to achieve such levels of redistribution. At temperatures approaching the melting point of the matrix material, the hydrostatic pressure gradient appears to be large enough to transport particles only up to a single particle diameter, and then over a relatively long time frame (~1 to 10 seconds). Since FSP mixing occurs in a very short time, less than 0.1 seconds, either additional / steeper gradients are present or another primary transport mechanism exists. To determine the total diffusive transport gradient, the effect of all relevant gradient potentials must be considered.

Microstructural evidence from FSP samples showed evidence of discrete layers that are repeatedly stripped off at the tool's pin-material interface, as well as thinner layers that appear to slide over one another as the material is sheared (discussed in

Chapter IV). This idea is shown schematically in Figure 6.1. Velocity and strain gradients may develop as a result of the sticking condition at the pin / matrix interface, resulting in a localized monotonic shear for the volume of material in that region, schematically shown in Figure 6.2. Instead of bulk deformation, sliding sub-layers form as a result of the material's plasticity at high temperature and the strain gradient developed across the width of the extrusion layer.
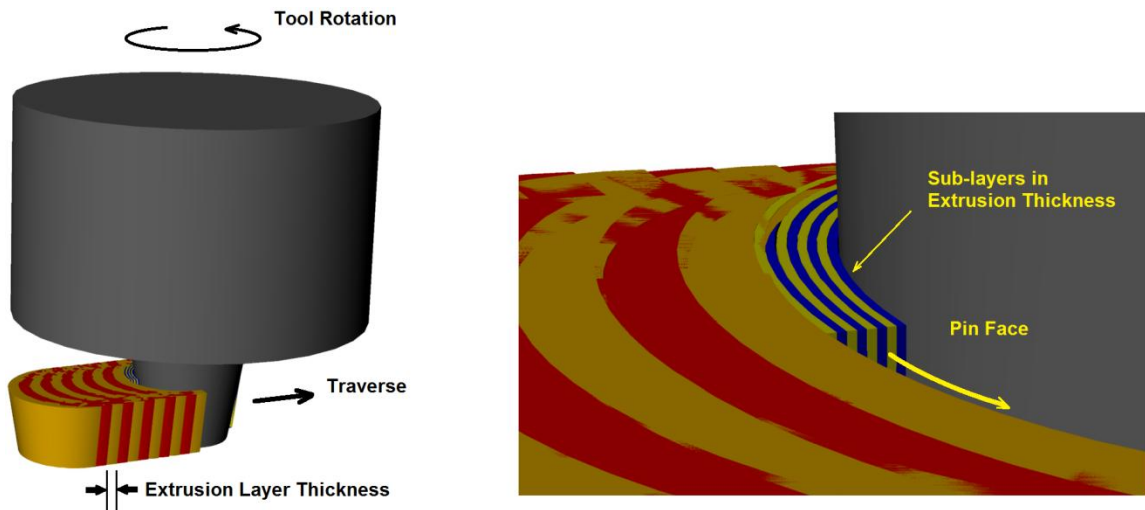
Figure 6.1 (a) Schematic of extrusion layers depositing at the rear of the pin and (b) a closer view of the extrusion layer consisting of sub-layers of notional thickness.
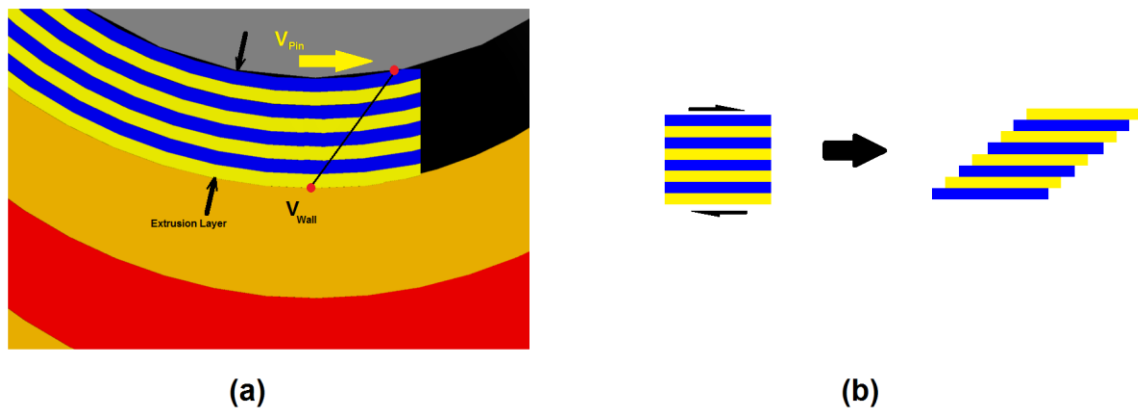
Figure 6.2 (a) Closer view of the extrusion layer at the pin face and (b) a volume of material experiencing a linear strain gradient at that location due to the velocity difference between the pin face and the wall of previously deposited material.

154

Monotonic shearing of a similar nature was seen in the earlier 400°C ECAP experiment, which produced thin, highly elongated bands of constituent particles. Geometrically, FSP differs from ECAP in that a rotation is involved. The majority of redistribution must occur during a single rotation around the pin, i.e., in the short time between the initial shearing and the deposition at the rear of the tool. It is more convenient to visualize this process in a discrete manner, as depicted in Figure 6.3. Consider a RVE of material that is sheared at some location. However, at the next discrete angular location, $\delta\theta$, the same volume of material is again subject to the pin's shearing action, but at a new orientation. The layers, in turn, are sheared across their initial boundaries. Such a process is very effective at intermixing material and can be best described as nondispersive mixing, previously discussed in Chapter II.

Figure 6.3 shows a schematic of a simple case where an RVE of layered material is initially sheared at the advancing side of a counter-clockwise rotating pin. In successive operations, the RVE is sheared repeatedly across the layers. Sub-layer stretching and thinning (i.e., dispersive-mixing), combined with repetitive shearing of the material at a continuously changing angle, may be instrumental in describing how a nondeforming second-phase particle (which may or may not have fractured depending on whether or not it's fracture strength has been exceeded) is redistributed in soft matrix that has undergone plastic deformation.

A generalized explanation of redistribution occurring during FSP will be proposed by showing the separate effects of particle diffusive motion (drift) and geometric shearing in the matrix, as illustrated by Figure 6.3 To confirm the minimal role of diffusive processes in redistribution, diffusive models will evaluate particle drift in a simulated pressure gradient using a synthetic microstructure of nonoverlapping spheres. Later, a simplified shearing modeled is developed by digitally imposing a repetitive strain gradient and a 90° rotation (i.e., $\delta\theta$ of 90°) across an RVE (a digitized micrograph of AA356 base material) having periodic boundary conditions. The resulting sheared RVE dispersions are then quantitatively compared to experimental FSP samples. Following that discussion, a geometric RVE shearing model will be proposed whereby the shearing angle, $\delta\theta$, can vary incrementally.
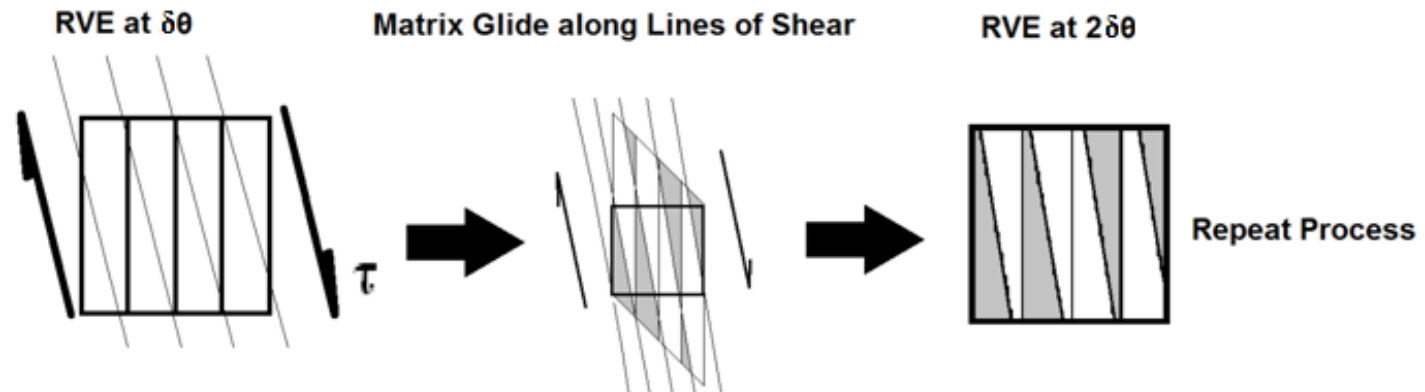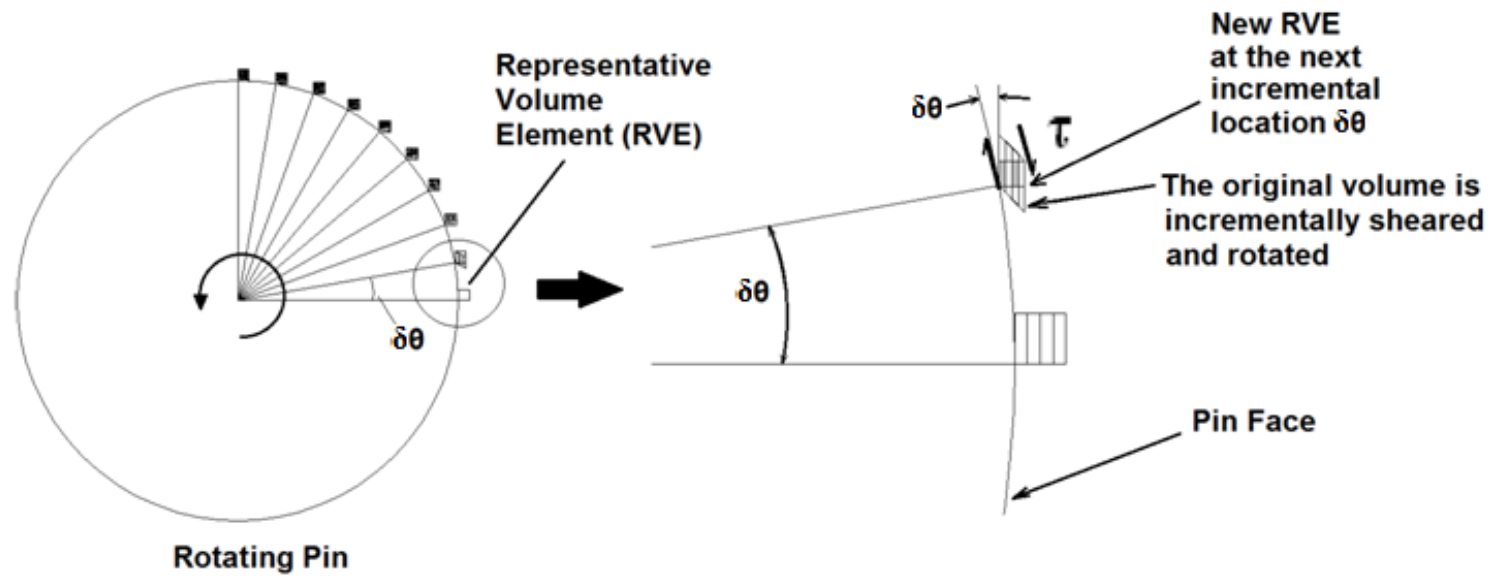
Figure 6.3 Schematic of an extrusion layer volume element with periodic boundary conditions at the pin-material interface experiencing a incremental rotation while subject to continuous shear.

C.   CALCULATION OF THE DRIVING POTENTIAL VELOCITIES

In this section, the magnitudes of relevant driving gradients will be calculated to determine the net effect of all the combined gradients on particle motion. The gradients considered are: 1) pressure gradients due to deformation and 2) centrifugal pressure gradients caused by the difference in density between the particle and matrix material. Electrical potential gradients are assumed negligible.   Chemical-Thermal Diffusivity gradients are ignored due the atomistic nature of lattice diffusion.   Pressure gradients forming due to pin rotation in a viscous material are also evaluated and discussed.

1.   Pressure

a.   Deformation-Induced Pressure Field

As calculated in Chapter III, a hydrostatic differential pressure ranging from 10 to 1000 MPa should only result in particle motion of 1 or 2 particle diameters during the time frame of a conventional deformation process such as ECAP or hot-rolling. In FSP, where the time frame is much shorter, the expected particle travel would be much lower. Even if extraordinarily high pressure gradients were present, the time during one revolution of the pin is on the order of 10^{-1} to 10^{-2} sec, thus particle / matrix relative motion should be negligible.

b.   Pressure Development Due to Pin Rotation

In a fluid with velocity U, a rotating cylinder generates a pressure differential as the fluid flows over its surface. The total lift pressure (L) integrated around the rotating cylinder is given by the Kutta-Joukowski Lift theorem [133] for a cylinder (Equations 6.1 and 6.2). The pressure for any point on the cylinder is given by Equation 6.3.

$$L = \rho U \Gamma$$

$$\Gamma = 2\pi r V$$

$$P(\theta) = P_{static} + \frac{1}{2}\rho \left[-2U sin(\theta) + \frac{\Gamma}{2\pi r} \right]^2$$

Here, L is total lift pressure across the cylinder, ρ is the matrix density, U represents the inlet velocity of the flow (or traversing rate), Γ is the vortex strength, V is the velocity of a point on the rotating cylinder, r is the radius of the pin, P(θ) is the pressure on the cylinder as a function of angle θ, and P_{static} is the static pressure in the fluid.

Although this formulation is for the potential flow of an inviscid fluid and not reflective of possible rotationally induced pressures during FSP, the calculation provides insight as to the expected magnitude of pressure to be expected in the fluid flow case. By inserting appropriate values (radius of the pin, density of molten aluminum, RPM, and traversing rate), the maximum pressure difference on the pin face at any point may be estimated. The values range from 40 to 400 Pa above the far field pressure, depending on RPM. A simulation of a 1200 RPM rotating cylinder in molten Al was conducted using Lattice Boltzman methods [134]. The results were comparable to the inviscid solution for surface pressure. The point being made is that the pin is probably too small to generate significant changes in absolute pressure in a molten aluminum matrix, even at very high RPM. Aluminum has relatively low molten viscosity and thus probably does not accurately represent FSP conditions. Certainly the required pressure changes (100 MPa or greater) for inducing measureable particle motion would not be expected from pin-induced flow effects in a molten material. In a semi-solid form, Al has a measured dynamic viscosity of 0.127 m^2/sec [71], compared to 5×10^{-7} m^2/sec [135]

when molten. This difference may result in a more significant pressure field development, but semi-solid flow pressures are extremely difficult to measure or model rigorously.
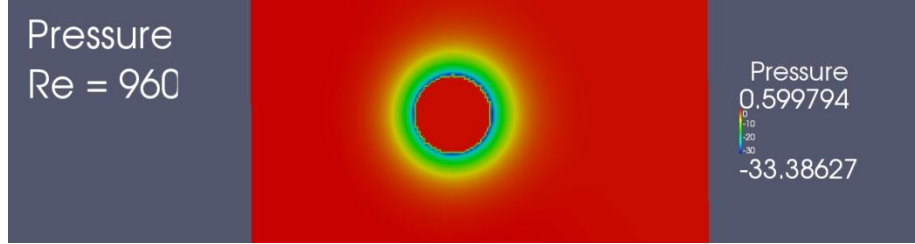
Figure 6.4 Lattice Boltzman simulation of the surface pressure gradient (Pa) on a cylinder rotating at 1200 RPM in a molten aluminum flow passing at 0.00127 m/sec (3 IPM). The surface shows a total gradient of approximately 34 Pa. From [134].

If the semi-solid Al matrix were to be treated as a Stokes flow, using the semi-solid dynamic viscosity data from [71], the upper bound on a particle's travel, given by Equation 6.4 [136], can be computed based on some initial particle velocity. Given that the fastest moving point in the flow is at the face of the rotating pin, that velocity could be used as an initial estimate for velocity. A 3 mm diameter pin rotating at 2000 RPM has a face velocity of 0.314 m/sec. When these values are applied to a 1 µm Si particle in an aluminum matrix at 0.9 $T_{Melt,}$ a travel distance of .0065 particle diameters results, supporting the previous findings of Chapter III.

$$D_{Travel} = \frac{U \rho_{part} \left(d_{part} \right)^2}{36 \mu}$$

Equation 6.4

Here, DTravel is the maximum horizontal distance a particle of diameter d_{part}, density ρ_{part}, and initial velocity U, should travel through a static fluid of dynamic viscosity μ, under Stokes flow conditions.

2.   Chemical / Thermal

The shearing deformation process in FSP is one in which whole particles are transported bodily.   Since lattice diffusivity is an atomistic jump process, it is not physically valid to consider this type of transport potential.   Consequently, a chemical / thermal gradient will be ignored.

3.   Centrifugal

Due to the density difference between the particle and matrix, a particle may be transported through the matrix via centrifugal force.   The force generated on a particle in a rotating field can be calculated via Equation 6.4.

$$\Delta P = \frac{\left[(\rho_{Si} - \rho_{Al})(\frac{4}{3}\pi r_{Part}{}^3)\right]\omega^2 r_{pin}}{\pi r_{Part}{}^2} \qquad \text{Equation 6.4}$$

Here, ΔP is the differential pressure acting on the particle's cross section, ρ is material's density, r_{Part} is the particle radius, ω is the angular velocity in radians/sec, and r_{Pin} is the pin radius.

Given that the density difference between Al and Si is small (approximately 28 kg/m^3), the net effect of centrifugal separation is expected to be small. Figure 6.5 shows the predicted centrifugal pressure on a 1 µm diameter Si particle in an Al matrix at 0.9 T_{Melt}.   According to the approach presented in Chapter III, the centrifugal pressures developed are insufficient to account for any measurable particle travel.
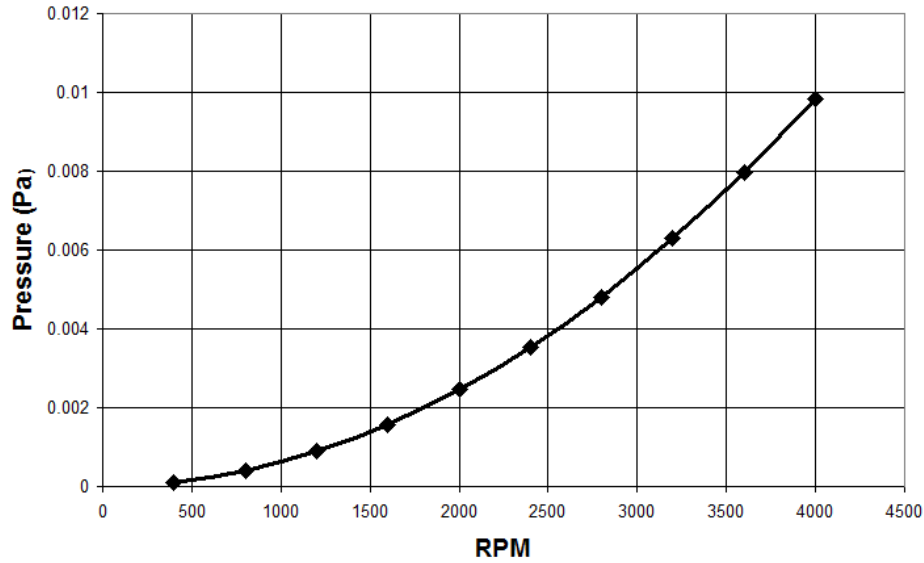
Figure 6.5 Plot of predicted centrifugal pressure developed across a 1 μm diameter Si particle in an Al matrix at 0.9 $T_{Melt,}$ rotating around a 3 mm diameter pin.

4. Total Drift Velocity

The total drift velocity for a particle may be found by adding all of the calculated velocities. In this case, the only additional driving potential (centrifugal) is negligible. As shown in Chapter III, a particle might be expected to move approximately 1 diameter/sec during deformation. Again, for the time frame of FSP, this velocity is insufficient to account for the level of redistribution often noted in the SZ. Consequently, it can be concluded that diffusive processes are playing a negligible role in particle dispersion during FSP, indicating that the role of advective processes should be more closely examined. First, however, a simulation of diffusive particle motion with a defined drift velocity will show the visual effects on a synthetic microstructure.

D. NON-OVERLAPPING, NON-DEFORMING PARTICLE DRIFT MODEL

The section briefly examines the qualitative effects on homogeneity that might be expected as a result of a diffusive mechanism. Nonoverlapping spherical particles are allowed to migrate for a defined period of time, with a prescribed drift velocity. The particle drift velocity may be seen as an analog to the strength of the driving gradient. A steeper gradient should produce higher particle velocities and the faster homogenization.

161

The final degree of homogeneity will also depend on the morphology of the original structure, i.e., in clustered structures with large, particle-depleted regions, homogenization will be less complete since the particles must travel greater distances. As previously noted in Al-7% Si, particles would have to travel over 30 particle diameters to reach the centers of unpopulated regions. Here, to amplify the effects of the visualization, the drift velocities are set at 5 times the value determined in the previous section (i.e., 5 diameters/sec). The MATLAB code developed for this simulation can be found in Appendix H.

Figure 6.6(a) shows a banded structure of clustered particles with a 7% area fraction. The particles are 1/30 the total width of the overall region, which is approximately the size of particles seen in the extrusion layers in FSP. Unlike random diffusion, a pressure gradient acting on a microstructure will have a directional bias, which could account for improved homogeneity. Accordingly, a directionally biased diffusive model was used to imitate the effects of pressure field. Figure 6.6 shows the results of a 5-second simulation, during which the particles were 25%, 50%, or 100% more likely to move in a direction perpendicular to the band's centerline. The results showed that a directed pressure field can better homogenize the structure, but a significant length of time is required. Figure 6.7 takes into account the short time frame of FSP, allowing the same simulation to run for 0.15 sec and .015 sec. For FSP, the time frame of deformation is one pin rotation (0.15 sec at 400 RPM or 0.015 sec at 4000 RPM).

The results in Figure 6.7 show that, even with very high particle velocities, diffusive processes are unlikely to play a large role in such a short time frame, since significant particle motion cannot be achieved. Furthermore, the simulations of Chapter III showed that, as the matrix material becomes softer at higher temperature, it is increasingly difficult to develop and sustain a gradient. Homogenization in FSP is more likely the result of an advective process in which the matrix material has been segmented as the result of shear.
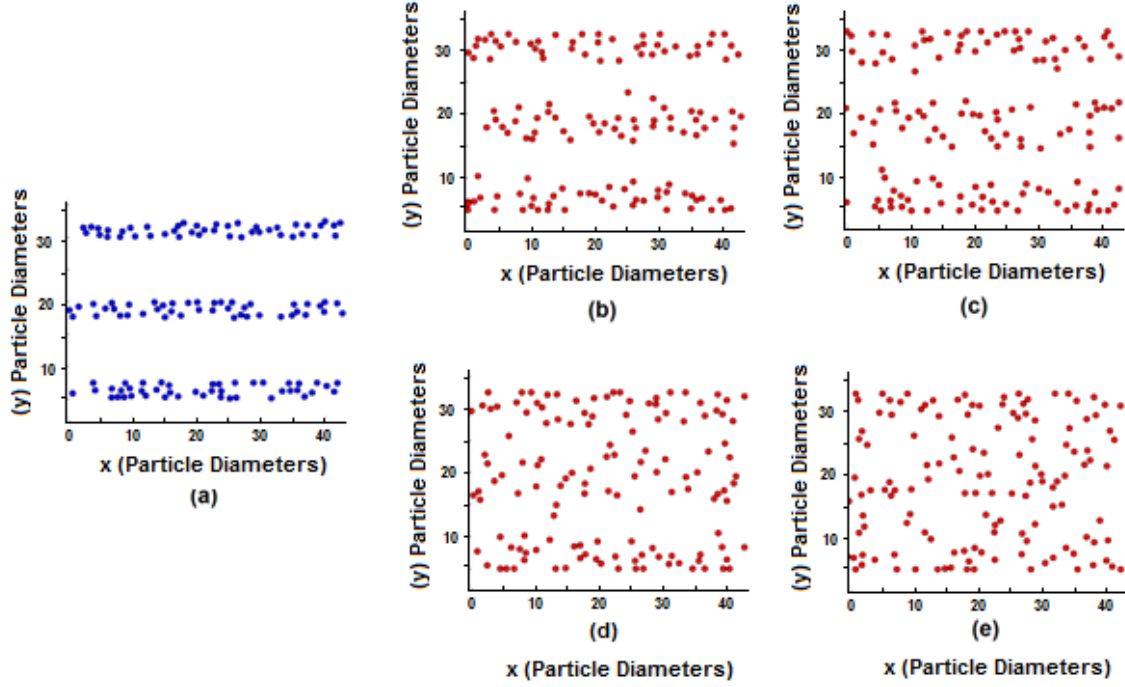
Figure 6.6 (a) Original banded structure of 132 spherical, nondeforming particle where each particle can migrate 5.0 diameters/sec and is biased to move in a direction perpendicular from the center of the band. Shown is the structure, after 5 seconds (b) no bias (c) 25% bias (d) 50% bias, and (e) 100% bias.
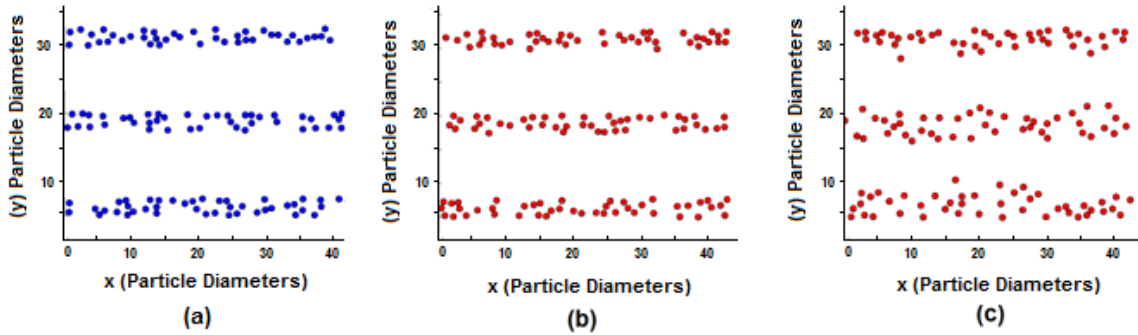
Figure 6.7 (a) The original banded structure of 132 spherical, nondeforming particles where each particle migrates at 5.0 diameters/sec. Particles are biased by 100% to move in a direction perpendicular from band centerline. Shown is the structure after (b) .015 sec (c) 0.15 sec.

E. SIMULATION OF FSP USING DIGITIZED MICROSTRUCTURE IMAGES

In this section, digitized binary images of as-cast Al-7% Si and AA356 microstructures are treated as representative volume elements (RVE) of base material that are subjected to FSP-like shearing conditions. When a cropped square image is digitized, individual black and white pixels are represented discretely as either 1 or 0 elements in a square matrix [137]. By shifting pixels via a series of matrix row operations, the image can be artificially sheared to a specified strain. The RVE is divided into discrete layers and subsequently sheared along those layers. As the volume is sheared, an image rotation can be introduced, as well as nonlinearity in the strain gradient. The purpose is to investigate the impact of a strain gradient, rotation, and shearing layer thickness on the material's transition to a more homogeneous state. Also, by comparing artificially strained images, an estimate of SZ strain can be made through comparisons with actual SZ microstructures. The MATLAB code developed for this process can be found in Appendix H.

1. Monotonically Strained Material

To demonstrate this method, an example of the strain path through Route A during ECAP is presented. A secondary electron image digitized from the Al-7% Si alloy is shear in Figure 6.8(a) and the corresponding digitized image is shown in Figure 6.8(b). This microstructure was sheared four times in succession, with a strain of 1.0 per shearing operation. This simulation mimics the strain path of route A in ECAP. The gradient in displacement is linear across the microstructure. Figure 6.9 shows the microstructure after each shearing operation.
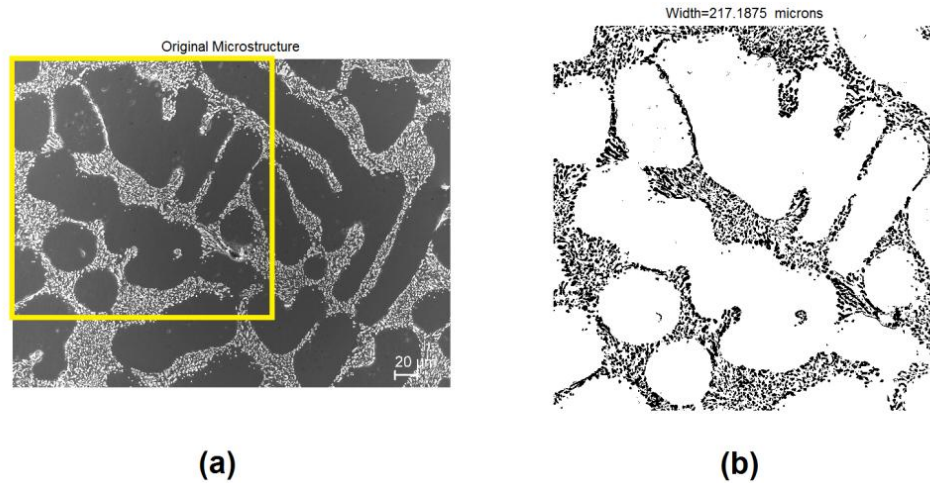
Figure 6.8 (a) Original secondary electron image of as-cast Al-7% Si microstructure (b) cropped 1200 x 1200 pixel digitized image of the Al-7% Si microstructure.
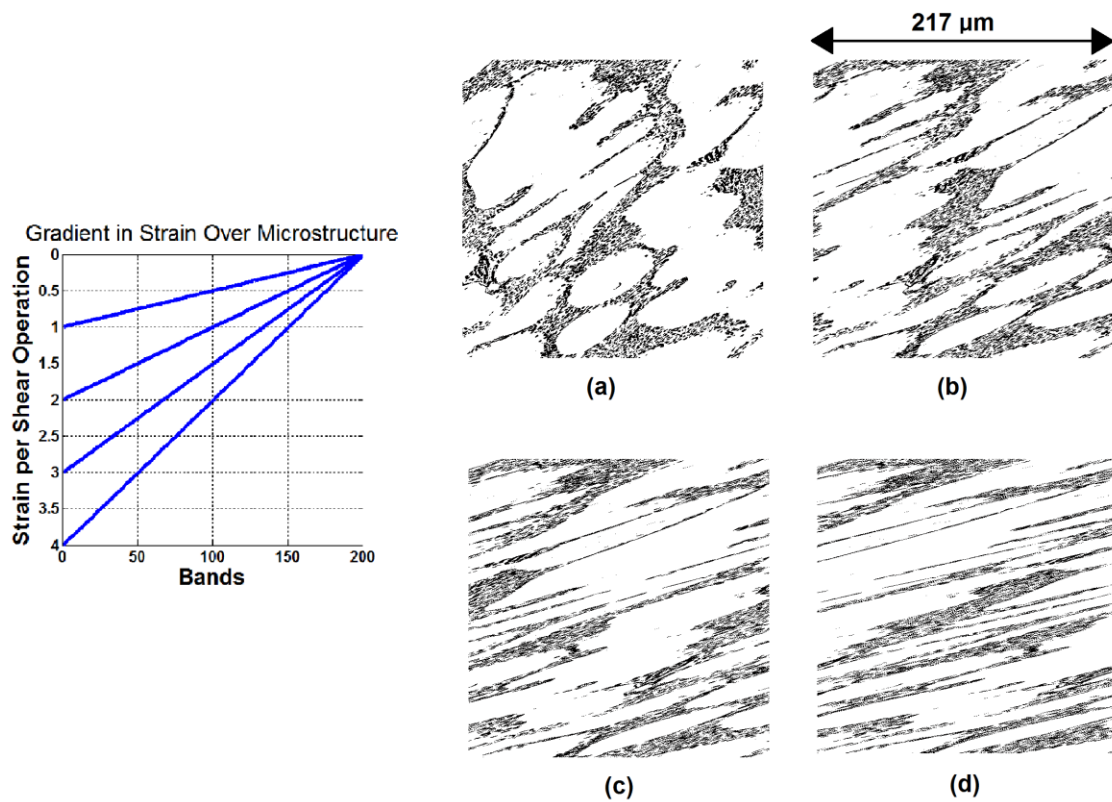
Figure 6.9 Al-7% Si digitized image after a shear strain of (a) 1 (b) 2 (c) 3 (d) 4. In each case, the strain gradient is linear across the microstructure.

Figure 6.10 shows the theoretical thickness reduction for a body of notional starting thickness when subjected to a monotonic shear. The original primary regions in Figure 6.9 are seen to be approximately 100 to 150 microns thick. After very large strains, the thickness reduction obtained through digitized shearing is in good agreement with Figure 6.10. The image in figure 6.8(b) was further subjected to strains of 10, 40, and 70 and the results are shown Figure 6.11. Here, it can be seen that at extraordinarily high strains, a monotonic shear with a linear strain gradient still results in a striated or banded structure. While the final structure may more homogeneous than the as-cast material, it appears distinctly different from a typical FSP SZ.
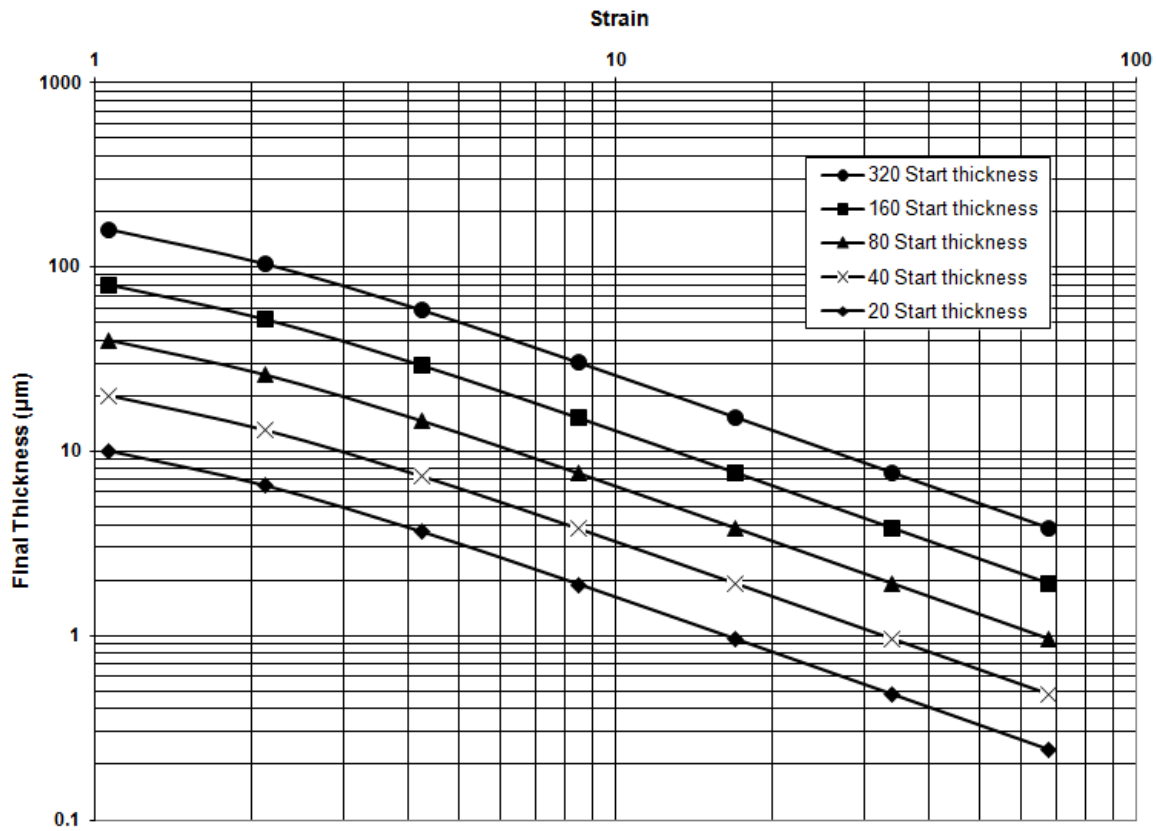
Figure 6.10 Log-log plot of the expected final thickness of a body after a monotonic shear strain. Shown are the starting thicknesses for a 320 μm, 160μm, 80 μm, 40 μm, and 20 μm body.

(a)   (b)   (c)
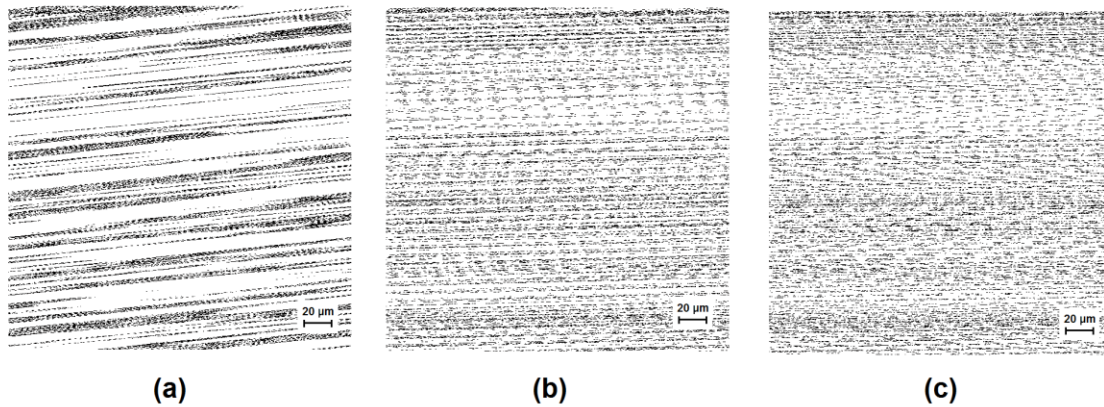
Figure 6.11 Monotonically sheared Al-7% Si at a strain of (a) 10 (b) 40 (c) 70. In each case, the strain gradient is linear across the microstructure.

2.   Nonlinear Strain Gradient

To visualize the effects of a nonlinear gradient in the SZ, a nonlinear strain profile was imposed on an AA356 microstructure image. Figures 6.12 and 6.13 show the contrasting effects of the linear and nonlinear gradients.

256 μm

(a)   (b)   (c)
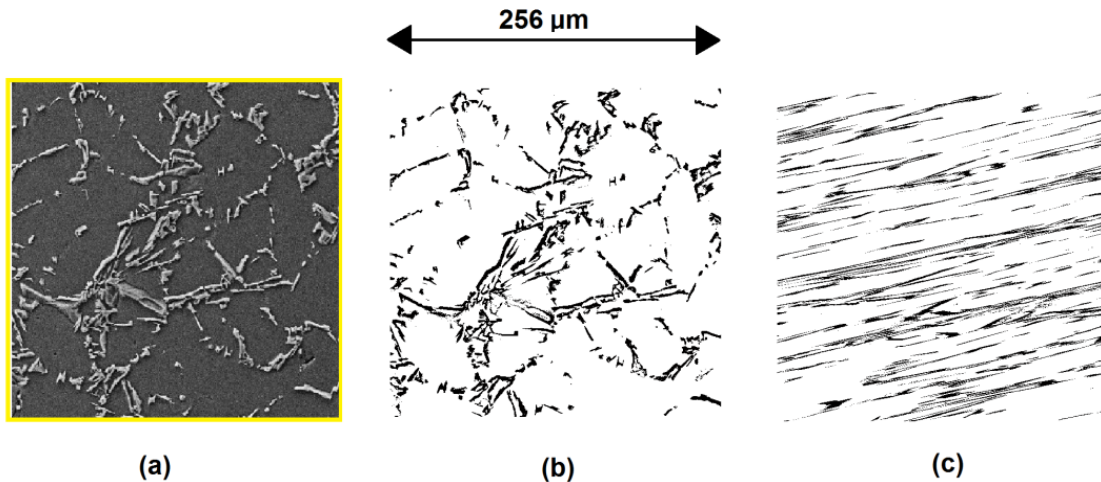
Figure 6.12 (a) Secondary electron image of as-cast AA356 (b) binary image of as-cast (c) binary image of AA-356 digitally sheared in a linear, monotonic strain gradient to a strain of 4.
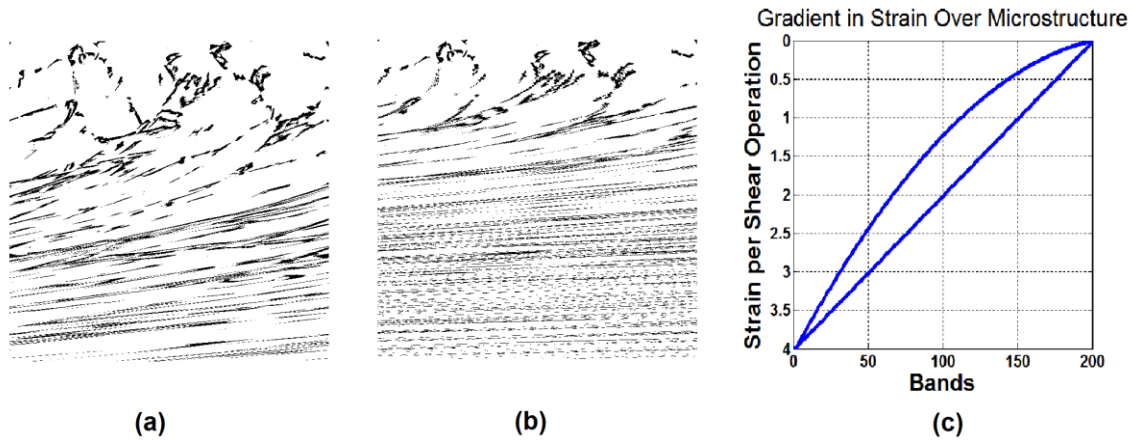
Figure 6.13 (a) Binary image of as-cast digitally sheared with a nonlinear strain gradient across the microstructure for (a) one shearing operation (b) four consecutive shearing operations. (A maximum shear strain of 4 per shear is experienced at the bottom of the structure.) (c) Plot of linear and non-linear strain profiles across the microstructure during one shearing operation.

The nonlinear strain gradient does not significantly improve homogeneity; however, the resulting image accurately reflects the structure of material seen in the TMAZ. If the strain in the lower portion were to continue to higher magnitudes, the structure would continue to be monotonically sheared, again resulting in a striated or banded pattern. This finding indicates that, by itself, a gradient in monotonic shear should not uniformly homogenize the structure.

3. Effects of Strip Thickness

Since the digital shearing is executed by shifting rows of matrix values, the degree of observable homogenization will be affected by the thickness of the discrete layers that are shifted. The minimum thickness layer which can be shifted is 1 pixel, which would approximate a continuous deforming body, shown in Figure 6.14. By choosing thicker layers, the effect of layer thickness on a nondispersive mixing may be observed. Since the sliding layers will shear particle images at the sliding boundary, this methodology will lead to maximum particle sizes on the order of the layer thickness.

168

Figure 6.14 (a) An notional particle shown as a matrix of binary elements and its corresponding image (b) the deformed matrix and image after shearing by row shifts using a 1 pixel layer thickness.
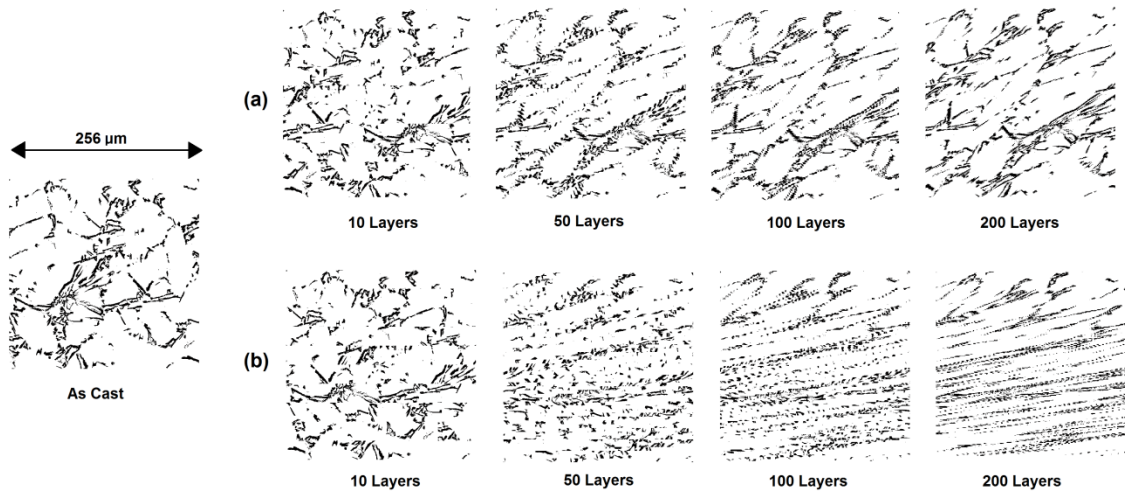
Figure 6.15 (a) Digitally sheared image with a linear gradient using various strip thicknesses using a (a) linear strain gradient with a shear strain of 1 (b) nonlinear strain gradient with a shear strain of 4.

Figure 6.15 shows the effect of increasing the number of shearing layers within the volume element and illustrates two ideas in regard to FSP. First, sufficiently thin layers are required to capture the behavior of a continuous deforming body. It is important to note however, microscopic evidence shown in Chapter IV showed that

169

material subjected to FSP does not necessarily remain continuous during travel around the pin. Secondly, if the material ahead of the pin is being sheared in thick strips (~25 microns or larger), the second-phase material is simply re-arranged into an order not unlike the original microstructure.

If the diffusive mechanism is not important, constituent particle transport must be largely a result of displacement of broken particles with the matrix material. In Chapter IV, particles were shown to fracture far ahead of the tool pin, as well as at the point of initial shear when the particle first encounters the pin. The pieces of an already sheared particle, however are not displaced and separated until the matrix material carrying them is moved, i.e., by an advective process. Figure 6.16 shows how a particle can be fractured in place, well ahead of the tool due to the matrix deformation
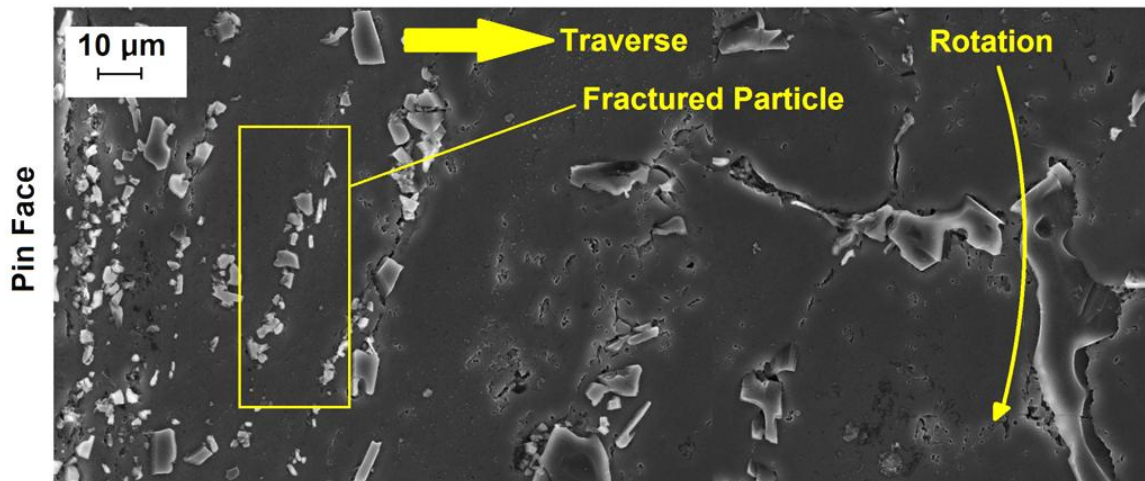
Figure 6.16 Secondary electron image of the plan view plane on the front side of the tool for smooth-pin FSP at 400 RPM. The image shows an acicular particle just entering the SZ which has fractured but the fragments have not yet separated.

Aside from a diffusive process, a matrix advection mechanism is the only means for particle segments to gain separation. If two adjacent particle pieces move apart in this manner, it is necessary to conclude that the pieces are traveling in volumes of matrix material that are moving with different velocities and / or direction, and that a volume has a similar characteristic dimension as the particle fragment it contains. This idea is

170

illustrated schematically in Figure 6.17, where a large, previously broken Si particle in the AA356 base material is shown with an overlay of notional layers that are moving at different horizontal velocities. This idea also suggests that that the final particle dimensions and layer thickness may be related. Figure 6.17 also shows that, without a means to travel in varying directions, the particle pieces will remain generally aligned resulting in the striated structures previously shown. Therefore, it can be reasoned that directional variations in particle travel are introduced by the rotation of the pin.
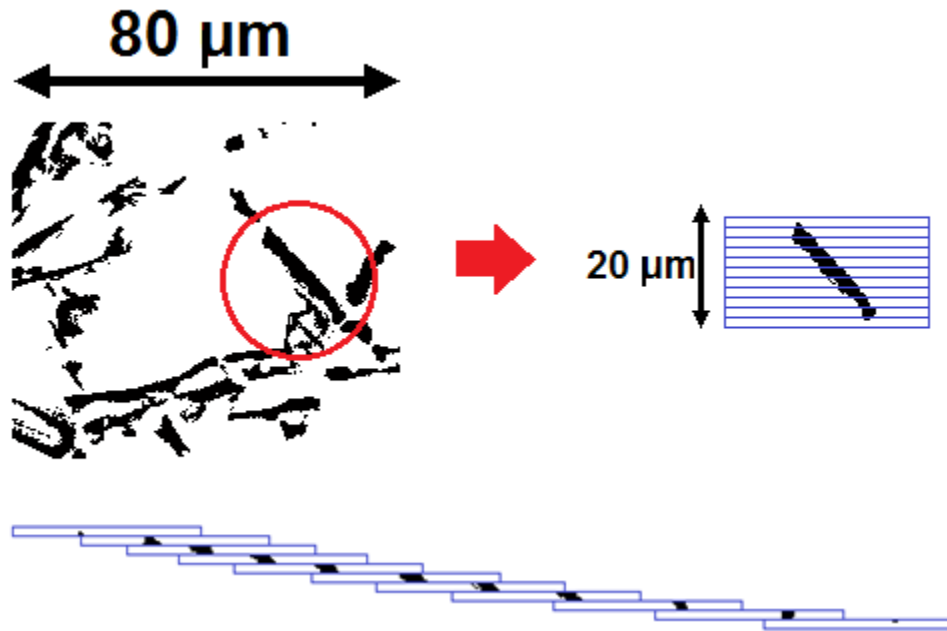
Figure 6.17 (a) Schematic of the layered advective separation mechanism for a Si particle within the Al matrix.

4. Monotonic Shearing with Rotation

A rotation was introduced between consecutive shearing operations to assess the effect on the as-cast AA356 microstructure. Because of the rotation, opposite sides on the RVE are strained in each consecutive shearing operation. The simulation was conducted for a variety of layer thicknesses, using both linear and nonlinear strain gradients.

171

a.   *Linear Strain Gradient*

Figure 6.18 shows a volume element of AA356 with periodic boundaries which is sheared in 4 discrete operations (each time with a shear strain of 1), but it is rotated 90$^\text{o}$ in between shearing operations. The figure implies that volume element is moving around a tool pin as it rotates. The result is a visibly more homogeneous structure as compared to the microstructure when sheared monotonically to the same strain.

Figure 6.19 shows the qualitative results obtain by repeatedly shearing and rotating the AA356 RVE with the linear strain gradient. The result in Figure 6.19 suggests that to obtain FSP-like structures in one pin rotation, either a larger strain is required over 90$^\text{o}$ or the material is sheared more frequently than at 90$^\text{o}$ intervals. The simulation showed that smaller particle sizes (i.e., smaller shearing layer widths) require a higher level of cumulative strain for the particle dispersion to appear uniform. For the 5 μm particle size, a visibly homogeneous structure develops at a cumulative shear strain of 8, versus a cumulative shear strain of 12 for the 2 μm particle size. A higher cumulative strain can be achieved through either a higher strain per shear between rotations or more shearing operations. More importantly, the striations that remain visible in the monotonically sheared structures dissipate rapidly when a rotation is introduced.
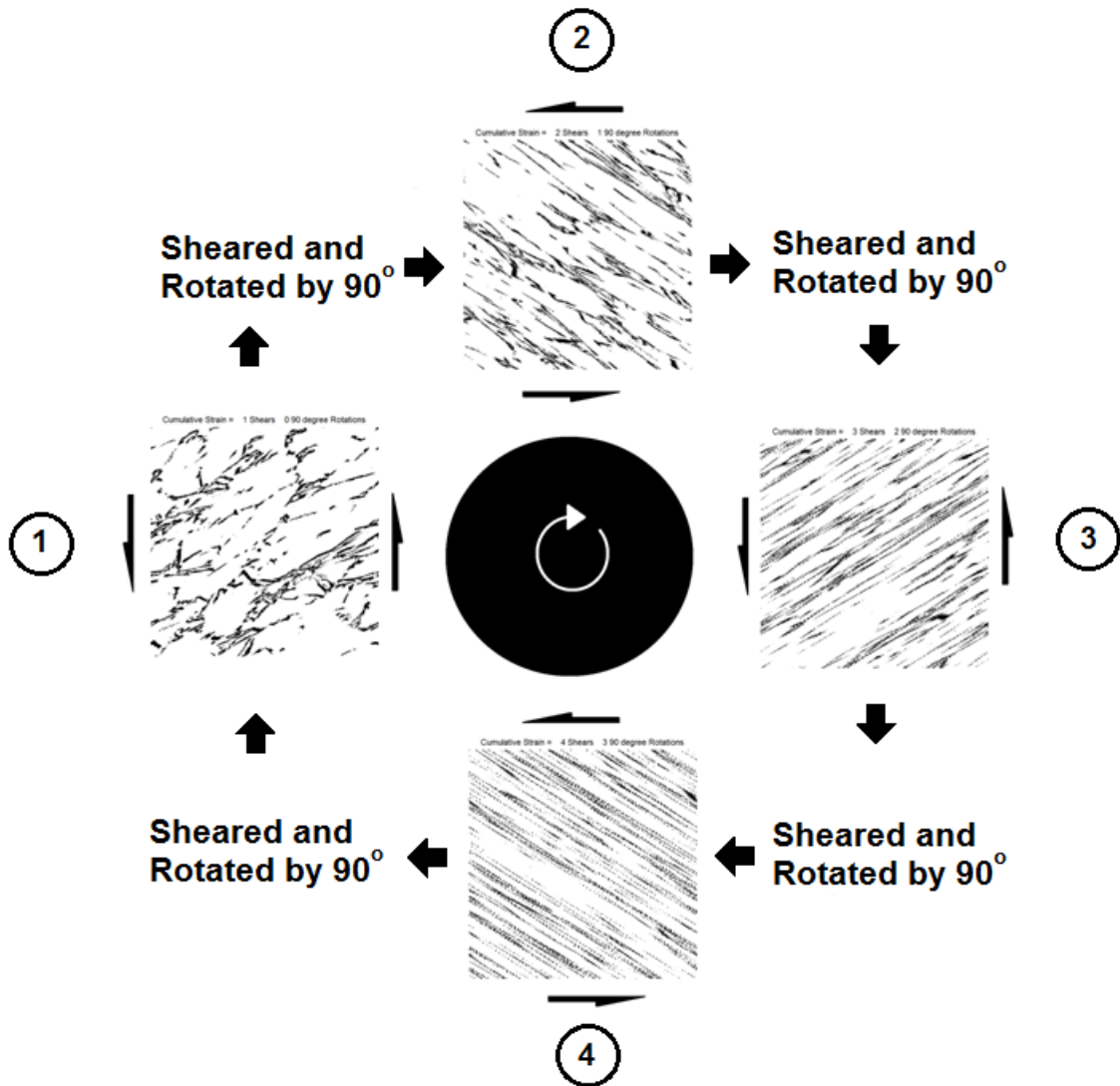
Figure 6.18 (a) Schematic of an AA356 RVE being sheared and rotated around a pin with a shear strain of 1 per shearing operation.

Maximum Cumulative Strain in a Linear Strain Gradient after 4 Shearing Operations (with rotation)
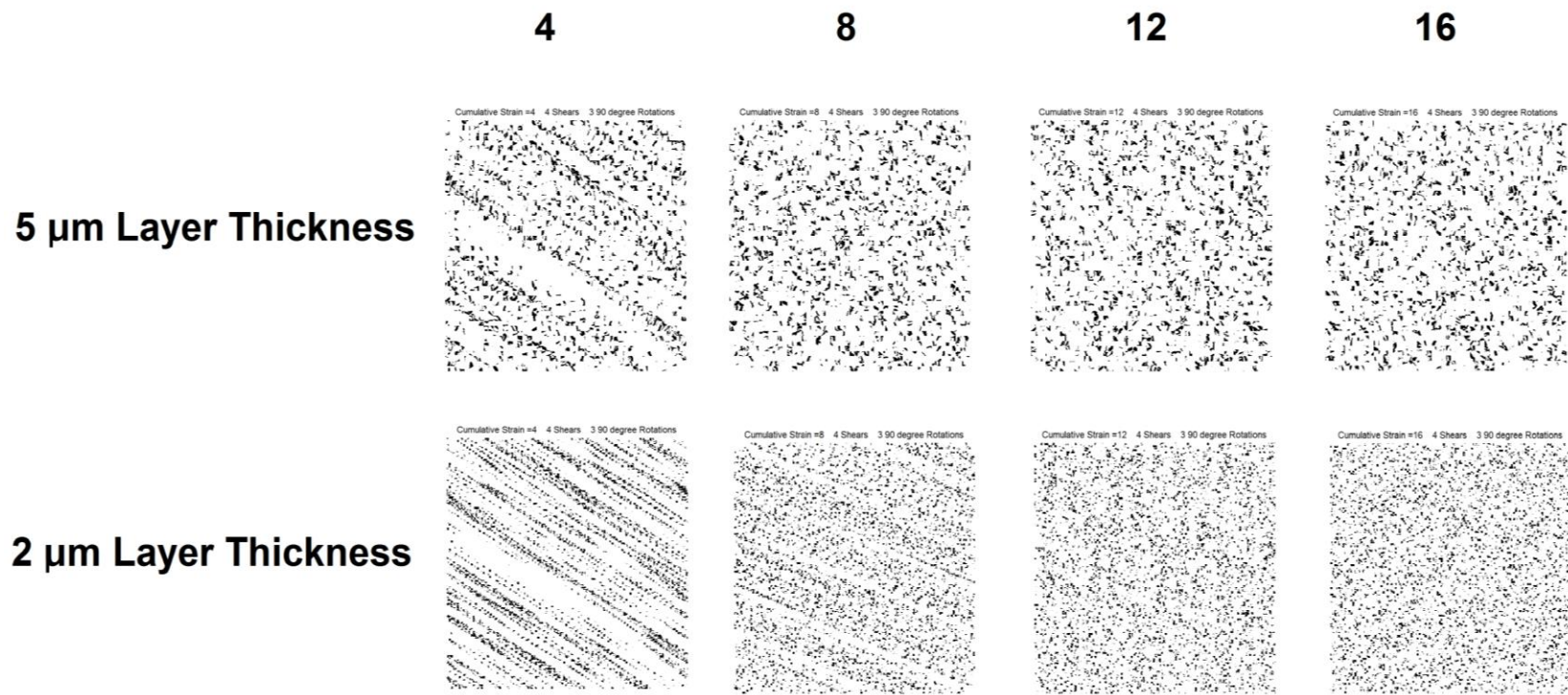
Figure 6.19 Result from the shearing and rotation of an AA356 RVE around a pin after 4 shears and 3 rotations. Shown are results after shearing with a shear strain of 1, 2, 3, and 4 per shearing operation. The simulation used 2 μm and 5μm thicknesses and a linear strain gradient.

b.   *Nonlinear Strain Gradient*

A nonlinear strain gradient, shown in Figure 6.20, was imposed on the same AA356 microstructure. The microstructure was sheared multiple times using 2 μm and 5 μm layer thickness and an interim 90° rotation. The shearing continued until strain levels were obtained equivalent to those in Figure 6.18. Results for the simulation are shown in Figure 6.21. As compared to a linear strain gradient, the nonlinear gradient results in slightly decreased homogeneity and continued striation in the regions of lower shear strain.
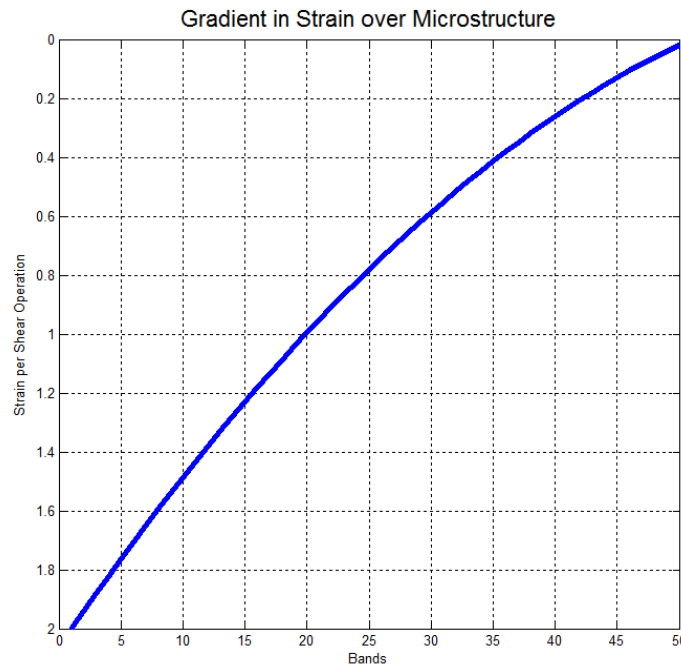
Figure 6.20 The nonlinear strain gradient imposed on the AA356 microstructure during the shear and rotation simulation.

Maximum Equivalent Strain in a Non-linear Strain Gradient after Multiple Shearing Operations (with Rotation)
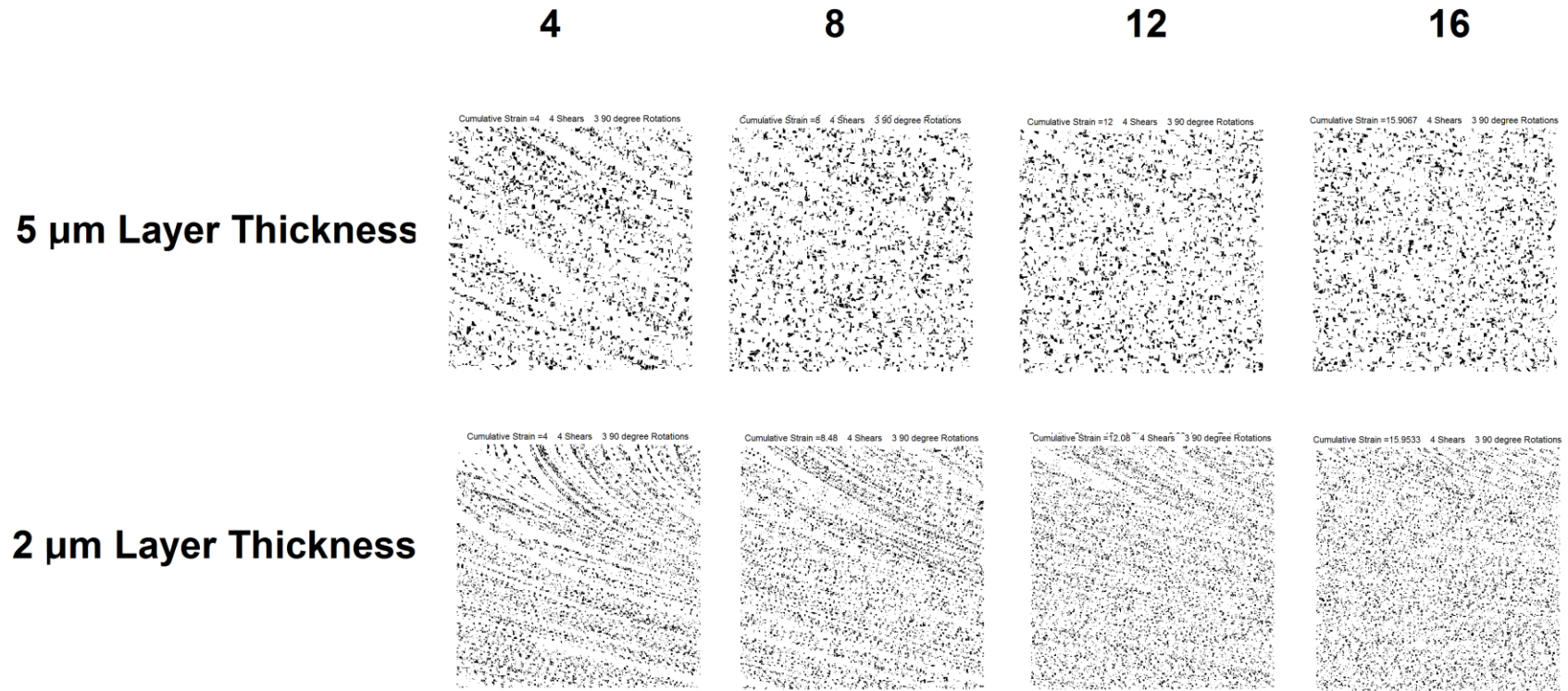
Figure 6.21 Result from the shearing and rotation of an AA356 RVE around a pin after 4 shears and 3 rotations. Shown are results after shearing with a shear strain of 1, 2, 3, and 4 per shearing operation. The simulation used 2 μm and 5μm thicknesses and a nonlinear strain gradient.

F.   MORPHOLOGICAL AND HOMOGENEITY COMPARISON

The maximum particle sizes were measured for the 800 RPM and 3200 RPM threaded tool FSP samples taken in the geometric center of the SZ. This measurement was used to select the layer width with which to simulate the layered shear of a binary image of the as-cast material. The selected layer widths were 10 μm and 15 μm for the 800 and 3200 RPM samples, respectively. Using a linear strain gradient and a 90° rotation, visible mixing was mostly complete after 8 shearing operations (using a shear strain of 1 per shear) and 7 interim rotations. Both simulated samples were then qualitatively and quantitatively compared to the experimentally obtained FSP SZ samples.

1.   Qualitative Comparison

Figure 6.22 shows a comparison of the FSP SZ samples and the final synthetically-sheared microstructures after the shearing / rotation operations. The samples are 256 μm x 256 μm (600 pixels x 600 pixels) and are shown at 200X magnification. The synthetic and FSP samples were remarkably similar in both cases, although the artificial shearing under-predicted the number of particles by approximately 10%. This variation could easily be the result of differences in the initial morphology in the original base material.

The similarity in the two samples was an indication that the proposed shearing and rotation mechanism may be an appropriate geometric model. Particle count, shape, and spacing anomalies appeared to be accurately captured. To confirm the consistency between the synthetic and FSP samples, a quantitative analysis was carried out using the methodologies developed in Chapter V.
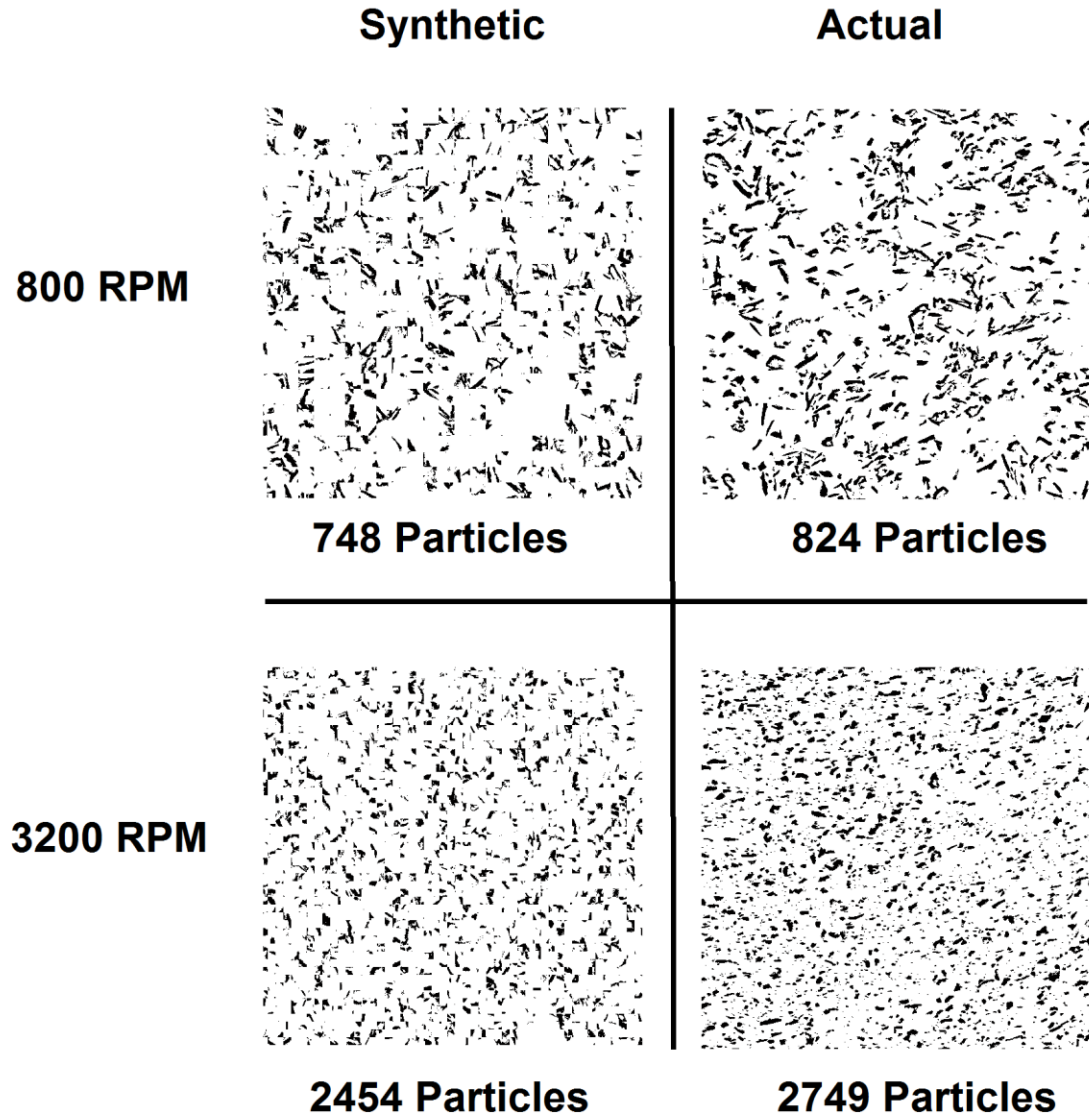
Figure 6.22 Comparison of synthetic microstructures (generated using shear layer thicknesses corresponding to expected particle size) and actual FSP microstructures at 800 and 3200 RPM.

2.   Morphological Comparisons

Particle size, aspect ratio, orientation, and spacing characteristics were measured for both the synthetic and FSP samples, shown previously in Figure 6.29. The results of the analysis are displayed in Figures 6.23 through 6.26. The measured data for the two sets of samples was in good agreement, supporting the similarity in the microstructures' physical appearance.   The largest disparity was in the measurement of particle

orientation. As mentioned in Chapter V, when particles become increasingly equiaxed due to fracture, they tend to be measured as having either a 0° or a 90° orientation. The synthetic shearing may be producing an artifact resulting in a high number of 90° orientations, causing the overall distribution plot to shift downwards.

a. *Particle Size*
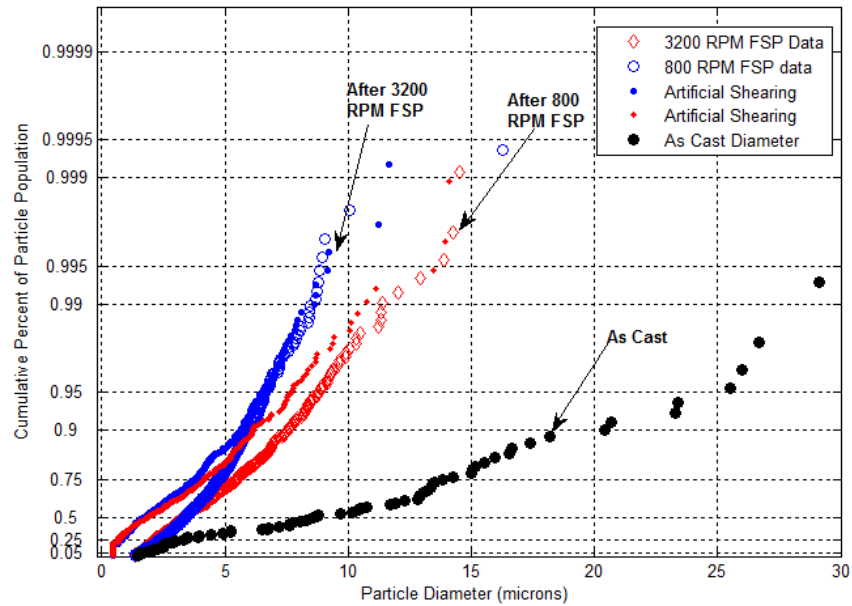
Figure 6.23 Comparison of particle diameter for the synthetic microstructures actual FSP microstructures at 800 and 3200 RPM.

b. ***Aspect Ratio***
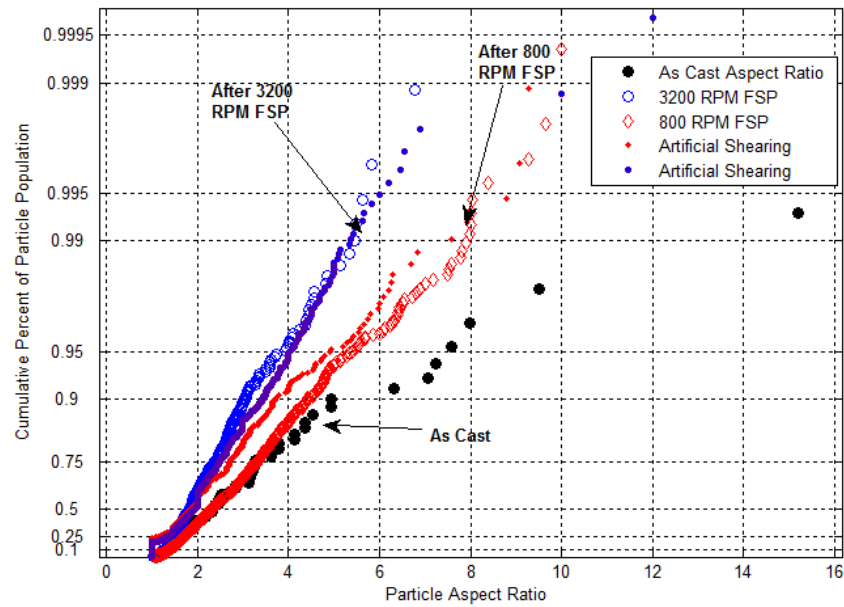
Figure 6.24 Comparison of particle aspect ratio for the synthetic microstructures and actual FSP microstructures at 800 and 3200 RPM.

c. ***Particle Orientation***
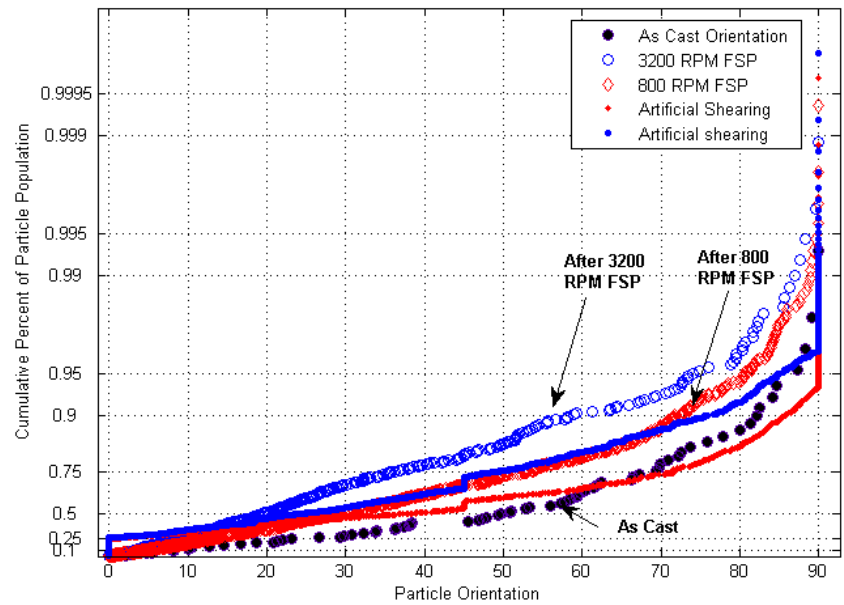
Figure 6.25 Comparison of particle orientation for the synthetic microstructures and actual FSP microstructures at 800 and 3200 RPM.

d. ***Particle Spacing***
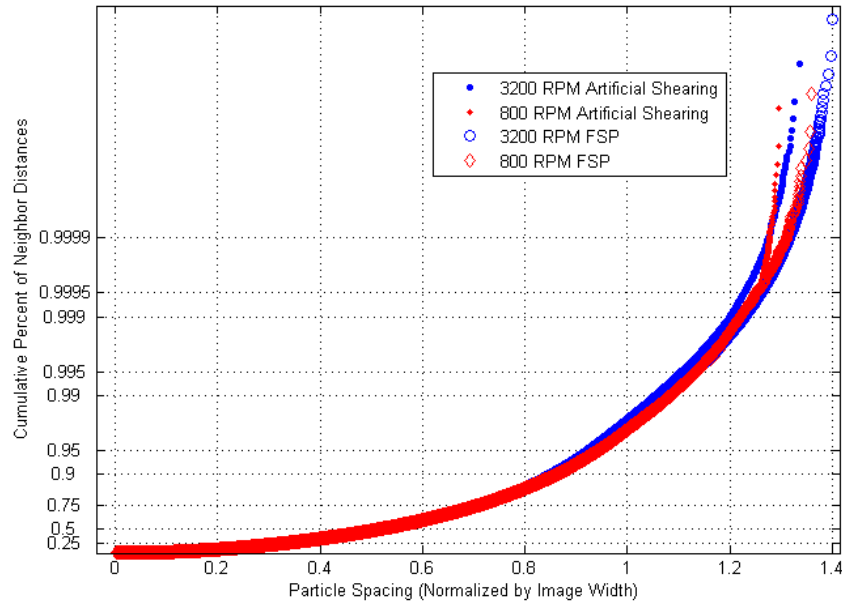
Figure 6.26 Comparison of particle spacing for the synthetic microstructures and actual FSP microstructures at 800 and 3200 RPM.

3. **Homogeneity Measurement**

Homogeneity was measured for both the synthetic and FSP SZ samples. The results of the analysis are shown in Figures 6.27. The homogeneity of the synthetically sheared images samples compared well to that of the actual FSP microstructures at 800 and 3200 RPM. Again, this result is a reasonable indication that redistribution in FSP is probably a result of repeated shear and rotation of the particle-containing matrix material.
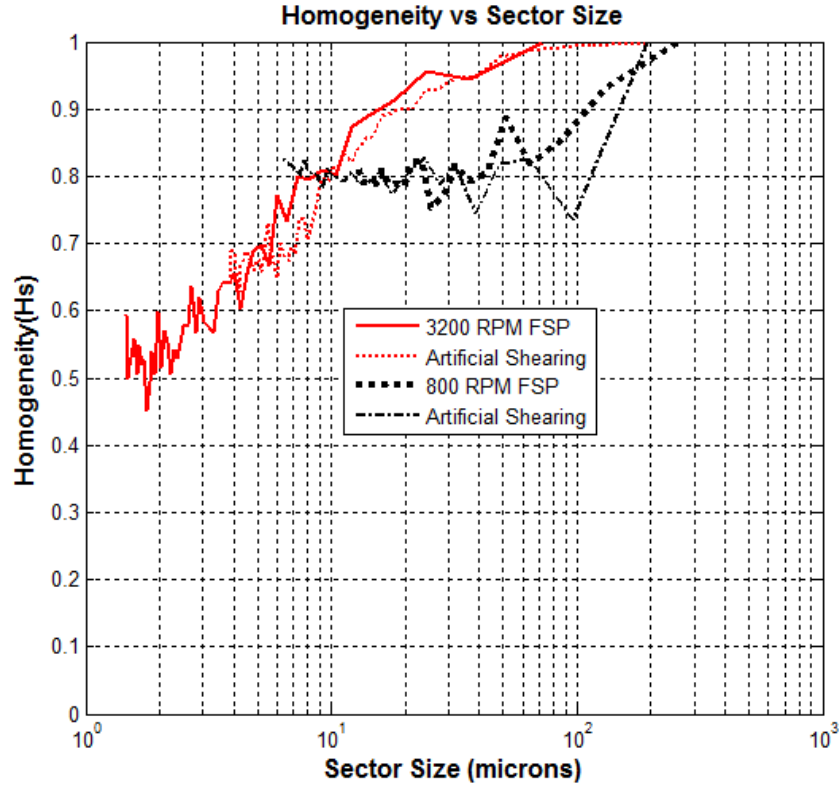
Figure 6.27 Homogeneity measurements for the synthetic microstructures and actual FSP microstructures at 800 and 3200 RPM.

G.   DISCUSSION

The layer shearing process is a sliding mechanism, with sliding also occurring on the Al-Si interface and in which discrete volumes of matrix material are repeatedly slid past one another in varying directions. Primarily, the fractured particles are moving because they are contained in these sliding volumes. A similar process of volume "shuffling," was put forth by Embury, et al. [138], where dislocation glide on two active slips systems occurs across a hetero-interface, causing intermixing between two adjacent phases (shown in Figure 6.28). This phenomenon is often observed to cause phase mixing in thinly drawn wires [140]. Here, the difference is that an internal shuffling process occurs within the Al matrix itself, not across a phase boundary, and the internally "shuffled volumes" contain second phase constituents.
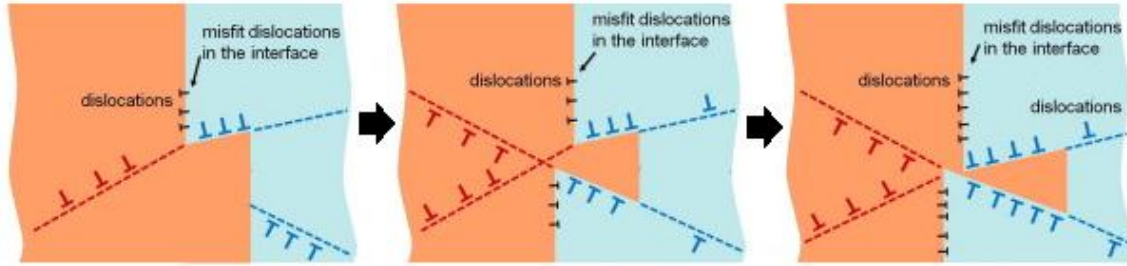
Figure 6.28 Schematic of a dislocation shuffle mechanism across a hetero-interface. After [138].

Mechanistically, the process can be viewed as a form of nondispersive mechanical mixing, characterized by slicing and twisting of the matrix caused by rotation of the pin face. For the simulations conducted earlier, the RVE's are sheared in discrete layers that move in a direction perpendicular to the sides of the square RVE. This motion is a limitation of the preliminary coding and produces a "checkerboard" pattern as the material is shuffled. For n layers, n^2 checkerboard squares will be produced and the largest resulting particle can be no larger than the area of intersection of two layers.

The process has the potential to be modeled in smaller increments of rotation angle ($\delta\theta$), which was previously illustrated in Figure 6.3. In such a case, the lines of shear repeatedly cross-cut the previously sheared layers at the incremental angle $\delta\theta$. Figure 6.29 shows a 4-layered RVE's geometric evolution when incrementally sheared at rotated at a 10° angle. Notice that, as $\delta\theta$ decreases, fewer layers are required to produce a highly segmented RVE after a full rotation around the pin.
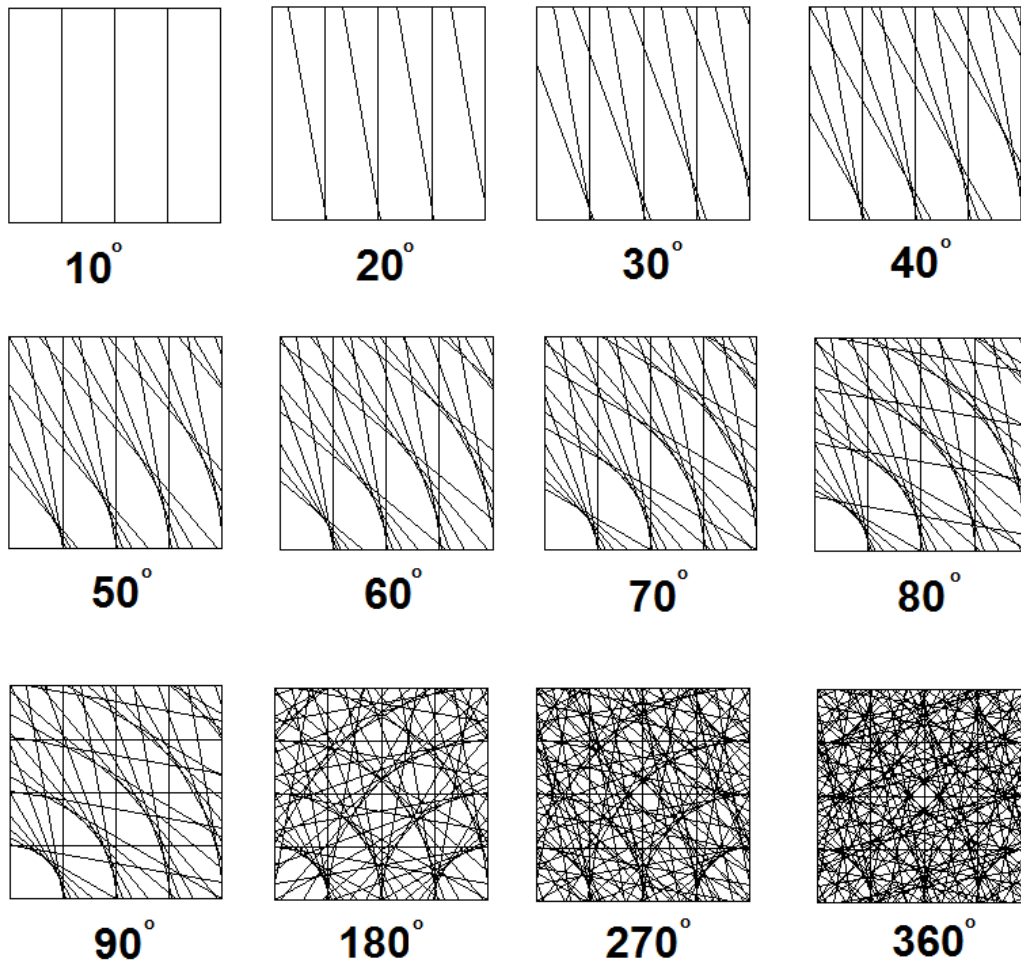
Figure 6.29 Geometric evolution of a four-layer RVE (with periodic boundaries) being sheared and rotated in 10° increments.

If, as in the 90° rotation simulations, maximum particle size is dictated by the largest dimension of the "layer intersections" (represented schematically in Figure 6.30), it could be reasoned that particle size and spatial distributions in FSP material might roughly correlate to the distribution of layer intersection size and spacing. This would imply that redistribution is affected by $\delta\theta$ and the layer thickness. Figures 6.31 and 6.32 show the results after measuring the dimensions and centroid spacing of RVE intersection areas for a scaled RVE sheared through 360° of rotation with a $\delta\theta$ of 10°. The measured maximum dimensions and centroid spacing of the segmented regions compare favorably to the measured particle size and spacing data from AA356 microstructures (of the same scale) after FSP.

184
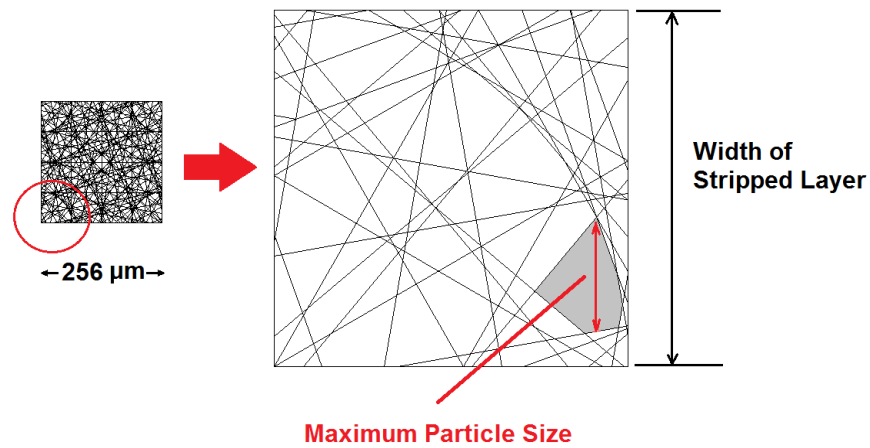
Figure 6.30 Predicted maximum particle size base on the maximum dimension of the RVE layer intersection area.
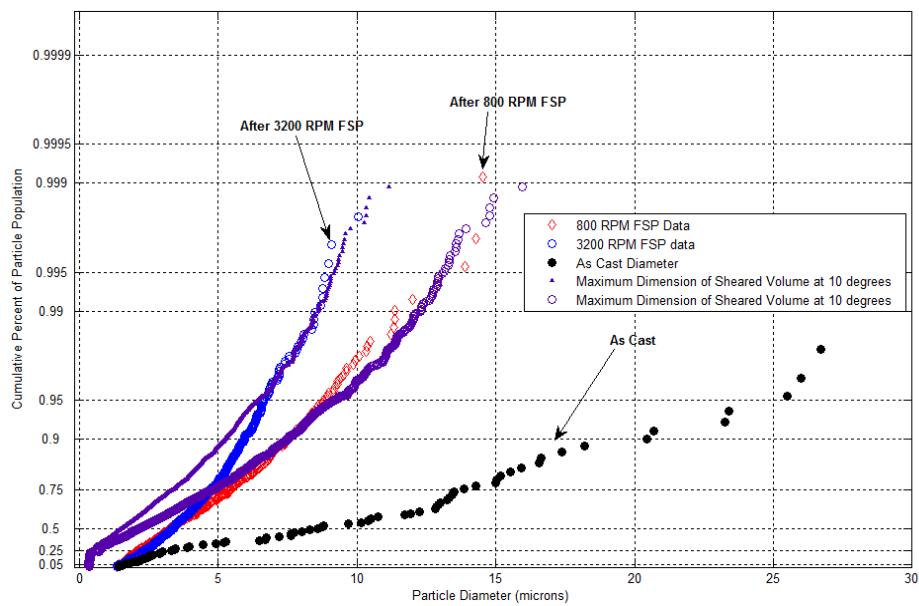
Figure 6.31 Plotted distribution of a scaled RVE's intersection area maximum width compared to the distribution of particle diameters in a microstructure after FSP.
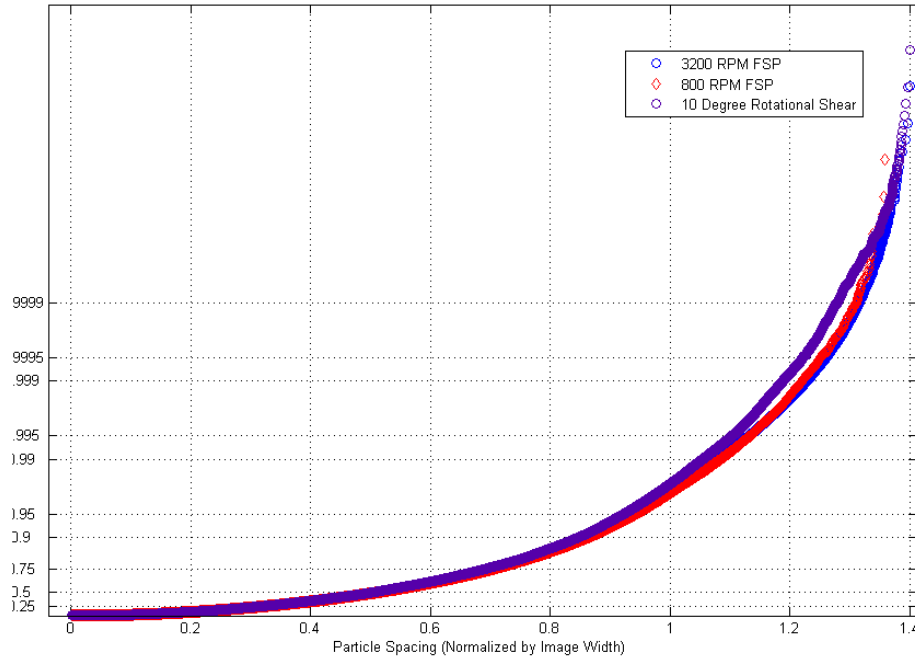
Figure 6.32 Plotted distribution of a scaled RVE's intersection area centroid spacing compared to the distribution of particle diameters in a microstructure after FSP.

In Figure 6.33, the shearing and rotation exercise is repeated for four discrete values of $\delta\theta$ using a 4-layered RVE. If the process is again repeated over a range of layer thicknesses, the relationship between $\delta\theta$ and layer thickness becomes more apparent. By scaling the RVE to a micrograph, the layer thickness / extrusion layer ratio required to approach a homogeneous length scale may be calculated as a function of $\delta\theta$, as shown in Figure 6.34.
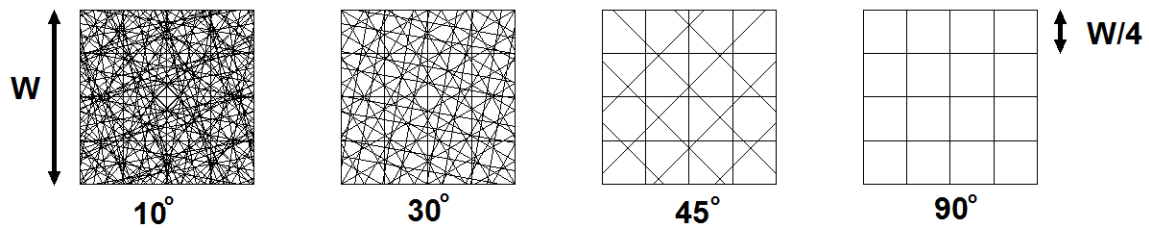
Figure 6.33 Geometric evolution of after 360° for a four-layer RVE (with periodic boundaries) being shear in increments of 10°, 30°, 45°, and 90°.

When the shearing angle ($\delta\theta$) is 10°, only four layers are required to obtain FSP sized segments, whereas when the same volume element is sheared with a $\delta\theta$ of 90°

(shown in Figure 6.34), 25 layers are required to approach a particle size consistent with that observed in FSP. The number of layers required to obtain FSP sized segments for 10°, 30°, 45°, and 90° values of $\delta\theta$ is shown in Table 6.1. Measured particle size / extrusion layer thickness ratios from the FSP RPM trial is shown in Table 6.2. The data from both tables is plotted for comparison in Figures 6.35 and 6.36. The figures show a similar trend, indicating that RPM may be affecting the angle of rotation at which a volume of material is sheared on the pin face.
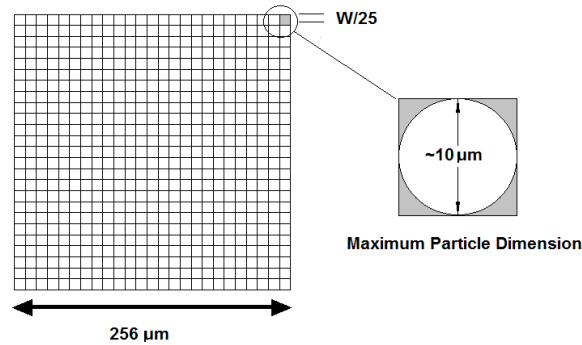
Figure 6.34 Geometric particle size after shearing a scaled RVE with a $\delta\theta$ of 90° through 360° of rotation. 25 sub-layers are required to achieve FSP particle size.

Table 6.1 Geometrically calculated strip layer width to extrusion layer width ratio required to achieve homogeneity at the FSP length scale.

Volume Element Thickness	Layers Required	$\delta\theta$	Strip Layer Width/ Extrusion Layer Thickness Ratio
1	4	10	0.2500
1	9	30	0.1111
1	16	45	0.0625
1	25	90	0.0400

Table 6.2 Measured particle size to extrusion layer thickness observed in FSP in the 400 to 4000 RPM range.

Mean Particle Size (µm)	Extrusion Layer Thickness (µm)	RPM	Particle Size/ Extrusion Layer thickness Ratio
9.79	200	400	0.049
6.8	100	800	0.068
5.66	65	1200	0.087
4.91	50	1600	0.098
4.6	40	2000	0.115
4.4	30	2400	0.147
4.5	25	2800	0.180
4.376	20	3200	0.219
3.96	20	3600	0.198
3.5	20	4000	0.175

187
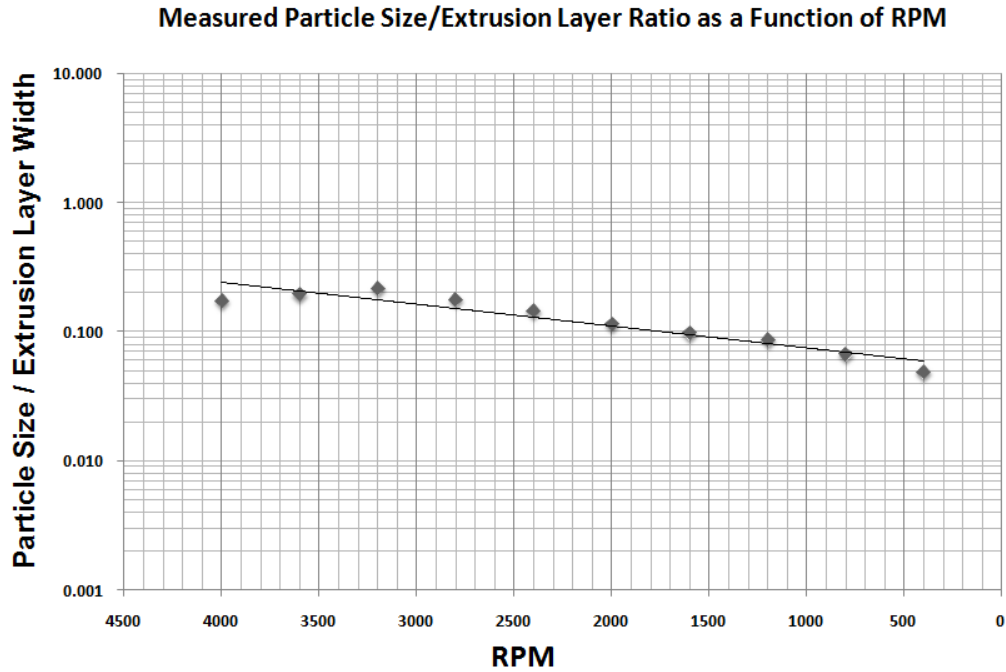
Figure 6.35 The measured particle size to extrusion layer thickness ratio over the range of RPM.
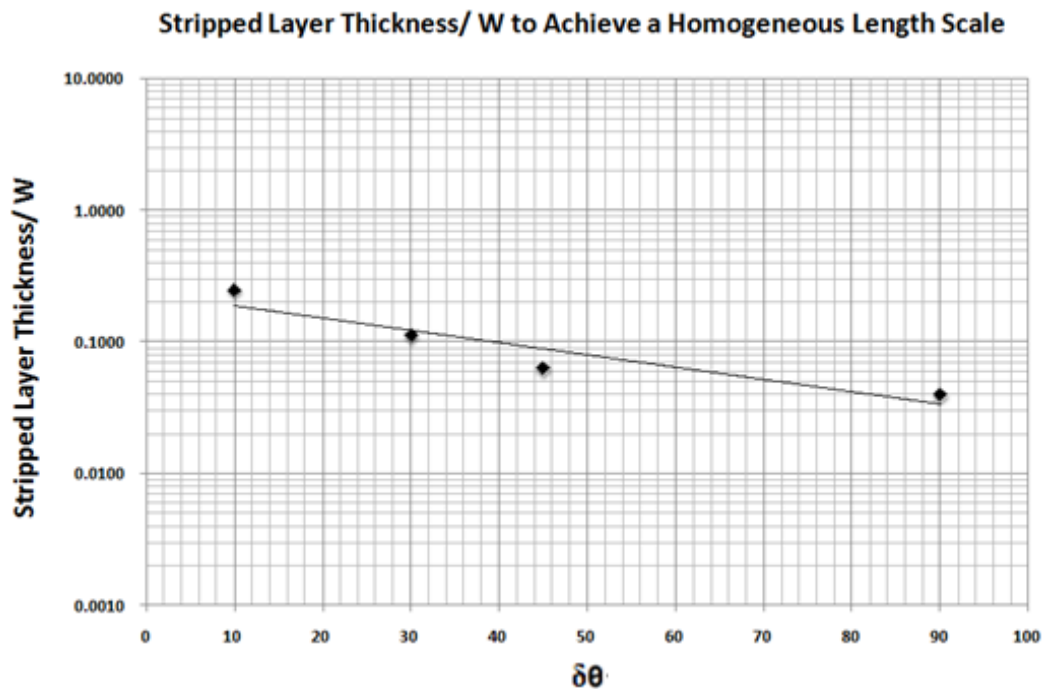
Figure 6.36 The geometrically calculated strip layer width to extrusion layer thickness ratio required to achieve a FSP particle size scale as a function of the shearing angle.

188

In general, all the results suggest that a relatively simple discontinuous geometric shearing approach might be able to explain the redistribution of constituent material in AA356 after FSP. This idea is compatible with the notion that material traveling around the tool returns to a location very near to where it was stripped from the base material. The RVE model implies that not all volumes of material at the pin interface are sheared to the same degree, depending on their original location. As a result, variations in the degree of redistribution should be expected across the SZ. As RPM increases, these variations should diminish, as each volume will be sheared more frequently with most volumes reaching mixing saturation, regardless of starting location. In fact, this was observed in the FSP conducted in Chapter IV.

The geometric similarities observed among the synthetically sheared microstructure images, the sheared RVE's with periodic boundaries, and experimental FSP samples strongly suggest a nondispersive mixing, advective mechanism is at work. If so, the shearing layer thicknesses required in FSP are on the order of 5 to 15 microns, considerably smaller than the extrusion layer on the pin's retreating side. Layered formations of similar thickness were observed to exist when examining void-prone regions in microscopy of FSP samples. Diffusive processes, although present, appear to be a much smaller and slower contributor to the overall motion of the particles.

It was also observed that after a certain number of shears and rotations, the level of mixing saturates. That is, after a certain point, an increased number of shearing and rotation operations did not substantially improve the uniformity of the distribution. This observation is analogous to the shuffling of a deck of cards. Bayer and Diaconis [141] showed that a standard deck of 52 cards reaches a finite limit on randomness after approximately 8 shuffles. The relationship represented Equation 6.6 depends on the size of the deck. They also show and that the increase in randomness falls of abruptly, or reaches a cutoff after 7 shuffles. Here, S is the number of shuffles and n is the number of cards in a deck

$$S \approx \frac{3}{2} \log_2 n$$
<div align="right">Equation 6.6</div>

While the card shuffling problem presents different considerations than the simulated 2D array mixing problem, the analogy suggests that if nondispersive mixing is the primary mixing mechanism, a saturation limit should exist for the level of uniformity achieved, which will be dictated by the layer thickness and shearing angle. Furthermore, since thinner layers will generate smaller areas of intersection areas, additional shearing and rotation is required to achieve the same level of homogeneity, i.e., the deck has more cards. Both of these phenomena were observed during the simulations.

H. CONCLUSIONS

The conclusions of this section of work are summarized in bullet form:

- The total drift velocity for a nondeforming Si particle in an Al matrix is small, on the order of 1 to 5 particle diameters per second.

- A random walk or directionally-biased diffusive model using the maximum drift computed velocity does not sufficiently rearrange nondeforming particles in a way that reflects the SZ morphology in FSP material.

- Through matrix row operations, an image can be artificially sheared to a known strain and the resulting image can accurately capture the morphology of a deformed material.

- Monotonically shear material, even at very high strain values, does not achieve the level of uniformity seen in a FSP SZ. A rotation of the material during the shear significantly improved the uniformity. Nonlinear gradients in the shear did not appear to improve homogeneity.

- Synthetic microstructures sheared with a rotation, visibly resembled actual FSP microstructures after 8 to 12 shearing operations (with a shear strain of 1 per shear). Direct measurement and homogeneity analysis of particle distribution parameters for the synthetic and FSP microstructures confirmed their morphological similarity.

- The maximum particle size may be an indication of the thickness of the shearing layer acting on an RVE. When the shearing layer thickness is set to this value, simulations produced accurate synthetic microstructures for a given FSP RPM.

- Improvement in homogeneity appears to have a cutoff value. Mixing homogeneity appears to plateau at a strain between 8 and 12, depending on layer thickness. Beyond this value, further shearing will not significantly change the material's uniformity. This phenomenon is a characteristic of nondispersive mixing.

190

- The simulation evidence, combined with previous observations in the FSP microscopy, strongly suggest glide/shear based advective or nondispersive mixing mechanism as the primary cause of particle transport.

- The process of volume "shuffling", and consequently homogeneity, may be strongly influenced by the angle at which the material (or RVE) experiences instability and shears on the pin face.

THIS PAGE INTENTIONALLY LEFT BLANK

VII. CONCLUSIONS AND FUTURE WORK

This work investigated the microstructural redistribution of non-deforming particles in a soft matrix undergoing high temperature deformation. In the process, several new datasets, processes, and models emerged:

- A 3D high strain rate ECAP and 2D volume element models of for high temperature material containing non-deforming particles having a frictional interface.

- An experimental method for conducting high temperature ECAP pressing at NPS.

- Documentation of the minimal role of diffusive processes in FSP.

- Documentation of the effects of FSP RPM on size of the SZ and damage zone.

- Documentation of advective layering effects occurring within a FSP SZ.

- The development of a generalized method to measure and quantify homogeneity for a microstructure through image analysis.

- The development of glide / shear based model to visualize and describe constituent redistribution during FSP.

- Documentation of the possible correlation to RPM and Homogeneity in FSP.

The following summarizes the conclusions of this research:

A. MICROSTRUCTURAL REDISTRIBUTION

Redistribution was investigated through experimental, modeling, and analytical approaches. The following sections describe the findings:

1. ECAP and Modeling

Experimental evidence for a low degree of second phase redistribution was obtained through a homogeneous redundant shearing of Al-7% Si at elevated temperature by ECAP using Route C. The resulting microstructures did not appear significantly different from those produced by the same strain path at ambient temperature. The

observed particle / matrix relative motion was minimal. An analytical solution for diffusive particle motion caused by the stress field around rigid inclusions in a deformable matrix confirmed that particle motion should be small under these circumstances. The diffusive potential appears not to have a significant role in particle redistribution in high deformation-rate processes such as FSP.

3D modeling of the ECAP process also showed that little, if any, redistribution occurs via diffusive processes, but that inhomogeneity in the strain path can produce particle advective transport. Experimentally, it was also observed that strain path inhomogeneity resulted in advective transport of the particles. The resulting microstructures appeared more homogeneous as compared to the parent material, although they retained a distinctly banded nature

2. FSP

Microstructural examination was conducted on AA356 samples after FSP over a range of RPM (400 to 4000 RPM). Inspection of void formations and the pin extraction sites suggested that very thin, discrete layers are stripped by the tool and cut into sections during travel around the pin. Material does not flow as single, contiguous volume. SZ homogeneity was greatly enhanced by particle fracture. It was observed that fractured particles travel advectively with the stripped layers. At the completion of the strain path, particles are generally of the same morphology as those in stir zone wall (where the material originated), indicating the majority of particle fracture occurs either before or during the moment at which material is sheared from the base.

B. HOMOGENEITY INDEX

Using digital image analysis, a new generalized homogeneity (H_s) index was developed for a two-phase microstructure and demonstrated for AA356 FSP microstructures. The index quantifies homogeneity by calculating the total variance of multiple normalized particle parameters across a range of microstructure sub-regions. The accuracy and consistency of the homogeneity index will depend on the selected sub-region size, the characteristic length of the microstructure (i.e., particle size), the pixel resolution of the image, and the number of features in the image.

The approach is flexible, in that parameters may be added or changed, so long as they can be accurately measured. Parameters may also be removed if they are not important in a particular material. The method can be extended to other types of materials, such as those with multiple phases or connected features. The main requirement is that a feature must have a distinct boundary in order to be discerned and measured.

C.   MECHANISM OF REDISTRIBUTION IN FSP

A generalized matrix shearing / glide advective redistribution mechanism is proposed for FSP. A geometric model was developed which simulates the discrete, repeated shearing and rotation of a representative volume element of matrix material having periodic boundary conditions. The simulation results strongly suggested that such a mechanism would produce microstructures very similar to those observed in FSP. Digitized microstructures closely resembled actual FSP microstructures after 8 to 12 shearing operations where the material rotated 90° after each operation. Further shearing did not significantly change the material's uniformity. Particle redistribution appeared to be strongly affected by the thickness of layers stripped at the pin interface, as well as by the angle of rotation ($\delta\theta$) following the shear. The angle of rotation also appeared to have some correlation to RPM.

D.   FUTURE WORK

The following recommendations are recommended areas for future research in the area of FSP redistribution and homogeneity characterization:

1. Modeling of FSP using meshless methods for very low Reynolds number flows ($\sim 10^{-3}$ or lower) to better estimate a viscous pressure field around the rotating pin.

2. Refinement of the MATLAB shearing model such that the image may be rotated and sheared in small increments to better simulate a RVE's travel around the pin. The possibility also exists to incorporate diffusive processes into such a model.

3. Comparison of other composite FSP materials using the presented homogeneity and shearing models.

4. Microscopic inspection of FSP void regions in other materials for indications of sub-layer formations.

5. Development of a larger scale FSP tool pin which shears an analogous viscous, particle containing material at a low speed under hydrostatic conditions. In this approach, individual volume elements could be could be observed directly during deformation.

6. Extension of the homogeneity model to materials containing more than one type of constituent. The current approach would require that multiple constituents have some discriminating factor such as shape, size, or contrast in order to be detected separately.

7. Extension of the homogeneity model to 3D by incorporating stereological methods.

APPENDIX A: ECAP DIE DESIGN SHEETS

Design Sheet for Heater Sizing for ECAP Die

Desired Temperature Change

$$\text{degC} := 1 \cdot K$$

$$T_1 := 18 \cdot \text{degC} \qquad T_2 := 500 \cdot \text{degC} \qquad \Delta T := T_2 - T_1 \qquad \Delta T = 482 \text{degC}$$

Desired Time of Heat Up

$$\text{Time} := 60 \cdot \text{min}$$

Die Dimensions Change

$$l := 3.05 \, \text{in} \qquad w := 5.6 \, \text{in} \qquad h := 11 \cdot \text{in}$$

$$\text{Vol} := h \cdot l \cdot w \qquad \text{Vol} = 187.88 \text{in}^3$$

Efficieny to account for Heat Loss to Ambient and Contact losses

$$\eta := .80$$

Heat Capacity and Specific Weight of Die Material

$$c_p := 434 \, \frac{J}{kg \cdot K} \qquad \gamma_{st} := 490 \, \frac{lb}{ft^3}$$

$$\text{mass} := \gamma_{st} \cdot \text{Vol} \qquad \text{mass} = \blacksquare \, lb$$

$$Q_1 := \text{mass} \cdot c_p \cdot \Delta T \qquad Q_1 = \blacksquare \, W$$

Minimum Required Heater Power

$$\text{Power} := \frac{Q_1}{\eta \cdot \text{Time}} \qquad \text{Power} = \blacksquare$$

Current drawn by 120V Heaters

$$\text{Amps} := \frac{\text{Power}}{120 \cdot V} \qquad \text{Amps} = \blacksquare$$

ECAP Plunger High Temperature Design Sheet

For a square cross section

$$b := \frac{7 \cdot in}{16} \qquad h := b \qquad L := 6.5\,in \qquad Temp := 573 \cdot F$$

$$E := 27.5 \cdot 10^6 \cdot \frac{lb}{in^2} \qquad Area := b \cdot h \qquad I := b \cdot \frac{h^3}{12}$$

$$L_{eff} := 1.6L \qquad F_{cr} := E \cdot \frac{I \cdot \pi^2}{L_{eff}^2} \qquad F_{cr} = 7.661 \times 10^3\,lb$$

$$\sigma := \frac{F_{cr}}{Area} \qquad \sigma = 4.003 \times 10^4 \frac{lb}{in^2} \qquad Expansion := Temp \cdot 6.61 \cdot 10^{-6} \cdot \frac{in}{F}$$

$$Expansion = 3.788 \times 10^{-3}\,in$$

For a circular cross section

$$D := \frac{7 \cdot in}{16} \qquad r := \frac{D}{2} \qquad L := 6.5\,in \qquad E := 27 \cdot 10^6 \cdot \frac{lb}{in^2}$$

$$Area_c := \pi \cdot r^2 \qquad I_c := \pi \cdot \frac{r^4}{4} \qquad L_{effc} := 1.6L$$

$$F_{circle} := E \cdot \frac{I_c \cdot \pi^2}{L_{effc}^2} \qquad F_{circle} = \blacksquare\,lb$$

$$\sigma := \frac{F_{circle}}{Area_c} \qquad \sigma = \blacksquare \frac{lb}{in^2}$$

$$Increase := \frac{F_{cr}}{F_{circle}} \qquad Increase = \blacksquare$$

APPENDIX B: TYPICAL MESH FOR 3D ECAP MODEL
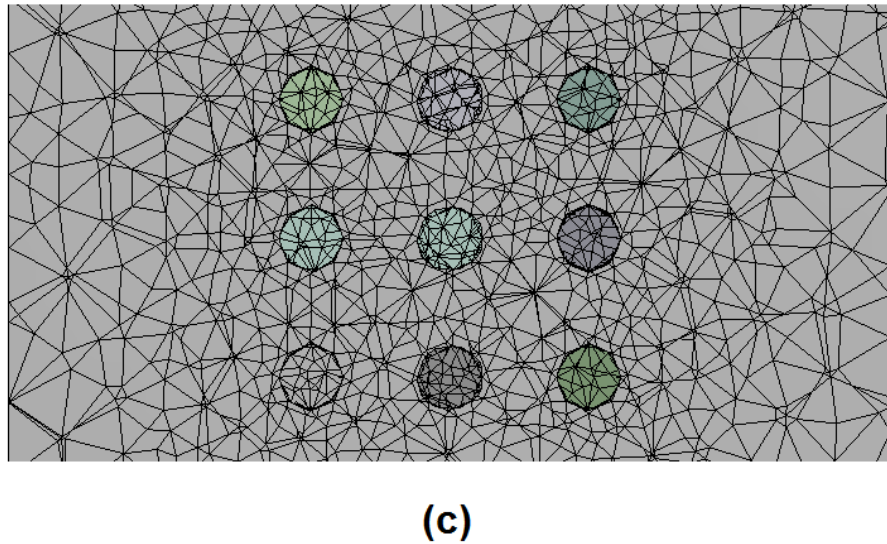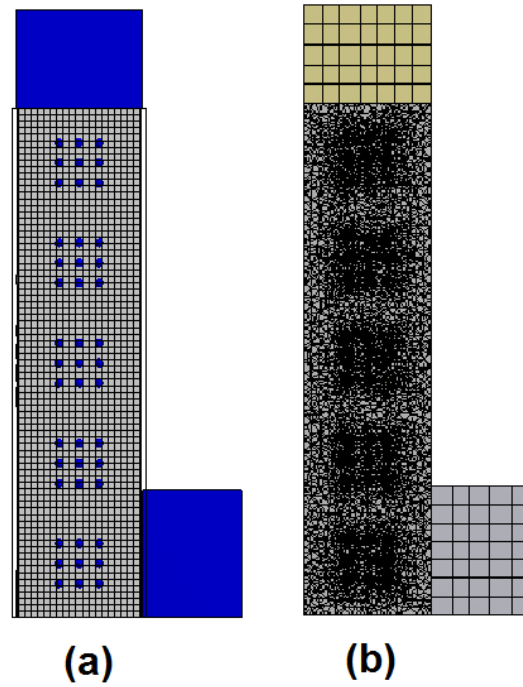
Figure B.1 Cutaway views of the typical 3D ECAP mesh: (a) Eulerian mesh for matrix material, (b) mesh connectivity for matrix material and Langrangian particles, and (c) detailed view of the connectivity mesh for a cluster of particles.

THIS PAGE INTENTIONALLY LEFT BLANK

APPENDIX C: HIGH STRAIN RATE ECAP VOID FORMATION
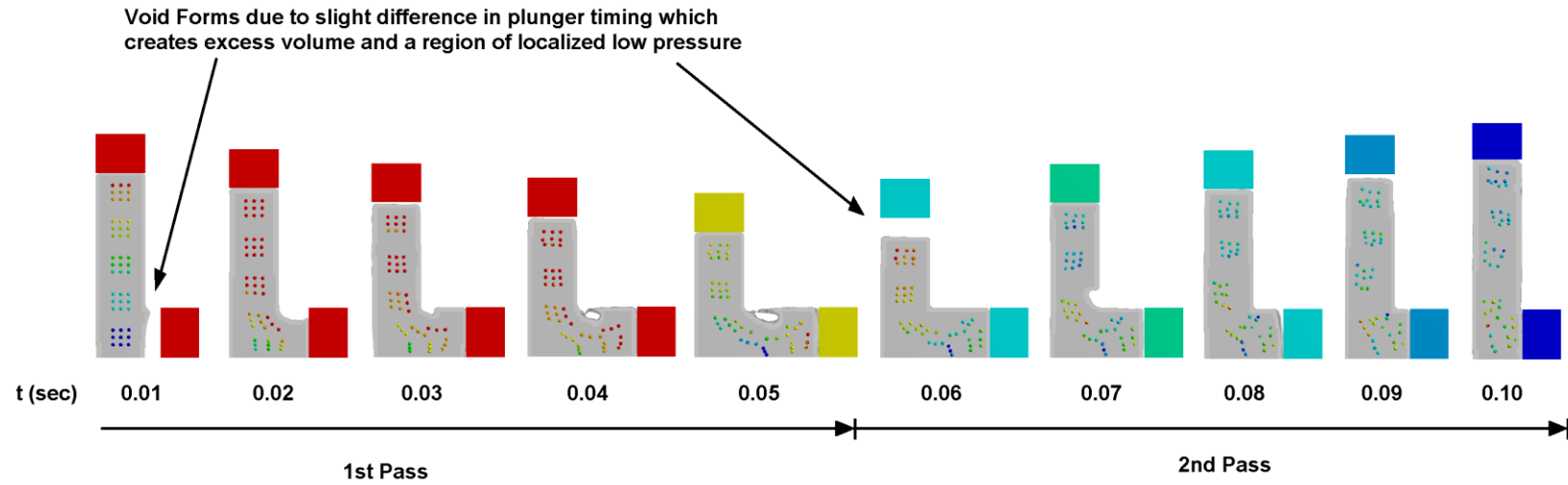
Figure C.1 Illustration of void formation due to aberrations in plunger displacement timing. The two pass simulation is conducted at 0.7 T_{Melt}, strain rate of $10^{1.3}$, and a C_f=0.9

THIS PAGE INTENTIONALLY LEFT BLANK

APPENDIX D: ANALOG ECAP EXPERIMENT

An analog ECAP experiment was carried out to validate the degree of particle cluster separation observed in the ANSYS modeling. An air-entrained copolymer gel, having an estimated viscosity of 50,000 cPs-sec^{-1} to 125,000 cPs-sec^{-1}, was subjected to repetitive ECAP by Routes C and A at low shear rates ($\sim 10^{-1}$ sec^{-1}). The gel viscosity approximates an Al-Si alloy viscosity at a temperature of approximately 0.9 T_{Melt} and shear rates ranging from 10^2 sec^{-1} to 10^3 sec^{-1}. The analog results generally agreed the modeling results. Significant cluster separation occurred in some cases, however particle motion was observed to occur due to an internal circulation of matrix material, caused by the gel's interaction with the channel boundaries.
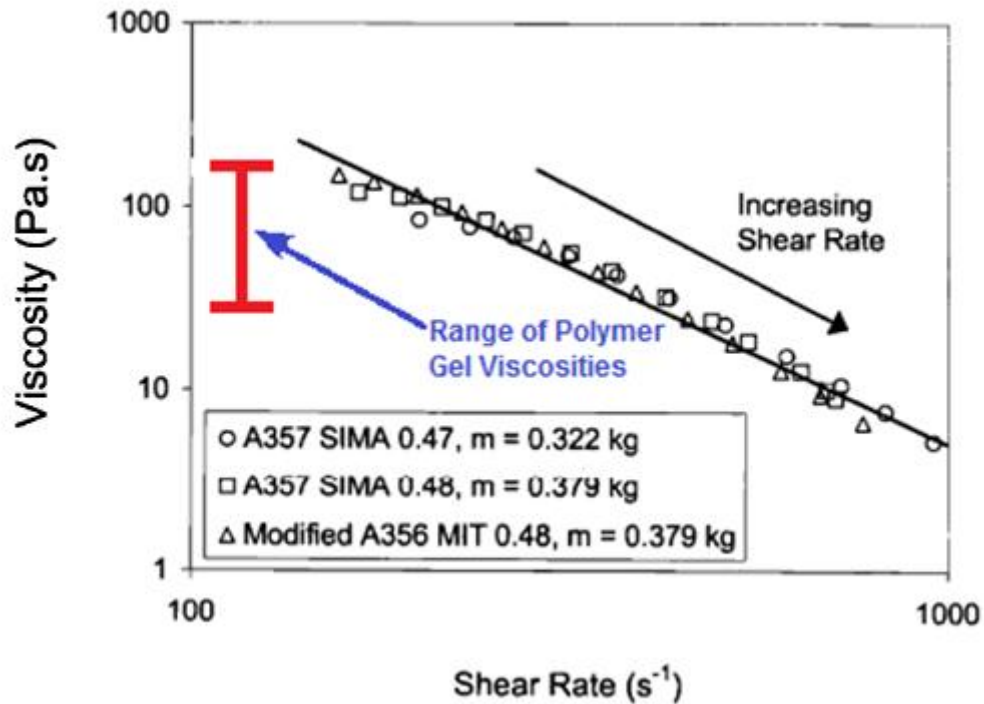
Figure D.1 Plot of AA356 and AA 357 measured viscosity at 0.9 T_{melt} as a function of shear rate. Also shown is the range of expected viscosity for an air-entrained copolymer gel for low shear rates at room temperature. After [135].

Starting Position

1 Pass
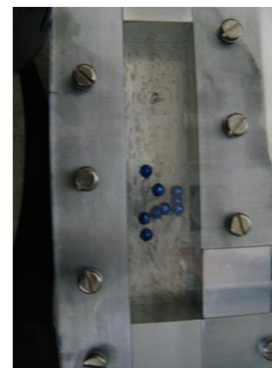
2 Pass

3 Pass

4 Pass

Figure D.2 4 Pass ECAP by Route C of an air-entrained copolymer gel containing a cluster of 9 particles, each particle having a diameter 1/6 the channel width. Processing was conducted at a shear rate of 10^{-1} sec^{-1}.

Starting Position

1 Pass
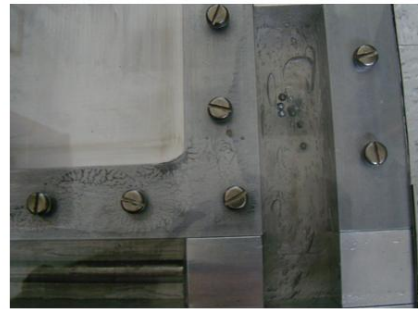
2 Pass

3 Pass
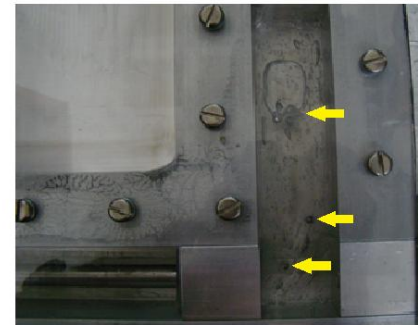
4 Pass

Figure D.3 4 Pass ECAP by Route C of an air-entrained copolymer gel containing a cluster of 9 particles, each particle having a diameter 1/10 the channel width. Processing was conducted at a shear rate of 10^{-1} sec^{-1}. Arrows denote particle cluster separation.

Start of Pass 1
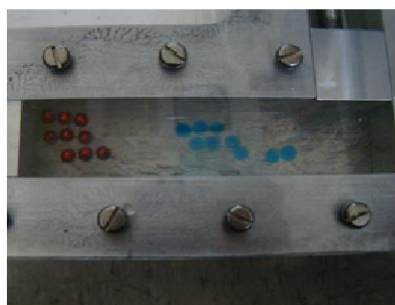
1 Pass

2 Pass

3 Pass
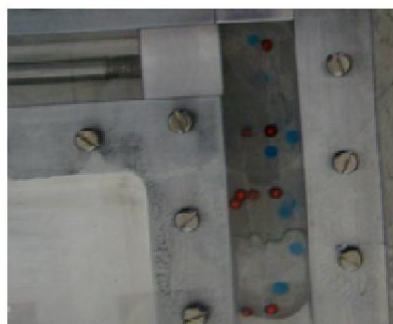
4 Pass

Figure D.4   4 Pass ECAP by Route A of an air-entrained copolymer gel containing a two clusters of 9 particles, each particle having a diameter 1/10 the channel width. Processing was conducted at a shear rate of 10^{-1} sec^{-1}.

APPENDIX E: ADDITIONAL ECAP IMAGES
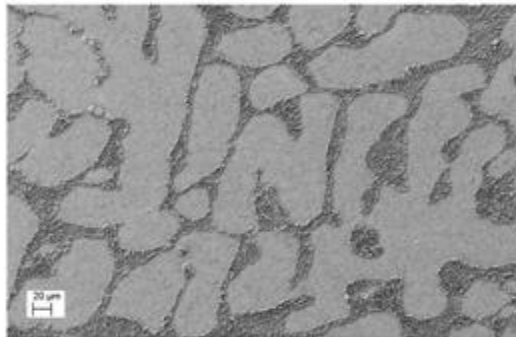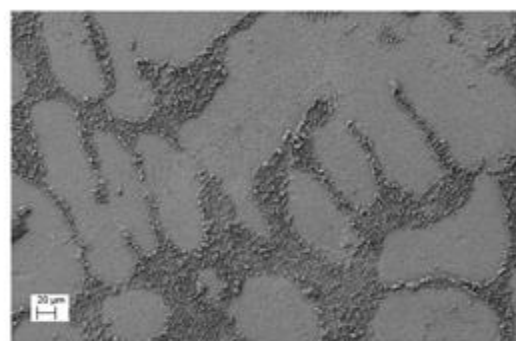
1.   300°C CROSS PLANE IMAGES

Figure E.1 Secondary electron images of the Al-7% Si cross plane after processing by ECAP Route A at 300°C.
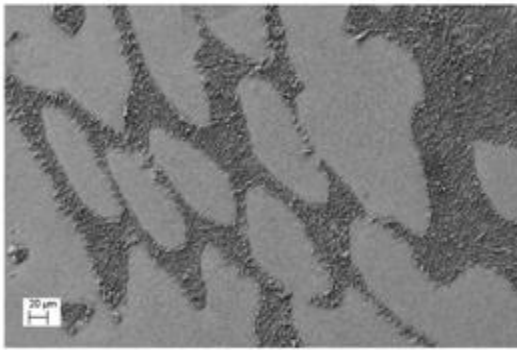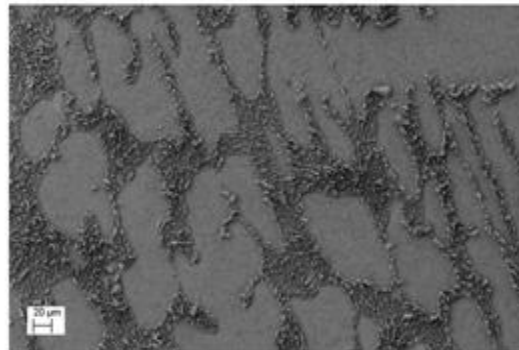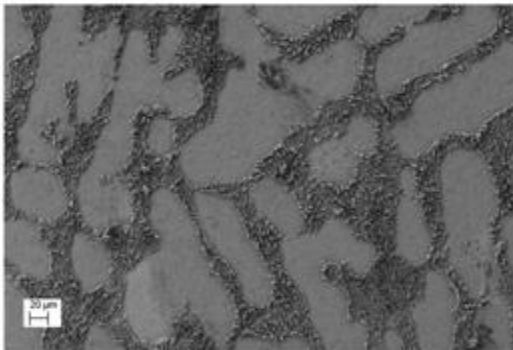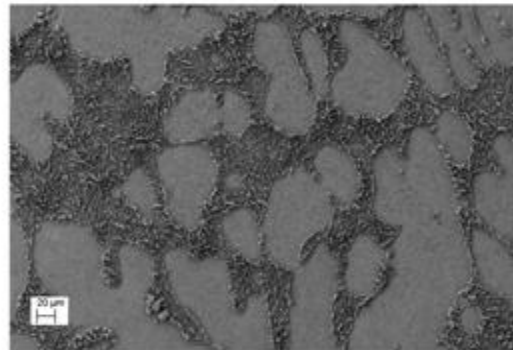
2.   300^OC TRANSVERSE PLANE

Figure E.2 Secondary electron images of the Al-7% Si transverse plane after processing by ECAP Route A at 300°C.

3.   400^OC CROSS PLANE IMAGES (AT CORE)
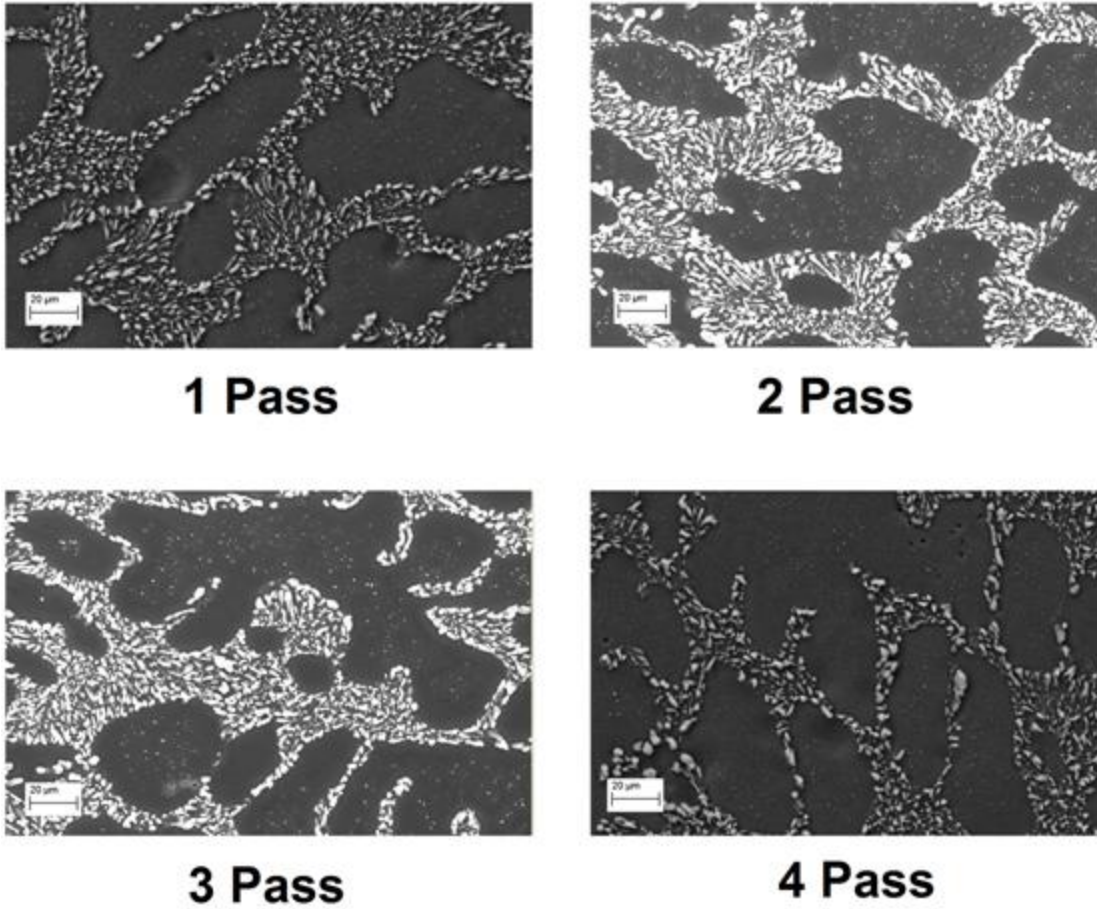
Figure E.3 Secondary Electron images of the Al-7% Si cross plane core after processing by ECAP Route A at 400^oC.

4.   400°C TRANSVERSE PLANE IMAGES (AT CORE)
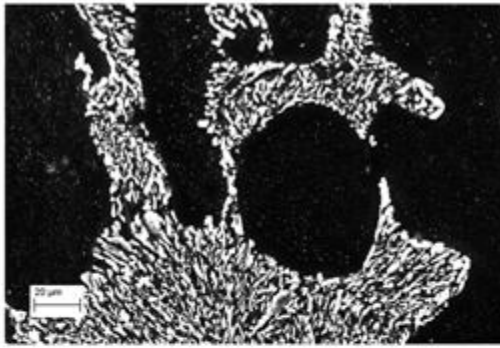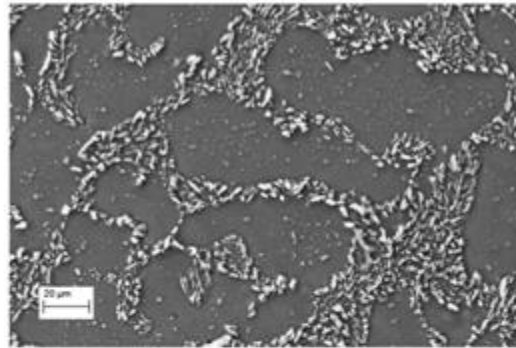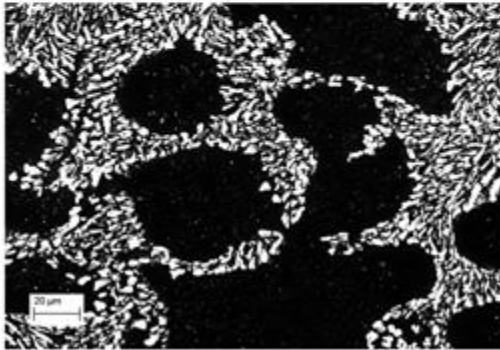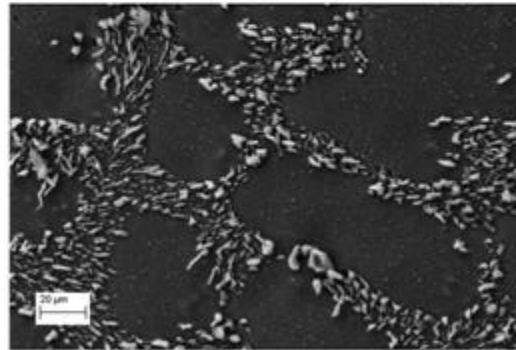
Figure E.4 Secondary Electron images of the Al-7% Si transverse plane core after processing by ECAP Route A at 400°C

APPENDIX F: PRESSURE INDUCED PARTICLE MOTION

Elevated Temperature Diffusional Motion Sample Calculation at 873K

Definitions

$$\text{micron} := 1 \times 10^{-6} \cdot \text{m} \qquad KPa := 1 \cdot 10^{3} \cdot Pa \qquad MPa := 1 \cdot 10^{6} \cdot Pa \qquad GPa := 1 \cdot 10^{9} \cdot Pa$$

$$k := 1.3807 10^{-23} \frac{J}{K} \qquad R_1 := 8.314 \frac{J}{\text{mol} \cdot K} \qquad eV := 1.602 10^{-19} \cdot J$$

Inputs:

$$d := 1 \cdot \text{micron} \qquad m_1 := 0 \qquad \nu := .33 \qquad T_1 := 873 \cdot K$$

$$r := \frac{d}{2} \qquad \text{diameters} := d \qquad r_a := 110 \cdot 10^{-12} \cdot m$$

d is the radius for a circular particle, an equivalent ellipse will have the same area

m_1 is the shape parameter governing the shape of the ellipse

Shape Equations

$$x(\theta) := d \cdot \cos(\theta) \sqrt{\frac{(1 + m_1)}{1 - m_1}} \qquad\qquad y(\theta) := d \cdot \sin(\theta) \sqrt{\frac{(1 - m_1)}{1 + m_1}}$$
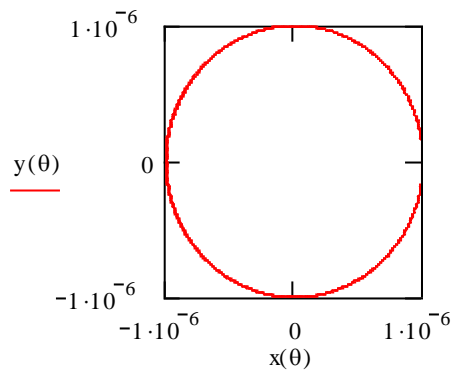
Material and Pressure Parameters:

$E_{incl} := 200 \cdot GPa$ $E_{bulk} := 20 \cdot GPa$

$\sigma_{ym} := 10 \cdot MPa$ $\sigma_x := 100 \cdot MPa$

$X := 0 \, micron$ $X = 0 \, m$

$p := 100 \cdot \dfrac{MPa}{micron}$ $\alpha := \dfrac{E_{incl}}{E_{bulk}}$

Eshelby Factors for an Ellipsoidal Inclusion:

$\eta := 5 \cdot \alpha - 8 \cdot v + 3$ $\eta = 50.36$

$\beta := 2 \dfrac{\left(1 - m_1\right)}{1 + m_1}$ $\beta = 2$

$\lambda := \dfrac{\alpha \cdot (1 - v)}{\left(4 \cdot \alpha^2 \cdot v - 6 \cdot \alpha \cdot v - 3 \cdot \alpha^2 + 4 \cdot \alpha + 2 \cdot v - 1\right) \cdot \left(m_1^2 - 1\right) + 8 \cdot \alpha \cdot (1 - v)^2}$ $\lambda = 0.036$

$F_2 := \lambda \cdot \left[(1 - \alpha) \cdot \left(m_1^2 - 4 \cdot v \cdot m_1 + 4 \cdot m_1 + 4 \cdot v \right) + \eta \right]$ $F_2 = 1.401$

$F_1 := F_2 - \beta \cdot \lambda \cdot (1 - \alpha) \cdot \left(1 + m_1\right) \cdot \left(4 \cdot v + m_1 - 1\right) - 1$ $F_1 = 0.61$

$F_3 := v \cdot \left(F_1 + F_2\right)$ $F_3 = 0.664$

$G_2 := \lambda \cdot (1 - \alpha) \cdot \left(1 - m_1\right) \cdot \left(4 \cdot v - m_1 - 1\right)$ $G_2 = -0.105$

$G_1 := G_2 - \beta \cdot \lambda \cdot \left[(1 - \alpha) \cdot \left(m_1^2 + 4 \cdot v \cdot m_1 - 4 \cdot m_1 + 4 \cdot v \right) + \eta \right] + \beta + 1$ $G_1 = 0.094$

$G_3 := v \cdot \left(G_1 + G_2\right)$ $G_3 = -3.708 \times 10^{-3}$

Principal Stresses

$$\sigma_1 := F_1 \cdot \left(\sigma_{ym} + p \cdot X \right) + G_1 \cdot \sigma_x \qquad\qquad \sigma_1 = 15.465 MPa$$

$$\sigma_2 := F_2 \cdot \left(\sigma_{ym} + p \cdot X \right) + G_2 \cdot \sigma_x \qquad\qquad \sigma_2 = 3.524 MPa$$

$$\sigma_3 := F_3 \cdot \left(\sigma_{ym} + p \cdot X \right) + G_3 \cdot \sigma_x \qquad\qquad \sigma_3 = 6.266 MPa$$

$$p_{bar} := p \cdot \frac{d}{E_{bulk}} \qquad\qquad \Omega_v := \frac{4 \cdot \pi \cdot r_a^3}{3}$$

$$V_{norm} := -\left[\sqrt{\frac{\left(1 + m_1 \right)}{\left(1 - m_1 \right)}} \right] \cdot F_2 \cdot p_{bar} \qquad\qquad V_{norm} = -7.004 \times 10^{-3}$$

$$\delta_v := 1 \cdot d \qquad Q_s := .92 eV \qquad Pipe := \exp\left(\frac{-Q_s}{\frac{mol}{R_1 \cdot T_1}} \right)$$

$$D_{Al\_Si} := \left(Pipe \exp\left(\frac{-136000\frac{J}{mol}}{R_1 \cdot T_1} \right) \right) \cdot 2.02\,10^{-4} \cdot \frac{m^2}{s} \qquad D_{Al\_Si} = 1.471 \times 10^{-8} \frac{cm^2}{s}$$

$$Normalizer := d^2 \cdot k \cdot \frac{T_1}{\Omega_v \cdot D_{Al\_Si} \cdot \delta_v \cdot E_{bulk}} \qquad Normalizer = 7.347 \times 10^4 \frac{s}{m}$$

$$V_{abs} := \frac{\left| V_{norm} \right|}{Normalizer} \qquad\qquad V_{abs} = 0.095 \frac{diameters}{sec}$$

THIS PAGE INTENTIONALLY LEFT BLANK

APPENDIX G: FLOW CHART OF HOMOGENEITY INDEX PROCEDURE

Format Image / Measure Data

10 µm
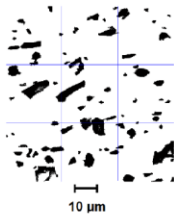
Record Data for each sector

Number of Particles

9	11	9
11	9	11
14	12	13

Area Fraction

0.0942	0.0817	0.0667
0.1313	0.1396	0.0786
0.1406	0.1373	0.1594

Mean Equivalent Diameter

2.3634	1.9178	1.7714
1.9548	2.7161	1.8384
2.2060	2.1654	2.2171

Mean Spacing between Particles

11.3623	14.5953	13.5959
12.3009	12.4525	13.0574
12.2171	12.6086	14.9554

Mean Aspect Ratio

2.0927	2.0429	1.9109
2.5370	2.9148	1.8373
2.2391	1.6412	2.0833

Mean Orientation

-12.1689	17.7530	3.1633
19.8962	16.6927	11.3347
-8.8351	13.2283	2.7715

Normalize Values and shape into a vector

0.6429
0.7857
1.0000
0.7857
0.6429
0.8571
0.6429
0.7857
0.9286

$\mu_{X_1} = .7857$

0.5908
0.8234
0.8821
0.5248
0.8759
0.8615
0.4186
0.4931
1.0000

$\mu_{X_2} = .7189$

Particle Population, Variance= 0.016582
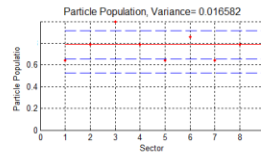
Calculate Parameter Variance

Ex:

$$(.6429 - .7857)^2$$
$$(.7857 - .7857)^2$$
$$(1.0000 - .7857)^2$$
$$(.7857 - .7857)^2$$
$$(.6429 - .7857)^2$$
$$(.8571 - .7857)^2$$
$$(.6429 - .7857)^2$$
$$(.7857 - .7857)^2$$
$$(.9286 - .7857)^2$$
$$= .132656$$

$$VAR(X_1) = \frac{1}{n-1}\sum_{i=1}^{n}[x_i - \mu]^2$$

$$VAR(X_1) = \frac{.149238}{9} = .016582$$

Repeat for each to obtain Variance for each parameter

Compute the Covariance for the parameters X_1 and X_2

$$COV(X_1, X_2) = \sum_{i=1}^{N}\frac{(x_{1i} - \mu_{X_1})(x_{2i} - \mu_{X_2})}{N}$$

$$COV(X_1, X_2) = \frac{-1.3968}{9} = -.1552$$

Ex:

$$(.6429 - .7857)(.5908 - .7189)$$
$$(.7857 - .7857)(.8234 - .7189)$$
$$(1.0000 - .7857)(.8881 - .7189)$$
$$(.7857 - .7857)(.5248 - .7189)$$
$$(.6429 - .7857)(.8759 - .7189)$$
$$(.8571 - .7857)(.8615 - .7189)$$
$$(.6429 - .7857)(.4186 - .7189)$$
$$(.7857 - .7857)(.4931 - .7189)$$
$$(.9286 - .7857)(1.000 - .7189)$$
$$= -1.3968$$

Repeat for each set of vectors to obtain all Covariances (X_1, X_2).....to (X_5, X_6)

For 6 Parameters, 15 Covariances will be calculated

Obtain total Variance

$$VAR\left[\sum_{i=1}^{N}X_i\right] = \sum_{i=1}^{N}VAR(X_i) + 2\sum_{i=1}^{N}\sum_{j=i+1}^{N}COV(X_i, X_j)$$

$$H_x = 1 - \left(\sum_{i=1}^{N}VAR(X_i) + 2\sum_{i=1}^{N}\sum_{j=i+1}^{N}COV(X_i, X_j)\right)$$

Subtract from 1 to obtain Homogeneity

215

THIS PAGE INTENTIONALLY LEFT BLANK

APPENDIX H: MATLAB CODES

1.   HOMOGENEITY PARAMETER MEASUREMENT

```matlab
%Code to calculate and plot the Homogeneity parameter
%%%%%%%%%%%%%%%%%%%%%%%%%%%%%%%%%%%%%%%%%%%%%%
clear all
close all

%The square pixel size to crop out of overall image
%%%%%%%%%%%%%%%%%%%%%%%%%%%%%%%%%%%%%%%%%%%%%%%
n=680;
%%%%%%%%%%%%%%%%%%%%%%%%%%%%%%%%%%%%%%%%%%%%%%%

%Scale to correct Magnification by input of "MAG"
%%%%%%%%%%%%%%%%%%%%%%%%%%%%%%%%%%%%%%%%%%%%%%%%
MAG=1000;

%N is the number of homogeneity scale length scales to be used
%%%%%%%%%%%%%%%%%%%%%%%%%%%%%%%%%%%%%%%%%%%%%%%%%
N=5;

% p is the square root of the number of grid sectors.
% If starting if p=2, four sectors will be used, if p=3,
% nine grid sectors, etc....
%%%%%%%%%%%%%%%%%%%%%%%%%%%%%%%%%%%%%%%%%%%%%%%%%
p=1;

if MAG==1000
scale=10;
scale_width=25.4/1.0;
end;

if MAG==500
scale=20;
scale_width=25.4/1.0;
end

if MAG==200
scale=20;
scale_width=25.4/2.0;
end

if MAG==100
scale=100;
scale_width=25.4/1.0;
end
```

```matlab
%The scaling values for the selected image
%%%%%%%%%%%%%%%%%%%%%%%%%%%%%%%%%%%%%%%%%%%%%%%%%%%
width=278.0;      % width in mm
pixels=1024;      % pixels in image width
%%%%%%%%%%%%%%%%%%%%%%%%%%%%%%%%%%%%%%%%%%%%%%%%%%%

%Pixel Connectivity, either 4 or 8 (this determines how pixels are
counted
%as individual particles
%%%%%%%%%%%%%%%%%%%%%%%%%%%%%%%%%%%%%%%%%%%%%%%%%%%
C=8;
%%%%%%%%%%%%%%%%%%%%%%%%%%%%%%%%%%%%%%%%%%%%%%%%%%%

%Determines filtering for the image to be converted to binary
%(choose a number between 0 and 1)
%%%%%%%%%%%%%%%%%%%%%%%%%%%%%%%%%%%%%%%%%%%%%%%%%%%
Filter_level=.5;
%%%%%%%%%%%%%%%%%%%%%%%%%%%%%%%%%%%%%%%%%%%%%%%%%%%


%Computes the scaling factors to convert pixels to microns
%%%%%%%%%%%%%%%%%%%%%%%%%%%%%%%%%%%%%%%%%%%%%%%%%%%%%
L1=width/scale_width;    %number of scale distances in picture
L=L1*scale;              %Entire Image width in microns
pw=pixels/L;             %pixels per micron
MIN_SIZE=(1/pw);         %Minimum detectable particle size
cropped_width=L*n/pixels;
cropped_area=cropped_width^2;
%%%%%%%%%%%%%%%%%%%%%%%%%%%%%%%%%%%%%%%%%%%%%%%%%%%%%

%Get original image from file
[filename, pathname] = uigetfile( ...
{'*.jpg;*.tif','Image Files (*.jpg,*.tif)';
   '*.jpg','Jpeg files (*.jpg)';
   '*.tif','Tiff files (*.tif)'; ...
   '*.*',  'All Files (*.*)'}, ...
   'Select the image');
x = (imread([pathname, filename]));

%Convert image to black and white and filter
I2 = im2bw(x,Filter_level);
bw1 = imcrop(I2,[0 0 n n]);
bw1 = bwareaopen(bw1, 8);
figure

%show the cropped binary image
imshow(~bw1)
xlabel(['Cropped Width = ' num2str(cropped_width),...
        'microns','FontSize',12]);

%Calculates the global mean Aspect ratio for the sample.
 CC = bwconncomp(bw1,C);
    s7 = regionprops(CC, 'MajorAxisLength');
    A7 = cat(1, s7.MajorAxisLength);
```

218

```matlab
    s8  = regionprops(CC, 'MinorAxisLength');
    A8 = cat(1, s8.MinorAxisLength);
    ARTotal=A7./A8;


%Begin segmenting the image into increasingly finer sectors. p is the
%starting value.
for cnt=1:N
    sectors=p^2;

%Initialize sector cropper start coordinates
x=0;
y=0;

%Determines number of sectors and location for each sector
sector_size=n/sqrt(sectors);
Q(cnt)=sectors;
QS(cnt)=sector_size/pw;
Length_Scale2=sector_size/(pw);
sector_area=sector_size^2;
sector_ratio=sqrt(sectors);
sector_fraction=sector_area/cropped_area;
xp1=sector_size/2;
yp1=sector_size/2;

%Subcrops each sector, measures parameters in each sector, and stores
that
%information as a separate vector for each parameter

for i=1:sqrt(sectors)
  for j=1:sqrt(sectors)
    bw = imcrop(bw1,[x y sector_size sector_size]);
    CC = bwconncomp(bw,C);

    s1  = regionprops(CC, 'Centroid');
    centroids = cat(1, s1.Centroid);
    CENT=(pdist(centroids,'euclidean'));
    m_dist(i,j)=mean(CENT/pw);
    std_dist(i,j)=std(CENT/pw);
    var_dist(i,j)=var(CENT/(pw*max(CENT)),1);
    NUM(i,j) = max(size(centroids));

    s2  = regionprops(CC, 'Area');
    area = cat(1, s2.Area);
    m_area(i,j)=mean(area/pw^2);
    std_area(i,j)=std(area/pw^2);
    var_area(i,j)=var(area/pw^2,1);
    Area_Fraction (i,j) =sum(area)/(sector_size^2);

    s3  = regionprops(CC, 'EquivDiameter');
    A3 = cat(1, s3.EquivDiameter);
    m_dia(i,j)=mean(A3/pw);
    std_dia(i,j)=std(A3/pw);
    var_dia(i,j)=var(A3/pw,1);
```

```matlab
    s4  = regionprops(CC, 'MajorAxisLength');
    A4 = cat(1, s4.MajorAxisLength);
    s5  = regionprops(CC, 'MinorAxisLength');
    s6  = regionprops(CC, 'Eccentricity');
    A5 = cat(1, s5.MinorAxisLength);
    AR=A4./A5;
    std_AR(i,j)=std(AR);
    m_AR(i,j)=mean(AR);
    var_AR(i,j)=var(AR,1);


    s6  = regionprops(CC, 'Orientation');
    A6 = cat(1, s6.Orientation);
    m_orient(i,j)=mean(A6);
    std_orient(i,j)=std(A6);
    var_orient(i,j)=var(A6,1);

    %sets starting point for next sector
     x=x+sector_size;
     xp(i,j)=xp1;
     yp(i,j)=yp1;

     xp1=xp1+sector_size;
     yp(i,j)=yp1;

  end
   x=0;
   y=y+sector_size;

   xp1=sector_size/2;
   yp1=yp1+sector_size;
end

% Variation Particle Numbers
%%%%%%%%%%%%%%%%%%%%%%%%%%%%%%%%%%%%%%%%%%%%%%%%%%%%%%%%%
F=reshape(NUM, sectors,1);
VAR_num(cnt)=var(F/max(F),1);
VN=VAR_num(cnt);
COV(1,:)=(F/max(F));
Guess=(F/max(F));

% Variation Particle Spacing
%%%%%%%%%%%%%%%%%%%%%%%%%%%%%%%%%%%%%%%%%%%%%%%%%%%%%%%%%

m_dist(isnan(m_dist)) = 0;
std_dist(isnan(std_dist)) = 0;
var_dist(isnan(var_dist)) = 0;

A=reshape(m_dist,sectors,1);
max_dist=max(A);          %This is the maximum of all sector means
VQD=var_dist;             %Spacing Variance for a single sector size
STDQD=std_dist;           %Spacing Std deviation for a single sector size
```

```matlab
m_dist;                  %Vector of all non-normalized sector means
mean_dist=mean2(m_dist);%Mean of all sector means ( i.e. global mean)
std_dist=std(A);         %Standard deviation of spacing
VD=var(A/max_dist,1);    %Normalized vector variances
Var_Norm_dist(cnt)=VD;  %Variance vector for all normalized sector
means
COV(2,:)=(A/max_dist);  %Compute the normalized covariance


% Variation Area Fraction
%%%%%%%%%%%%%%%%%%%%%%%%%%%%%%%%%%%%%%%%%%%%%%%%%%%%%%%%%%

Area_Fraction(isnan(Area_Fraction)) = 0;
Area_Fraction;
B=reshape(Area_Fraction,sectors,1);
max_AF=max(B);
mean_AF=mean2(Area_Fraction);
std_AF=std(B);
VAFF=var(B/max_AF,1);
Var_Norm_AF(cnt)=VAFF;
COV(3,:)=(B/max_AF);

% Variation Particle Diameter
%%%%%%%%%%%%%%%%%%%%%%%%%%%%%%%%%%%%%%%%%%%%%%%%%%%%%%%%%%%%%

m_dia(isnan(m_dia)) = 0;
std_dia(isnan(std_dia)) = 0;
var_dia(isnan(var_dia)) = 0;
MD=reshape(m_dia,sectors,1);
MD_norm=MD/max(MD);
m_dia=mean(MD);
std_dia=std(MD);
VMD=var(MD_norm,1);
Var_Norm_dia(cnt)=VMD;
COV(4,:)=(MD_norm);

m_AR(isnan(m_AR)) = 0;
std_AR(isnan(std_AR)) = 0;
var_AR(isnan(var_AR)) = 0;
m_AR;
D=reshape(m_AR,sectors,1);
max_AR=max(D);
VAR=var(D/max_AR);
Var_Norm_AR(cnt)=VAR;
COV(5,:)=(D/max_AR);
```

```matlab
% Variation Particle Orientation
%%%%%%%%%%%%%%%%%%%%%%%%%%%%%%%%%%%%%%%%%%%%%%%%%%%%%%%%%%%

m_orient(isnan(m_orient)) = 0;
std_orient(isnan(std_orient)) = 0;
var_orient(isnan(var_orient)) = 0;
E=reshape(m_orient, sectors,1);
VOR=var([(E/(max(E)))+1]/2);
VOR=var(m_orient/max(abs(m_orient)),1);
Var_Norm_orient(cnt)=VOR;
COV(6,:)=([(E/(max(E)))+1]/2);


if p>1
%Calculate Covariances for all six Parameter relations and sum them

    x=1;
for j=1:5
    SUMCOV=cov(COV(x,:),COV(j+1,:));
    SUMCOV=reshape(SUMCOV,4,1);
    COVVECTOR(j)=SUMCOV(2);
end
   sum1=sum(COVVECTOR);


    x=2;
for j=2:5
    SUMCOV2=cov(COV(x,:),COV(j+1,:));
    SUMCOV2=reshape(SUMCOV2,4,1);
    COVVECTOR2(j)=SUMCOV2(2);
end
   sum2=sum(COVVECTOR2);


    x=3;
for j=3:5
    SUMCOV3=cov(COV(x,:),COV(j+1,:));
    SUMCOV3=reshape(SUMCOV3,4,1);
    COVVECTOR3(j)=SUMCOV3(2);
end
   sum3=sum(COVVECTOR3);


    x=4;
for j=4:5
    SUMCOV4=cov(COV(x,:),COV(j+1,:));
    SUMCOV4=reshape(SUMCOV4,4,1);
    COVVECTOR4(j)=SUMCOV4(2);
end
   sum4=sum(COVVECTOR4);


    x=5;
for j=5
    SUMCOV5=cov(COV(x,:),COV(j+1,:));
    SUMCOV5=reshape(SUMCOV5,4,1);
    COVVECTOR5(j)=SUMCOV5(2);
end
   sum5=sum(COVVECTOR5);
```

```matlab
SUMCOVARIANCES=2*(sum1+sum2+sum3+sum4+sum5);
end

if p==1
    SUMCOVARIANCES=0;
end

H(cnt)=1-(VD+VAFF+VMD+VAR+VN+VOR+SUMCOVARIANCES);

clear COV
p=p+1;
end


MAR_max=max(D);
MAR=mean(D);
MAR_global=mean(MAR);

%Plot all variances and the Homogeneity Parameter

 figure
  loglog(Q,Var_Norm_dist,'-ms',Q,Var_Norm_AF, '-.ko',...
      Q,Var_Norm_dia,'--bx',...
      Q,Var_Norm_AR,':gd',...
      Q,Var_Norm_orient,'-c*',...
      Q,VAR_num,'-rV','MarkerSize',6,'LineWidth',1.5)
      legend('Area Fraction','Particle Spacing','Particle Diameter',...
      'Particle Aspect Ratio', 'Particle Orientation', 'Location',
'best')

title([' Normalized Variance vs Number of Sectors  '],'FontSize',12)
    grid on
    xlabel('sectors')
    ylabel('Normalized Variance')
    grid on

 figure
    semilogx(QS,H,'-ks','LineWidth',1.5 )
    title([' Homogeneity vs Sector Size '],'FontSize',12)
    grid on
    xlabel('Sector Size (microns)')
    ylabel('Homogeneity(Hs)')
    grid on

hold off
```

2. DISTRIBUTION ESTIMATION AND FITTING

```
%Code to fit various trial distributions to the measured data

clear all
close all

MAG=500;

%The pixel size height and width to crop out of overall image
%%%%%%%%%%%%%%%%%%%%%%%%%%%%%%%%%%%%%%%%%%%%%%%%%%%%%
n=680;
%%%%%%%%%%%%%%%%%%%%%%%%%%%%%%%%%%%%%%%%%%%%%%%%%%%%%

%Input the scaling factors for the selected image
%%%%%%%%%%%%%%%%%%%%%%%%%%%%%%%%%%%%%%%%%%%%%%%%%%%%%
width=278.0;            %mm
pixels=1024;           %pixels in image width
%%%%%%%%%%%%%%%%%%%%%%%%%%%%%%%%%%%%%%%%%%%%%%%%%%%%%

%Pixel Connectivity, either 4 or 8 (this determines how pixels are
counted
%as individual particles
%%%%%%%%%%%%%%%%%%%%%%%%%%%%%%%%%%%%%%%%%%%%%%%%%%%%%
C=8;
%%%%%%%%%%%%%%%%%%%%%%%%%%%%%%%%%%%%%%%%%%%%%%%%%%%%%

%Determines filtering for the image to be converted to binary
%(choose a number between 0 and 1)
%%%%%%%%%%%%%%%%%%%%%%%%%%%%%%%%%%%%%%%%%%%%%%%%%%%%%
Filter_level=.5;
%%%%%%%%%%%%%%%%%%%%%%%%%%%%%%%%%%%%%%%%%%%%%%%%%%%%%

%Computes the scaling factors to convert pixels to microns
%%%%%%%%%%%%%%%%%%%%%%%%%%%%%%%%%%%%%%%%%%%%%%%%%%%%%
L1=width/scale_width;   %number of scale distances in picture
L=L1*scale ;             %Entire Image width in microns
pw=pixels/L;            %pixels per micron
MIN_SIZE=(1/pw);        %Minimum discernable particle size
cropped_width=L*n/pixels;
cropped_area=cropped_width^2;
%%%%%%%%%%%%%%%%%%%%%%%%%%%%%%%%%%%%%%%%%%%%%%%%%%%%%


%Get original image from file
[filename, pathname] = uigetfile( ...
{'*.jpg;*.tif','Image Files (*.jpg,*.tif)';
   '*.jpg','Jpeg files (*.jpg)';
   '*.tif','Tiff files (*.tif)'; ...
   '*.*',  'All Files (*.*)'}, ...
   'Select the image');

x = (imread([pathname, filename]));
```

```matlab
%Show selected image
figure
imshow(x)
title('Raw Image')

%Convert image to black and white while filtering
I2 = im2bw(x,Filter_level);

%Crop the largest square image of n by n pixels where n is a power of 2
%this will be the overall image to be quilted. This section does the
%analysis for the entire image (a quilt of 1)

%Particles areas are normalized by the quilt area
%Distance is normalized by the quilt size(one side of the quilt square

%Crop and show the binary image
bw1 = imcrop(I2,[0 0 n n]);
bw1 = bwareaopen(bw1, 8);

if MAG==1000
scale=10;
scale_width=25.4/1.0;
end;

if MAG==500
scale=20;
scale_width=25.4/1.0;
end

if MAG==200
scale=20;
scale_width=25.4/2.0;
end

if MAG==100
scale=100;
scale_width=25.4/1.0;
end

%Measure Parameter values for entire sample. Values are scaled to
microns
%according to inputs for image
 CC = bwconncomp(bw1,C);
    s1  = regionprops(CC, 'Centroid');
    centroids = cat(1, s1.Centroid);
    CENT = pdist(centroids,'euclidean');
    m_dist=mean(CENT/pw);
    std_dist=std(CENT/pw);
    var_dist_samp=var(CENT/pw,1);
    NUM_samp = max(size(centroids));
```

```matlab
    s2  = regionprops(CC, 'Area');
    A2 = cat(1, s2.Area);
    m_area=mean(A2)/pw^2;
    SUM_A=sum(A2);
    std_area=std(A2/pw^2);
    var_area_samp=var(A2/pw^2,1);
    Area_Fraction =sum(A2)/(n^2);

    s3  = regionprops(CC, 'EquivDiameter');
    A3 = cat(1, s3.EquivDiameter);
    m_dia=mean(A3/pw);
    std_dia=std(A3/pw);
    var_dia_samp=var(A3/pw,1);
    number=max(size(A3));

    s4  = regionprops(CC, 'MajorAxisLength');
    A4 = cat(1, s4.MajorAxisLength);
    s5  = regionprops(CC, 'MinorAxisLength');
    A5 = cat(1, s5.MinorAxisLength);
    AR=A4./A5;
    m_AR_global=mean(AR);
    std_AR=std(AR);
    var_AR_samp=var(AR,1);

    s6  = regionprops(CC, 'Orientation');
    A6 = cat(1, s6.Orientation);
    m_orient=mean(A6);
    std_orient=std(A6);
    var_orient_samp=var(A6,1);

    Length_Scale=pixels/(m_dia*pw);

Area_Data=(A2/pw^2);
Diameter_Data=(A3/pw);
Spacing_Data=CENT/pw;
Aspect_Ratio_Data=AR;
Orientation_Data=abs(A6);

%Calls functions to fit distributions to global parameter data
%%%%%%%%%%%%%%%%%%%%%%%%%%%%%%%%%%%%%%%%
figure
ParticleDiameterFIT(Diameter_Data)
figure
ParticleOrientationFIT(Orientation_Data)
figure
ParticleSpacingFIT(Spacing_Data)
figure
ParticleAspectRatioFIT(Aspect_Ratio_Data)
%%%%%%%%%%%%%%%%%%%%%%%%%%%%%%%%%%%%%%%%%%%
```

```matlab
function ParticleOrientationFIT(Orientation_Data)
%   PARTICLEORIENTATIONFIT(ORIENTATION_DATA)
%   Sample code to create a distribution fit
%   using the measured data as input. This sample code fits
%   several types of distributions to the measured orientation.

% Data from dataset "Orientation_Data":
% Y = Orientation_Data
% Force all inputs to be column vectors
Orientation_Data = Orientation_Data(:);

% Set up figure to receive datasets and fits
f_ = clf;
figure(f_);
set(f_,'Units','Pixels','Position',[360 223 688 479.45]);
legh_ = []; legt_ = {};    % handles and text for legend
probplot('exponential');
ax_ = gca;
title(ax_,'');
set(ax_,'Box','on');
grid(ax_,'on');
hold on;

% --- Plot data originally in dataset "Orientation_Data data"
t_ = ~isnan(Orientation_Data);
Data_ = Orientation_Data(t_);
h_ = probplot(ax_,Data_,[],[],'noref'); % add to probability plot
set(h_,'Color',[0.333333 0 0.666667],'Marker','o', 'MarkerSize',6);
xlabel('Data');
ylabel('Probability')
legh_(end+1) = h_;
legt_{end+1} = 'Orientation_Data data';

% Nudge axis limits beyond data limits
xlim_ = get(ax_,'XLim');
if all(isfinite(xlim_))
   xlim_ = xlim_ + [-1 1] * 0.01 * diff(xlim_);
   set(ax_,'XLim',xlim_)
end

x_ = linspace(xlim_(1),xlim_(2),100);

% --- Create fit "Generalized Extreme Value"

% Fit this distribution to get parameter values
t_ = ~isnan(Orientation_Data);
Data_ = Orientation_Data(t_);
p_ = gevfit(Data_, 0.05);
h_ = probplot(ax_,@gevcdf,p_);
set(h_,'Color',[1 0 0],'LineStyle','-', 'LineWidth',2);
legh_(end+1) = h_;
legt_{end+1} = 'Generalized Extreme Value';

% --- Create fit "Exponential"
```

```matlab
% Fit this distribution to get parameter values
t_ = ~isnan(Orientation_Data);
Data_ = Orientation_Data(t_);
p_ = expfit(Data_, 0.05);
h_ = probplot(ax_,@expcdf,p_);
set(h_,'Color',[0 0 1],'LineStyle','-', 'LineWidth',2);
legh_(end+1) = h_;
legt_{end+1} = 'Exponential';


% --- Create fit "Normal"
% Fit this distribution to get parameter values
t_ = ~isnan(Orientation_Data);
Data_ = Orientation_Data(t_);
pargs_ = cell(1,2);
[pargs_{:}] = normfit(Data_, 0.05);
p_ = [pargs_{:}];
h_ = probplot(ax_,@normcdf,p_);
set(h_,'Color',[0.666667 0.333333 0],'LineStyle','-', 'LineWidth',2);
legh_(end+1) = h_;
legt_{end+1} = 'Normal';


% --- Create fit "t"
% Fit this distribution to get parameter values
t_ = ~isnan(Orientation_Data);
Data_ = Orientation_Data(t_);
p_ = mle(Data_, 'dist','tlocationscale', 'alpha',0.05);

% Fit t location-scale distribution
% Get a description of the t location-scale distribution
dist_ = dfswitchyard('dfgetdistributions','tlocationscale');

h_ = probplot(ax_,dist_.cdffunc,p_);
set(h_,'Color',[0.333333 0.333333 0.333333],'LineStyle','-',
'LineWidth',2);
legh_(end+1) = h_;
legt_{end+1} = 't';


hold off;
leginfo_ = {'Orientation', 'vertical', 'Location', 'NorthWest'};
h_ = legend(ax_,legh_,legt_,leginfo_{:});  % create legend
set(h_,'Interpreter','none');
ylabel('Cumulative Percent of Particle Population')
xlabel('Particle Orientation')
```

3. DIFFUSION OF BANDED NON-OVERLAPPING SPHERES

```
clear all
close all

%Biasing Factors to allow particles to jump in a particular direction


EB=1;
WB=1;
NB=3;
SB=3;


AF=.07;      % INPUT Area Fraction


timesteps=10;  %The number of allowed jumps
F=1;           %This is the number of Radii a particle can jump


Yo=0;          %Initial Y coordinate of first generation box
Yoo=Yo;
Xoo=0;         %Initial X coordinate of first generation box
h=5;           % vertical height of each cluster box
w=5;           % width of each cluster box


b=4;           % NUMBER OF DISCRETE BOXES GENERATED PER BAND (total
width)
bands=4;       % NUMBER OF BANDS
Xo=Xoo;
spacing=20;    % Verticle spacing between BANDs
CLS=2;         %Sets horizontalcluster spacing



Stripwidth=h*bands+(bands-1)*spacing;
Ratio=50;
Do=Stripwidth/Ratio;
Ro=Do/2;  %Diameter of Particle



%Height of total generation box
%Width of total generation box

W_est=(b*w)+(b-1)*CLS+Do;
H_est=h+(bands-1)*(h+spacing)+Do;
Area_Est=H_est*W_est/(b*bands);
%Compute number of particles needed to achieve the Area
Fraction%%%%%%%%
n=round(AF*Area_Est/(pi()*Ro^2)); % COMPUTES AN INTEGER NUMBER OF
PARTICLES

Particles=n*b*bands % TOTAL NUMBER OF PARTICLES
```

```matlab
%THIS LOOP GENERATES THE SPECIFIED NUMBER OF BANDS AT A SPECIFIED
SPACING
 for d=1:bands

Xo=rand(1); %Intital x location of first particle
xpt=0;
%THIS LOOP GENERATES A FULL BAND
for cl=1:b
    if cl==b
     Xo=Xoo+(b-1)*CLS+(b-1)*w;
    end

%%%%%%%%%%%%%%%%%%%%%%%%%%%%%%%%%%%%%%%%%%%%%%%%%%%%%%%%%%%%%%%%%%%%%%%%%%%%
%THIS IS THE GENERATION LOOP FOR EACH DISCRETE BOX OF PARTICLES
ENSURING NO
%OVERLAP
p1=0;

while p1<1
for k=1:n
    r(k)=Ro;

    if k==1
                    X=Xo+(w*rand(1));
                    Y=Yo+(h*rand(1));
                    x(k)=X;
                    y(k)=Y;
    else
                    X=Xo+(w*rand(1));
                    Y=Yo+(h*rand(1));
                    x(k)=X;
                    y(k)=Y;
          for i=1:k
              for j=1:k
               if i==j
                 dist(i,j)=2*r(k);
               else
                 dist(i,j)=sqrt((x(i)- x(j))^2 +(y(i)- y(j))^2);
               end
              end
          end
    end
end

dist=dist-(2*r(k));
if min(dist)>=0
    p1=p1+1;
else
    clear x
    clear y
    clear dist2
    p1=0;
end
end
```

```matlab
%%%%%%%%%%% x and y are coordinates of non overlapping particles
 x1=x;
 y1=y;
 clear x
 clear y
 clear dist
xPosition=x1;
yPosition=y1;

for steps=1:timesteps
%LOOP to take one directional step for each particle
p2=0;
while p2<1
for part=1:n
     %direction is chosen randomly from numbers 0-2pi
     theta(part)=rand(1)*2*pi();
     for t=1:1

         if theta(part)<=pi()/2 && theta(part) > 0%theta in 1st
quadrant
             xP(t)=xPosition(part)+EB*F*r(t)*cos(theta(part));
             yP(t)=yPosition(part)+NB*F*r(t)*sin(theta(part));
          end

        if theta(part)<=pi()&& theta(part)>pi()/2 %theta in 2nd
quadrant
            theta(part)=pi()-theta(part);
            xP(t)=(xPosition(part)-WB*F*r(t)*cos(theta(part)));
            yP(t)=(yPosition(part)+NB*F*r(t)*sin(theta(part)));
         end

        if theta(part)>pi()  && theta(part)<=3*pi()/2 %theta in 3rd
quadrant
            theta(part)=theta(part)-pi();
            xP(t)=(xPosition(part)-WB*F*r(t)*cos(theta(part)));
            yP(t)=(yPosition(part)-SB*F*r(t)*sin(theta(part)));
        end

        if theta(part)>3*pi()/2 && theta(part)<=2*pi()%theta in 4th
quadrant
            theta(part)=2*pi()-theta(part);
            xP(t)=(xPosition(part)+EB*F*r(t)*cos(theta(part)));
            yP(t)=(yPosition(part)-SB*F*r(t)*sin(theta(part)));
        end

        if yP(t)>bands*h+(bands-1)*spacing
            yP(t)=bands*h+(bands-1)*spacing;
        end

        if yP(t)<0;
            yP(t)=0;
        end

         if xP(t)>(b*w)+(b-1)*CLS;
```

231

```matlab
            xP(t)=Xoo;
         end

        if xP(t)<Xoo
            xP(t)=(b*w)+(b-1)*CLS;
        end

    end
    %New coordinates after one step
    XX(part)=xP(t);
    YY(part)=yP(t);
 end

%%%CHECK DISTANCES TO ENSURE NO OVERLAP AFTER A STEP
 for k=1:n
   r(k)=Ro;
                    x2(k)=XX(k);
                    y2(k)=YY(k);
        for i=1:k
            for j=1:k
             if i==j
                distm(i,j)=2*r(k);
             else
                distm(i,j)=sqrt((x2(i)- x2(j))^2 +(y2(i)- y2(j))^2);
             end
            end
        end
 end
distm=distm-(2*Ro);

if min(distm)>=0
    p2=p2+1;
else
    clear x2
    clear y2
    clear distm

end
end %%%END of distance checking loop after a timestep


%DISTANCES ARE CHECKED OKAY IN ORDER TO RESET NEW COORDINATES
%TO THE NEW STEPPED SITES
%XX AND YY ARE THE NEW LOCATIONS AFTER THE STEP
  xPosition=XX;
  yPosition=YY;
  p2=0;

end
```

```matlab
xxx(:,cl)=x1;
yyy(:,cl)=y1;
XXX(:,cl)=XX;
YYY(:,cl)=YY;

Xo=Xo+CLS+w;
xpt=cl*(CLS+w);

end %%%%%END CLuster Loop

vectxxx=reshape(xxx,cl*n,1);
vectyyy=reshape(yyy,cl*n,1);
vectXXX=reshape(XXX,cl*n,1);
vectYYY=reshape(YYY,cl*n,1);

xxxx(:,d)=vectxxx;
yyyy(:,d)=vectyyy;
XXXX(:,d)=vectXXX;
YYYY(:,d)=vectYYY;

Yo=Yo+h+spacing;
end

vectxxxx=reshape(xxxx,Particles,1);
vectyyyy=reshape(yyyy,bands*cl*n,1);
vectXXXX=reshape(XXXX,bands*cl*n,1);
vectYYYY=reshape(YYYY,bands*cl*n,1);

% Set Periodic Boundary conditions at boders
 for check=1:Particles

     for i=1:Particles
            for j=1:Particles
             if i==j
                distm2(i,j)=2*r(k);
              else
                distm2(i,j)=sqrt((vectXXXX(i)- vectXXXX(j))^2 +...
                           (vectYYYY(i)- vectYYYY(j))^2)-Do;
              if distm2(i,j)<0
                 vectXXXX(i)=1.1*vectXXXX(i);
               if vectXXXX(i)  >(b*w)+(b-1)*CLS-Do;
                  vectXXXX(i)=Xoo;
                end
               end
              end
           end
       end
 end


distm2=reshape(distm2,Particles^2,1);
Hrect=max(vectXXXX)-Yoo+Do;
Wrect=max(vectYYYY)+Do;
```

```matlab
% Draw Results
figure
for c=1:n*cl*bands%
hold on
angle = linspace(0, 2*pi, 360);
xp = r(k)*cos(angle);
yp = r(k)*sin(angle);
fill(vectxxxx(c)+xp,vectyyyy(c)+yp, 'b')
rectangle('Position',[Xoo-Ro,Yoo-Ro,Hrect,Wrect])
axis('equal')
ylabel('y')
xlabel('x')
%grid on
end

figure
for c=1:n*cl*bands%
angle = linspace(0, 2*pi, 360);
xp = r(k)*cos(angle);
yp = r(k)*sin(angle);
fill(vectXXXX(c)+xp,vectYYYY(c)+yp, 'r')
hold on
axis('equal')
ylabel('y')
xlabel('x')
%grid on
rectangle('Position',[Xoo-Ro,Yoo-Ro,Hrect,Wrect])
end
```

4.   STRIP SHEARING AND ROTATION OF A MICROSTRUCTURE

```matlab
clear all
close all

%Get original image from file
[filename, pathname] = uigetfile( ...
{'*.jpg;*.tif','Image Files (*.jpg,*.tif)';
   '*.jpg','Jpeg files (*.jpg)';
   '*.tif','Tiff files (*.tif)'; ...
   '*.*',   'All Files (*.*)'}, ...
   'Select the image');

X = (imread([pathname, filename]));

figure
imshow(X)
Title(['Original Microstructure' ],'FontSize',16);

 bg = imopen(X,strel('disk',10));
 y = imsubtract(X,bg);
 level = graythresh(y);
 bw = im2bw(y,level);
 X=~bw;

%INPUTS
%%%%%%%%%%%%%%%%%%%%%%%%%%%%%%%%%%%%%%%%%%%%%%%%%%%%%%%%%%%%%%%%%%%%%%%%%%
%%%%
fullwidth=600;%Microscopy image width in microns
n=600;        %Number of pixels cropped
bands=50;     %Number of bands in image
theta=0;      %Rotation angle
shears=1;     %Number of shearing operations
strainpershear=0;% Specify the strain per shear to determine layer
motion
gradient_intensity=0; %Specifiy a value for strength of the strain
gradient


%Input the scaling factors for the selected image
%%%%%%%%%%%%%%%%%%%%%%%%%%%%%%%%%%%%%%%%%%%%%%%%%%
width=278.0;        %mm
scale =20.0;        %microns
scale_width=25.4/2.0;  %mm
pixels=1024;     %pixels in image width
%%%%%%%%%%%%%%%%%%%%%%%%%%%%%%%%%%%%%%%%%%%%%%%%%%
```

235

```
%Computes the scaling factors to convert pixels to microns
%%%%%%%%%%%%%%%%%%%%%%%%%%%%%%%%%%%%%%%%%%%%%%%%%%%
L1=width/scale_width;    %number of scale distances in picture
L=L1*scale ;             %Entire Image width in microns
pw=pixels/L;             %pixels per micron
MIN_SIZE=(1/pw);         %Minimum discernable particle size
cropped_width=L*n/pixels;
cropped_area=cropped_width^2;
band_width=n/bands/pw;
%%%%%%%%%%%%%%%%%%%%%%%%%%%%%%%%%%%%%%%%%%%%%%%%%%%
t=shears*strainpershear*(1+gradient_intensity);

micronperpixel=1/pw;
figure
I2 = imcrop(X,[0 0 n n]);
%subplot(2,1,2)
imshow(I2)
Title(['Width=', num2str(max(size(I2))*micronperpixel), '  microns
',...
    'Strip Width=', num2str(band_width), '  microns' ],'FontSize',16);
figure

if theta==0
    rotations=0;
else
    rotations=shears-1;
end

B=zeros(n,n);
W=(n*strainpershear/bands); %Layer step size in pixels
g=gradient_intensity;
step=1;

for z=1:shears

s=0; %This is the shear at the base of the material
k=1;%k is a counter

%This section determines either monotonic or reversing shearing during
%rotation. By making "fact" opposite in sign, the strain is monotonic
%as the image is rotated, changing the sense of the shear for each 90
%degree rotation. If "fact" is the same sign, the strain is reversed
after
%180 degrees of rotation

if theta>0
  if floor(z/2) == z/2
   fact=1;
  else
   fact=-1;
  end
else
    fact=-1;
end
```

236

```matlab
for r=1:bands
    for i=1:n/bands
        B(k,:) = circshift(I2(k,:),[0 fact*s]);
        k=k+1;
    end
    s=floor(s+W+g*r);% the number of pixels to shift the next band
    gradient(r)=s/n;
    ypos(r)=r;
end

    if rotations>0
        J = imrotate(B,theta,'bilinear');
        I2=J;
    else
        I2=B;
    end

imshow(B);
F(z)=getframe;

Title(['Cumulative Strain =',num2str(t),'     ',num2str(step),'
Shears'...
    ,'     ',num2str(step-1),' 90 degree Rotations' ],'FontSize',16);
step=step+1;
end

gradient=reshape(gradient,bands,1);
gradient=sort(gradient,'descend');
ypos=reshape(ypos,bands,1);

plot(ypos, gradient,'-b','LineWidth',4)
set(gca,'YDir','rev')
Title(['Gradient in Strain over Microstructure' ],'FontSize',16);
xlabel('Bands')
ylabel ('Strain per Shear Operation')
grid on

figure
imshow(B)
Title(['Cumulative Strain =',num2str(t),'     ',num2str(z),' Shears',...
    '     ',num2str(rotations),' 90 degree Rotations' ],'FontSize',16);

movie2avi(F,'shearing animation.avi','FPS',2,'COMPRESSION','none',...
    'QUALITY',100,'KEYFRAME',2);
```

THIS PAGE INTENTIONALLY LEFT BLANK

LIST OF REFERENCES

[1]   A. Askari, S. Silling, B. London, M. Mahoney, K. V. Jata, M. W. Mahoney, R. S. Mishra, S. L. Semiatin, and D. P. Field, Eds., "Temperature distribution and resulting metal flow," in *Friction Stir Welding and Processing IV*, 2001, pp. 43–54.

[2]   Oishi, K. and McNelley, T., "Microstructural modification of as-cast NiAl bronze by friction stir processing," *Metallurgical and Materials Transactions A,* vol. 35, pp. 2951–2961, 9, 2004.

[3]   D. Chae, D.A. Koss, P. R. Howell, and A. L. Wilson, "The effect of microstructural banding on failure initiation of HY-100 steel," *Acta Materialia,* vol. 31, pp. 995–1005, 2000.

[4]   A. Geltmacher. (2011, Sep. 15). 2D Image-based modeling of HY100 steel [Online]. Available: http://www.mstd.nrl.navy.mil/6350/6352/IBM2D.html.

[5]   C. Nan and D. R. Clarke, "The influence of particle size and particle fracture on the elastic/plastic deformation of metal matrix composites," *Acta Materialia,* vol. 44, pp. 3801–3811, 1996.

[6]   K. Gall, M. Horstemeyer, D. L. McDowell and J. Fan, "Finite element analysis of the stress distributions near damaged Si particle clusters in cast Al–Si alloys," *Mechanics of Materials,* vol. 32, pp. 277–301, 2000.

[7]   R. M. Cleveland, A. K. Ghosh and J. R. Bradley, "Comparison of superplastic behavior in two 5083 aluminum alloys," *Materials Science and Engineering: A,* vol. 351, pp. 228–236, 6/25, 2003.

[8]   J. E. Spowart, B. Maruyama and D. Miracle, "Multiscale characterization of spatially heterogeneous systems: Implications for discontinuously reinforced metal-matrix composite microstructures," *Material Science and Engineering: A,* vol. 37, pp. 51–66, 2001.

[9]   J. E. Spowart, "Microstructural characterization and modeling of discontinuously-reinforced aluminum composites," *Materials Science and Engineering: A,* vol. 425, pp. 225–237, 6/15, 2006.

[10]   A. Tewari, J. E. Spowart, A. M. Gokhale, R. S. Mishra and D. B. Miracle, "Characterization of the effects of friction stir processing on microstructural changes in DRA composites," *Materials Science and Engineering: A,* vol. 428, pp. 80–90, 7/25, 2006.

[11]   G. B. Wilks, M. A. Tschopp and J. E. Spowart, "Multi-scale characterization of inhomogeneous morphologically textured microstructures," *Materials Science and Engineering: A,* vol. 527, pp. 883–889, 2/15, 2010.

[12]   A. Tewari, A. M. Gokhale, J. E. Spowart and D. B. Miracle, "Quantitative characterization of spatial clustering in three-dimensional microstructures using two-point correlation functions," *Acta Materialia,* vol. 52, pp. 307–319, 1/19, 2004.

[13]   M. A. Tschopp, G. B. Wilks and J. E. Spowart, "Multi-scale characterization of orthotropic microstructures," *Modeling and Simulation in Materials Science Engineering,* vol. 16, 2008.

[14]   J. M. García-Infanta, S. Swaminathan, A. P. Zhilyaev, F. Carreño, O. A. Ruano and T. R. McNelley, "Microstructural development during equal channel angular pressing of hypo-eutectic Al–Si casting alloy by different processing routes," *Materials Science and Engineering: A,* vol. 485, pp. 160–175, 6/25, 2008.

[15]   J. M. García-Infanta, S. Swaminathan, C. M. Cepeda-Jiménez, T. R. McNelley, O. A. Ruano and F. Carreño, "Enhanced grain refinement due to deformation-induced precipitation during ambient-temperature severe plastic deformation of an Al–7%Si alloy," *Journal of Alloys and Compounds,* vol. 478, pp. 139–143, 6/10, 2009.

[16]   J. J. Lewandowski, C. Liu and W. H. Hunt Jr., "Effects of matrix microstructure and particle distribution on fracture of an aluminum metal matrix composite," *Materials Science and Engineering: A,* vol. 107, pp. 241–255, 1, 1989.

[17]   J. M. García-Infanta, A. P. Zhilyaev, F. Carreño, O. A. Ruano, J. Q. Su, S. K. Menon, and T. R. McNelley, "Strain path and microstructure evolution during severe deformation processing of an as-cast hypoeutectic Al–Si alloy," *Journal of Materials Science*, vol. 45, pp. 4613–4620, 17, 2010.

[18]   M. J. Leon, "Three-dimensional numerical testing of microstructures of particle reinforced composites," *Acta Materialia,* vol. 52, pp. 4177–4188, 8/16, 2004.

[19]   J. J. Stephens, J. P. Lucas and F. M. Hosking, "Cast Al-7 Si composites: effect of particle type and size on mechanical properties," *Scripta Metallurgica,* vol. 22, pp. 1307–1312, 1988.

[20]   D. F. Watt, X. Q. Xu and D. J. Lloyd, "Effects of particle morphology and spacing on the strain fields in a plastically deforming matrix," *Acta Materialia,* vol. 44, pp. 789–799, 1996.

[21]   W. M. Thomas, E. D. Nicholas, J. C. Needham, M. G. Murch, P. Templesmith, and C. J. Dawes: G. B. Patent Application No. 9125978.8, Dec. 1991.

[22]   F. D. Incropera, D. P. DeWitt, Bergmann, T. L., Lavine, A. S. *Fundamentals of Heat and Mass Transfer*, 6th ed. Wiley: New York, 2006.

[23]   J. Philibert, *Atom Movements Diffusion and Mass Transport in Solids,* Les editions de physique. Les Ulis, France, 1991.

[24]   D. Buslik, "A proposed universal homogeneity and mixing index," *Powder Technology,* vol. 7, pp. 111–116, 2, 1973.

[25]   M. F. Ashby, "The mechanical effects of a dispersion of a second phase," Second International Conference on the Strength of Metals and Alloys, Conference proceedings, Volume II, American Society for Metals, pp. 507–542, 1970.

[26]   M. F. Ashby, "The deformation of plastically non-homogeneous alloys," *Philosophical Magazine*, vol. 21 , pp. 399–424, 1970.

[27]   M. F. Ashby, "Boundary defects and the mechanism of particle movement through crystals," *Scripta Materialia*, vol. 3, pp. 771–870, 11, 1969.

[28]   Y. Li and K. T. Ramesh, "Influence of particle volume fraction, shape, and aspect ratio on the behavior of particle-reinforced metal–matrix composites at high rates of strain," *Acta Materialia,* vol. 46, pp. 5633–5646, 10/9, 1998.

[29]   M. Geni and M. Kikuchi, "Damage analysis of aluminum matrix composite considering non-uniform distribution of SiC particles," *Acta Materialia,* vol. 46, pp. 3125–3133, 5/22, 1998.

[30]   J. Segurado, C. González and J. L. Lorca, "A numerical investigation of the effect of particle clustering on the mechanical properties of composites," *Acta Materialia,* vol. 51, pp. 2355–2369, 5/7, 2003.

[31]   A. Sreeranganathan, A. M. Gokhale and P. Young, "Realistic micromechanical modeling of discontinuously reinforced composites," *Computational Materials Science,* vol. 49, pp. 407–413, 8, 2010.

[32]   M. Song and Y. He, "Effects of die-pressing pressure and extrusion on the microstructures and mechanical properties of SiC reinforced pure aluminum composites," *Material Design,* vol. 31, pp. 985–989, 2, 2010.

[33]   E. Law, S. D. Pang and S. T. Quek, "Effects of particle arrangement and particle damage on the mechanical response of metal matrix nanocomposites: a numerical analysis," *Acta Materialia,* vol. 60, pp. 8–21, 1, 2012.

[34]   A. Ayyar and N. Chawla, "Microstructure-based modeling of the influence of particle spatial distribution and fracture on crack growth in particle-reinforced composites," *Acta Materialia,* vol. 55, pp. 6064–6073, 10, 2007.

241

[35]   V. A. Romanova, R. R. Balokhonov and S. Schmauder, "The influence of the reinforcing particle shape and interface strength on the fracture behavior of a metal matrix composite," *Acta Materialia,* vol. 57, pp. 97–107, 1, 2009.

[36]   Z. Y Ma, S. R. Sharma and R. S. Mishra: "Effect of processing friction stir processing on the microstructure of cast A356 aluminum," *Materials Science and Engineering: A,* Vol. 433, pp. 269–78, 2006.

[37]   Y. Zha and T. Moan, "Ultimate strength of stiffened aluminum panels with predominantly torsional failure modes," *Thin-Walled Structures,* vol. 39, pp. 631–648, 8, 2001.

[38]   R. D. Doherty, D. A Hughes, F. J. Humphreys, J.J. Jonas, D. Juul Jensen, M. E. Kassner, W. E. King, T. R. McNelley, H. J. McQueen and A. D. Rollett: "Recrystallization: a review," *Materials Science and Engineering: A*, vol. A238, p. 219–94, 1997.

[39]   R. Rahmani Fard and F. Akhlaghi, "Effect of extrusion temperature on the microstructure and porosity of A356-SiC composites," *Journal of Materials Processing Technology,* vol. 187–188, pp. 433–436, 6/12, 2007.

[40]   A. El-Sabbagh, M. Soliman, M. Taha and H. Palkowski, "Hot rolling behaviour of stir-cast Al 6061 and Al 6082 alloys – SiC fine particulates reinforced composites," *Journal of Materials Processing Technology,* vol. 212, pp. 497–508, 2, 2012.

[41]   H. Xu and E. J. Palmiere, "Particulate refinement and redistribution during the axisymmetric compression of an Al/SiC metal matrix composite," *Composites Part A: Applied Science and Manufacturing,* vol. 30, pp. 203–211, 3, 1999.

[42]   W. G. Hutchison and E. J. Palmiere, "Microstructural development in a metal matrix composite during thermomechanical processing," *Materials Transactions, JIM,* vol. 37, pp. 203–211, 3, 1996.

[43]   M. Haghshenas, A. Zarei-Hanzaki and S. M. Fatemi-Varzaneh, "The effects of thermo-mechanical parameters on the microstructure of thixocast A356 aluminum alloy," *Materials Science and Engineering: A,* vol. 480, pp. 68–74, 5/15, 2008.

[44]   K. B. Nie, K. Wu, X. J. Wang, K. K. Deng, Y. W. Wu and M. Y. Zheng, "multidirectional forging of magnesium matrix composites: effect on microstructures and tensile properties," *Materials Science and Engineering: A,* vol. 527, pp. 7364–7368, 10/25, 2010.

[45]   V. M. Segal, "Materials processing by simple shear," *Materials Science and Engineering A*, vol. A197, pp. 157–164, 1995.

[46]   C. M. Cepeda-Jiménez, J. M. García-Infanta, A. P. Zhilyaev, O. A. Ruano and F. Carreño, "Influence of the supersaturated silicon solid solution concentration on the effectiveness of severe plastic deformation processing in Al–7 Wt.% Si casting alloy," *Materials Science and Engineering: A,* vol. 528, pp. 7938–7947, 10/15, 2011.

[47]   N. A. Akhmadeev, V. I. Kopylov, R. R. Mulyoukov and R. Z. Valiev, "Formation of submicron grain structure in copper and nickel by extensive shear deformation," *Izvestija Akademii nauk SSSR, Metally; "Russian Metallurgy"*, vol. 5, pp. 96–101, 1992

[48]   S. Swaminathan, M. R. Shankar, S. Lee, J. Hwang, A. H. King, R. F. Kezar, B. C. Rao, T. L. Brown, S. Chandrasekar, W. D. Compton and K. P. Trumble, "Large strain deformation and ultra-fine grained materials by machining," *Materials Science and Engineering: A,* vol. 410–411, pp. 358–363, 11/25, 2005.

[49]   M. Kawasaki, B. Ahn and T. G. Langdon, "Microstructural evolution in a two-phase alloy processed by high-pressure torsion," *Acta Materialia,* vol. 58, pp. 919–930, 2, 2010.

[50]   W. Wang, I. Manas-Zloczower, and M. Kaufman, "Characterization of distributive mixing in polymer processing equipment using Renyi entropies," *International Polymer Process*ing, 16, 315 (2001).

[51]   N. Harnby, M.F. Edwards, A. W. Nienow, *Mixing in the Process Industries*, 2nd ed. London: Butterworth-Heinemann, 1997.

[52]   GAO Report 96-4 on Nuclear safety, "Concerns with nuclear facilities and other sources of radiation in the former soviet union," 1995.

[53]   M. M. Alvarez-Hernández, T. Shinbrot, J. Zalc and F. J. Muzzio, "Practical chaotic mixing," *Chemical Engineering Science,* vol. 57, pp. 3749–3753, 9, 2002.

[54]   S. K. Samanta, N. Mandal and C. Chakraborty, "Development of structures under the influence of heterogeneous flow field around rigid inclusions: insights from theoretical and numerical models," *Earth-Science Review,* vol. 58, pp. 85–119, 7, 2002.

[55]   B. A. Bilby, J. D. Eshelby and A. K. Kundu, "Change of shape of a viscous ellipsoidal region embedded in a slowly deforming matrix having a different viscosity," *Tectonophysics,* vol. 28, pp. 265–274, 1975.

[56]   G. B. Jeffery, "The motion of ellipsoidal particles immersed in a viscous fluid," *Proceedings of the Royal Society of London A,* vol. 102, pp. 102–161, 179, 1922.

[57]   S. H. Peighambardoust, A. J. van der Goot, R. J. Hamer and R. M. Boom, "Effect of simple shear on the physical properties of glutenin macro polymer (GMP)," *Journal of Cereal Science,* vol. 42, pp. 59–68, 7, 2005.

[58]   A. K. S. Chesterton, B. E. Meza, G. D. Moggridge, P. A. Sadd and D. I. Wilson, "Rheological characterization of cake batters generated by planetary mixing: elastic versus viscous effects," *Journal of Food Engineering,* vol. 105, pp. 332–342, 7, 2011.

[59]   S. V. Goncharov, "Mixing and homogenization of components in the manufacture of antifrictional materials," *Russian Engineering Research*, vol. 31, pp 873–876, 2011.

[60]   A. Arora, T. DebRoy and H. K. D. H. Bhadeshia, "Back-of-the-envelope calculations in friction stir welding – velocities, peak temperature, torque, and hardness," *Acta Materialia,* vol. 59, pp. 2020–2028, 3, 2011.

[61]   P. Ho, "Motion of inclusion induced by a direct current and a temperature gradient," *Journal of Applied Physics*, vol. 41, pp. 64–68, 1, 1970.

[62]   Z. Li and N. Chen, "EM-driven motion of an elliptical inclusion," *Applied Physics Letters,* vol. 93, p. 051908 , 5, 2008.

[63]   X. Dong and Z. Li, "Analytical solution for motion of an elliptical void under a gradient stress field," *Applied Physics Letters,* vol. 94, p. 071909 ,7, 2009.

[64]   Y. Li, Z. Li, X. Wang and J. Sun, "Analytical solution for motion of an elliptical inclusion in a gradient stress field," *Journal of the Mechanics and Physics of Solids,* vol. 58, pp. 1001–1010, 7, 2010.

[65]   J. S. H., "Homogenization of milk and cream," *Journal of the Franklin Institute,* vol. 216, pp. 416, 9, 1933.

[66]   S. Rwei, I. Manas-Zloczower, D. L. and Feke, "Observation of Carbon Black Agglomerate Dispersion in Simple Shear Flows," *Polymer Engineering and Science*, vol. 30, pp. 701–706, 1990.

[67]   C. Pomchaitaward, I. Manas-Zloczower and D. L. Feke, "Investigation of the dispersion of carbon black agglomerates of various sizes in simple-shear flows," *Chemical Engineering Science,* vol. 58, pp. 1859–1865, 5, 2003.

[68]   Eckstein, Eugene C., "Particle migration in a linear shear flow", Ph.D. Dissertation, Dept. Mech. Eng., Massachusetts Institute of Technology, Cambridge, MA, 1975.

[69]   D. Broday, M. Fichman, M. Shapiro and C. Gutfinger, "Motion of spheroidal particles in vertical shear flows," *Physics of Fluids,* vol. 10, pp. 86–86, 1998.

[70]   B. C. Liechty and B. W. Webb, "The use of plasticine as an analog to explore material flow in friction stir welding," *Journal of Materials Processing Technology,* vol. 184, pp. 240–250, 4/12, 2007.

[71]   Yurko, James A., "Fluid flow behavior of semi-solid aluminum at high shear rates," Ph.D. Dissertation, Dept. Materials Science Eng. Massachusetts Institute of Technology, Cambridge, MA, 2001.

[72]   T. Hyoe, P. A. Colegrove and H. R. Shercliff, "Thermal and microstructure modeling in thick plate aluminum alloy 7075 friction stir welds," in *Friction Stir Welding and Processing II, March 2, 2003 – March 6,* 2003, pp. 33–42.

[73]   W. J. Arbegast, Z. Jin, A. Beaudoin, T. A. Bieler, B. Radhakrishnan, Eds., *Hot Deformation of Aluminum Alloys III*, TMS, 2003.

[74]   D. Butan and J. Monahan, "Thermomechanical modeling friction stir welding aluminum 2024-T3," *International Journal of Computational Materials Science and Surface Engineering*, vol. 2, pp. 63–72, 2009.

[75]   G. J. Bendzsak, C. B. Smith, in: Proceedings of the Second International Symposium on Friction Stir Welding, Gothenburg, Sweden, June 26–28, 2000.

[76]   R. Nandan, G. G. Roy, T. J. Lienert and T. Debroy, "Three-dimensional heat and material flow during friction stir welding of mild steel," *Acta Materialia,* vol. 55, pp. 883–895, 2, 2007.

[77]   G. Buffa, J. Hua, R. Shivpuri and L. Fratini, "A continuum based fem model for friction stir welding model development," *Materials Science and Engineering: A,* vol. 419, pp. 389–396, 3/15, 2006.

[78]   C. Cox, D. Lammlein, A. Strauss, G. Cook. "Modeling the control of an elevated tool temperature and the effects on axial force during friction stir welding," *Materials and Manufacturing Processes*, vol. 25, pp. 1278–1282 11, 2010.

[79]   J. Cho and P. R. Dawson, "Investigation on texture evolution during friction stir welding of stainless steel," *Metallurgical and Materials Transactions A,* vol. 37, pp. 1147–1164, 2006.

[80]   D. E. Boyce, P. R. Dawson, B. Sidle and T. Gnaupel-Herold, "A multiscale methodology for deformation modeling applied to friction stir welded steel," *Computational Materials Science,* vol. 38, pp. 158–175, 2006.

[81]   N. Birnbaum, N. Francis, B. Gerber, "Coupled techniques for the simulation of fluid-structure and impact problems," presented at the *8th International Conference on Numerical Mathematics and Computational Mechanics*, 1999.

[82]   I. Manas-Zloczower (1997, Jan. 15), "Analysis of Mixing in Polymer Processing Equipment." [Online]. Available: http:\\:www.rheology.org/sor/publications/ rheology_b/Jan97/mixing.pdf.

[83]   K. Danzer and R. Singer, "Application of pattern recognition methods for the investigation of chemical homogeneity of solids," *Microchimica Acta,* vol. 85, pp. 219–226, 1985.

[84]   K. Danzer and G. Erhrlich, *Tagungsber Techn*ische *Hochschule*, *Karl-Marx-Stadt 4. Tagung Festk6rperanalytik*, *Plenar* und *Hauptvortrige*, vol. *12*, p. 547, *1984*.

[85]   V. Liebich, G. Ehrlich, U. Herrmann, L. Siegert and W. Kluge, "Characterization of the chemical homogeneity of solid-state materials by chemometric methods, multivariate aspects and general recommendations," *Fresenius' Journal of Analytical Chemistry,* vol. 343, pp. 251–258, 1992.

[86]   W. Spitzig, J. Kelly, and O. Richmond, "Quantitative characterization of second-phase populations," *Metallography,* vol. 18, pp. 235–261, 1985.

[87]   N. Yang, J. Boselli, P. J. Gregson, and I. Sinclair," Simulation and quantitative assessment of finite-size particle distributions in MMC's," *Material Science Technology,* vol. 16, pp. 797–805, 2000

[88]   S. Torquato and S. B. Lee, "Computer simulations of nearest-neighbor distribution functions and related quantities for hard-sphere systems," *Physica A: Statistical Mechanics and its Applications,* vol. 167, pp. 361–383, 8/15, 1990.

[89]   Y. Mao, A. M. Gokhale, and J. Harris, "Computer simulations of realistic microstructures of coarse constituent particles in a hot-rolled aluminum alloy," *Computational Materials Science,* vol. 37, pp. 543–556, 10, 2006.

[90]   A. Tewari and A. M. Gokhale, "Computations of contact distributions for representation of microstructural spatial clustering," *Computational Materials Science,* vol. 38, pp. 75–82, 11, 2006.

[91]   A. Tewari, A. M. Gokhale, J. E. Spowart, and D. B. Miracle, "quantitative characterization of spatial clustering in three-dimensional microstructures using two-point correlation functions," *Acta Materialia,* vol. 52, pp. 307–319, 1/19, 2004.

[92]   Z. Horita, M. Furukawa, K. Oh-ishi, M. Nemoto, and T. G. Langdon, "Equal-channel angular pressing for grain refinement of metallic materials" published for *The Fourth International Conference on Recrystallization and Related Phenomena*, The Japan Institute of Metals, 1999.

[93]   A. Ma, M. Takagi, N. Saito, H. Iwata, Y. Nishida, K. Suzuki and I. Shigematsu, "Tensile properties of an Al–11 mass%Si alloy at elevated temperatures processed by rotary-die equal-channel angular pressing," *Materials Science and Engineering: A,* vol. 408, pp. 147–153, 11/5, 2005.

[94]   I. Gutierrez-Urrutia, M. A. Muñoz-Morris, I. Puertas, C. Luis and D. G. Morris, "Influence of processing temperature and die angle on the grain microstructure produced by severe deformation of an Al–7% Si alloy," *Materials Science and Engineering: A,* vol. 475, pp. 268–278, 2/25, 2008.

[95]   J. M. García-Infanta, A. P. Zhilyaev, C. M. Cepeda-Jiménez, O. A. Ruano and F. Carreño, "Effect of the deformation path on the ductility of a hypoeutectic Al–Si casting alloy subjected to equal-channel angular pressing by routes A, B$_A$, B$_C,$ and C," *Scripta Materialia.,* vol. 58, pp. 138–141, 1, 2008.

[96]   A. Ma, N. Saito, M. Takagi, Y. Nishida, H. Iwata, K. Suzuki, I. Shigematsu and A. Watazu, "Effect of severe plastic deformation on tensile properties of a cast Al–11 mass% Si alloy," *Materials Science and Engineering: A,* vol. 395, pp. 70–76, 3/25, 2005.

[97]   ANSYS/AUTODYN, vol. 13.0, Manual, ANSYS Inc., Canonsburg, PA, 2010

[98]   E. Chen, L. Duchêne, A. Habraken and B. Verlinden, "Multiscale modeling of back-stress evolution in equal-channel angular pressing: from one pass to multiple passes," *Journal of Materials Science,* vol. 45, pp. 4696–4704, 2010.

[99]   Y. G. Jin, I. Son, S. Kang, and Y. Im, "Three-dimensional finite element analysis of multi-pass equal-channel angular extrusion of aluminum AA1050 with split dies," *Materials Science and Engineering: A,* vol. 503, pp. 152–155, 3/15, 2009.

[100]   E. Cerri, P. P. De Marco and P. Leo, "FEM and metallurgical analysis of modified 6082 aluminum alloys processed by multipass ECAP: influence of material properties and different process settings on induced plastic strain," *Journal of Materials Processing Technology,* vol. 209, pp. 1550–1564, 2/1, 2009.

[101]   N. Mahallawy, F. Shehata, M. Hameed, M. Aal and H. Kim, "3D FEM simulations for the homogeneity of plastic deformation in Al–Cu alloys during ECAP," *Materials Science and Engineering: A,* vol. 527, pp. 1404–1410, 3/15, 2010.

[102]   M. Ashby, F. Blunt, and M. Bannister, 'Flow characteristics of highly constrained metal wires," *Acta Metallurgica*, vol. 37, p. 1857, 1989.

[103]   Y. Huang, J. Hutchinson, and V. Tvergard, "Cavitation instabilities in elastic-plastic solids," *Journal Of Mechanical Physics Of Solids*, vol. 32, pp. 223–242, 1991.

[104] S. Lathabai, M. J. Painter, G. M. D. Cantin and V. K. Tyagi, "Friction spot joining of an extruded Al–Mg–Si alloy," *Scripta Materialia.,* vol. 55, pp. 899–902, 11, 2006.

[105] V. Balasubramanian, "Relationship between base metal properties and friction stir welding process parameters," *Materials Science and Engineering: A,* vol. 480, pp. 397–403, 5/15, 2008.

[106] H. W. Zhang, Z. Zhang and J. T. Chen, "The finite element simulation of the friction stir welding process," *Materials Science and Engineering: A,* vol. 403, pp. 340–348, 8/25, 2005.

[107] C. J. Smithells, E. A. Brandes, "Metallography," in *Smithells Metals Reference Book* (5th Edition)*,* Butterworth and Co. Ltd, New York, 1978, pp. 300–302.

[108] H. Okamoto, *Phase Diagrams for Binary Alloys*, Desk Handbook, vol. 1, 2000.

[109] Aoki Y., Hayashi S., and Komatsu H., "Liquidus and eutectic temperature measurements of al-rich alloys containing Cu and Si in a magnetic field of 3.5 TJ," *Crystal Growth*, vol. 123, pp. 313–316, 1992.

[110] S. Fujikawa, K. Hirano and Y. Fukushima, " Diffusion of silicon in aluminum," *Metallurgical and Materials Transactions A*, vol. 9, 12, pp. 1811–1815, 1978.

[111] A. Paccagnella, G. Ottaviani, P. Fabbri, G. Ferla and G. Queirolo, "Silicon diffusion in aluminum," *Thin Solid Films,* vol. 128, pp. 217–223, 6/28, 1985.

[112] M. Okabe, T. Mori, T. Mura, "Internal friction caused by diffusion around a second-phase particle Al-Si alloy", Philosophical Magazine A , vol. 44, pp. 1–12, 1, 1981.

[113] D. J. Fisher, Ed., *Diffusion in Silicon: 10 Years of Research*. Zurich, Switzerland: Trans Tech Publications, 1998.

[114] W. Yuan, R. S. Mishra, B. Carlson, R. Verma and R. K. Mishra, "Material flow and microstructural evolution during friction stir spot welding of AZ31 magnesium alloy," *Materials Science and Engineering: A,* vol. 543, pp. 200–209, 5/1, 2012.

[115] M. E. Seniw, J. G. Conley and M. E. Fine, "The effect of microscopic inclusion locations and silicon segregation on fatigue lifetimes of aluminum alloy A356 castings," *Materials Science and Engineering: A,* vol. 285, pp. 43–48, 6/15, 2000.

[116] S. Nafisi and R. Ghomashchi, "Effects of modification during conventional and semi-solid metal processing of A356 Al-Si alloy," *Materials Science and Engineering: A,* vol. 415, pp. 273–285, 1/15, 2006.

[117] M. L. Santella, T. Engstrom, D. Storjohann and T. Pan, "Effects of friction stir processing on mechanical properties of the cast aluminum alloys A319 and A356," *Scripta Materialia,* vol. 53, pp. 201–206, 7, 2005.

[118] Y. J. Kwon, I. Shigematsu and N. Saito, "Mechanical properties of fine-grained aluminum alloy produced by friction stir process," *Scripta Materialia.,* vol. 49, pp. 785–789, 10, 2003.

[119] W. J. Arbegast, "A flow-partitioned deformation zone model for defect formation during friction stir welding," *Scripta Materialia,* vol. 58, pp. 372–376, 3, 2008.

[120] Y. G. Kim, H. Fujii, T. Tsumura, T. Komazaki and K. Nakata, "Three defect types in friction stir welding of aluminum die casting alloy," *Materials Science and Engineering: A,* vol. 415, pp. 250–254, 1/15, 2006.

[121] K. N. Krishnan, "On the formation of onion rings in friction stir welds," *Materials Science and Engineering: A,* vol. 327, pp. 246–251, 4/30, 2002.

[122] K. Kumar and S. V. Kailas, "The role of friction stir welding tool on material flow and weld formation," *Materials Science and Engineering: A,* vol. 485, pp. 367–374, 6/25, 2008.

[123] H. N. B. Schmidt, T. L. Dickerson and J. H. Hattel, "material flow in butt friction stir welds in AA2024-T3," *Acta Materialia,* vol. 54, pp. 1199–1209, 2, 2006.

[124] J. Beck, "Effect of orientation and of shape similarity on perceptual grouping," *Behavioral Science,* vol. 1, pp. 300–302, 5, 1966

[125] J. Beck, "Perceptual grouping produced by line figures," *Behavioral Science,* vol. 2, pp. 491–495, 11, 1967.

[126] P. H. S. W. Kulatilake, D. N. Wathugala, M. Poulton and O. Stephansson, "Analysis of structural homogeneity of rock masses," *Engineering Geology.,* vol. 29, pp. 195–211, 10, 1990.

[127] F. Tomita, M. Yachida, and S. Tsjui, "Detection of homogeneous regions by structural analysis," Proceedings of the 3rd international joint conference on Artificial intelligence, pp. 564–571, 1973.

[128] Y. Yakimovsky, "Boundary and object detection in real world images", *Journal of the Association for Computing Machinery*, vol. 23, p. 599–618, 4, 1976.

[129] A. Papoulis, *Probability, Random Variables, and Stochastic Processes*, 2nd ed., New York, McGraw-Hill, 1984.

[130] M. J. Roberts, M. J. and R. Riccardo, "An introduction to factorial designs and interactions," in *A Student's Guide to Analysis of Variance,* London, Routledge, 1999, pp. 134–152.

[131] G. W. Snedecor and W. G. Cochran, "Analysis of covariance," in *Statistical Methods,* 7th ed. Ames, IA: Iowa State Press, 1980, pp. 374–393.

[132] A. Torrala, "How many pixels make an image?," *Visual Neuroscience*, vol. 26, pp. 123–131, 1, 2009.

[133] B. Munson, D. Young, and T Okiishi, "Superposition of basic, plane potential flows," in *Fundamentals of Fluid Mechanics*. New York: John Wiley and Sons, 1990, pp. 363–369.

[134] S. R. Blair and J. C. Woertz (private Communication), Naval Postgraduate School, Monterey, CA, 2012.

[135] J. E. Hatch, *Aluminum Properties and Physical Metallurgy*, ed. John E. Hatch, American Society for Metals, Metals Park, Ohio, 1984.

[136] M. Rhodes, "Single particles in a fluid," in *Introduction to Particle Technology*, 2nd ed. West Sussex, England: John Wiley & Son, 2008, pp. 29–49.

[137] Y. Beygelzimer, "Vortices and mixing in metal during sever plastic deformation," *Material Science Forum,* vol. 683, pp. 213–224, 2011.

[138]   C. W. Sinclair, J. D. Embury and G. C. Weatherly, "Basic aspects of the co-deformation of BCC/FCC materials," *Materials Science and Engineering: A,* vol. 272, pp. 90–98, 11/15, 1999.

[139] J. D. Embury and C. W. Sinclair, "The mechanical properties of fine-scale two-phase materials," *Materials Science and Engineering: A,* vol. 319–321, pp. 37–45, 12, 2001.

[140] D. Raabe, S. Ohsaki and K. Hono, "Mechanical alloying and amorphization in Cu–Nb–Ag in situ composite wires studied by transmission electron microscopy and atom probe tomography," *Acta Materialia,* vol. 57, pp. 5254–5263, 10, 2009.

[141] D. Aldous and P. Diaconis, "Trailing the dovetail shuffle to its lair," *The American Mathematical Monthly*, vol. 95, pp. 333–348, 5, 1992.

INITIAL DISTRIBUTION LIST

3.   Defense Technical Information Center
        Ft. Belvoir, Virginia

4.   Dudley Knox Library
        Naval Postgraduate School
        Monterey, California

5.   Professor Terry R. McNelley
        Department of Mechanical Engineering
        Naval Postgraduate School
        Monterey, California

6.   Jeffrey C. Woertz
        Wye Mills, Maryland